Doctoral theses at NTNU, 2021:217

Andreas Liudi Mulyo

Molecular Beam Epitaxy of GaN/AlGaN Nanocolumns on Graphene

for Potential Application in Ultraviolet Light-Emitting Diodes

Doctoral thesis

NTNU
Norwegian University of Science and Technology
Thesis for the Degree of
Philosophiae Doctor
Faculty of Information Technology and Electrical
Engineering
Department of Electronic Systems

NTNU
Norwegian University of
Science and Technology

Andreas Liudi Mulyo

Molecular Beam Epitaxy of GaN/AlGaN Nanocolumns on Graphene

for Potential Application in Ultraviolet Light-Emitting Diodes

Thesis for the Degree of Philosophiae Doctor

Trondheim, June 2021

Norwegian University of Science and Technology
Faculty of Information Technology and Electrical Engineering
Department of Electronic Systems

NTNU
Norwegian University of
Science and Technology

NTNU
Norges teknisk-naturvitenskapelige universitet
Norwegian University of Science and Technology

Thesis for the Degree of Philosophiae Doctor
Faculty of Information Technology and Electrical Engineering
Department of Electronic Systems

Submitted 22 March 2021;
Approved 11 May 2021;
Date of defense 16 June 2021; Rådsrommet G144 | 13:15

Supervisors
Prof. Bjørn-Ove Fimland & Prof. Helge Weman

Assessment Committee
- 1st opponent
  Dr. Lutz Geelhaar,
  Paul-Drude-Institut für Festkörperelektronik
  Paul Drude Institute for Solid State Electronics
  Berlin, Germany
- 2nd opponent
  Dr. Marta Sobańska,
  Instytut Fizyki Polskiej Akademii Nauk
  Institute of Physics of the Polish Academy of Sciences
  Warsaw, Poland
- Additional members of the committee and administrator
  Prof. Astrid Aksnes

MOLECULAR BEAM EPITAXY OF GAN/ALGAN NANOCOLUMNS ON GRAPHENE:
FOR POTENTIAL APPLICATION IN ULTRAVIOLET LIGHT-EMITTING DIODES

ISBN 978-82-326-6610-2 (printed ver.)
ISBN 978-82-326-5572-4 (electronic ver.)
ISSN 1503-8181 (printed ver.)
ISSN 2703-8084 (online ver.)

Doctoral theses at NTNU, 2021:217

Printed by NTNU Grafisk senter

Dedicated to my mother,
Lili Anita Luwanto

And to my father,
Sampurno Liudi Mulyo

Whom have I in heaven [but You]?
And besides You, I desire nothing on earth.
My flesh and my heart may fail,
But God is the rock *and* strength of my heart and my portion forever.

- A psalm of Asaph

◆

But no one except Lucy knew that
as it circled the mast it had whispered to her,

"Courage, dear heart,"

and the voice, she felt sure, was Aslan's,
and with the voice a delicious smell breathed in her face.

- C.S. Lewis, The Voyage of the Dawn Treader

◆

"My own plans are made.
While I *can*, I sail east in the Dawn Treader.
When she *fails* me, I paddle east in my coracle.
When she *sinks*, I shall swim east with my four paws.
And when I *can swim no longer*, if I have not reached Aslan's country,
or shot over the edge of the world into some vast cataract,
I shall sink with my nose to the sunrise."

Reepicheep, the talking mouse
- C.S. Lewis, The Voyage of the Dawn Treader

Abstract

Hybrid integration of defect-free III-nitride semiconductor nanocolumns and two-dimensional graphene as their substrate is an extremely promising route towards the development of ultraviolet light emitters, as graphene can be simultaneously utilized as a transparent conductive electrode. Nevertheless, a proof-of-concept of such hybrid device system has not been achieved before this work, and the study of highly dense vertical nanocolumns on graphene is also inadequately discussed. This PhD dissertation presents the investigation on the molecular beam epitaxial growth and the associated structural, optical and electrical properties of GaN nanocolumns and GaN/AlGaN nanocolumn ultraviolet light-emitting diode structures formed on graphene.

Self-organized GaN nanocolumns are grown firstly on amorphous fused silica, and then on graphene substrates by employing AlN buffer layer. High density of vertical nanocolumns characterized with excellent crystalline quality is achieved on these substrates. Particularly for the growth on graphene possessing no dangling bonds in its surface, additional study is carried out to clarify the role of the thin AlN as an intermediate layer between the formation of self-assembled GaN nanocolumns and graphene. Besides leading to the distinct arrangements of AlN that can affect the growth orientation of GaN nanocolumns, different AlN growth conditions unintentionally alter the structural properties of graphene.

Based on the understandings gained through the studies mentioned above, vertical growth of heterostructured GaN/AlGaN self-organized nanocolumns is subsequently realized on graphene. This growth orientation of the nanocolumns on graphene is essential for the light-emitting diode fabrication from as-grown nanocolumn samples. Here, graphene is employed as the growth substrate and simultaneously as the transparent conducting electrode for wurtzite GaN/AlGaN nanocolumns. In spite of high sheet resistance of graphene after the nanocolumn growth, a single excitonic emission peak can be observed at 365 and ~350 nm (ultraviolet-A region) for the devices grown on double-layer graphene and single-layer graphene, respectively.

This PhD thesis shows a vivid example on the development of nitride nanocolumn/graphene-based device technology. In this regard, the combination between these two materials provides a new approach in designing the ultraviolet light-emitting diodes, owing to the unique graphene properties.

Preface

This thesis is submitted as a partial fulfilment of the requirements for the Degree Philosophiae Doctor (Ph.D.) at the Norwegian University of Science and Technology (NTNU). This doctoral work has been carried out at the Department of Electronic Systems, Faculty of Information Technology and Electrical Engineering, with Professor Bjørn-Ove Fimland and Professor Helge Weman as main supervisor and co-supervisor, respectively.

A total time of seven years (from March 2014 to March 2021) was spent to complete the main portion of this research work, teaching duties (of more than one and a half year) and five courses of 32.5 *studiepoeng* (equivalent to 32.5 points in the European Credit Transfer System, or one semester). Within the time frame of this Ph.D. work, I also spent altogether one year and nine months for research stay (from October 2015 to December 2016, from June 2017 to September 2017 and from June 2018 to September 2018) in Professor Katsumi Kishino's research group at the Department of Engineering and Applied Physics, Faculty of Science and Technology, Sophia University in Tokyo, Japan.

This research has been part of the FRINATEK and NANO2021 projects, which were funded through the Norwegian Research Council, Grant number No. 214235 and No. 239206/No. 259553, respectively. The Research Council of Norway is also acknowledged for the support to NTNU NanoLab through the Norwegian Micro- and Nano-Fabrication Facility, NorFab (Grant No. 197411/No. 245963/No. 295864), the NORTEM facility (Grant No. 197405/F50), and the Norwegian PhD Network on Nanotechnology for Microsystems (FORSKERSKOLER-221860/F40). The research activities conducted while I was in Professor Katsumi Kishino's laboratory were supported by Japan Society for the Promotion of Science KAKENHI with Grant No. 24000013/No. 19H00874.

OBJECTIVES AND SCOPE

One of the key issues in advancing the progress of the electronic and optoelectronic devices based on the group-III nitride material system is the availability of high-quality (native) substrates. The present commercially available substrates, such as sapphire, SiC and Si suffer from high lattice mismatch with the group-III nitrides. Although the quality of the large GaN substrates has been improved over the last years, the defect density in this substrate is not negligible. Hence, the pursuit of optional substrates for III-nitride semiconductors is of importance for the basis of the improvements of future device applications.

In this regards, the synthesis of III-V nitride nanocolumns on graphene substrates can emerge to be a promising alternative combination of materials to mitigate the current issues as well as open up a number of new possibilities for more device functionalization. While the crystalline quality of GaN/AlGaN nanocolumn UV-LEDs is exceptional, their EQE is rather low due to absorbing nature of the conventional substrates (except for those grown on sapphire. However, sapphire has its own limitation as introduced previously). For this reason, graphene was investigated in this PhD thesis to study its feasibility as a growth substrate and simultaneously as a transparent conductive electrode for GaN/AlGaN nanocolumn LED structures. The choice of using graphene is primarily due to its good transparency across all wavelength region (including UV to deep UV) and high electrical conductivity.

The main objectives of this PhD thesis are broken down as follows:

Objective 1. Conducting preliminary growth studies of *n*-GaN nanocolumns on fused silica (amorphous glass or silica glass) substrates.

Objective 2. Performing and understanding the growth of *n*-GaN nanocolumns on transferred graphene on fused silica substrates.

Objective 3. Carrying out the growth of a UV-A LED structure consisting of *n*-AlGaN/*i*-GaN/*p*-AlGaN nanocolumns on graphene (transferred onto silica glass as the substrate carrier).

All the nanocolumn growth studies were conducted using MBE technique. Requisite structural and optical characterizations of the grown nanocolumn samples have been consistently performed to support the claims and findings of the aforementioned studies. Device fabrications and electrical characterizations have been carried out especially for nanocolumn LED samples in objective 3.

OUTLINES

The first four chapters (Part I consisting of Chapters 1 through 4) are written to introduce an overall perspective of III-nitride material system, provide basic understanding of nanocolumn and graphene, as well as summarize the experimental methods that have been performed during the PhD study.

The main results of this doctoral thesis are presented as a collection of four published academic papers and one manuscript under review, systematically organized in Chapters 5 to 9 (Part II). The title and content of the published papers presented in the aforementioned chapters are basically the accepted manuscript version in their respective journals (copyright information and author contributions are given in the first page of each chapter). They have been re-typeset from their original sources for integration into this PhD dissertation. While for the manuscript under review, it will undergo further modifications, and the accepted version of that manuscript will be different compared to that presented here.

In the last chapter (Part III consisting of Chapter 10), the conclusions of the current topic and outlook for further researches are presented. Below is further description for all chapters given in this document:

Chapter 1 is drafted to give readers a brief background, general context as well as inherent growth challenges of group III-nitride compound semiconductors.

Chapter 2 contains the short information regarding Si whisker and its relation with GaN nanocolumn. Some important findings concerning the growth mechanism of GaN nanocolumns mainly on the silicon substrate are presented. Their structural, optical and electrical properties are then listed. This chapter is then ended with the basic information on the LEDs based on nanocolumn structure.

Chapter 3 is started with short information on the alternative substrates to silicon and sapphire. Next, the role of graphene as the prospective substrate material for III-V nitride is discussed. Within the same section, the synthesis of graphene along with its mainstream utilization are concisely reviewed. The examinations on the recent related works of III-V nitride nanocolumns on exotic and unusual amorphous substrates, including graphene, are then given.

Chapter 4 provides a brief description of the nitride nanocolumn growth using an MBE technique. Together with the structural and optical characterization techniques applied to nanocolumns and graphene, the device fabrication methods and its corresponding electrical measurements are shortly explained.

Chapter 5 studies the growth of GaN nanocolumns on fused silica glass substrates, along with their related structural and optical characterization results. This chapter serves as an initial study for nanocolumn growth on amorphous substrate, which is used as the graphene substrate carrier for the following studies. This chapter is based on the accepted manuscript published in the Journal of Crystal Growth (© 2017 Elsevier).

Chapter 6 introduces the growth results of GaN nanocolumns on graphene using AlN as a buffer layer. Afterwards in *Chapter 7*, the investigation on how the AlN buffer layer can influence the growth of GaN nanocolumns is provided. To properly interpret the MBE growth outcomes, structural and optical investigations accompany each of these studies. These two chapters are based on the accepted manuscripts published in the Nanotechnology (© 2018 IOP Publishing Ltd.) and Scientific Reports (© 2020 Andreas Liudi Mulyo, *et al*), respectively.

Chapter 8 focuses on the utilization of *double-layer* graphene as the growth substrate and transparent conductive electrode for GaN/AlGaN nanocolumn-based UV LEDs in a flip-chip configuration. Structural properties of the grown nanocolumns and graphene (after MBE growth), as well as optical properties of the nanocolumns are briefly discussed. At the end, the flip-chip nanocolumn UV LEDs on graphene and their electrical characterizations are reported. This chapter is based on the accepted manuscript published in the Nano Letters (© 2019 American Chemical Society).

Chapter 9 discusses the concept of *single-layer* graphene as the transparent conducting substrate for flip-chip GaN/AlGaN nanocolumn-based ultraviolet LEDs. Similar characterization methods as those used in chapter 8 are carried out to study the properties of the nanocolumns, graphene as well as the device performance. In addition, the role of the AlN buffer layer in maintaining the verticality of nanocolumns is also highlighted. This chapter is based on the manuscript which is now under review (© 2021 Andreas Liudi Mulyo, *et al*).

Chapter 10 presents the audience with a summary and conclusions of the present works defined within the scope of this dissertation, and possible measures that can be carried out in the future works in order to improve the efficiency of the UV LEDs based on the hybrid III-V nitride nanocolumns on graphene substrates.

Three appendixes are included following Chapter 10. Appendix A contains an additional figure for Subsection 3.2.3 (Chapter 3). Appendixes B and C are the supporting information for Chapters 8 and 9, respectively. Curriculum vitae of the author, full list of the dissemination of research (i.e., published papers, manuscript under review and conference presentations), summary of copyright permissions for the figures, and index are provided after the appendixes.

NAVIGATING THIS PHD THESIS

As important as the content of this PhD work, I have spent a quite number of hours in choosing the right font and designing the layout (using LaTeX) that are decent enough to hold the information written in this book. The draft of this thesis was firstly prepared in typical word processing software, but its final version was then converted to LaTeX. During the writing of this dissertation, I attempted to incorporate two major features, which from my perspective, can aid the reader in browsing the content of this thesis. For further detail, the reader is referred to see the colophon given at the very end of this book.

The first one being the reference section is given at the end of each chapter, due to ease of access for the reader who reads the physical copy. (Because of this however, readers might find duplicated references in other chapters.) Importantly, the page/s where that reference/s is/are cited will be displayed at the end of each reference. This can help particularly for the reader who reads the digital copy, meaning that the reader does not need to remember the page where they were before clicking that specific reference.

The second feature is two-way link between any item displayed in the table of content and any chapter/section/subsection in this PhD thesis. The reader might find this function useful for quick navigation back to the table of content. It is used here to let the reader navigate this PhD thesis in ease.

FINALLY

"Why do you spend *too much time* writing your thesis? Just do it as fast as possible, get a job and move on with your life!" said a colleague of mine in our several meetings last year. Contemplating this message, I questioned myself what another main motivation of me writing this lengthy PhD thesis is, besides to conform with the conditions to obtain a PhD degree, obviously. Then I found my own answer to that comment.

This thesis is, in the first place, written for myself as my personal quest, i.e., how I see and comprehend the involved subjects based on my understanding. I have to admit that my dissertation is relatively longer than other published doctoral theses at NTNU. However, I need to provide any necessary information here with the purpose to remind myself how matters are defined and connected with each other. Because of this, some readers might find some parts are redundant. In the course of writing this book, I have received a tremendous amount of help from Professor Bjørn-Ove Fimland and Professor Helge Weman, in shaping how the thesis is presented at the very moment. Indeed, this is the thesis I envisioned once I finished the first draft of Chapter 1 in November 2019.

This PhD dissertation is my humble contribution to science, my endeavor to catch a glimpse of beauty and elegance of how small matters are formed and harmoniously combined together in order to achieve certain functions. There are, certainly, many aspects that can be improved, but for now, this is the best piece of work I have ever written (along with the assistance from many co-authors whose names will be mentioned later). I am fortunate to have several years of opportunities to get paid for doing what I enjoy the most, and can only hope to get involved with more exciting research themes to come within the near future. Besides gathering dust in the library and sinking in the sea of the internet, I hope this work can be a stepping stone to someone, somewhere, to further advance this field. If it is deemed appropriate, be sure to cite!

「何が幸せかわからないです。

正しい道を進む中の出来事なら

峠の上り下りもみんな本当の

幸せに近づく一足づつですから」

- 宮沢賢治，「銀河鉄道の夜」

"No one knows what true happiness is, least of all me. But no matter how hard it is, if you keep to the path you deem to be true, you can overcome any mountain. With each step in that direction, people come closer to happiness."

- Kenji Miyazawa,
Night on the Galactic Railroad

Acknowledgements

Never have I imagined that I am allowed to write this part of the thesis. As a note, this is composed after I got permission from my supervisor to submit my thesis. Meaning that this part is scribbled at the very last of my PhD thesis. This is the only part of my PhD thesis that I can be subjective, and no correction from my supervisors has been done here either. So, please bear it in case there are many English typos. Perhaps some might argue that my section of Acknowledgments is unnecessarily (or rather extremely) long, but this thesis itself in total is already lengthy (~300 pages!). Thus, I don't see any difference if I put in an extra five to six-page more. Also, there is no rule on how long this part can be, so I will take that literally. Besides, I realize that these particular pages will probably be the most interesting for my family and friends who are not into the nanotechnology field. In this case, the rest of you will have to bear with me. Here, I would like to mention *every* individual whom I have encountered and contribute in their own way during this phase of my life, academically and emotionally.

The first and the foremost person whom I should thank for is clear, that is Professor Bjørn-Ove Fimland, for his persistent support and enduring guidance during the course of my PhD (and thank you for driving me every other night during the winter). With the utmost gratitude I would also like to thank Professor Helge Weman for being the "watcher" of my PhD, i.e., a person who always reminds me the big picture of my research, after I get lost in the detail (thank you also for your dinner invitations as well!). Their enthusiasm in education and research, along with their experience and knowledge has taught me how to become a full-fledged researcher. Moreover, their guidance and vision have truly shaped me into the researcher that I am today. With that being said, they have the habit of being always right (which I find, most of the time, annoying) and an extremely keen eye for spotting my mistakes. But because of that, they have saved me many times from self-embarrassment on a number of papers and presentations. Thank you for spending so much time on revising my writing. This thesis can never be done without them.

No word can I find how I should express my gratitude to Professor Katsumi Kishino (Sophia University), who, although on a paper is not officially listed as my supervisor, has transformed into one of the most prominent figures for me to reach this stage. My respect towards him is not merely due to his influential works in this field, but more on a personal level. His dedication and work ethics

are second to none. Thank you very much for accepting me in your lab and letting (believing) me run wild with your MBE on whatever ideas I came up with. I consider myself fortunate enough to be one of his last PhD students before his official retirement in March 2018. Without him, the end of my PhD research would have not been visible.

I would also like to acknowledge Dr. Lutz Geelhaar (Paul Drude Institute for Solid State Electronics), Dr. Marta Sobańska (Institute of Physics of the Polish Academy of Sciences) and Professor Astrid Aksnes (Department of Electronic Systems, NTNU) for serving as the Assessment Committee for my thesis and defense. Additionally, I cannot begin to express my thanks to Professor Thomas Tybell and Professor Odd Kr. Pettersen (Department of Electronic Systems, NTNU), who gave me their support and guidance in finishing my thesis as timely as possible.

Special thanks to my co-authors who provided me with support throughout the duration of my PhD work. In the order of their appearance in my papers, they are listed as follows: Mr. Yuta Konno (presently at Panasonic, Osaka), Dr. Julie S. Nilsen (presently at Nordic Semiconductor, Trondheim), Professor Antonius T. J. van Helvoort (Department of Physics, NTNU), Dr. Mohana Rajpalke (presently at Microsoft Quantum Materials Lab, Copenhagen), Professor Haruhiko Kuroe (Department of Engineering and Applied Science, Sophia University), Dr. Per Erik Vullum (SINTEF Materials and Nanotechnology, Trondheim), Dr. Ida Marie Høiaas (presently at CrayoNano, Trondheim), late Dr. Dong-Chul Kim, Dr. Lyubomir Ahtapodov (presently at VitreaLab, Vienna), Mr. Anjan Mukherjee (presently at CrayoNano, Trondheim), Mr. Tron Arne Nilsen (Department of Electronic Systems, NTNU), and Mr. Håvard Hem Toftevaag (presently at European Space Agency, Noordwijk).

Ms. Nina Lundberg, Ms. Randi Hostad, Ms. Trude Elisabeth Jenssen, and Ms. Kirsti Klemetsaune have all been very helpful in administrative and practical matters. I also appreciate the efficiency of Ms. Berit Myhre when she was an adviser to Norwegian PhD Network on Nanotechnology for Microsystems. I would like to extend my sincere gratitude to Ms. Keiko Tosano and Ms. Misato Hironaka, who have been of tremendous help in assisting me in many bureaucratic issues, arranging my coming to Tokyo and ensuring that I had a pleasant stay in Sophia University. Even after my return to Trondheim, they still contacted me whenever there was something that involved me.

Staffs in NanoLab NTNU should also deserve recognition, particularly Ms. Trine Østlyng Hjertås (for her Raman training and further assistance), Mr. Mark Giulio Chiappa and Dr. Mathilde Isabelle Barriet (for their assistance in ensuring the smoothness of the lab course with students). Regarding the semiconductor-related lab courses with students, these duty works I have had for more than one and a half years has been actually a great labor for averting

my focus from my research. Maybe, I can consider these activities as a "positive procrastination" because I can actually train (force) myself to speak in front of two students for each lab session. I have to acknowledge that I really enjoyed the sessions with students, because I have met many interesting students. I can't recall their names as there have been hundreds of them graduating from these courses so far, but I wish them all the best!

I gratefully acknowledge the helpful advice and encouragement from Professor Akihiko Kikuchi and Professor Ichiro Nomura while I was staying in Sophia University. To the staffs of Kishino's laboratory, Mr. Isamu Matsuyama, Mr. Makoto Mizuno, Ms. Natsuki Tanifuji, Ms. Akiko Hayano, Mr. Shigeo Yamashita, and Mr. Kohki Hikosaka, thank you very much for assisting me with the related MBE experiments. Many thanks to the researchers of Kishino's lab, Dr. Koji Yamano, Dr. Shunsuke Ishizawa and Dr. Takao Oto for our discussions concerning the growth of III-nitrides. I would like to thank to the students of Kishino's lab who have taught and assisted me in adapting with the equipment in Kishino's lab: Mr. Yuta Konno, Mr. Yohei Nakagawa, Mr. Yuzo Matsui, Mr. Naoki Sakakibara, Mr. Jun Yoshida, Ms. Rin Miyagawa, Mr. Kai Matsumoto, Mr. Shiba Daijiro, Mr. Yutaro Mizuno, Mr. Daishi Fukushima, Mr. Suzuki, Mr. Masashi Fukuda, Mr. Kazuki Narita, Mr. Kazuma Kikuchi, Mr. Gyo Imamura, Mr. Koji Sogo, and Mr. Daiki Hatakeyama.

Thanks also to my ex-office mate, Dr. Saroj Kumar Patra, Dr. Dheeraj Dasa Lakshmi Narayana and Mr. Ashkan Moradi. I, particularly, very much appreciate to Dr. Mohana Rajpalke and Dr. Amir Maghoul, for giving me their listening ears whenever I had to rant. For the frequent visitors to my office: Mr. Mukesh Yadav, Ms. Yang Li, Mr. Tron Arne Nilsen, Mr. Anjan Mukherjee, and Dr. Dingding Ren, thank you for being quiet and not interrupting me whenever I complained about any random stuff. Both past and present, I enjoyed my daily conversation with Dr. Mazid Munshi, Dr. Sverre Vegard Pettersen, Dr. Gaurav Sharma, Dr. Jong Wook Noh, Dr. Roghayeh Shamshiri, Ms. Somayeh Hossein Zadeh, Dr. Ambjørn Dahle Bang, and Mr. Thanh-Nam Tran.

Being far away from my home country, these Indonesia friends in Trondheim have reminded me how to be at home: Ko Halim and Ce Rosa, Cik Djenny, Mbak Maya, Mbak Kiki, Mbak Zakia, and Stefanus. A number of dinner invitations I received from them literally reminded me the taste of Indonesian food, and occasionally, demanded me to speak in formal *Bahasa Indonesia*. When Mbak Rani was a postdoc at NTNU, I often went to her office for short discussions about my PhD. I appreciate her help for Raman assistance and accurately plotting one of my XRD results. Several e-mails back and forth with kopral Iis (who is now a holder of Dr. Eng. degree From Hiroshima University) for the past few years supported me in her own way. Having similar struggles, I often can relate her fight in getting this degree, and because of that I don't feel alone.

And of course Herry and Lucia, who have recently kept me busy with the chat and video call. Thanks guys for reaching me out again!

Friends from afar who have spent their time contacting me: Nadège and family (France), Axel and family (Germany), Brenda and family (Zambia), Emilia and family (Poland) and Charissa (US), thank you so much for remembering me in your prayer for these years, I owe you all. A good friend I made when I stayed in Sophia University, Fr. Gandhi (India), I really appreciate all of our conversations and lunch together. You have listened to all of my anxiety so patiently. May God bless you my brother! Ko Adi and Ce Grace, who are now living in Australia, thanks for consistently reading my long e-mail and I am really grateful for including me in your family prayer.

I am grateful to friends (past and present) in the Trondheim Baptist Church, particularly Pastor Egil, Pastor Arnfinn, Sang, Piotr and Tania, Lilia, Gunnar, Eigil and Synnøve, Kåre Olav, Elvira and Jan, Ruth, Daisy, Shine, Elska, Andreas, Geir, Hanna, Jedi, Victor, Peter, Anne, Elisabeth, Wei, and Yixiao. I very much appreciate Bengta and late Gunnar, Dan and family for their support and prayer for me. I especially thank Erling and Inger Lise, who have been more than friends to me personally. I always appreciate and will be cherishing our fellowship and *sødd/lapskaus* meeting. Our numerous discussions in the faith have opened my eyes, and I am sorry for always making us talk in English most of the time! For these reasons (and many more), I will not forget your kindness and encouragement. My life in Tokyo would not have been the same if I had not attended Sunday service in Okubo Baptist Church: Kawano sensei and family, Ishigaki sensei and family, Megumi sensei and family, Chan Sik-Myoung Seok and family, Koyanagi san and family, late Kouyama san, Yoshida san, Ishikane san and family, Hara san, Konno san, Miyashita san and family, Edberg san and family, Zhaochun and family, Mikiko san, and Shirai san. Thank you for keeping me in your prayer, although I am just an outsider. Especially for Miyamoto san, Serizawa san, Shin Rei san, Nakamura san, and Shion, I am extremely grateful for our discussion and 青年会 fellowship.

For Bernadette, thank you for letting me rent your room for these years. I pretty much own her a lot. Living far away from home, I see her as the surrogate of my parents. To this day, I admire her consistency and life principles, as well as her stand in faith. She was not only giving me very good hair cut (and free), but also pouring me with a ton of wisdom. Every now and then we talked about being a human and simultaneously as a Christian. Thank you for always reminding me to stand firm for the truth, but also to be meek at the same time. Living pridefully and being compassionate, those values I learned directly from her life. Also, I hope I can have a similar house like hers! Thanks for the occasional ride to the church, and for the lunch/dinner. Living under the same roof with her was one of the best decisions I have ever made in Norway.

Memorable events I have had with my ex-housemates, Ce Yenny, Kak Joy, Theresia, Eriab, Rachelle, Veronica, and Angga. Because of them, my life after coming home was sparkling. In similar fashion, Mila and Rosaline for being enjoyable and fun housemates. Thank you for introducing me to the taste of many kinds of foods! Also, all the talks that we had made me temporarily forget the problems I faced.

I will repeat these names again: Nakamura san and Shion. They have been an influential figures in my life, very close individuals to my heart. For Nakamura san, thank you for being there for me monthly via Skype since 2017. Although I have pretty much limited Japanese speaking ability, he has always been there listening to me rambling about how I struggle with my research. If it not were because of him, I might have quit my PhD. Then it comes the dear Shion. The time and attention that she has provided for me are just beyond belief. I have not met anyone who can deal with my daily e-mail until I meet her. Our Skype session every week discussing about many things has been one of the things I long for. Her smile and kind heart have been another reason of mine to finish this journey and looking forward for the future.

Finally, it is my family. No reason is needed here. My deepest appreciation goes to them who have never cease to pray for me since I embarked my PhD journey in March 2014. I am so sorry for just being able to go home once (just ten days in August 2016) during this seven-year period. Thank you for not pestering me even further to return home more than I could due to this demanding education. To my sister and brother, Debora and Albert, thanks for double-checking my papers when they were re-typed (despite having no clue what exactly is going on there). And for my mother and father, Lili Anita Luwanto and Sampurno Liudi Mulyo, they were the first who taught me what honesty, kindness, persistence, hard work, integrity, dignity, and essence of life were all about. Not only verbally, but I have witnessed them conscientiously practicing these ever since my childhood. Although they did not have any fancy academic degrees attached to their names, they are the ones I sought for advice. And the very first reason I dared to take this degree was because of them. I hope, by having *this*, I can bring them closer to see the beauty of this world. Mom, dad, this PhD degree is for you.

Ad majórem Dei glóriam

Trondheim, 12th of March 2021

Andreas Liudi Mulyo

Andreas Liudi Mulyo

Additional note

Having lived in Trondheim for about seven years (counting my years prior to PhD as well), I have to admit that this city has a special meaning to me: it has become a part of my life. I can't put it into a sentence how my coming to Trondheim has changed me. Leaving that aside, the night in Trondheim is just indescribable: it has its own serenity, particularly when the winter night (November-January) is extremely long. The song by Åge Aleksandersen, called *Trondheimsnatt* explains the best how I feel about this city. A remainder for my future self! Some of its lines resonating within me are shown below:

Æ sjer stjerna som skinn over Trondhjem i natt,
Som et smykke mot gråkallens rand.
Æ sjer lys fra et skip mot et skimranes hav, stille legg det fra land.

Æ sjer Munkholmen bade i gull i natt, deinn stråle som ein vakker rubin.
Æ sjer dis'n over elva lage eventyrland, som spoinne av fineste lin.

Verden den viske god natt og sov godt,
Og den gamle dom'en hold vakt.
Over hjerta som banke, over store og små,
Over ei Trondhjemsnatt.

This song is in Trøndersk, a Norwegian dialect widely spoken in Trøndelag. Its translation in English is roughly as follows:

I see the star that shines over Trondheim tonight,
Like a jewel against gråkallens edge.
I see light from a ship against a shimmering ocean, quietly it puts out from land.

I see Munkholmen bathe in gold tonight, it shines like a beautiful ruby.
I see the haze over the river make a fairytale land, as if spun by the finest linnen.

The world whispers good-night and sleep tight,
and the old dome keeps guard.
Over the hearts that beat, over big and small,
in a Trondheim night.

Contents

PART II RESULTS 113

List of Figures

Chapter 1

Chapter 2

Chapter 3

Chapter 4

CHAPTER 5

CHAPTER 6

CHAPTER 7

CHAPTER 8

CHAPTER 9

APPENDIX A

APPENDIX B

APPENDIX C

DISSEMINATION OF RESEARCH

List of Tables

CHAPTER 5

CHAPTER 8

CHAPTER 9

APPENDIX B

APPENDIX C

Nomenclature

The following are lists of acronyms and symbols used in this PhD thesis (in alphabetical order). After Chapter 4, notations might be re-defined several times in the accepted manuscripts presented from Chapters 5 to 8, as the author has an intention to present the chapters (i.e., manuscripts) as it is when it was accepted for publications. The manuscript under review in Chapter 9 has also notations that are re-specified as in the previous chapters (5-8). Despite of this irregularity that the reader might find it unusual, the author chooses and uses these notations as consistent as possible across the chapters in this Doctoral dissertation to avoid further confusions.

Acronyms

ADF	annular dark field
Al	aluminum, aluminium
Al_2O_3	sapphire
Al_xO_y	aluminum oxide
ALD	atomic layer deposition
AlGaAs	aluminium gallium arsenide
AlGaInN	aluminium gallium indium nitride
AlGaInP	aluminium gallium indium phosphide
AlN	aluminium nitride
BF	bright field
BFTEM	bright-field transmission electron microscope
BN	boron nitride
C	carbon
CCD	charge-coupled device
CIE	current injection efficiency
CTE	coefficient of thermal expansion
CVD	chemical vapor deposition
CW	continuous-wave
DAP	donor-acceptor pairs
DF	dark field
DLG	double-layer graphene
e-beam	electron-beam
EDX, EDS	energy dispersive x-ray spectroscopy
EELS	electron energy loss spectroscopy
EL	electroluminescence
EMCCD	electron multiplying charge-coupled device
EQE	external quantum efficiency
FIB	focused ion beam
FWHM	full width at half maximum

Ga	gallium
GaAs	gallium arsenide
GaAsP	gallium arsenide phosphide
GaN	gallium nitride
h-BN	hexagonal-boron nitride
HAADF	high-angle annular dark-field
He-Cd	helium-cadmium
HRTEM	high-resolution transmission electron microscopy
HRXRD	high resolution x-ray diffraction
HVPE	hydride-vapor phase epitaxy
I-V	current-voltage
ICP-RIE	inductively coupled plasma-reactive ion etching
InAs	indium arsenide
InAsSb	indium arsenide antimonide
InGaAs	indium gallium arsenide
InN	indium nitride
IQE	internal quantum efficiency
ITO	indium tin oxide
JEOL	Japan Electron Optics Laboratory
LDs	laser diodes
LED	light-emitting diode
LEDs	light-emitting diodes
LEE	light extraction efficiency
LEEBI	low-energy electron-beam irradiation
LO	longitudinal optical
LPP	longitudinal phonon-plasmon
LT	low-temperature
MBE	molecular beam epitaxy
MEE	migration enhanced epitaxy
MOCVD	metal-organic chemical vapour deposition
MoS_2	molybdenum disulfide
MOVPE	metal-organic vapour phase epitaxy
N, N_2	nitrogen
NC	nanocolumn
NCs	nanocolumns
Nd:YAG	neodymium-doped yttrium aluminum garnet
nm	nanometer
NorFab	Norwegian Infrastructure for Micro and Nanofabrication
NORTEM	Norwegian Centre for Transmission Electron Microscopy
NTNU	Norwegian University of Science and Technology
NW	nanowire
O	oxygen
Pa	pascal
PA-MBE	plasma-assisted molecular beam epitaxy
PL	photoluminescence
QCSE	quantum-confined Stark effect
RF	radio-frequency
RHEED	reflection high-energy electron diffraction

RPM	rotations per minute
RT	room-temperature
SAED	selected area electron diffraction
sccm	standard cubic centimeters per minute
SEM	scanning electron microscope
Si	silicon
SiC	silicon carbide
SIMS	secondary-ion mass spectroscopy
SiN, Si_xN_y	silicon nitride
SiO_2	silicon dioxide
SLG	single-layer graphene
SO	surface optical
STEM	scanning transmission electron microscopy

TCE	transparent conductive electrode
TCS	transparent conducting substrate
TEM	transmission electron microscopy
Ti	titanium
TiN	titanium nitride
TO	transverse optical
UHV	ultra-high vacuum
UV	ultraviolet
UV LED	ultraviolet light-emitting diode
VLS	vapor-liquid-solid
YL	yellow luminescence
ZnO	zinc oxide
ZnSe	zinc selenide

ROMAN SYMBOLS

C-H	hydrocarbon
C_{Ga}	C substituting Ga
C_N	C substituting N
$E_{A,\,Mg}$	activation energy of Mg
$E_{A,\,Si}$	activation energy of Si
E_F	Fermi level
E_g	bandgap energy
E_{vac}	vacuum energy
eV	electron volt
h	Planck constant

$h\nu$	energy of the emitted photons
I	injected current
P_{opt}	measured optical power
q	electron charge
Q_N	N_2 flow rate
T_{sub}	substrate temperature
V_{th}	threshold voltage
W	work function
Z	atomic number

GREEK SYMBOLS

2θ-ω	2 theta-omega scan
ϕ_B	potential barrier
χ	electron affinity
ν	energy
ω	rocking curve scan

φ	phi scan
Φ_{Ga}	Ga flux
μ-PL	micro-photoluminescence
μm	micrometer

Part I

BACKGROUND

CHAPTER 1

A brief introduction to GaN and its associated material systems

As one of the third generation of semiconductor materials, i.e., materials with the bandgap $\geqslant 2.3$ eV[1], gallium nitride (GaN) has been well-utilized in electronic and optoelectronic applications, with the most prominent one being the basis material system for blue light-emitting diodes (LEDs), as shown in Figure 1.1. Compared to incandescent and fluorescent bulbs, GaN based solid-state lighting has much higher efficiency, longer life-time, smaller size, better physical robustness, and faster switching. Despite of its present success, GaN at some point was shunned by the research communities[2], regarded as "the material with no future" because it had proven extremely challenging to develop.

FIGURE 1.1. **BLUE LED** based on the GaN semiconductor material system[2,3] (adapted with permission from ref. 2 © 2015 John Wiley and Sons).

If it had not been for the perseverance and great risk taken by a handful of researchers in the 1980s and early 1990s, including most notably Nobel Laureates Professor Isamu Akasaki, Professor Hiroshi Amano and Professor Shuji Nakamura, any research topic related with GaN semiconductor would not have been as advanced as it is today. Following the series of crucial breakthroughs in the growth studies[4–13] and the device-related works[3,14–20], to this date there are still a strong indication of tireless pursuit in making this class of material even more versatile and functional than before, in addition to improving the efficiency of the devices.

1.1 GENERAL INTEREST AND SHORT HISTORY OF III-NITRIDE SEMICONDUCTORS

GaN and its related alloys, namely aluminum gallium nitride (AlGaN), indium gallium nitride (InGaN) and aluminum gallium indium nitride (AlGaInN), belong to the group-III nitride compound semiconductors that are also known as the group III-V nitride semiconductors. This group of material system normally crystallizes in the hexagonal or wurtzite crystal structure and it is characterized with a direct energy bandgap, which is extremely useful for the fabrication of light sources, such as laser diodes (LDs) and LEDs. It has a continuous energy bandgap (Figure 1.2)[21–23] ranging from 0.64 eV for indium nitride (InN) to 6.2 eV for aluminum nitride (AlN), with the energy bandgap of GaN (3.45 eV) roughly in between that of InN and AlN. Presently, there is no other known material system[24] that allows light emission over such wide spectral range, while at the same time maintaining a direct bandgap. This make the AlGaInN-based light emitters technologically important for applications in the infrared, visible and ultraviolet (UV) wavelength regions.

While the ternary alloy InGaN provides enormous practical benefits in the LED industry for full-color displays, blue LEDs for solid-state lighting as well as 400 nm LDs for optical storage, GaN and AlGaN have gained their own merits for applications of UV LEDs related to surface treatment, disinfection/purification, medical diagnostics, sensing, and non-line-of-sight communications[27–29].

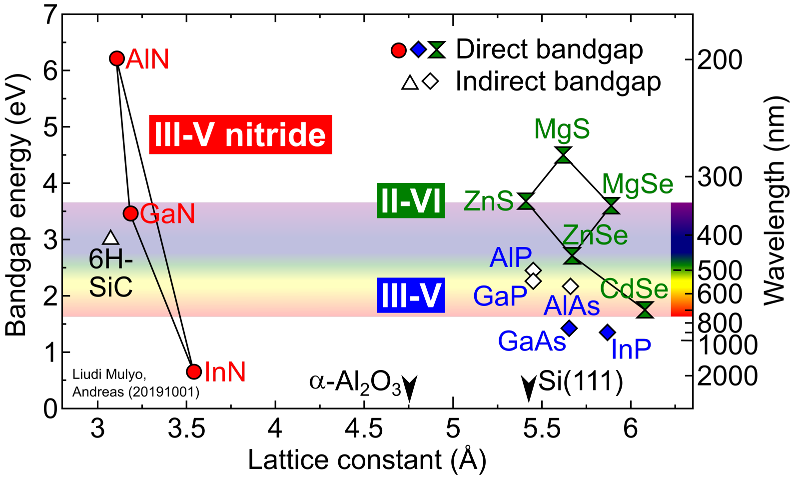

FIGURE 1.2. **Energy bandgap of different binary III-V compound semiconductors**, silicon carbide (6H-SiC) and a few II-VIs[25,26] as a function of lattice constant (bowing parameters are neglected). Sapphire (α-Al_2O_3) and Si(111), along with 6H-SiC, belong to a class of indirect bandgap materials that are typically used as epitaxial growth substrates for the GaN-based material system.

It should be noted that polarization fields (spontaneous and piezoelectric) existing in the wurtzite III-V nitrides may give rise to what is known as the quantum-confined Stark effect (QCSE), limiting the internal quantum efficiency (IQE) of the light emitter. Single crystalline growth of III-V nitrides has been achieved historically using hydride-vapor phase epitaxy (HVPE)[30], electron beam plasma[31], molecular beam epitaxy (MBE)[32], and metalorganic chemical vapour deposition (MOCVD) or metalorganic vapour-phase epitaxy (MOVPE)[33,34]. To date, the aforementioned techniques, except electron beam plasma, have been extensively exploited for the commercialization (especially MOVPE) and research purposes of III-V nitrides.

Despite of its present significance, in fact this material system was rather slow in its early development, mainly hampered by poor crystalline quality[35]. The demonstration of visible red emissions was reported from the non-III-nitride materials, namely gallium arsenide phosphide (GaAsP) in 1962[36]. Further progress of LDs and LEDs from 1970s to 1980s heavily relied on other non-III-nitride materials, mainly aluminum gallium arsenide (AlGaAs)[37,38] and aluminum gallium indium phosphide (AlGaInP)[39–42] for obtaining emitters with a working wavelength in the red and orange-yellow-green regions, respectively. Although both material systems have the availability of direct energy bandgaps, the non-III-nitride compound semiconductors have much narrower range of possible energy bandgaps, as shown in Figure 1.2. Despite that visible LDs and LEDs can be fabricated from the non-III-nitride materials, it was shown difficult to realize high-brightness visible light sources based on these material systems[43], particularly at shorter wavelength (blue) needed for solid-state lighting.

For that purpose, other wide bandgap materials such as group II-VI (notably zinc selenide [ZnSe]) and silicon carbide (SiC), as presented in Figure 1.2, were thoroughly explored due to their promising results. ZnSe was the serious material contender for the blue light emitters because of its relatively high crystalline quality, with the-state-of-art dislocation densities of less than 10^4 cm^{-2} already achieved in 1989[43]. Nevertheless, the II-VI-based devices could not go to market due to their short lifetime issues. SiC on the other hand, was commercialized as the material for blue LEDs[43] for quite a long time despite of its poor performance. This was anticipated as the bandgap nature of SiC is indirect, which severely limits the efficiency of the light emitters.

In 1973 Maruska *et al.*[44] originally reported the electroluminescent properties of HVPE-grown GaN. At that time, single crystalline GaN thin films had been achieved on sapphire substrates but the crystal quality and surface morphology were quite miserable due to the large lattice mismatch. Efficient *p*-type doping was another major problem for GaN, rendering lack of interest from the research community, especially during the rise of ZnSe in the 1970s

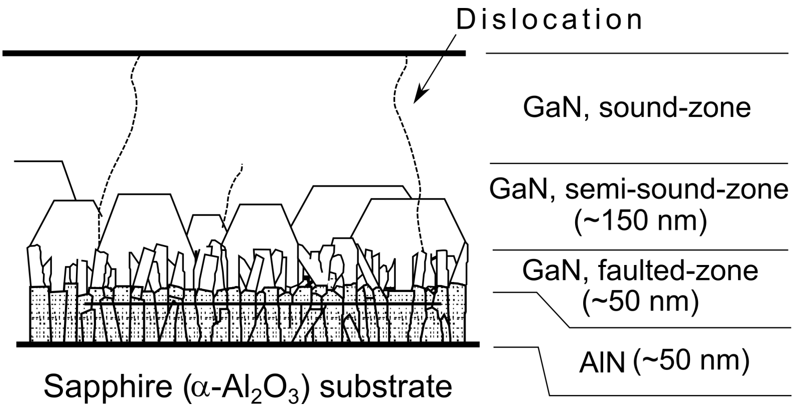

FIGURE 1.3. **AlN buffer layer (or GaN buffer layer) formed on top of the sapphire substrate** developed by Hiramatsu *et al.*[45] for reducing the dislocations of GaN thin films grown on a large lattice mismatched sapphire substrate (adapted with permission from ref. 45 © 1991 Elsevier).

and 1980s. Pioneering work of Yoshida *et al.*[4] in 1985 by using AlN as the buffer layer on sapphire substrates for MBE-grown GaN films effectively improved the GaN crystalline quality, along with an enhancement of its electrical and optical properties. It was then followed-up by Amano *et al.*[5] and later by Nakamura[8], who successfully obtained optically-flat MOVPE-grown GaN films with equally good crystalline quality by utilizing thin AlN and GaN buffer layers, respectively. The key lies in the presence of buffer layer, which acts as a sacrificial layer to mitigate the defects caused by the large lattice mismatch (~16%) with the sapphire substrate (Figure 1.3)[45].

After that, the post-growth treatment known as low-energy electron-beam irradiation (LEEBI), introduced by Amano *et al.*[7] in 1989, resulted in the first realization of low-resistivity *p*-type Mg-doped GaN, along with the enhancement of the electroluminescence efficiency in their *p*-*n* homojunction GaN LED. In 1991, the improvement of the electrical and optical properties of *p*-type GaN was further demonstrated by Nakamura *et al.*[9] using a post-growth N_2-ambient thermal annealing, which had a similar local heating effects as the LEEBI method. The phenomenon in both treatments involves the removal of atomic hydrogen from Mg-H neutral complexes that formed during the MOCVD growth of Mg-doped GaN under NH_3 ambient (i.e., hydrogen passivation[46,47]), and thus increasing the free charge carrier density in *p*-type GaN[2]. These important findings subsequently provided the method to obtain high-quality InGaN films[10] and quickly paved the way for mass-production and commercialization of the visible light emitters, including blue LEDs[3,14–16] and violet LDs[17,18].

1.2 INGAN ACTIVE LAYER VS GAN AND ALGAN ACTIVE LAYERS

One bewildering observation regarding InGaN is that, despite of its extremely large density of dislocations (10^8-10^{11} cm^{-2})[2], InGaN-based LEDs performed efficiently with an external quantum efficiency (EQE) as high as 12%, much higher than what was observed in AlGaAs, AlInGaP and ZnSe-based LEDs although their crystalline quality were much more superior[2]. Lester *et al.*[48] noted that dislocations in GaN-based LEDs (with InGaN as an active layer) do not act as efficient non-radiative recombination sites. This fundamental property, i.e., the benign behavior of dislocations in GaN, could be associated with the more ionic character of the bonding in this material system compared to non-III-nitrides. Another outlook by Chichibu *et al.*[13], suggested that before the carriers are trapped by non-radiative recombination centers (crystal defects), they are captured by efficient localized energy states of radiative recombination centers. These localized centers, that can be thought of as enhanced emission centers of light[2], are caused by In composition fluctuation in the active layers (e.g., quantum wells) to form quantized (confined) excitons[20].

Nevertheless, such phenomenon is only observed when the active layer is InGaN. When the LED working wavelength ranges are shorter, i.e., the active layer is GaN or AlGaN, the EQE becomes extremely poor[19,27]. Additionally, optical study revealed that the photoluminescence intensity of band-to-band GaN emission[11,20] is much weaker than that of InGaN[12,20]. At this point, it should be noted that the QCSE resulting from the strain-induced polarization field exists in the III-N material system, including InGaN, AlGaN and GaN. However, the absence of In composition fluctuations that form the deep localized energy state in the GaN and AlGaN causes the QCSE to become dominant[20], which will eventually decrease the oscillator strength of electron-hole pairs, reducing the efficiency of the GaN and AlGaN-based devices.

1.3 CHALLENGES AND PRESENT STRATEGY FOR GAN-ALGAN SYNTHESIS

Beyond light emitters, the III-nitride materials have been utilized for a broad range of electronic and optoelectronic applications, thanks to their direct wide bandgap tunability, high carrier mobility, large electron saturation velocity, good electrical-thermal conductivity, and excellent chemical stability[21–23,49–53]. InGaN for instance, has been investigated as a material in solar cells[54] and as a photocathode in solar water splitting systems[55]. The high breakdown voltage of GaN-AlGaN is of particular interest for power devices, such as high electron mobility transistors[56] and heterojunction field-effect transistors[57], with the applications ranging from high-frequency communication to electric power systems[23,58,59]. Here, the performance of III-nitride-based devices are still strictly limited by high density of structural defects. Therefore, it is necessary to develop new growth strategies to realize high quality III-nitride materials, as well as in giving a new approach using alternative substrates.

One method to obtain high quality III-V nitride materials grown on foreign substrates like sapphire, is by forming so-called nanocolumns (also known as nanowires). A nanocolumn is defined as a low-dimensional nanostructure in the form of a column (wire) which has cross-sections ranging from tenth to few hundredth of nanometers and height in the order of few micrometers. Structural issues in III-V nitride thin-film structures, such as large stacking faults and threading dislocation densities, are typically a result of the large lattice mismatch with the underlying substrate. Such problems can be minimized in the nanocolumn structure thanks to its small nanometer-sized footprint on the substrate, making the strain generated at the interface to be relaxed to a lateral nanostructure surface. While sapphire and Si have been the most common substrates for the growth of GaN nanocolumns since their first demonstrations in 1996[60] and 1998[61], respectively, their usage for optoelectronic devices in the UV region (e.g. LEDs) are limited to some extent.

An obvious example of limitation is the absorbing nature of Si material, which can tremendously reduce the light output of the UV light emitter[62]. For sapphire material, on the other hand, despite having high UV transmittance, its insulating nature designates the utilization of thick "buffer layer", for instance GaN thin-film template of around 3.5 μm[63]. In such circumstance, the readers should realize that the current transports along the lateral direction causing non-uniform distribution of current density near the edge of the contact (current crowding)[64], which in practice limits the efficiency of LEDs. Moreover, GaN is a material that starts absorbing UV light when its wavelength is shorter than 365 nm. In principle, the drawback of aforementioned substrates (along with 6H-SiC) have turned into one of the major challenges in advancing UV LEDs based on a nanoscale structure.

From this description, it can be argued that a new class of substrate materials with suitable properties is needed for growth of nitride nanocolumns. Desirable features like maintaining good transparency, while at the same time electrically conducting can be beneficial for the LED development. With regards to lattice mismatch, the ability of nanocolumn in reducing structural defects should not put restrictions on the material of choice. Unexpected materials that fulfill such criteria have arisen, for example indium tin oxide (ITO) and titanium carbide that have been reported in the early 2019 and 2020[65,66]. However, the transmittance of these substrates performs poorly in the UV wavelength region, and thus are not able to answer the present challenges.

Concerning ITO, which is commonly used as a transparent conducting electrode for LEDs and solar cells, it has been projected to be replaced by graphene in the coming years. This “oldest” two-dimensional material that was successfully isolated in 2004 has favorable characteristics required for the new class of substrate materials, and particularly graphene has better UV transparency compared to the aforementioned materials in the preceding paragraph. Furthermore, graphene has been commercialized for quite some time now, ensuring high quality material and making its availability easily accessible for the research and development. Therefore, it is of particular interest to explore graphene as a *transparent conducting substrate*, i.e., transparent electrode and substrate for the growth of III-nitride nanocolumns and their integration for UV-LEDs.

1.4 REFERENCES

[1] J. Y. Tsao, *et al.* Ultrawide-Bandgap Semiconductors: Research Opportunities and Challenges. *Advanced Electronic Materials* **4** (1), 1600501 (2018). Cited on page/s 3.

[2] S. Nakamura. Background Story of the Invention of Efficient InGaN Blue-Light-Emitting Diodes (Nobel Lecture). *Angewandte Chemie* **54** (27), 7770–7788 (2015). Cited on page/s 3, 6, 7.

[3] S. Nakamura, T. Mukai, and M. Senoh. Candela-class high-brightness InGaN/AlGaN double-heterostructure blue-light-emitting diodes. *Applied Physics Letters* **64** (13), 1687–1689 (1994). Cited on page/s 3, 6.

[4] S. Yoshida, S. Misawa, and S. Gonda. Improvements on the electrical and luminescent properties of reactive molecular beam epitaxially grown GaN films by using AlN-coated sapphire substrates. *Applied Physics Letters* **42** (5), 427–429 (1983). Cited on page/s 3, 6.

[5] H. Amano, N. Sawaki, I. Akasaki, and Y. Toyoda. Metalorganic vapor phase epitaxial growth of a high quality GaN film using an AlN buffer layer. *Applied Physics Letters* **48** (5), 353–355 (1986). Cited on page/s 3, 6.

[6] I. Akasaki, H. Amano, Y. Koide, K. Hiramatsu, and N. Sawaki. Effects of AlN buffer layer on crystallographic structure and on electrical and optical properties of GaN and $Ga_{1-x}Al_xN$ ($0 < x \leqslant 0.4$) films grown on sapphire substrate by MOVPE. *Journal of Crystal Growth* **98** (1), 209–219 (1989). Cited on page/s 3.

[7] H. Amano, M. Kito, K. Hiramatsu, and I. Akasaki. P-Type Conduction in Mg-Doped GaN Treated with Low-Energy Electron Beam Irradiation (LEEBI). *Japanese Journal of Applied Physics* **28** (Part 2, No. 12), L2112–L2114 (1989). Cited on page/s 3, 6.

[8] S. Nakamura. GaN Growth Using GaN Buffer Layer. *Japanese Journal of Applied Physics* **30** (Part 2, No. 10A), L1705–L1707 (1991). Cited on page/s 3, 6.

[9] S. Nakamura, T. Mukai, M. Senoh, and N. Iwasa. Thermal Annealing Effects on P-Type Mg-Doped GaN Films. *Japanese Journal of Applied Physics* **31** (Part 2, No. 2B), L139–L142 (1992). Cited on page/s 3, 6.

[10] S. Nakamura and T. Mukai. High-Quality InGaN Films Grown on GaN Films. *Japanese Journal of Applied Physics* **31** (Part 2, No. 10B), L1457–L1459 (1992). Cited on page/s 3, 6.

[11] S. Nakamura, T. Mukai, and M. Senoh. Si- and Ge-Doped GaN Films Grown with GaN Buffer Layers. *Japanese Journal of Applied Physics* **31** (9), 2883–2888 (1992). Cited on page/s 3, 7.

[12] S. Nakamura, T. Mukai, and M. Senoh. Si-Doped InGaN Films Grown on GaN Films. *Japanese Journal of Applied Physics* **32** (Part 2, No.1A/B), L16–L19 (1993). Cited on page/s 3, 7.

[13] S. Chichibu, T. Azuhata, T. Sota, and S. Nakamura. Spontaneous emission of localized excitons in InGaN single and multiquantum well structures. *Applied Physics Letters* **69** (27), 4188–4190 (1996). Cited on page/s 3, 7.

[14] S. Nakamura, M. Senoh, and T. Mukai. P-GaN/N-InGaN/N-GaN Double-Heterostructure Blue-Light-Emitting Diodes. *Japanese Journal of Applied Physics* **32** (Part 2, No.1A/B), L8–L11 (1993). Cited on page/s 3, 6.

[15] S. Nakamura, M. Senoh, N. Iwasa, S.-I. Nagahama, T. Yamada, and T. Mukai. Superbright Green InGaN Single-Quantum-Well-Structure Light-Emitting Diodes. *Japanese Journal of Applied Physics* **34** (Part 2, No. 10B), L1332–L1335 (1995). Cited on page/s 3, 6.

[16] S. Nakamura, M. Senoh, N. Iwasa, and S.-I. Nagahama. High-Brightness InGaN Blue, Green and Yellow Light-Emitting Diodes with Quantum Well Structures. *Japanese Journal of Applied Physics* **34** (Part 2, No. 7A), L797–L799 (1995). Cited on page/s 3, 6.

[17] S. Nakamura, M. Senoh, S.-I. Nagahama, N. Iwasa, T. Yamada, T. Matsushita, H. Kiyoku, and Y. Sugimoto. InGaN-Based Multi-Quantum-Well-Structure Laser Diodes. *Japanese Journal of Applied Physics* **35** (Part 2, No. 1B), L74–L76 (1996). Cited on page/s 3, 6.

[18] S. Nakamura, M. Senoh, S.-I. Nagahama, N. Iwasa, T. Yamada, T. Matsushita, Y. Sugimoto, and H. Kiyoku. Room-temperature continuous-wave operation of InGaN multi-quantum-well structure laser diodes. *Applied Physics Letters* **69** (26), 4056–4058 (1996). Cited on page/s 3, 6.

[19] T. Mukai, D. Morita, and S. Nakamura. High-power UV InGaN/AlGaN double-heterostructure LEDs. *Journal of Crystal Growth* **189-190**, 778–781 (1998). Cited on page/s 3, 7.

[20] S. Nakamura. The Roles of Structural Imperfections in InGaN-Based Blue Light-Emitting Diodes and Laser Diodes. *Science* **281** (5379), 956–961 (1998). Cited on page/s 3, 7.

[21] I. Vurgaftman and J. R. Meyer. Band parameters for nitrogen-containing semiconductors. *Journal of Applied Physics* **94** (6), 3675–3696 (2003). Cited on page/s 4, 7.

[22] J. Wu. When group-III nitrides go infrared: New properties and perspectives. *Journal of Applied Physics* **106** (1), 011101 (2009). Cited on page/s 4, 7.

[23] S. Fujita. Wide-bandgap semiconductor materials: For their full bloom. *Japanese Journal of Applied Physics* **54** (3), 030101 (2015). Cited on page/s 4, 7, 8.

[24] M. A. Caro Bayo. Theory of elasticity and electric polarization effects in the group-III nitrides. *Doctoral thesis*. University College Cork (2013). Cited on page/s 4.

[25] M. Isshiki and J. Wang. Wide-Bandgap II-VI Semiconductors: Growth and Properties, in Springer Handbook of Electronic and Photonic Materials. Springer Handbooks. Springer, Cham. (2017). Cited on page/s 4.

[26] H. Okuyama, K. Nakano, T. Miyajima, and K. Akimoto. Epitaxial Growth of ZnMgSSe on GaAs Substrate by Molecular Beam Epitaxy. *Japanese Journal of Applied Physics* **30** (Part 2, No. 9B), L1620–L1623 (1991). Cited on page/s 4.

[27] M. Kneissl, J. Han T.-Y. Seong, and Hiroshi Amano. The emergence and prospects of deep-ultraviolet light-emitting diode technologies. *Nature Photonics* **13**, 233–244 (2019). Cited on page/s 4, 7.

[28] S. Zhao and Z. Mi. AlGaN Nanowires: Path to Electrically Injected Semiconductor Deep Ultraviolet Lasers. *IEEE Journal of Quantum Electronics* **54** (6), 1–9 (2018). Cited on page/s 4.

[29] M. D. Brubaker, K. L. Genter, A. Roshko, P. T. Blanchard, B. T. Spann, T. E. Harvey, and K. A. Bertness. UV LEDs based on p–i–n core–shell AlGaN/GaN nanowire heterostructures grown by N-polar selective area epitaxy. *Nanotechnology* **30** (23), 234001 (2019).

Cited on page/s 4.

[30] H. P. Maruska and J. J. Tietjen. THE PREPARATION AND PROPERTIES OF VAPOR-DEPOSITED SINGLE-CRYSTAL-LINE GaN. *Applied Physics Letters* **15** (10), 327–329 (1969). Cited on page/s 5.

[31] K. Osamura, K. Nakajima, Y. Murakami, P. H. Shingu, and A. Ohtsuki. Fundamental absorption edge in GaN, InN and their alloys. *Solid State Communications* **11** (5), 617–621 (1972). Cited on page/s 5.

[32] S. Yoshida, S. Misawa, and A. Itoh. Epitaxial growth of aluminum nitride films on sapphire by reactive evaporation. *Applied Physics Letters* **26** (8), 461–462 (1975). Cited on page/s 5.

[33] Toshiharu Kawabata, Toshio Matsuda, and Susumu Koike. GaN blue light emitting diodes prepared by metalorganic chemical vapor deposition. *Journal of Applied Physics* **56** (8), 2367–2368 (1984). Cited on page/s 5.

[34] T. Nagatomo, T. Kuboyama, H. Minamino, and O. Omoto. Properties of $Ga_{1-x}In_xN$ Films Prepared by MOVPE. *Japanese Journal of Applied Physics* **28** (Part 2, No. 8), L1334–L1336 (1989). Cited on page/s 5.

[35] A. Shintani, Y. Takano, S. Minagawa, and M. Maki. X-Ray Diffraction Topography and Crystal Characterization of GaN Epitaxial Layers for Light-Emitting Diodes. *Journal of the Electrochemical Society* **125** (12), 2076–2078 (1978). Cited on page/s 5.

[36] N. Holonyak and S. F. Bevacqua. COHERENT (VISIBLE) LIGHT EMISSION FROM $Ga(As_{1-x}P_x)$ JUNCTIONS. *Applied Physics Letters* **1** (4), 82–83 (1962). Cited on page/s 5.

[37] J. Nishizawa, M. Koike, and C. C. Jin. Efficiency of GaAlAs heterostructure red light-emitting diodes. *Journal of Applied Physics* **54** (5), 2807–2812 (1983). Cited on page/s 5.

[38] H. Ishiguro, K. Sawa, S. Nagao, H. Yamanaka, and S. Koike. High efficient GaAlAs light-emitting diodes of 660 nm with a double heterostructure on a GaAlAs substrate. *Applied Physics Letters* **43** (11), 1034–1036 (1983). Cited on page/s 5.

[39] H. Sugawara, M. Ishikawa, and G. Hatakoshi. High-efficiency InGaAlP/GaAs visible light-emitting diodes. *Applied Physics Letters* **58** (10), 1010–1012 (1991). Cited on page/s 5.

[40] C. P. Kuo, R. M. Fletcher, T. D. Osentowski, M. C. Lardizabal, M. G. Craford, and V. M. Robbins. High performance AlGaInP visible light-emitting diodes. *Applied Physics Letters* **57** (27), 2937–2939 (1990). Cited on page/s 5.

[41] M. Ishikawa, Y. Ohba, H. Sugawara, M. Yamamoto, and T. Nakanisi. Room-temperature cw operation of InGaP/InGaAlP visible light laser diodes on GaAs substrates grown by metalorganic chemical vapor deposition. *Applied Physics Letters* **48** (3), 207–208 (1986). Cited on page/s 5.

[42] M. Ikeda, M. Honda, Y. Mori, K. Kaneko, and N. Watanabe. Yellow-emitting AlGaInP double heterostructure laser diode at 77 K grown by atmospheric metalorganic chemical vapor deposition. *Applied Physics Letters* **45** (9), 964–966 (1984). Cited on page/s 5.

[43] S. Nakamura, S. Pearton, and G. Fasol. The Blue Laser Diode: The Complete Story. Springer, Berlin, Heidelberg (2000). Cited on page/s 5.

[44] H.P. Maruska, D.A. Stevenson, and J.I. Pankove. Violet luminescence of Mg-doped GaN. *Applied Physics Letters* **22** (6), 303–305 (1973). Cited on page/s 5.

[45] K. Hiramatsu, S. Itoh, H. Amano, I. Akasaki, N. Kuwano, T. Shiraishi, and K. Oki. Growth mechanism of GaN grown on sapphire with AlN buffer layer by MOVPE. *Journal of Crystal Growth* **115** (1), 628–633 (1991). Cited on page/s 6.

[46] S. Nakamura, N. Iwasa, M. Senoh, and T. Mukai. Hole Compensation Mechanism of P-Type GaN Films. *Japanese Journal of Applied Physics* **31** (Part 1, No. 5A), 1258–1266 (1992). Cited on page/s 6.

[47] J. Neugebauer and C. G. Van de Walle. Hydrogen in GaN: Novel Aspects of a Common Impurity. *Physical Review Letters* **75** (24), 4452–4455 (1995). Cited on page/s 6.

[48] S. D. Lester, F. A. Ponce, M. G. Craford, and D. A. Steigerwald. High dislocation densities in high efficiency GaN-based light-emitting diodes. *Applied Physics Letters* **66** (10), 1249–1251 (1995). Cited on page/s 7.

[49] C. Buttay, *et al.* State of the art of high temperature power electronics. *Materials Science and Engineering: B* **176** (4), 283–288 (2011). Cited on page/s 7.

[50] M. Yanagihara, Y. Uemoto, T. Ueda, T. Tanaka, and D. Ueda. Recent advances in GaN transistors for future emerging applications. *Physica Status Solidi A - Applications and Materials Science* **206** (6), 1221–1227 (2009). Cited on page/s 7.

[51] H. Morkoç, S. Strite, G. B. Gao, M. E. Lin, B. Sverdlov, and M. Burns. Large-band-gap SiC, III-V nitride, and II-VI ZnSe-based semiconductor device technologies. *Journal of Applied Physics* **76** (3), 1363–1398 (1994). Cited on page/s 7.

[52] S. Strite and H. Morkoç. GaN, AlN, and InN: A review. *Journal of Vacuum Science & Technology B* **10** (4), 1237–1266 (1992). Cited on page/s 7.

[53] S. C. Jain, M. Willander, J. Narayan, and R. V. Overstraeten. III–nitrides: Growth, characterization, and properties. *Journal of Applied Physics* **87** (3), 965–1006 (2000). Cited on page/s 7.

[54] A. G. Bhuiyan, K. Sugita, A. Hashimoto, and A. Yamamoto. InGaN Solar Cells: Present State of the Art and Important Challenges. *IEEE Journal of Photovoltaics* **2** (3), 276–293 (2012). Cited on page/s 7.

[55] Y. Wang, S. Vanka, J. Gim, Y. Wu, R. Fan, Y. Zhang, J. Shi, M. Shen, R. Hovden, and Z. Mi. An $In_{0.42}Ga_{0.58}N$ tunnel junction nanowire photocathode monolithically integrated on a nonplanar Si wafer. *Nano Energy* **57**, 405–413 (2019). Cited on page/s 7.

[56] M. Kuzuhara, J. T. Asubar, and H. Tokuda. AlGaN/GaN high-electron-mobility transistor technology for high-voltage and low-on-resistance operation. *Japanese Journal of Applied Physics* **55** (7), 070101 (2016). Cited on page/s 7.

[57] N. Ikeda, Y. Niiyama, H. Kambayashi, Y. Sato, T. Nomura, S. Kato, and S. Yoshida. GaN Power Transistors on Si Substrates for Switching Applications. *Proceedings of the IEEE* **98** (7), 1151–1161 (2010). Cited on page/s 7.

[58] H. Kambayashi, Y. Satoh, S. Ootomo, T. Kokawa, T. Nomura, S. Kato, and T. Pawl Chow. Over 100A operation normally-off AlGaN/GaN hybrid MOS-HFET on Si substrate with high-breakdown voltage. *Solid-State Electronics* **54** (6), 660–664 (2010). Cited on page/s 8.

[59] Y. Uemoto, M. Hikita, H. Ueno, H. Matsuo, H. Ishida, M. Yanagihara, T. Ueda, T. Tanaka, and D. Ueda. Gate Injection Transistor (GIT)—A Normally-Off AlGaN/GaN Power Transistor Using Conductivity Modulation. *IEEE Transactions on Electron Devices* **54** (12), 3393–3399 (2007). Cited on page/s 8.

[60] M. Yoshizawa, A. Kikuchi, M. Mori, N. Fujita, and K. Kishino. Growth of Self-Organized GaN Nanostructures on Al_2O_3(0001) by RF-Radical Source Molecular Beam Epitaxy. *Japanese Journal of Applied Physics* **36** (Part 2, No. 4B), L459–L462 (1997). Cited on page/s 8.

[61] M.A. Sanchez-Garcia, E. Calleja, E. Monroy, F.J. Sanchez, F. Calle, E. Munoz, and R. Beresford. The effect of the III/V ratio and substrate temperature on the morphology and properties of GaN- and AlN-layers grown by molecular beam epitaxy on Si(1 1 1). *Journal of Crystal Growth* **183** (1), 23–30 (1998). Cited on page/s 8.

[62] S. Zhao and Z. Mi. Chapter Five - Al(Ga)N Nanowire Deep Ultraviolet Optoelectronics. In Zetian Mi and Chennupati Jagadish, editors, *Al(Ga)N Nanowire Deep Ultraviolet Optoelectronics, III-Nitride Semiconductor Optoelectronics* volume 96 of *Semiconductors and Semimetals* pages 167–199. Elsevier (2017). Cited on page/s 8.

[63] K. Kishino and K. Yamano. Green-Light Nanocolumn Light Emitting Diodes With Triangular-Lattice Uniform Arrays of InGaN-Based Nanocolumns. *IEEE Journal of Quantum Electronics* **50** (7), 538–547 (2014). Cited on page/s 8.

[64] X. Guo and E. F. Schubert. Current crowding in GaN/InGaN light emitting diodes on

insulating substrates. *Journal of Applied Physics* **90** (8), 4191–4195 (2001). Cited on page/s 8.

[65] A. Prabaswara, J.-W. Min, R. C. Subedi, M. Tangi, J. A. Holguin-Lerma, C. Zhao, D. Priante, T. K. Ng, and B. S. Ooi. Direct Growth of Single Crystalline GaN Nanowires on Indium Tin Oxide-Coated Silica. *Nanoscale Research Letters* **14**, 45 (2019). Cited on page/s 8.

[66] A. Prabaswara, *et al.* Titanium Carbide MXene Nucleation Layer for Epitaxial Growth of High-Quality GaN Nanowires on Amorphous Substrates. *ACS Nano* **14** (2), 2202–2211 (2020). Cited on page/s 8.

CHAPTER 2

GaN nanocolumns and their application in light emitters

The very first observation of high-density, vertically-aligned GaN nanocolumns was obtained on sapphire substrate. It was presented by Professor Katsumi Kishino's group from Sophia University (Japan) during the 23rd International Symposium on Compound Semiconductors in 1996 [1], and the results were subsequently published within the following two years [2,3]. In 1998, Professor Enrique Calleja's group from Universidad Politécnica de Madrid (Spain) demonstrated that such nanostructure can also be synthesized on Si(111) substrate [4,5]. These works pioneered the heteroepitaxial growth of vertical-high density GaN nanocolumns on foreign substrates. Examples of the initial attempts on the GaN nanocolumn growth are shown in the scanning electron microscope (SEM) images in Figure 2.1. A common characteristic of these precursor works was that the GaN nanocolumns could be achieved without the aid of any catalyst, distinguishing themselves from other III-V semiconductor nanocolumn material classes.

The findings of beneficial properties of GaN nanocolumn have driven curiosity among the III-nitride community, stimulating the dedicated research on the growth studies and potential applications in electronic and optoelectronic

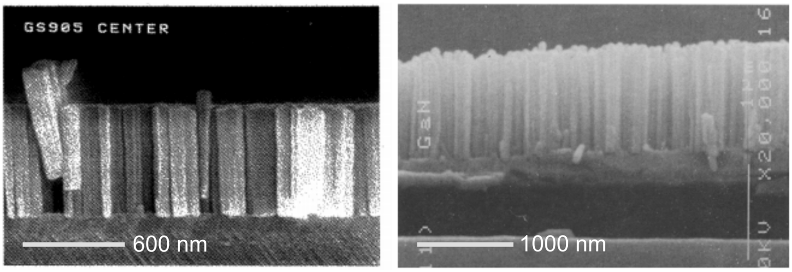

FIGURE 2.1. Cross-sectional SEM images of the first GaN nanocolumns on (left) sapphire substrate using a thin AlN buffer layer (adapted with permission from ref. 2 © 1997 The Physical Society of Japan and The Japan Society of Applied Physics) and on (right) Si(111) substrate (adapted with permission from ref. 4 © 1998 Elsevier).

devices to this date. Such investigations include attempts to recreate similar kind of growth architectures which have been achieved by the planar structure of III-nitrides, and recent focus on nanocolumn growth has been on non- or poly-crystalline substrates, including amorphous glass and graphene. Early 2010s, few start-up companies in Europe have endeavored to commercialize optoelectronic devices based on the III-nitride nanocolumn technology on Si platform, for example glō AB and Aledia (visible LEDs). In Trondheim itself, CrayoNano AS founded by Professor Helge Weman, Professor Bjørn-Ove Fimland and Dr. Dong-Chul Kim is currently developing UV LEDs based on III-nitride nanocolumns grown on graphene, with the aim for commercialization by the end of 2021[6].

Bottom-up route, using e.g., MBE, MOVPE or HVPE[7], and top-down approach via dry-etching are two methods that can be utilized to obtain the GaN nanocolumn structure. While top-down approach offers simplicity in the creation of GaN nanocolumns, bottom-up approach is generally more preferable due to the fact that the top-down method can possibly deteriorate the crystalline quality of the nanostructure surface caused by the ion-induced damages at the interface and near-surface region of the nanocolumn[8]. Along with the creation of point defects acting as non-radiative recombination centers at the nanocolumn sidewalls, it has been observed that the inherent yellow luminescence from a GaN thin-film can be found in the top-down GaN nanocolumns[9,10].

2.1 SI WHISKER AND GAN NANOCOLUMNS

Wagner and Ellis[11] in 1964 introduced three-dimensional Si nanostructure with a high aspect ratio known as filamentary crystal/whisker (nanocolumn). A nanostructure with high aspect ratio implies that the ratio of length to diameter is at least sufficient to form a long, narrow nanostructure, e.g., $\geqslant 5$. The whiskers were of high crystalline quality, i.e., single crystalline and free from the screw dislocation, and they were achieved via bottom-up route, wherein the synthesis approach is based on the additional process of building blocks (adatoms) onto the substrate. Adatoms are stacked onto each other to form a crystal plane, and the infinite repetition of these crystal planes will eventually constitute the nanostructure, which in this case is nanocolumn.

The vapor-liquid-solid (VLS) mechanism[11], which was used to obtain single crystal Si whiskers, has also been exploited for nanocolumn growth studies reported for III-V[12–14] as well as III-V nitride semiconductors[15,16]. While the VLS method is still used for non-nitride III-Vs to date, it is perhaps not so much for III-V nitride after 2010[17]. Principally, this mechanism relies on metal droplets, such as Au as the catalyst, where they gather and form a liquid alloy with the incoming atoms (vapor). Continuous supply of these atoms will then supersaturate the liquid droplet, and eventually the atoms in this droplet start to precipitate at the liquid-solid interface, initiating the growth of nanocolumn [18]. However, because of the detrimental effects on the structural and optical properties of semiconductors introduced by non-negligible incorporation of deep level metal impurities into the nanocolumns [19–22], other alternative growth mechanisms not involving foreign metal catalyst are more preferable for the development of the nanocolumn based device.

Interestingly, the original works of GaN nanocolumns on sapphire [2,3] and Si(111) substrates [4,5] were in fact attainable without the use of foreign metal catalyst. The formation of these GaN nanocolumns can be explained by means of self-induced approach [23]. Along with that, GaN nanocolumns can be spontaneously formed using the help of Ga droplets [24–26], of which the process is coined as self-assisted/self-catalyzed mechanism. In this process, Ga droplets are postulated to serve as a catalyst, similar to that of VLS mechanism. However, this mechanism is still not clear as the *ex-situ* investigations [25,26] did not show the presence of Ga droplets, either on the surface of the substrate or the tip of the nanocolumns [27]. Because of this uncertainty, the discussion in this thesis will be mainly emphasized on the self-induced approach, which was also employed (became the basis) for the nitride nanocolumn growth throughout this thesis.

2.2 THE FORMATION MECHANISM OF GaN NANOCOLUMNS BY MOLECULAR BEAM EPITAXY

Most of the GaN nanocolumn syntheses have been carried out on Si(111) substrate and their growth are typically intermediated with AlN [24,28–33], Si_xN_y [24–27,34–50], SiO_2 [51,52], or Al_xO_y [53–56]. Another important substrate for the growth studies conducted so far have been sapphire, SiC and Si(001), as well as recently explored substrates like diamond, amorphous materials (e.g., metal, fused silica glass) and 2D materials (e.g., graphene, MoS_2). Just like for the synthesis on Si(111) substrate, similar buffer layers are generally required for forming GaN nanocolumns grown on the aforementioned materials. These GaN nanocolumns share common traits, including the formation of single-crystalline of wurtzite crystal structure, and the growth axis along [0001] direction (*c*-axis).

To obtain the nanocolumn growth mode, the conditions for GaN growth are generally required to be at N-rich conditions (i.e., V/III ratio larger than 1), along with high growth temperature. Note that the substrate temperature to successfully synthesize GaN nanocolumns is rather narrow [44]: lower growth temperature will form thin-film, and higher growth temperature often induces no growth due to massive Ga desorption and GaN decomposition. The investigation on the formation mechanism of GaN nanocolumns sheds two important phases[23]: (i) nucleation phase and (ii) growth phase, which will be further discussed below. Please note that although these studies were conducted primarily on Si(111) substrates with different buffer layers, they share similarities with each other whose conclusions may apply to other types of substrates.

2.2.1 Nucleation phase

Self-induced GaN nuclei are formed during the nucleation phase. An important feature is the presence of critical radius, which possibly determines the smallest radius of the subsequent GaN nanocolumns. Additionally, the density of these formed nuclei is expected to govern the final density of the GaN nanocolumns. In this phase, GaN nuclei undergo a series of shape transitions governed by thermodynamics, mainly stating that the preferential island shape is given by the minimization of its total free energy per unit volume. Hence, the observed structural evolutions of these GaN nanostructures aim at reducing their total free energy per unit volume by elastically relieving the lattice-mismatch-induced strain with the substrate and accordingly by decreasing their stored elastic strain energy[31]. Generally, the formation of these nuclei is the result from three successive sub-phases[31,36,38], initiated with an *incubation period*, followed by a *nucleation period* and ended with a *transition period*.

The onset of *incubation period* takes place when the substrate is exposed to Ga and N atoms. Few crucial *in-situ* characterization techniques which have been used to investigate this period are reflection high-energy electron diffraction (RHEED)[31,32,34,36,38,39,53,56], line-of-sight quadrupole mass spectrometry[34,54,56] and grazing incidence X-ray diffraction measurements with synchrotron radiation[30,39]. One particular characteristic of the incubation period is the massive Ga desorption at a high nanocolumn growth temperature ($\geqslant 700$ °C), leading to the scarce incorporation of Ga adatoms on substrate surface[34], thus delaying the formation of stable nuclei. It is indicated with no transmission spot of GaN on the RHEED signal[31,36]. An interplay between growth temperature and gallium rate, as well as the influence on the substrate determines the incubation time[38,42,53]. Separated works indicate that the duration of the incubation time can be shortened by incorporating Mg atoms during the growth[40,42]. Physical phenomena, such as the processes of desorption and surface diffusion on different kinds of substrates affect the activation energy, which in turns determines the incubation time, e.g., lower activation energy results in shorter incubation time[38,40,53].

Incoming Ga atoms can adsorb, diffuse, and aggregate with other atoms on the buffer layer or interlayer, such as AlN or Si_xN_y to form GaN 3D metastable nuclei or even desorb from the surface, especially at high substrate temperature[24,31,36]. In addition to growth conditions governing the physical phenomena on the surface, the activation energy is influenced by the presence of surface defects such as surface steps or surface roughness[38]. According to the capillarity model, favorable nucleation takes place at surface steps because of a lower surface free energy for the formation of the nuclei[24]. Particularly, the existence of surface defects on Si_xN_y can act as preferential nucleation sites for the incorporation of GaN nuclei[23].

Depending on the growth condition, RHEED transmission spot intensity (hereafter in this chapter referred to as just "GaN RHEED intensity") eventually starts to increase[31,34,36,39,42], marking the beginning of the *nucleation period*. The process of Ga adatom incorporation leads to the massive growth of 3D GaN nuclei[34], formed as spherical cap-shaped islands, e.g., high-resolution transmission electron microscopy (HRTEM) images in Figure 2.2. It is most likely that they are nucleated on the surface defects[36,56] of the amorphous interlayer or crystallite boundaries on the AlN[23,57]. According to the capillarity theory of Volmer and Weber, these nuclei are stable in terms of total free energy when they pass certain critical size[24]. Depending on the growth conditions, the nucleation phase could be either due to the Volmer-Weber growth mechanism[24,31,32,34,36,42] or Stranski-Krastanov growth regime[28,30,51]. While the former indicates direct growth of 3D GaN nuclei, the latter is characterized with the intermediate 2D GaN wetting layer prior to 3D GaN nuclei growth.

As growth proceeds to the *transition period*, the shape of the nuclei is gradually coarsened and density continuously increases, covering more surface area of the Si_xN_y (or AlN buffer) layer and thus causing the rise of the GaN RHEED intensity, progressing the trend observed from the previous period[31,36]. Here, one or several shape developments are observed, including coarsening of clus-

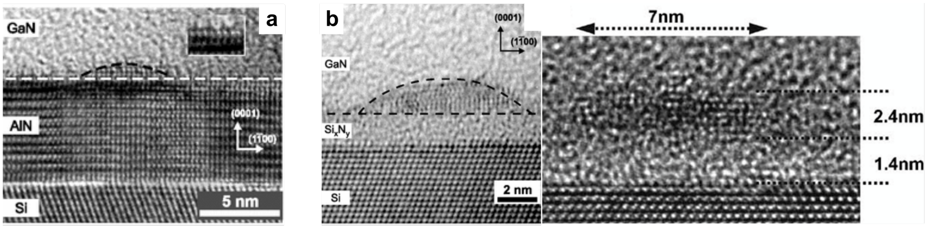

FIGURE 2.2. **Nucleation period.** HRTEM images of a spherical cap-shaped GaN island formed during nucleation period on **a,** AlN/Si, with the inset showing a high magnification of the first AlN monolayers at the interface (adapted with permission from ref. 31 © 2010 American Physical Society) and **b,** Si_xN_y/Si (adapted with permission from [left] ref. 36 © 2011 American Physical Society and [right] ref. 51 © 2008 John Wiley and Sons).

ters, which lead to the self-induced formation of nanocolumn nuclei[30–32,36]. Such physical phenomena are determined by the crystalline nature of the surface where the GaN nucleates and accordingly with its epitaxial relationship: AlN buffer layer or Si_xN_y interlayer, and their respective structural morphology can be seen in Figure 2.3.

Specific for the GaN nanocolumn growth on AlN/Si[31], the transition period is associated with the relaxation of the epitaxial constraint between GaN—AlN[30–32], having a lattice mismatch of 2.54 %[32]. In principle, elastic strain and plastic strain relaxation processes are important mechanisms for the formation of self-induced nanocolumn nuclei[30–32]. With this respect, 3D GaN nuclei firstly undergo elastic strain relaxation through shape transition from coarsened spherical cap- (Figure 2.2a) to truncated pyramid-, and subsequently pyramid-shaped islands (Figure 2.3a-i and Figure 2.3a-ii, respectively)[31]. This faceting transformation is due to the minimization of the total free energy per unit volume. As reported by Consonni *et al.*[31], each shape transition is categorized as a coherent island, which is characterized as a dislocation free nanostructure. These successive island developments occur in order to elastically relieve the lattice-mismatch-induced strain, i.e., each island shape transformation contributes to reduce the residual elastic strain energy of the epitaxial structures[23,31].

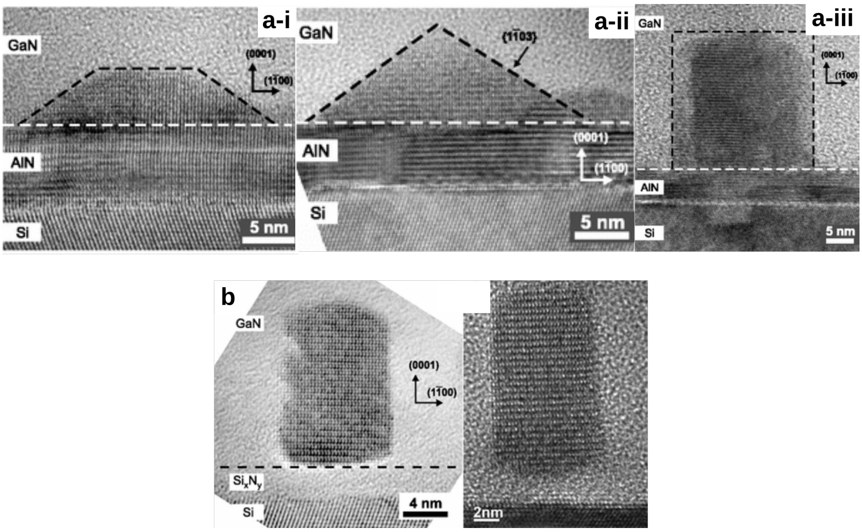

FIGURE 2.3. Transition period. a, HRTEM images of **-i** GaN truncated pyramid-, **-ii** pyramid-shaped islands and **-iii** nanocolumn formed during transition period on AlN/Si (adapted with permission from ref. 31 © 2010 American Physical Society). **b,** HRTEM images of GaN nanocolumn formed during transition period on Si_xN_y (adapted with permission from [left] ref. 36 © 2011 American Physical Society and [right] ref. 51 © 2008 John Wiley and Sons).

However, each unique island shape is associated with a certain level of increasing strain relaxation. Eventually, the accumulated stored elastic strain energy reaches a threshold at which plastic relaxation will induce *at least* one misfit dislocation at the interface to relieve the residual epitaxial strain[31]. This happens for pyramid-shaped islands whose radii are beyond specific critical radiuses or critical sizes (based on several theoretical approaches listed in ref. 31). Remarkably, the out-of-plane stress component within pyramid-shaped islands acts as a driving force for the horizontal shift of the misfit dislocation on the basal plane from their edges (where the stress concentration is maximum, indicated with white circle in Figure 2.4a), toward their center (white circle in Figure 2.4b). Once it reaches their quasi-central position, the complete strain relaxation state is achieved and thus yielding the final shape transition towards the nanocolumn morphology, as shown in Figure 2.3a-iii[31].

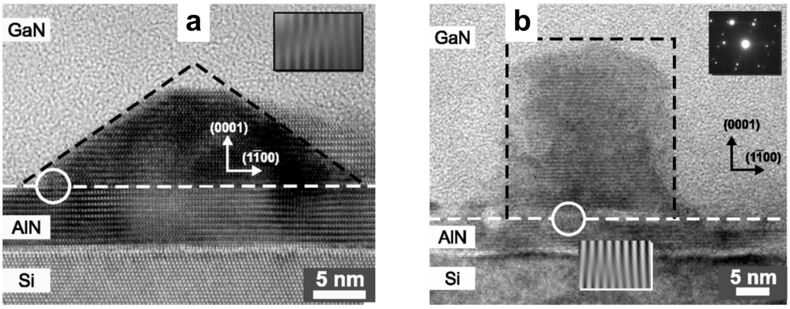

FIGURE 2.4. Motion of the misfit dislocation in the GaN grown on AlN/Si during the transition period. HRTEM image of **a,** pyramid-shaped island and **b,** nanocolumn with misfit dislocation indicated within the white circles (adapted with permission from ref. 31 © 2010 American Physical Society). The inset in **a** and **b** (bottom) reveals a Fourier-filtered enhancement showing only {1-100} lattice planes within the white circle. Unexpected top facet in pyramid-shaped island is due to cut during TEM sample preparation. Selective area electron diffraction pattern in **b** (top inset) demonstrates that this nanostructure is completely relaxed.

In the case of Si_xN_y/Si, no transition to pyramid-shaped island is observed due to weak epitaxial constraint on this amorphous interlayer. The transition period cannot be strongly affected by strain relaxation effects. As a result, the coarsened spherical-cap islands (Figure 2.2b) retain their shape and once the critical radius is achieved, they directly undergo the final transformation towards nanocolumn geometry, depicted in Figure 2.3b. Like the previous case, this shape transition is induced due to the nanocolumn's higher ability to relieve the strain[36]. Typically, nanocolumn morphology has a {0001} top facet and vertical sidewalls consistent with the presence of {1-100} planes, i.e., *m*-planes. It neglects the faceting processes of island transformation phases due to the exclusion of the epitaxial constraint, leading to the self-induced formation of nanocolumn nuclei that are free of misfit dislocation.

Basically, the formation of Si_xN_y on top of Si surface should remove the epitaxial constraint of the substrate due to its amorphous characteristics. It is expected that the orientation of the GaN nanocolumn nuclei heavily depends on the smoothness of the underlying Si_xN_y layer[34]. In the event of inhomogeneous Si_xN_y layer, non-vertical GaN nanocolumn growth is obtained[42,43,51]. Interestingly, a strong in-plane orientation relationship can exist between GaN nanocolumns and the Si substrate[46], despite the presence of Si_xN_y amorphous layer with a thickness similar to the ones presented above. Coherent twist of GaN nanocolumns may exist depending on the nitridation temperature during the early growth stage, i.e., substrate nitridation step. To reconcile these discrepancies, it is proposed that both amorphous and crystalline domains may co-exist in the Si_xN_y interlayer[23,34,39,46].

Despite the difference during early stage of transition period, the phenomena that trigger the final phase transition of GaN nuclei on AlN/Si and Si_xN_y/Si substrates are in fact identical. We know from the thermodynamic considerations that the small strain energy density induced by nanocolumn geometry favors this particular shape transformation. In addition to this, the anisotropy of surface energy is another important driving force[31,36], due to the fact that the *c*- and *m*-planes in the wurtzite structure of GaN nanocolumn have very low surface energies as compared to the free surface composed of high-index planes in GaN island, for instance {1-103} side facets.

It is also deduced that at GaN island critical radius, the shape transition leading to the self-induced formation of the very first GaN nanocolumns occurs due to the fact that their (top) corners retain high edge energy, which can overcome the energy barrier required for the shape transition[31,36]. The value of the critical radius is affected by the growth conditions as they can alter the surface energy, resulting in the change of the wetting behavior of the spherical caps on the substrate and thus the energy balance between the strain energy, the surface energy and edge energy[36].

The RHEED intensity of GaN in transition period steadily increases as the time progresses, and it will maintain this trend until the final shape transition to nanocolumn nuclei is completed[31,36]. However, for the growth on AlN/Si it is noticed that the RHEED intensity temporarily saturates when plastic strain relaxation process takes place[31], indicating the transition from pyramid-shaped islands to nanocolumn-shaped islands in order to relieve the strain[31]. Finally, the GaN RHEED intensity will enter the constant state[31,36], which could be associated with the saturation of the overall nanocolumn nuclei density. For self-induced GaN nanocolumns, there is a possibility for the late nucleation of newly-formed GaN nuclei, yielding an inhomogeneity of nanocolumn dimension once the whole growth process is complete.

2.2.2 *Growth phase*

Subsequent to the formation of GaN nanocolumn nuclei is the prolongation process mainly along their vertical axes, as seen in Figure 2.5. Unlike the previous phase which is solely governed by thermodynamics, the growth phase is suggested to have kinetics[24,26,27,41,47,58,59] *and/or* thermodynamics[33,59] as its main driving force. The phenomena observed in this phase are more straightforward compared to the nucleation phase. The growth phase consists of an *elongation period* that is often succeeded by a *coalescence period*[23]. Keep in mind that these two periods can also occur at the same time. Under N-rich conditions, Ga adatoms will prefer to incorporate at the nanocolumn top, and this behavior is apparent through the formation of nanocolumns. However, when N-rich conditions are reduced, for instance by increasing Ga flux or reducing N flux, the radial growth rate of the nanocolumns will be enhanced, which can cause premature coalescence, and further might lead to a 2D layer morphology[24].

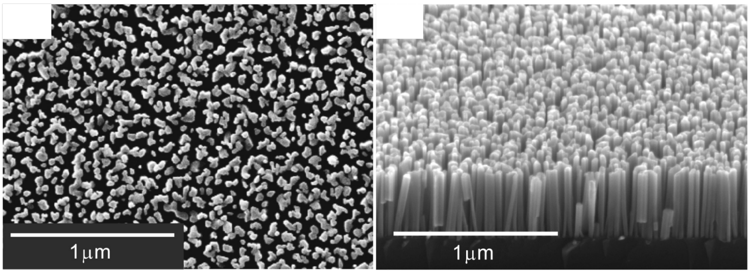

FIGURE 2.5. Elongation period. SEM image (top-view and bird's eye-view) of vertically-oriented GaN nanocolumns grown on Si(111) with the length of 400 nm (adapted with permission from ref. 43 © 2006 AIP Publishing).

From a kinetic point of view, the mechanisms contributing to the growth of GaN nanocolumns during the *elongation period* are the direct impingement of Ga adatoms on the nanocolumn top facet and the diffusion of Ga adatoms on the nanocolumn sidewall to the top facet[24,27,33,41]. One should also consider that the desorption of Ga adatoms from the substrate surface is a part of the kinetic adatom processes although it does not necessarily contribute to the nanocolumn growth[27]. However, the desorbed Ga adatoms hitting the nanocolumn sidewall may contribute to the nanocolumn growth. According to the diffusion-induced mechanism[27], the preference to grow in axial direction is induced by the top surface (i.e., tip) of nanocolumns acting as an efficient collector of adatoms, and adatom diffusions from lateral side to column apex are driven by a lower chemical potential at the top surface. It is similarly suggested that the low nucleation barrier on the nanocolumn top facet favors elongation in the axial direction[41].

Once the nanocolumn length is greater than the diffusion length of adatoms on the vertical sidewalls (40-45 nm [27,41]), Ga adatoms condensing at the surface or arriving farther down on the sidewall (whose distance to the top is larger than their diffusion length) may no longer be able to diffuse through nanocolumn sidewall all the way to the top because of desorption [27,33]; another reason is the preferential incorporation of such Ga adatoms in the radial growth. Thus, the major determining factor for the axial growth rate is the direct impingement of Ga adatoms on the column tip. Since the contribution toward nanocolumn growth rate is discounted, one should expect that up to certain elongation period the nanocolumn growth rate will be reduced, and shortly afterwards becomes constant with the growth time [27,41].

Evidences on the formation of GaN nanocolumns via thermodynamics come from the variations in surface sticking coefficients that is higher for *c*-plane compared to *m*-plane [33]. The relative magnitudes of the sticking coefficients and surface diffusion depend on growth conditions [33], e.g., high substrate temperature can enhance the surface diffusion of Ga adatoms. The density-functional theory [59] on *m*-planes reveals that Ga adatoms have large diffusion barriers along the *c*-axis. From this perspective alone, nanocolumn growth should be slower in the *c*-axis compared to *m*-axis. However, *m*-planes are intrinsically unstable against atomic N, resulting in an easy desorption of N_2 molecules. This is in contrast to the *c*-plane GaN surfaces, where N adatoms can be stabilized either thermodynamically in the form of a 2×2 N adatom reconstruction for extreme N-rich conditions, or kinetically due to huge N adatom diffusion barriers [59]. Therefore, the incorporation and nucleation events of Ga adatoms are expected to be more probable to take place on the polar *c*-planes (nanocolumn growth front), rather than on the non-polar *m*-planes (side facets).

One might argue that the direct impingement of Ga adatoms on the nanocolumn top may as well diffuse toward its sidewall, making them ineffective toward the contribution of nanocolumn vertical growth. However, these Ga adatoms actually have much lower diffusion length on the *c*-plane than on the *m*-plane due to the availability of more adsorption sites in the *c*-plane surface of nanocolumn main growth front. In other words, the number of dangling bonds related to the adatom trapping is larger on *c*-planes than on *m*-planes. The strong growth rate anisotropy of nanocolumn top relative to sidewalls is caused by higher surface energy (directly affecting the growth rate) on *c*-plane facets compared to *a*- and *m*-plane facets (under N-rich conditions) [24].

It is important to know that radial growth is inevitable during the elongation period, although its rate is much lower compared to the axial growth rate [26–28,42]. The radial growth of nanocolumn is expected to start immediately once the nanocolumn length exceeds the Ga adatom diffusion length. In other words, the Ga adatoms which do not contribute to the vertical lengthening might have a chance to assist the radial growth of nanocolumns. However, the radial growth rate is gradually reduced when the nanocolumn is long enough to induce shadowing effect. Basically, this effect emerges due to two factors[60]: (i) impinging atoms at nonzero angles (coming from an incident angle) with respect to the substrate surface normal; (ii) length of individual (vertical) nanocolumns that can shadow the neighboring nanocolumns from collecting incoming atoms. Together with the reduction of N-rich conditions[3,44,47], an incorporation of Si or Mg atoms can enhance the radial growth rate (simultaneously reducing the axial growth rate), as their presence are known to influence the surface kinetics during GaN growth by forming "step bunches" along nanocolumn sidewalls, which can increase the GaN nucleation on nonpolar facets[42].

With increasing growth time[26,28,42], there is a likelihood for the transition from elongation to *coalescence period*, a phenomenon where individual nanocolumns merge with other nanocolumns in the vicinity and thus form nanocolumn bundles, as depicted in Figure 2.6a and Figure 2.6b (four white arrows at the left of the image). Other possible scenarios for coalescence to prevail is the growth of two or more close GaN nanocolumns which are slightly tilted away from the substrate normal[33], with an example shown for the GaN nanocolumns indicated with two white arrows at the right in Figure 2.6b. Additionally, surface profile (roughness) of the interlayer/buffer layer is partly responsible for the verticality of the GaN nanocolumns[42,43,51]. Nevertheless, coalescence degree can be generally suppressed by using higher growth temperature[28,61] and/or increasing V/III ratio, i.e., by reducing Ga flux[44,61,62] and/or raising N_2 flow rate.

Despite the fact that tilted nanocolumns have the same growth axis along the *c*-axis direction as vertical nanocolumns, they contain crystallographic defects which are not present in the "normal" (vertical) nanocolumns[33], e.g., I_1-type basal plane stacking faults[63], misfit dislocations[43], zipper dislocation

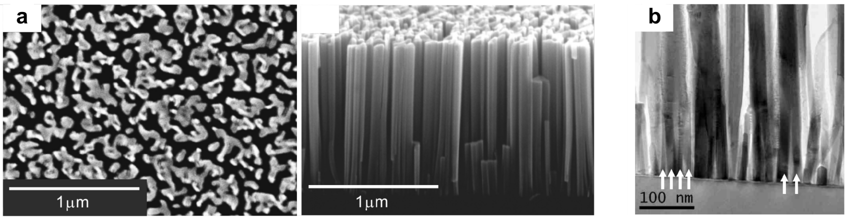

FIGURE 2.6. Coalescence period. a, SEM image (top-view and bird's eye-view) of coalesced GaN nanocolumns with the length of 1000 nm (adapted with permission from ref. 43 © 2006 AIP Publishing). **b,** Bright-field scanning TEM image showing the merging of adjacent vertical (four white arrows at the left of image) and tilted GaN nanocolumns (two white arrows at the right of image) (adapted with permission from ref. 42 © 2008 AIP Publishing).

arrays[62], and/or generation of stacking fault-strain[45,64]. Generally, the coalescence phenomenon of individual nanocolumns merging into nanocolumn bundles can reduce the areal density of GaN nanocolumns, nearly one order of magnitude compared to those grown with limited merging events[43]. The density evolution of GaN nanocolumns is shown to have a certain peak in which their density reach the maximum magnitude[26,37,42]. Prior to this event, the density will increase significantly with growth time, which is closely related to the development of spherical cap-shaped islands during the nucleation phase. Immediately after reaching its peak, the density will gradually decrease, marking the starting point of the coalescence period.

Coalescence events are also likely to influence the optical properties of GaN nanocolumns. In the locally coalesced part of the nanocolumn, it was reported that there is an additional radiative transition at 3.42 eV which is assigned to excitons bound to I_1-type basal plane stacking faults[63]. Other radiative emissions identified at 3.21 and 3.35 eV are believed to originate from excitons trapped by unidentified point defects at edge threading dislocations, or excitons bound to the dislocations formed at the boundaries of the coalesced nanocolumns[43,61]. In addition, the coalesced nanocolumns can broaden the linewidth of GaN near-bandgap emission, because of the introduction of microstrain[35]. In short, dislocations introduced during the coalescence period are not desired since they give rise to nonradiative recombination centers and therefore suppress the GaN band-edge emission intensity.

2.3 THE CHARACTERISTICS OF GaN NANOCOLUMNS

Since a GaN nanocolumn is geometrically different from a GaN thin-film, the properties of such three-dimensional structure are anticipated to be unique compared to its planar counterpart. Typical lattice-mismatched heteroepitaxy of GaN thin-film with traditional substrates leads to a grown structure that is more prone to the issues related with crystal imperfection, including stacking faults, misfit and threading dislocations. Additionally, crack generations are usually observed in the GaN thin-film due to large coefficient of thermal expansion (CTE) difference with the substrate. On the other hand, GaN nanocolumn is associated with defect-free structure, which is beneficial for optical and electrical properties that can be useful for various optoelectronic devices, for instance LEDs.

2.3.1 Structural properties

Just as for GaN planar structures, GaN nanocolumns crystallize in a thermodynamically stable wurtzite structure having hexagonal symmetry, which can be observed during the growth by means of RHEED. In this in-situ characterization technique, vertical GaN nanocolumns are normally characterized with well-defined spot shape patterns[28], indicating electron transmission through 3D formation of GaN crystals in the wurtzite structure, for example along the [11-20] direction[65]. As a general rule, the more stretched the RHEED spot patterns are (appearing like broken rings/faint ringlike patterns), the more misaligned the GaN nanocolumns are with respect to the substrate. Examples of the RHEED patterns for well-oriented and poor-oriented GaN nanocolumns grown on AlN/Si(111) and Si(111) respectively can be seen in ref. 28. Similar cases can be found in refs. 22,65.

High resolution x-ray diffraction (HRXRD) is one of the common techniques used to evaluate the structural qualities of GaN nanocolumns, including the alignment (to substrate normal) and the spread of tilt of the nanocolumns using 2θ-ω and ω (rocking) curve scans of the GaN (0002) reflection, respectively. Wurtzite crystal structure of GaN with growth orientation along the c-axis is typically characterized with the 2θ-ω peak at 34.56°. Additional GaN reflections imply that the growth happens in different crystallographic directions as well. For the ω peak located at 17.28°, its full width at half maximum (FWHM) can be utilized to evaluate the spread in orientation for the probed nanocolumn collection. Large FWHM value indicates more spread of tilt of the nanocolumns (and vice versa). In addition, the twist of the grown nanocolumns can be deduced through the X-ray pole figures and additional φ scans across the GaN (10-14) reflection[65].

Similar to HRXRD, the presence of wurtzite crystal structure of GaN nanocolumns can be quantified by Raman spectroscopy[66,67]. It is characterized with a number of features[68,69], such as (531.5±0.5), (557.9±0.9) and (566±1.0) cm^{-1} corresponding to A_1 transverse optical (TO), E_1 (TO) and E_2 (high) phonon modes, respectively. Others are 734 and 741 cm^{-1} which can be categorized as A_1 longitudinal optical (LO) and E_1 (LO) phonon modes. If there is a zinc-blende crystal structure within GaN, a TO phonon mode additionally appears at 555 cm^{-1}. The FWHM of E_2 (high) mode can be used to justify the crystalline quality of the GaN nanocolumns. Raman is a versatile tool to characterize the material composition, crystalline quality and strain of GaN.

Top-view SEM of fully developed self-induced single GaN nanocolumns on Si(111) or Si(001) substrates demonstrates a hexagonal cross-section, although its six facets are not always equal in size[65]. Perhaps, the most compelling element offered by GaN nanocolumns is their ability to generate high crystalline quality structure. HRTEM investigation, as depicted in Figure 2.7, indicates minimal threading dislocations, misfit dislocations and/or stacking faults in GaN near the interface between the nanocolumns and an Si_xN_y interlayer (~2 nm thin, partially amorphous). It is observed that the crystalline quality of this GaN is comparable to its precursor nanocolumn nucleus, shown in Figure 2.3 and Figure 2.4. The proof of high structural quality of nanocolumns has been documented by Wagner and Ellis[11] in Si whisker structure, i.e., by demonstrating a grown Si nanostructure without axial screw dislocation. The importance of nanocolumn high aspect ratio in suppressing various defects will be explained in the following paragraphs.

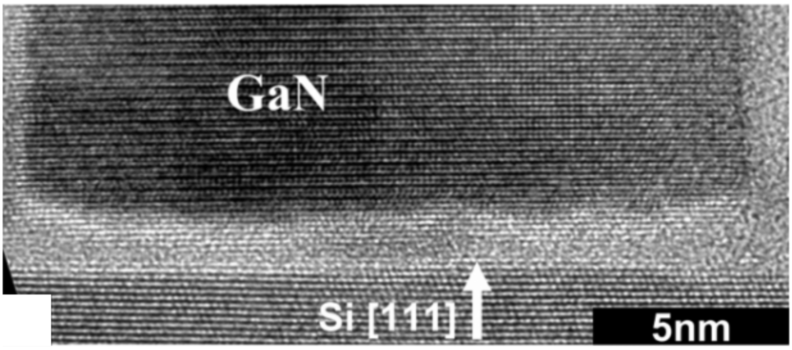

FIGURE 2.7. HRTEM image of the interface area of a GaN nanocolumn grown on Si(111) with the formation of a Si_xN_y interlayer (partially amorphous) in between (adapted with permission from ref. 65 © 2011 IEEE).

Theoretically, one can suppress the misfit dislocations (i.e., achieving pseudomorphic growth) as long as the strain energy density of the grown structure does not exceed the energy density associated with the formation of a screw dislocation. Strain energy of the epilayer is proportional to its thickness, and the thickness of the epilayer at which misfit dislocations started to nucleate in order to relieve the strain energy is known as the *critical layer thickness*[70] or *critical thickness*[71]. In GaN thin-film, its critical layer thickness is very much limited, given the high lattice-mismatch with common foreign substrates. However, by initiating *small seed pad* growth to limit the strained zone, this thickness can be greatly expanded[72] up to 10 times thicker than a structure with infinite lateral dimension, i.e., conventional thin-film[70]. This concept is further formulated through elongated nanoscale islands, where the stress relief mechanism can be mitigated *both* in vertical and lateral direction[73]. Furthermore, any possible generated dislocations can be glided to the lateral surface of this nanostructure.

In this regard, the geometry of a nanocolumn closely resembles the description of the elongated nanoscale island described above. A possible elastic relaxation at the lateral free surface can be achieved due to the existence of nanocolumn *m*-plane sidewalls. Like for the nanostructures in previous studies[70,72,73], the lateral size of the nanostructure, which in this case is the nanocolumn radius, has to be less than certain values to obtain large critical thickness[74]. However, with greater lattice mismatches, smaller nanocolumn radius is required to simultaneously achieve infinite critical thickness and coherent strain mismatch mitigation[75,76]. If the nanocolumn is grown with radius exceeding the critical value, dislocations in the structure are expected[77,78]. Along with the ability to accommodate lattice strain, the small footprint of nanocolumn can also reduce wafer bowing and prevent crack generations in GaN due to the mismatch of CTE with the underlying substrate[79].

The relatively small cross-section of the nanocolumns supports the defect-free integration of lattice-mismatched heterostructure materials within the nanocolumn structure[76]. Model developed by Ertekin *et al.*[76] describes that the strain induced by the lattice mismatch is shared by the nanocolumn over- and underlayer, and can be partially accommodated by the introduction of a perpendicular pair of misfit dislocations in both x and y directions[76]. This work shows that for the same given lattice mismatch condition, the critical radius of the nanocolumn is at least one order of magnitude larger than the critical thickness of the equivalent thin-film system, diminishing the strict requirement to obtain GaN with high crystalline quality. Hence, nanocolumn geometry offers more flexibility in the growth substrate choice and warrants improved crystalline quality of the grown material compared to planar thin films.

Indeed, many groups have claimed to obtain dislocation-free GaN nanocolumns characterized using transmission electron microscopy (TEM) analysis[49,50,80]. Nevertheless, we should realize that TEM is a locally resolved method with very limited local probing area, implying that it is difficult to derive the global, statistically averaged properties of as-grown nanocolumns[79]. An observation using deep level optical spectroscopy technique noted a surface state located approximately 2.6 eV above the valence band[81]. Furthermore, deep-level transitions corresponding to yellow, green and blue bands were found by spatially-resolved cathodoluminescence[82] and spectral photoconductivity[83] measurements across the nanocolumn surface layer and bulk.

Note that high aspect ratio of GaN nanocolumns can potentially enhance surface-related effects which are not significant in thin-films, known as band bending due to surface Fermi-level pinning. Such Fermi-level pinning causes surface depletion layer which can induce the variation of electrical properties on the nanocolumns, particularly for those whose diameter is comparable with the depletion region[84]. Space-charge-limited current behavior[85,86] is often observed in thin nanocolumns due to its poor electrostatic screening[86,87]. Other reasons can be low doping level and carrier depletion caused by surface states.

This phenomenon can further lead to large effective carrier concentrations required to obtain an Ohmic behavior, i.e., Ohmic contact for devices[86]. Additionally, the Fermi-level pinning at the surface of the nanocolumns results in the separation of electrons and holes by the depletion field, reducing the recombination of non-equilibrium carriers (i.e., electron-hole pairs)[85].

2.3.2 *Optical properties*

The near-bandgap emission intensity of room-temperature photoluminescence (Figure 2.8a) at ~3.39 eV from as-grown GaN nanocolumns is typically much higher than in HVPE-bulk GaN film[88,89]. In addition, defect-related emission known as yellow luminescence is normally suppressed, but its intensity can be enhanced for coalesced nanocolumns[63], indicating the existence of structural defects and/or chemical impurities within the nanocolumn structure[90,91]. Low-temperature (5 K) photoluminescence measurements of single GaN nanocolumns show donor-bound exciton peak at ~3.472 eV corresponding to strain-free GaN, and free exciton peaks at ~3.478 and ~3.483 eV[92,93], denoted respectively as D^0X_A, X_A and X_B in Figure 2.8b. Surface-related effects of GaN nanocolumns (Ga-polar) might generate emission related to two-electron satellite at ~3.448 eV. However its origin is still under debate[65], whether this localization of excitons is caused by the enhanced formation of Ga vacancies as point defects[48] or inversion domain boundaries[94].

Another interesting peak that might appear at low-temperature is an emission at ~3.42 eV[63]. This peak is associated with radiative recombinations of excitons bound to basal-plane stacking faults. Such crystal imperfections

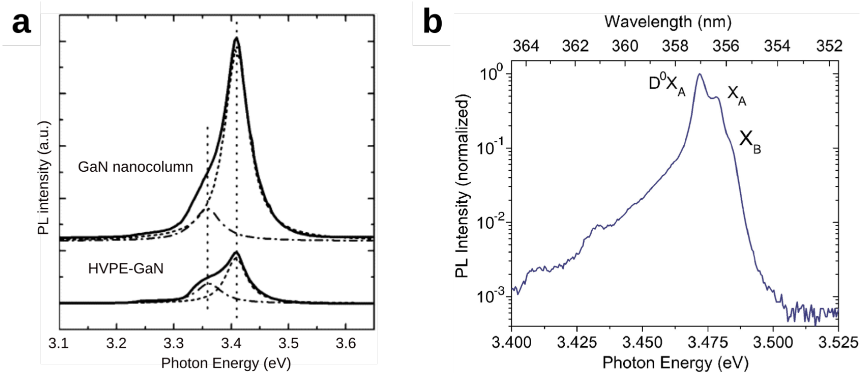

FIGURE 2.8. The photoluminescence spectra of GaN nanocolumns. **a,** Si-doped GaN nanocolumns at room-temperature (adapted with permission from ref. 57 © 2007 Elsevier), and **b,** unintentionally Si-doped GaN nanocolumns at low-temperature (reproduced with permission from ref. 92 © 2008 AIP Publishing).

are caused by the coalescence of close-standing nanocolumns. In addition, a donor-acceptor pair band is observed, which consists of a zero phonon line centered at ~3.28 eV and two LO phonon replicas at ~3.19 and ~3.10 eV. It is worth to note that the metal catalyst-induced nanocolumns demonstrate much lower GaN band-edge photoluminescence intensity compared to that of self-induced nanocolumns[22]. This reduced luminescence intensity is likely due to the contamination of the metal catalyst unintentionally incorporated into the nanocolumns, which acts as a nonradiative recombination center.

Time-resolved photoluminescence of GaN nanocolumns reveals that the dominant recombination processes are altered as a function of temperature[91,92]. Around 5 K, radiative recombination of donor-bound excitons dominates the process, but at 70 K the thermally activated nonradiative process related to the dissociation of the exciton from the neutral donor event takes place, causing a slight decrease in decay time. Above 70 K, free exciton radiative recombination becomes dominant, which is marked with an increased lifetime up to 150 K (provided that nonradiative recombination processes are saturated).

Near room-temperature, it has been observed that there is a dependency between the photoluminescence lifetime and the nanocolumn diameter. This is caused by the surface recombination effect of nanocolumn which further provokes nonradiative recombination at the nanocolumn surface. As a consequence, surface recombination limits the photoluminescence lifetime, where its lifetime linearly depends on the nanocolumn diameter, e.g., thicker nanocolumns have longer lifetimes and vice versa[91]. Such phenomenon is a strong indication that the observed lifetimes are determined by the nonradiative surface recombination, and this can be minimized by proper surface passivation using e.g., an AlGaN shell[91]. Nevertheless, even without such surface passivation the surface recombination velocity of GaN nanocolumns at room-temperature (~9×10^3 cm/s) is five times smaller than for its thin-film counterparts, and two orders of magnitude smaller than for GaAs, making this compound semiconductor nanostructure as a promising candidate for nanoscale optoelectronic device applications.

Compared to conventional planar structures, defect and dislocation densities in nanocolumns can be reduced, which can lead to the minimization of the strain and thus weaken the piezoelectric polarization field. Along with the carrier confinement in the radial direction, the weak piezoelectric field can thus shorten the radiative lifetime in nanocolumns[95]. Furthermore, high crystalline quality of the GaN nanocolumns can improve the IQE up to ~58%[96]. Such high IQE is associated with the enhancement of radiative recombination rate (shortening the radiative lifetime), as well as suppression of nonradiative recombination processes. Bear in mind that the nonradiative recombination process can be a limiting factor of the IQE due to the surface effects in nanocolumns[97].

Early demonstration of nanocolumn LEDs showed an improvement of light extraction with respect to the planar structure, attributed to its large sidewall surface area[98] and subwavelength size that eliminates the guiding modes responsible for trapping the light[99]. Additionally, the decrease in the number of guided-modes in nanocolumn structure induces the radiation pattern of nanocolumn-based LEDs to be much more directional than in planar LEDs[99,100]. Inside the nanocolumn, the electromagnetic wave propagates along the vertical direction with a well-defined phase front, resulting in a strong forward emission. Whereas for planar LEDs, it does not have a defined direction, and it has stronger backward emission than the forward emission[100]. This nanostructure also increases the possibility for photons to overcome the total internal reflection via multiple scattering events[99,101], and acts as light guiding pillars to extract photons in the longitudinal direction[101–104].

2.3.3 Electrical properties

Typical electrical property studies on III-nitride nanocolumns have been mostly performed on single nanocolumn field effect transistor devices, due to difficulty in Hall-bar fabrication process on as-grown samples[87]. These devices consist of a dispersed nanocolumn onto an oxidized Si substrate, which is used as a back gate, with two contacts formed on both ends of the nanocolumn as its source and drain[91]. The findings reveal that the electron concentrations of Si-doped *n*-GaN nanocolumns are in the order of 10^{17} to 10^{19} cm^{-3}, with their Hall mobilities varying widely from 10 to 800 $\mathrm{cm}^2\ \mathrm{V}^{-1}\ \mathrm{s}^{-1}$[91,105–107]. On the other hand, *p*-type doping of single GaN nanocolumns using Mg atoms has been reported to be a challenge since their absence of ohmic behavior hinder assessment of the true electrical properties of *p*-GaN nanocolumns. Because of this reason, the following discussion below will be limited to *n*-type GaN nanocolumns.

Photoconductivity measurement of single *n*-GaN nanocolumn devices shows a persistent photocurrent behavior[87]. Essentially this behavior can be explained as the inability for the current to return to its initial state (dark current value) after there is no light illuminating on the sample (a considerable current persists in the dark), even after certain period of time. Such phenomenon stems from the hindered surface recombination due to the presence of depletion space charge layers, which are formed due to Fermi-level pinning in the vicinity of nanocolumn surface. Figure 2.9a depicts the upward bend of conduction and valence bands causing the electrons to remain in the inner part of the columns, while holes tend to drift toward the surface where they are trapped. This spatial separation of electrons and holes significantly reduces the recombination

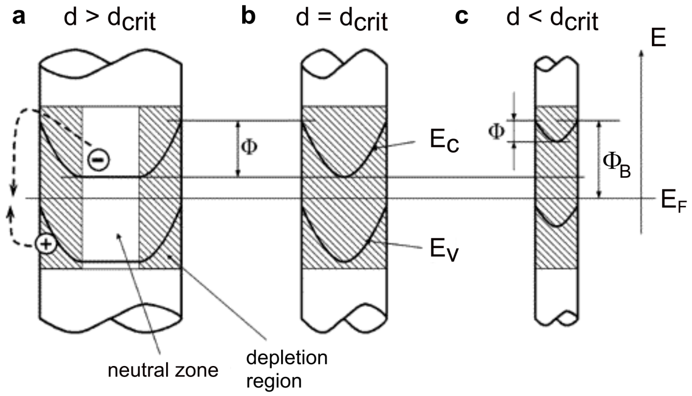

FIGURE 2.9. Dependence of depletion region (shaded), conduction band (E_C), valence band (E_V) and surface potential barrier (Φ) with nanocolumn diameter (d; d_{crit} is critical diameter of nanocolumn). **a**, **b** and **c** illustrate the alteration of surface potential barrier within the nanocolumn when $d > d_{crit}$, $d = d_{crit}$ and $d < d_{crit}$, respectively. Schematic model of the surface recombination mechanism of the photoexcited carriers in GaN nanocolumn is described in **a** (adapted with permission from ref. 85 © 2005 American Chemical Society).

process of carriers. In order to recombine with the holes at the surface, the electrons must overcome the surface potential barrier at the surface[85].

Such condition depicted in Figure 2.9a is true for thick nanocolumn, where the center of nanocolumn remains unperturbed. For thinner nanocolumn where its diameter is equal to the critical diameter (Figure 2.9b), the depletion region can be extended over the complete volume of the nanocolumn. In this state, the recombination rate and photocurrent behavior are almost the same as for the nanocolumn whose diameter is larger than the critical diameter, because the surface barrier height remains unchanged. When the nanocolumn diameter is less than the critical diameter, the band bending becomes smaller and therefore reduces the barrier for the surface electron-hole pair recombination, as shown in Figure 2.9c. Thus in this state the recombination process is enhanced, causing the photocurrent at the surface (which previously dominated the process) to rapidly decay due to lower barrier height[85]. Mathematical model for critical diameter developed in refs. 85,87 can be used to estimate the doping concentration (as well as surface potential value). As an example of this approach, the donor concentrations of unintentional- and slightly Si-doped GaN nanocolumns were estimated to be approximately 6.2×10^{17} and 1.8×10^{18} cm^{-3}, respectively[87].

Raman spectroscopy can also be utilized to evaluate the basic electrical properties of GaN nanocolumns[87]. The strong interaction of the free carrier gas with long-wave LO phonons results in phonon-plasmon coupled modes with low (L-) and high (L+) energy branches in Raman spectra. Using the information of these coupled modes (peak positions and line shapes) one can correlate with the free carrier concentration and mobility of the GaN nanocolumns, either as-grown[67,108] or free-standing sample (single nanocolumn)[109], by fitting a theoretical model to the experimental data[110]. For example, Wang *et al.*[108] derived an electron concentration of 3.3×10^{17} cm^{-3} and an electron mobility of 140 cm^2 V^{-1} s^{-1} for an as-grown sample, while Jeganathan *et al.*[109] extracted an electron concentration of 1×10^{18} cm^{-3} and an electron mobility of 15 cm^2 V^{-1} s^{-1} for a free-standing sample.

All of these electrical measurements mentioned in previous paragraphs assume that the doping concentrations are constant for different nanocolumns and uniformly distributed within the volume of nanocolumns. However, spatial mapping studies of the dopants show that both Si and Mg atoms are inhomogeneously distributed in the nanocolumns[111,112]. Energy-dispersive x-ray spectroscopy (EDX) and atom probe tomography mapping indicate that higher concentrations of these dopants are generally observed at the periphery than in the bulk of GaN nanocolumn. The preferential incorporation of Si and Mg atoms in the m-plane sidewalls of nanocolumns can be associated with the growth mechanism of nanocolumns carried out in N-rich conditions, where these dopant atoms reach the growth front at the nanocolumn top through diffusion on the nonpolar facets of the nanocolumns[17].

2.4 NANOCOLUMN-BASED LEDS

Just as its thin-film counterparts, III-V nitride nanocolumns have been explored for their opportunities as the nanostructure materials for various kind of optoelectronic devices[113–115], of which the discussion in this section is centered on LEDs. As this material system has tunable direct energy bandgap from 0.65 eV (InN) to 6.1 eV (AlN), it is thus attractive for light emitter applications from near infrared to deep ultraviolet. Fundamentally, the nanocolumn structure of III-V nitride offers a few advantages that could be utilized to overcome the challenges that classically have confronted thin-film based emitters, such as achieving high quality material, obtaining sufficient Mg p-doping efficiency and limited substrate options. Exploiting nanocolumn devices has the potential to deliver an unrivaled capability in integration with other devices and systems (e.g., Si technology), particularly for emerging flexible photonic and electronic devices[116].

2.4.1 Basics of the light emission in semiconductors

Principally, light can be emitted from a semiconductor material due to the electron-hole recombination. Note that the nature of the material energy bandgap is preferable to be direct, i.e., the conduction band minimum and the valence band maximum occur in the same crystal momentum (at $k = 0$ in the Brillouin zone), as shown in Figure 2.10. This is to ensure band-to-band transitions can take place without the simultaneous participation of a phonon[117]. Nevertheless, materials that are capable of emitting such light cannot glow or luminesce by their own at equilibrium conditions, e.g., room-temperature because the concentrations of thermally excited electrons and holes are insufficient to produce discernible radiation. An external source is required to produce sufficient non-equilibrium concentration of electron-hole pairs in order to achieve large amounts of spontaneous recombination radiation[118].

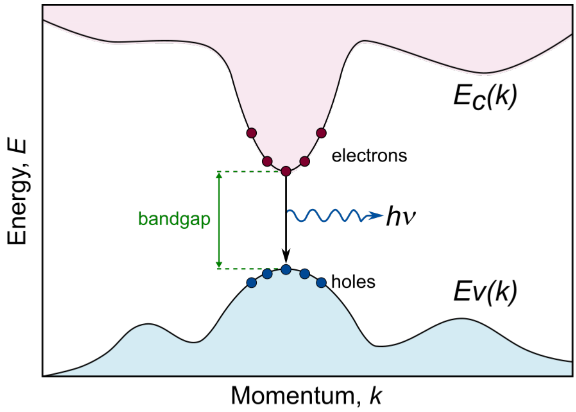

FIGURE 2.10. An efficient electron-hole recombination process occurs in direct bandgap semiconductor band structure.

The very basic of LEDs can be constructed from a *p*-*n* junction fabricated from a direct bandgap semiconductor. Let us use a *p*-*n* GaN (homo-) junction as an example. Fusion between *p*-type GaN and *n*-type GaN will align the Fermi levels, resulting in a band diagram as shown in Figure 2.11a. Because extra electrons from the *n*-side can diffuse to the *p*-side (and vice versa for holes), they leave behind positive ions (holes leave behind negative ions) in the vicinity of the junction on the *n*-side (*p*-side). Therefore, a region near the *p*-*n* junction is depleted from free carriers, known as the *depletion region*. Forward biasing this structure using a battery (or any other voltage source) lowers the potential barrier in the depletion region, allowing more free electrons (holes) from the *n*-side (*p*-side) to diffuse across the junction to the *p*-side (*n*-side) where

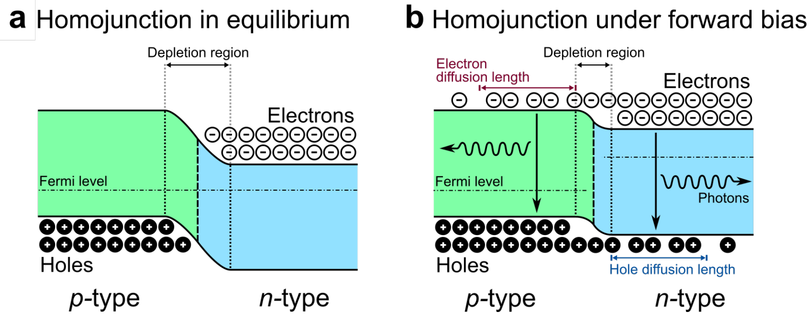

Figure 2.11. Schematic energy band diagram for *p-n* GaN homojunction LEDs under **a,** equilibrium and **b,** forward bias.

they recombine with holes (electrons), and thus emitting photons[117]. Figure 2.11b illustrates the representative energy band diagram for this homojunction structure.

However, the LEDs based on the homojunction structure cannot reach the same efficiency as the structure named *double-heterostructure* without generating substantial amount of heat. The difference which makes the double-heterostructure stand out from homojunction is the presence of an active layer in between the cladding layers. A material with an appropriate energy bandgap is employed as the active layer, and it is "sandwiched" between materials with larger energy bandgap that is used for the cladding (outer) layers. To comprehend the advantage of the double-heterostructure over homojunction LEDs, one should consult the definition of IQE, as the ratio between generated photons to injected electrons within the active region. It is the ratio of the radiative recombination rate to the recombination rate due to all processes, including the non-radiative ones.

While radiative processes produce emission of photons, non-radiative processes emit phonons that typically lower the light generation efficiency and increase heat loss. Shockley-Read-Hall (trap-assisted recombination, due to defect or dopant) and Auger recombination processes (resulting energy from band-to-band transition is given off to another electron or hole causing it to move higher into the conduction band or lower into the valence band, respectively) contribute to the non-radiative processes. In *p*-*n* homojunction LEDs, electrons diffuse into the *p*-type layer and holes diffuse into the *n*-type layer (Figure 2.11b). Now, these minority carriers are mostly distributed over the electron and hole diffusion lengths, which in GaN are approximately 1 μm. Such wide distribution of minority carriers and correspondingly low minority carrier concentrations (particularly toward the end of each diffusion tail) reduce the radiative recombination probability[117,119]. This condition is opposite to double-heterostructure, which is explained in the following paragraph.

Basic structure of double-heterostructure LED exemplified by a blue LED based on InGaN/AlGaN planar material system [120], is illustrated in Figure 2.12a. The LED is composed of *n*-type and *p*-type AlGaN layers sandwiching *an active layer* of undoped InGaN. Forward biasing this structure causes the injection of electrons and holes into the active layer from *n*- and *p*-type layer, respectively. Thus, a radiative recombination of electrons and holes takes place in the active layer, resulting in electroluminescence. Smaller bandgap energy of InGaN active layer with respect to *n*- and *p*-type AlGaN cladding layer is beneficial because carriers can be confined in this region (~20-200 nm thick), leading to a higher recombination probability to generate photons. Figure 2.12b depicts the schematic energy band diagram for this structure. The resulting photons have energy equal to the bandgap of the InGaN active layer, except for the active layer whose thickness is equivalent to or less than InGaN Bohr radius (3.4 nm for GaN and 13.8 nm for InN). In the latter case, the photon emission energy is larger than the expected bandgap, which is associated with the quantum confinement effect.

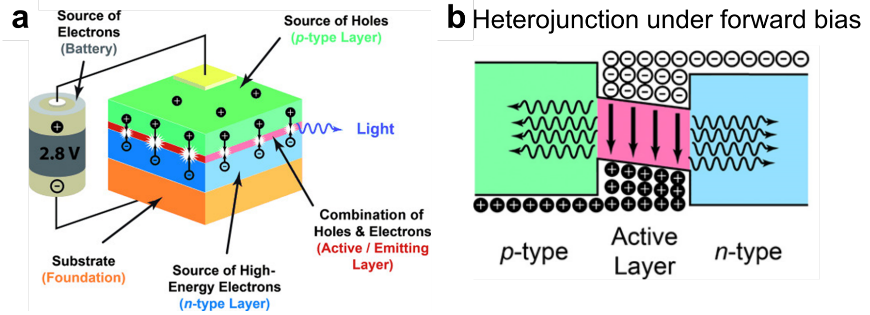

FIGURE 2.12. Illustration of double-heterostructure LED a, where electrons and holes recombine within the active layer, emitting light with a wavelength equal to the bandgap of the active layer. **b,** Schematic energy band diagram for double-heterostructure LED under forward bias (adapted with permission from ref. 119 © 2015 John Wiley and Sons).

Figure 2.13 further illustrates the advantages of the double-heterostructure over homojunction. The much narrower recombination region implies that the contribution of non-radiative Shockley-Read-Hall process via deep (defect) levels is significantly reduced as the number of defects within the recombination region is pretty much smaller than that of a homojunction. This leads to higher radiative efficiency in double-heterostructure. In addition, cladding (confinement) layers are optically transparent to the light generated in the active region because of their wider energy bandgap being larger than the emitted photon energy. Thus, the light is not absorbed by the cladding layers.

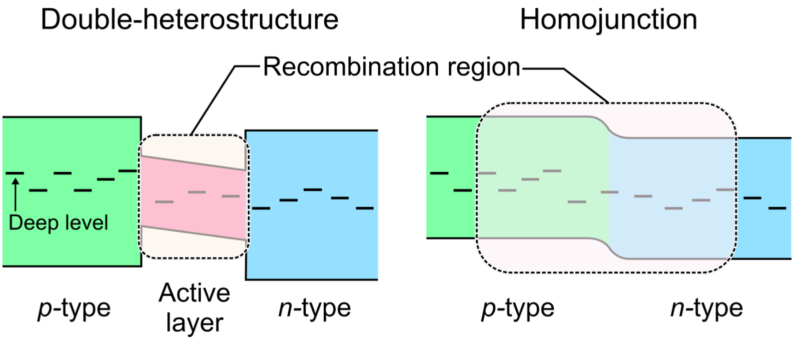

FIGURE 2.13. Double-heterostructure vs homojunction. Smaller recombination region in double-heterostructure involving less number of defects suppresses participation of non-radiative Shockley-Read-Hall recombination process. Homojunction behaves differently.

Generally, the turn-on or threshold voltage of LEDs, V_{th} is expressed as E_g/e[117], where E_g is the energy bandgap and e is the elementary charge. This approach is based on an ideal diode, wherein every electron injected into the active region will generate a photon. Thus, conservation of energy requires that the electron energy eV equals to the photon energy $h\nu$. One can use this threshold voltage formula to calculate the lower limit of the turn-on voltage in a LED. As an example, an infrared LED based on GaAs with the bandgap energy of 1.42 eV (emitting at 870 nm) has a threshold voltage of around 1.42 V. Likewise, a blue LED based on $In_{0.15}Ga_{0.85}N$ with the bandgap energy of 2.7 eV (emitting at 460 nm) has a threshold voltage of about 2.7 V. This implies that it is not possible to have a working device whose threshold voltage is below the turn-on voltage derived from an ideal diode.

As a final note in this subsection, one should be aware of that the thermal energy of carriers can broaden the emission linewidth of the nitride LEDs, and this phenomenon was coined as *thermal broadening*. This indicates that the linewidth broadens with increasing temperature, and it becomes narrower at cryogenic temperature (4 K). In practice, the linewidth is not only affected by thermal broadening, but also by other broadening mechanisms. This happens when the nitride semiconductors are alloyed, which is true in most of the cases. Such broadening is known as *alloy broadening*, i.e., statistical fluctuation of the active region's alloy composition, and it is independent of temperature. Addition to alloy broadening is *alloy clustering* and *phase separation*, and the perfect example of alloyed nitride materials that experience these broadenings are InGaN with indium mole fractions exceeding 25%[117].

2.4.2 Nanocolumn structure as the light emitter

From the breakthrough in 1993 led by Nakamura *et al.*[120], III-nitride semiconductor material system in the form of thin-film has been intensively explored for LEDs, covering from deep UV to visible spectral range[113,121]. However, the LED development of its equivalent being based on the as-grown III-nitride nanocolumns was just started as early as 2004[98,122], despite the fact that their growth and optimization had been commenced since 1996[1]. With the efficient reduction of threading dislocation densities of the grown III-nitride material, the adoption of nanocolumn geometry holds promise for the demonstration of highly efficient LEDs. Prominent literatures in 2002 and 2003 reported the device fabrication based on GaN single-column[105,123]. The challenges in realizing the LEDs using nanocolumn arrays are closely attributed to the device fabrication itself, which is inherently more complicated as compared to that of planar based LEDs.

The standard III-V nitride nanocolumn devices have identical junction as that of thin-film counterparts that is being constructed from axial *p*-*i*-*n* junction. Mg and Si atoms are normally utilized to dope the nanocolumn structure into *p*- and *n*- type semiconductor, respectively. The undoped nanocolumn section can be just composed of plain 20-200 nm thick part[95], as well as more complex designs by incorporating nanostructures like quantum wells[98,122,124] or quantum dots[97,113–115] to engineer and/or enhance the efficiency of photon generations. Using these different active layer structures, the demonstrations of III-V nitride nanocolumn LEDs on conventional Si substrate have been proven to be technologically feasible, wherein their spontaneous peak emission wavelengths can be tuned from deep UV (210 nm) to blue, green and red (440-675 nm) spectral regions[113–115].

Kim *et al.*[98] and Kikuchi *et al.*[122] have proposed two different approaches that fundamentally have been utilized for the fabrication of nanocolumn-based LEDs. In general, both fabrication processes involve elements of photolithography and dry etching for defining an area and making *p*- or *n*-type contact electrodes. The former method[98] relies in the isolation of individual nanocolumns by means of burying them within spin-on glass (transparent isolating materials). At this configuration, the top part of the spin-on glass containing most of the buried nanocolumn device structures only exposes the *p*-GaN segments, which can be brought into contact with *p*-type electrodes. Meanwhile, *n*-GaN planar buffer layer is contacted with *n*-type electrodes. Figure 2.14a illustrates the schematic diagram of the visible LEDs based on InGaN/GaN multi-quantum well nanocolumn arrays, along with the respective electroluminescence spectra.

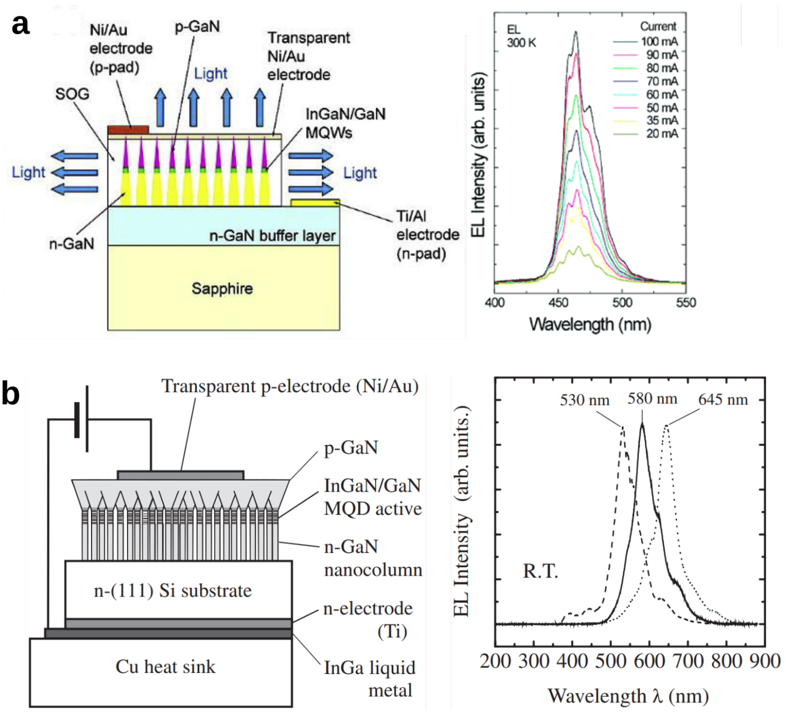

FIGURE 2.14. InGaN/GaN nanocolumn-based LEDs. Cross-section schematic diagram of InGaN/GaN **a,** multi-quantum well nanocolumn LED structures using sapphire substrate from Kim *et al.*[98] (adapted with permission from ref. 98 © 2004 American Chemical Society) and **b,** multi-quantum disk nanocolumn LED using n-Si(111) substrate from Kikuchi *et al.*[122] (adapted with permission from ref. 122 © 2004 The Japan Society of Applied Physics). Electroluminescence spectra of the devices from **a** and **b** are presented as well.

Contrary to the first method[98], the latter technique[122] did not employ any filler on the grown nanocolumns. Instead, they intentionally merge the *p*-type region of GaN at the very top of the nanocolumns, as shown in Figure 2.14b. In this circumstance, the top part of the nanocolumns is connected with each other where the surface of the nanocolumn resembles a continuous film with grainy texture without any void/gap, as seen from the top-view SEM image. Although the *p*-GaN looks like an inverse cone structure, the *n*-GaN and an undoped InGaN/GaN multi-quantum well active layer are still maintaining the columnar structure. This novel structure has its own merit in easing the device processing, i.e., by enabling the formation of *p*-type electrodes to be fabricated on top of nanocolumn device structure by the conventional method without relying on the usage of filler, while keeping the superior structural and optical properties of the isolated nanocolumn active region. The electroluminescence spectra with slight growth variation for the active regions are presented in Figure 2.14b.

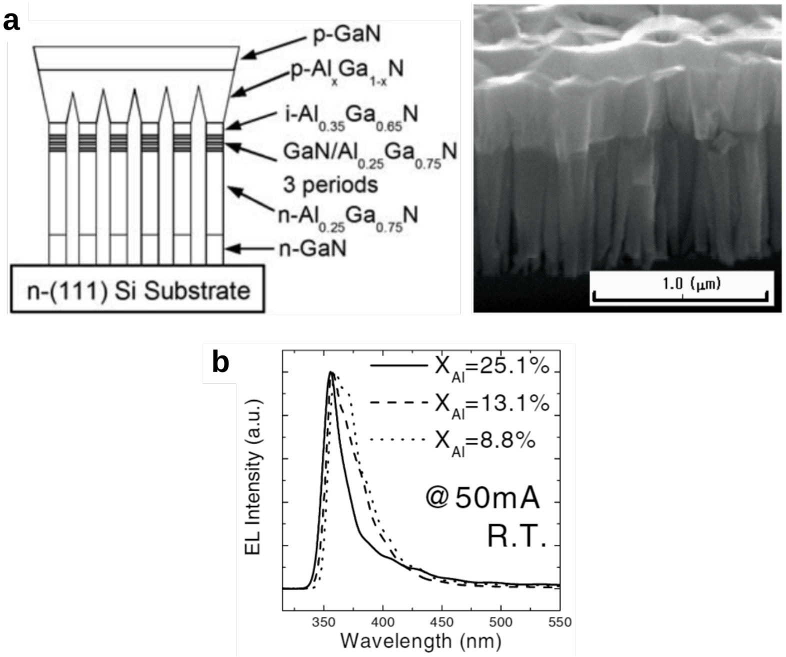

FIGURE 2.15. GaN/AlGaN nanocolumn LED on Si(111) substrate. a, Schematic diagram and bird's eye-view SEM image, along with **b,** electroluminescence spectra using different Al contents in the *p*-AlGaN layer (adapted with permission from ref. 124 © 2008 John Wiley and Sons).

Applying the same fabrication technique, Sekiguchi *et al.*[124] demonstrated, for the first time, the nanocolumn LEDs with UV emission from GaN/AlGaN multi-quantum disks active region. A cross-sectional schematic diagram of this nanocolumn device structure and its bird's eye-view SEM image are shown in Figure 2.15a. Similar to the preceding work[122], the *n*-GaN, *n*-AlGaN and undoped GaN/AlGaN growth regions sustain their columnar shape, whereas coalescence is gradually enhanced in the *p*-AlGaN and *p*-GaN sections. Continuous film in the *p*-GaN allows direct deposition of *p*-type electrodes, i.e., without the aid from insulating layer. Figure 2.15b presents the electroluminescence spectra of this nanocolumn LED device featuring a peak emission wavelength at 354 nm, and showing the reduction of FWHM with higher Al contents in the *p*-AlGaN layer. This narrowing linewidths are attributed to the suppression of electron flow reaching the *p*-AlGaN that decreases the deep-level emissions at longer wavelengths.

Reported works after 2004 concerning the developments of nitride nanocolumn LEDs in the UV to visible spectral ranges are dominated with the similar fabrication approach developed by Kim *et al.*[98]. Dielectric material, such as SiO_2, spin-on glass, polyimide or parylene, is utilized to fill the gap between nanocolumns and also to planarize the surface of nanocolumn arrays[115]. Reason is that the absence of coalescence in the whole nanocolumn device structure can prevent possible formation of crystal imperfections: strain, inverse domains, low-angle grain boundaries and networks of structural defects including dislocations at the coalescence boundary.

An important advancement in this field is the introduction towards emission control of InGaN nanocolumns from blue to red via selective-area growth technique by increasing nanocolumn diameter[125]. Such occurrence can be explained by the beam shadowing effect of the neighboring nanocolumns, and diffusion length difference between Ga and In adatoms on the nanocolumn sidewall[125]. In contrast to the self-induced GaN nanocolumn growth technique described so far, the selective-area growth technique allows uniform geometrical size of nanocolumn growth as well as consistent interval between nanocolumns. Many interesting results[126–136] derived from this method, revolving around visible III-nitride nanocolumn LEDs, can thus bring closer the realization of the monolithic integration of three-primary-color LEDs for use in micro displays. This growth technology was further utilized by Le *et al.*[137] to manipulate the coalescence properties of AlGaN nanocolumn structural arrays. As a result, the grown nanocolumns can be better controlled over their size, height, morphology and twist/tilt in crystal orientation. Using the same fabrication technique as Kikuchi *et al.*[122] the AlGaN nanocolumn-based UV LEDs demonstrate good performance with emission at 340 nm[137].

2.5 REFERENCES

[1] M. Yoshizawa, A. Kikuchi, M. Mori, N. Fujita, and K. Kishino. Self-organization of GaN nano-structures on c-Al_2O_3 by RF-radical gas source molecular beam epitaxy. In M. S. Shur and R. A. Suris, editors, *Compound Semiconductors 1996: Proceedings of the 23rd International Symposium on Compound Semiconductors held in St Petersburg, Russia, 23-27 September 1996* number 155 in Institute of Physics Conference Series pages 187–190. Institute of Physics (1997). Cited on page/s 15, 39.

[2] M. Yoshizawa, A. Kikuchi, M. Mori, N. Fujita, and K. Kishino. Growth of Self-Organized GaN Nanostructures on Al_2O_3(0001) by RF-Radical Source Molecular Beam Epitaxy. *Japanese Journal of Applied Physics* **36** (Part 2, No. 4B), L459–L462 (1997). Cited on page/s 15, 17.

[3] M. Yoshizawa, A. Kikuchi, N. Fujita, K. Kushi, H. Sasamoto, and K. Kishino. Self-organization of GaN/$Al_{0.18}Ga_{0.82}N$ multi-layer nano-columns on (0001) Al_2O_3 by RF molecular beam epitaxy for fabricating GaN quantum disks. *Journal of Crystal Growth* **189-190**, 138–141 (1998). Cited on page/s 15, 17, 25.

[4] M.A. Sanchez-Garcia, E. Calleja, E. Monroy, F.J. Sanchez, F. Calle, E. Munoz, and R. Beresford. The effect of the III/V ratio and substrate temperature on the morphology and properties of GaN- and AlN-layers grown by molecular beam epitaxy on Si(1 1 1). *Journal of Crystal Growth* **183** (1), 23–30 (1998). Cited on page/s 15, 17.

[5] E. Calleja, M. A. Sanchez-Garcia, F. J. Sanchez, F. Calleja, F. B. Naranjo, E. Munoz, S. I.

Molina, A. M. Sanchez, F. J. Pacheco, and R. Garcia. Growth of III-nitrides on Si(111) by molecular beam epitaxy Doping, optical, and electrical properties. *Journal of Crystal Growth* **201-202**, 296–317 (1999). Cited on page/s 15, 17.

[6] Anders Horntvedt. Jo Uthus overtar som ny sjef i Crayonano, der Rune Rinnans Televenture er hovedeier. *Finansavisen* (2020). Cited on page/s 16.

[7] H.-M. Kim, D. S. Kim, D. Y. Kim, T. W. Kang, Y.-H. Cho, and K. S. Chung. Growth and characterization of single-crystal GaN nanorods by hydride vapor phase epitaxy. *Applied Physics Letters* **81** (12), 2193–2195 (2002). Cited on page/s 16.

[8] W. J. Tseng, M. Gonzalez, L. Dillemans, K. Cheng, S. J. Jiang, P. M. Vereecken, G. Borghs, and R. R. Lieten. Strain relaxation in GaN nanopillars. *Applied Physics Letters* **101** (25), 253102 (2012). Cited on page/s 16.

[9] Q. Li, K. R. Westlake, M. H. Crawford, S. R. Lee, D. D. Koleske, J. J. Figiel, K. C. Cross, S. Fathololoumi, Z. Mi, and G. T. Wang. Optical performance of top-down fabricated InGaN/GaN nanorod light emitting diode arrays. *Optics Express* **19** (25), 25528–25534 (2011). Cited on page/s 16.

[10] B. Damilano, S. Vezian, M. Portail, B. Alloing, J. Brault, A. Courville, V. Brandli, M. Leroux, and J. Massies. Optical properties of $In_xGa_{1-x}N/GaN$ quantum-disks obtained by selective area sublimation. *Journal of Crystal Growth* **477**, 262–266 (2017). Proceeding of the 19th International Conference on Molecular Beam Epitaxy. Cited on page/s 16.

[11] R. S. Wagner and W. C. Ellis. VAPOR-LIQUID-SOLID MECHANISM OF SINGLE CRYSTAL GROWTH. *Applied Physics Letters* **4** (5), 89–90 (1964). Cited on page/s 16, 28.

[12] D. L. Dheeraj, G. Patriarche, L. Largeau, H. L. Zhou, A. T. J. van Helvoort, F. Glas, J. C. Harmand, B.-O. Fimland, and H. Weman. Zinc blende GaAsSb nanowires grown by molecular beam epitaxy. *Nanotechnology* **19** (27), 275605 (2008). Cited on page/s 16.

[13] D. L. Dheeraj, G. Patriarche, H. Zhou, T. B. Hoang, A. F. Moses, S. Gronsberg, A. T. J. van Helvoort, B.-O Fimland, and H. Weman. Growth and Characterization of Wurtzite GaAs Nanowires with Defect-Free Zinc Blende GaAsSb Inserts. *Nano Letters* **8** (12), 4459–4463 (2008). Cited on page/s 16.

[14] A. Fontcuberta i Morral, C. Colombo, G. Abstreiter, J. Arbiol, and J. R. Morante. Nucleation mechanism of gallium-assisted molecular beam epitaxy growth of gallium arsenide nanowires. *Applied Physics Letters* **92** (6), 063112 (2008). Cited on page/s 16.

[15] Z. Zhong, F. Qian, D. Wang, and C. M. Lieber. Synthesis of p-Type Gallium Nitride Nanowires for Electronic and Photonic Nanodevices. *Nano Letters* **3** (3), 343–346 (2003). Cited on page/s 16.

[16] L. Geelhaar, C. Cheze, W. M. Weber, R. Averbeck, H. Riechert, Th. Kehagias, Ph. Komninou, G. P. Dimitrakopulos, and Th. Karakostas. Axial and radial growth of Ni-induced GaN nanowires. *Applied Physics Letters* **91** (9), 093113 (2007). Cited on page/s 16.

[17] E. Barrigon, M. Heurlin, Z. Bi, B. Monemar, and L. Samuelson. Synthesis and Applications of III–V Nanowires. *Chemical Reviews* **119** (15), 9170–9220 (2019). Cited on page/s 16, 34.

[18] Abdul Mazid Munshi. Epitaxial Growth of Self-Catalyzed GaAs Nanowires by Molecular Beam Epitaxy. *Doctoral thesis*. Norwegian University of Science and Technology (2014). Cited on page/s 17.

[19] M. C. Putnam, M. A. Filler, B. M. Kayes, M. D. Kelzenberg, Y. Guan, N. S. Lewis, J. M. Eiler, and H. A. Atwater. Secondary Ion Mass Spectrometry of Vapor-Liquid-Solid Grown, Au-Catalyzed, Si Wires. *Nano Letters* **8** (10), 3109–3113 (2008). Cited on page/s 17.

[20] M. Bar-Sadan, J. Barthel, H. Shtrikman, and L. Houben. Direct Imaging of Single Au Atoms Within GaAs Nanowires. *Nano Letters* **12** (5), 2352–2356 (2012). Cited on page/s 17.

[21] S. Breuer, C. Pfuller, T. Flissikowski, O. Brandt, H. T. Grahn, L. Geelhaar, and H. Riechert. Suitability of Au- and Self-Assisted GaAs Nanowires for Optoelectronic Applications.

Nano Letters **11** (3), 1276–1279 (2011). Cited on page/s 17.

[22] C. Cheze, *et al.* Direct comparison of catalyst-free and catalyst-induced GaN nanowires. *Nano Research* **3**, 528–536 (2010). Cited on page/s 17, 27, 31.

[23] V. Consonni. Self-induced growth of GaN nanowires by molecular beam epitaxy: A critical review of the formation mechanisms. *Physica Status Solidi (RRL) – Rapid Research Letters* 7 (10), 699–712 (2013). Cited on page/s 17, 18, 19, 20, 22, 23.

[24] J. Ristic, E. Calleja, S. Fernandez-Garrido, L. Cerutti, A. Trampert, U. J., and K. H. Ploog. On the mechanisms of spontaneous growth of III-nitride nanocolumns by plasma-assisted molecular beam epitaxy. *Journal of Crystal Growth* **310** (18), 4035–4045 (2008). Cited on page/s 17, 19, 23, 24.

[25] R. Meijers, T. Richter, R. Calarco, T. Stoica, H.-P. Bochem, M. Marso, and H. Luth. GaN-nanowhiskers: MBE-growth conditions and optical properties. *Journal of Crystal Growth* **289** (1), 381–386 (2006). Cited on page/s 17.

[26] R. Calarco, R. J. Meijers, R. K. Debnath, T. Stoica, E. Sutter, and H. Luth. Nucleation and Growth of GaN Nanowires on Si(111) Performed by Molecular Beam Epitaxy. *Nano Letters* 7 (8), 2248–2251 (2007). Cited on page/s 17, 23, 24, 25, 26.

[27] R. K. Debnath, R. Meijers, T. Richter, T. Stoica, R. Calarco, and H. Luth. Mechanism of molecular beam epitaxy growth of GaN nanowires on Si(111). *Applied Physics Letters* **90** (12), 123117 (2007). Cited on page/s 17, 23, 24.

[28] R. Songmuang, O. Landre, and B. Daudin. From nucleation to growth of catalyst-free GaN nanowires on thin AlN buffer layer. *Applied Physics Letters* **91** (25), 251902 (2007). Cited on page/s 17, 19, 24, 25, 27.

[29] K.A. Bertness, A. Roshko, N.A. Sanford, J.M. Barker, and A.V. Davydov. Spontaneously grown GaN and AlGaN nanowires. *Journal of Crystal Growth* **287** (2), 522–527 (2006). The 16th American Conference on Crystal Growth and Epitaxy The 12th Biennial Workshop on OMVPE. Cited on page/s 17.

[30] O. Landre, C. Bougerol, H. Renevier, and B. Daudin. Nucleation mechanism of GaN nanowires grown on (111) Si by molecular beam epitaxy. *Nanotechnology* **20** (41), 415602 (2009). Cited on page/s 17, 18, 19, 20.

[31] V. Consonni, M. Knelangen, L. Geelhaar, A. Trampert, and H. Riechert. Nucleation mechanisms of epitaxial GaN nanowires: Origin of their self-induced formation and initial radius. *Physical Review B* **81** (8), 085310 (2010). Cited on page/s 17, 18, 19, 20, 21, 22.

[32] M. Knelangen, V. Consonni, A. Trampert, and H. Riechert. In situanalysis of strain relaxation during catalyst-free nucleation and growth of GaN nanowires. *Nanotechnology* **21** (24), 245705 (2010). Cited on page/s 17, 18, 19, 20.

[33] K. A. Bertness, A. Roshko, L. M. Mansfield, T. E. Harvey, and N. A. Sanford. Mechanism for spontaneous growth of GaN nanowires with molecular beam epitaxy. *Journal of Crystal Growth* **310** (13), 3154–3158 (2008). Cited on page/s 17, 23, 24, 25.

[34] C. Cheze, L. Geelhaar, A. Trampert, and H. Riechert. In situ investigation of self-induced GaN nanowire nucleation on Si. *Applied Physics Letters* **97** (4), 043101 (2010). Cited on page/s 17, 18, 19, 22.

[35] C. Cheze, L. Geelhaar, B. Jenichen, and H. Riechert. Different growth rates for catalyst-induced and self-induced GaN nanowires. *Applied Physics Letters* **97** (15), 153105 (2010). Cited on page/s 17, 26.

[36] V. Consonni, M. Hanke, M. Knelangen, L. Geelhaar, A. Trampert, and H. Riechert. Nucleation mechanisms of self-induced GaN nanowires grown on an amorphous interlayer. *Physical Review B* **83** (3), 035310 (2011). Cited on page/s 17, 18, 19, 20, 21, 22.

[37] V. Consonni, M. Knelangen, A. Trampert, L. Geelhaar, and H. Riechert. Nucleation and coalescence effects on the density of self-induced GaN nanowires grown by molecular

beam epitaxy. *Applied Physics Letters* **98** (7), 071913 (2011). Cited on page/s 17, 26.

[38] V. Consonni, A. Trampert, L. Geelhaar, and H. Riechert. Physical origin of the incubation time of self-induced GaN nanowires. *Applied Physics Letters* **99** (3), 033102 (2011). Cited on page/s 17, 18, 19.

[39] K. Hestroffer, C. Leclere, V. Cantelli, C. Bougerol, H. Renevier, and B. Daudin. In situ study of self-assembled GaN nanowires nucleation on Si(111) by plasma-assisted molecular beam epitaxy. *Applied Physics Letters* **100** (21), 212107 (2012). Cited on page/s 17, 18, 19, 22.

[40] F. Limbach, R. Caterino, T. Gotschke, T. Stoica, R. Calarco, L. Geelhaar, and H. Riechert. The influence of Mg doping on the nucleation of self-induced GaN nanowires. *AIP Advances* **2** (1), 012157 (2012). Cited on page/s 17, 18.

[41] V. Consonni, V. G. Dubrovskii, A. Trampert, L. Geelhaar, and H. Riechert. Quantitative description for the growth rate of self-induced GaN nanowires. *Physical Review B* **85** (15), 155313 (2012). Cited on page/s 17, 23, 24.

[42] F. Furtmayr, M. Vielemeyer, M. Stutzmann, J. Arbiol, S. Estrade, F. Peiro, J. R. Morante, and M. Eickhoff. Nucleation and growth of GaN nanorods on Si (111) surfaces by plasma-assisted molecular beam epitaxy - The influence of Si- and Mg-doping. *Journal of Applied Physics* **104** (3), 034309 (2008). Cited on page/s 17, 18, 19, 22, 24, 25, 26.

[43] H.-Y. Chen, H.-W. Lin, C.-H. Shen, and S. Gwo. Structure and photoluminescence properties of epitaxially oriented GaN nanorods grown on Si(111) by plasma-assisted molecular-beam epitaxy. *Applied Physics Letters* **89** (24), 243105 (2006). Cited on page/s 17, 22, 23, 25, 26.

[44] S. Fernandez-Garrido, J. Grandal, E. Calleja, M. A. Sanchez-Garcia, and D. Lopez-Romero. A growth diagram for plasma-assisted molecular beam epitaxy of GaN nanocolumns on Si(111). *Journal of Applied Physics* **106** (12), 126102 (2009). Cited on page/s 17, 25.

[45] B. Jenichen, O. Brandt, C. Pfuller, P. Dogan, M. Knelangen, and A. Trampert. Macro- and micro-strain in GaN nanowires on Si(111). *Nanotechnology* **22** (29), 295714 (2011). Cited on page/s 17, 26.

[46] A. Wierzbicka, *et al.* Influence of substrate nitridation temperature on epitaxial alignment of GaN nanowires to Si(111) substrate. *Nanotechnology* **24** (3), 035703 (2012). Cited on page/s 17, 22.

[47] R. Mata, K. Hestroffer, J. Budagosky, A. Cros, C. Bougerol, H. Renevier, and B. Daudin. Nucleation of GaN nanowires grown by plasma-assisted molecular beam epitaxy: The effect of temperature. *Journal of Crystal Growth* **334** (1), 177–180 (2011). Cited on page/s 17, 23, 25.

[48] F. Furtmayr, M. Vielemeyer, M. Stutzmann, A. Laufer, B. K. Meyer, and M. Eickhoff. Optical properties of Si- and Mg-doped gallium nitride nanowires grown by plasma-assisted molecular beam epitaxy. *Journal of Applied Physics* **104** (7), 074309 (2008). Cited on page/s 17, 30.

[49] M. Tchernycheva, *et al.* Growth of GaN free-standing nanowires by plasma-assisted molecular beam epitaxy: structural and optical characterization. *Nanotechnology* **18** (38), 385306 (2007). Cited on page/s 17, 29.

[50] L. Cerutti, J. Ristic, S. Fernandez-Garrido, E. Calleja, A. Trampert, K. H. Ploog, S. Lazic, and J. M. Calleja. Wurtzite GaN nanocolumns grown on Si(001) by molecular beam epitaxy. *Applied Physics Letters* **88** (21), 213114 (2006). Cited on page/s 17, 29.

[51] T. Stoica, E. Sutter, R. J. Meijers, R. K. Debnath, R. Calarco, H. Luth, and D. Grutzmacher. Interface and Wetting Layer Effect on the Catalyst-Free Nucleation and Growth of GaN Nanowires. *Small* **4** (6), 751–754 (2008). Cited on page/s 17, 19, 20, 22, 25.

[52] S. Zhao, M. G. Kibria, Q. Wang, H. P. T. Nguyen, and Z. Mi. Growth of large-scale vertically aligned GaN nanowires and their heterostructures with high uniformity on SiO_x by

catalyst-free molecular beam epitaxy. *Nanoscale* **5**, 5283–5287 (2013). Cited on page/s 17.

[53] M. Sobanska, V. G. Dubrovskii, G. Tchutchulashvili, K. Klosek, and Z. R. Zytkiewicz. Analysis of Incubation Times for the Self-Induced Formation of GaN Nanowires: Influence of the Substrate on the Nucleation Mechanism. *Crystal Growth & Design* **16** (12), 7205–7211 (2016). Cited on page/s 17, 18.

[54] M. Sobanska, Z. R. Zytkiewicz, G. Calabrese, L. Geelhaar, and S. Fernandez-Garrido. Comprehensive analysis of the self-assembled formation of GaN nanowires on amorphous Al_xO_y: *in-situ* quadrupole mass spectrometry studies. *Nanotechnology* **30** (15), 154002 (2019). Cited on page/s 17, 18.

[55] M. Sobanska, A. Wierzbicka, K. Klosek, J. Borysiuk, G. Tchutchulashvili, S. Gieraltowska, and Z.R. Zytkiewicz. Arrangement of GaN nanowires grown by plasma-assisted molecular beam epitaxy on silicon substrates with amorphous Al2O3 buffers. *Journal of Crystal Growth* **401**, 657–660 (2014). Proceedings of 17th International Conference on Crystal Growth and Epitaxy (ICCGE-17). Cited on page/s 17.

[56] M. Sobanska, S. Fernandez-Garrido, Z. R. Zytkiewicz, G. Tchutchulashvili, S. Gieraltowska, O. Brandt, and L. Geelhaar. Self-assembled growth of GaN nanowires on amorphous AlxOy: from nucleation to the formation of dense nanowire ensembles. *Nanotechnology* **27** (32), 325601 (2016). Cited on page/s 17, 18, 19.

[57] H. Sekiguchi, T. Nakazato, A. Kikuchi, and K. Kishino. Structural and optical properties of GaN nanocolumns grown on (0001) sapphire substrates by rf-plasma-assisted molecular-beam epitaxy. *Journal of Crystal Growth* **300** (1), 259–262 (2007). First International Symposium on Growth of Nitrides. Cited on page/s 19, 30.

[58] R. Songmuang, T. Ben, B. Daudin, D. Gonzalez, and E. Monroy. Identification of III–N nanowire growth kinetics via a marker technique. *Nanotechnology* **21** (29), 295605 (2010). Cited on page/s 23.

[59] L. Lymperakis and J. Neugebauer. Large anisotropic adatom kinetics on nonpolar GaN surfaces: Consequences for surface morphologies and nanowire growth. *Physical Review B* **79** (24), 241308 (2009). Cited on page/s 23, 24.

[60] R. Armitage and K. Tsubaki. Multicolour luminescence from InGaN quantum wells grown over GaN nanowire arrays by molecular-beam epitaxy. *Nanotechnology* **21** (19), 195202 (2010). Cited on page/s 25.

[61] P. Lefebvre, S. Fernandez-Garrido, J. Grandal, J. Ristic, M.-A. Sanchez-García, and E. Calleja. Radiative defects in GaN nanocolumns: Correlation with growth conditions and sample morphology. *Applied Physics Letters* **98** (8), 083104 (2011). Cited on page/s 25, 26.

[62] K.A. Grossklaus, A. Banerjee, S. Jahangir, P. Bhattacharya, and J.M. Millunchick. Misorientation defects in coalesced self-catalyzed GaN nanowires. *Journal of Crystal Growth* **371**, 142–147 (2013). Cited on page/s 25, 26.

[63] V. Consonni, M. Knelangen, U. Jahn, A. Trampert, L. Geelhaar, and H. Riechert. Effects of nanowire coalescence on their structural and optical properties on a local scale. *Applied Physics Letters* **95** (24), 241910 (2009). Cited on page/s 25, 26, 30.

[64] V. M. Kaganer, B. Jenichen, O. Brandt, S. Fernandez-Garrido, P. Dogan, L. Geelhaar, and H. Riechert. Inhomogeneous strain in GaN nanowires determined from x-ray diffraction peak profiles. *Physical Review B* **86** (11), 115325 (2012). Cited on page/s 26.

[65] L. Geelhaar, *et al.* Properties of GaN Nanowires Grown by Molecular Beam Epitaxy. *IEEE Journal of Selected Topics in Quantum Electronics* **17** (4), 878–888 (2011). Cited on page/s 27, 28, 30.

[66] T. Sekine, S. Suzuki, H. Kuroe, M. Tada, A. Kikuchi, and K. Kishino. Raman Scattering in GaN Nanocolumns and GaN/AlN Multiple Quantum Disk Nanocolumns. *e-Journal of Surface Science and Nanotechnology* **4**, 227–232 (2006). Cited on page/s 27.

[67] L. H. Robins, E. Horneber, N. A. Sanford, K. A. Bertness, M. D. Brubaker, and J. B. Schlager. Raman spectroscopy based measurements of carrier concentration in n-type GaN nanowires grown by plasma-assisted molecular beam epitaxy. *Journal of Applied Physics* **120** (12), 124313 (2016). Cited on page/s 27, 34.

[68] H. Harima. Properties of GaN and related compounds studied by means of Raman scattering. *Journal of Physics: Condensed Matter* **14** (38), R967–R993 (2002). Cited on page/s 27.

[69] A. Tabata, R. Enderlein, J. R. Leite, S. W. da Silva, J. C. Galzerani, D. Schikora, M. Kloidt, and K. Lischka. Comparative Raman studies of cubic and hexagonal GaN epitaxial layers. *Journal of Applied Physics* **79** (8), 4137–4140 (1996). Cited on page/s 27.

[70] R. People and J. C. Bean. Calculation of critical layer thickness versus lattice mismatch for Ge_xSi_{1-x}/Si strained-layer heterostructures. *Applied Physics Letters* **47** (3), 322–324 (1985). Cited on page/s 28, 29.

[71] M. A. Herman and H. Sitter. Molecular Beam Epitaxy: Fundamentals and Current Status. Springer Series in Materials Science, vol 7. Springer, Berlin, Heidelberg (1996). Cited on page/s 28.

[72] S. Luryi and E. Suhir. New approach to the high quality epitaxial growth of lattice-mismatched materials. *Applied Physics Letters* **49** (3), 140–142 (1986). Cited on page/s 28, 29.

[73] D. Zubia and S. D. Hersee. Nanoheteroepitaxy: The Application of nanostructuring and substrate compliance to the heteroepitaxy of mismatched semiconductor materials. *Journal of Applied Physics* **85** (9), 6492–6496 (1999). Cited on page/s 28, 29.

[74] F. Glas. Critical dimensions for the plastic relaxation of strained axial heterostructures in free-standing nanowires. *Physical Review B* **74** (12), 121302 (2006). Cited on page/s 29.

[75] L. C. Chuang, M. Moewe, C. Chase, N. P. Kobayashi, C. Chang-Hasnain, and S. Crankshaw. Critical diameter for III-V nanowires grown on lattice-mismatched substrates. *Applied Physics Letters* **90** (4), 043115 (2007). Cited on page/s 29.

[76] E. Ertekin, P. A. Greaney, D. C. Chrzan, and T. D. Sands. Equilibrium limits of coherency in strained nanowire heterostructures. *Journal of Applied Physics* **97** (11), 114325 (2005). Cited on page/s 29.

[77] S. Sburlan, A. Nakano, and P. D. Dapkus. Effect of substrate strain on critical dimensions of highly lattice mismatched defect-free nanorods. *Journal of Applied Physics* **111** (5), 054907 (2012). Cited on page/s 29.

[78] H. Geng, X. Yan, X. Zhang, J. Li, Y. Huang, and X. Ren. Analysis of critical dimensions for axial double heterostructure nanowires. *Journal of Applied Physics* **112** (11), 114307 (2012). Cited on page/s 29.

[79] S. Li and A. Waag. GaN based nanorods for solid state lighting. *Journal of Applied Physics* **111** (7), 071101 (2012). Cited on page/s 29.

[80] S.-Y. Kuo, C. C. Kei, C. N. Hsiao, and C. K. Chao. Growth of gallium nitride nanorods by metalorganic molecular beam epitaxy. *Journal of Vacuum Science & Technology B* **24** (2), 695–699 (2006). Cited on page/s 29.

[81] A. Armstrong, Q. Li, Y. Lin, A. A. Talin, and G. T. Wang. GaN nanowire surface state observed using deep level optical spectroscopy. *Applied Physics Letters* **96** (16), 163106 (2010). Cited on page/s 29.

[82] Q. Li and G. T. Wang. Spatial Distribution of Defect Luminescence in GaN Nanowires. *Nano Letters* **10** (5), 1554–1558 (2010). Cited on page/s 29.

[83] A. Cavallini, L. Polenta, M. Rossi, T. Richter, M. Marso, R. Meijers, R. Calarco, and H. Luth. Defect Distribution along Single GaN Nanowhiskers. *Nano Letters* **6** (7), 1548–1551 (2006). Cited on page/s 29.

[84] A. Waag, *et al.* The nanorod approach: GaN NanoLEDs for solid state lighting. *Phys-*

ica Status Solidi C - Current Topics in Solid State Physics **8** (7-8), 2296–2301 (2011). Cited on page/s 29.

[85] R. Calarco, M. Marso, T. Richter, A. I. Aykanat, R. Meijers, A. v.d. Hart, T. Stoica, and H. Luth. Size-dependent Photoconductivity in MBE-Grown GaN-Nanowires. *Nano Letters* **5** (5), 981–984 (2005). Cited on page/s 29, 30, 33.

[86] A. A. Talin, F. Leonard, B. S. Swartzentruber, X. Wang, and S. D. Hersee. Unusually Strong Space-Charge-Limited Current in Thin Wires. *Physical Review Letters* **101** (7), 076802 (2008). Cited on page/s 29, 30.

[87] T. Stoica and R. Calarco. Doping of III-Nitride Nanowires Grown by Molecular Beam Epitaxy. *IEEE Journal of Selected Topics in Quantum Electronics* **17** (4), 859–868 (2011). Cited on page/s 29, 32, 33.

[88] K. A. Bertness, N. A. Sanford, J. M. Barker, J. B. Schlager, A. Roshko, A. V. Davydov, and I. Levin. Catalyst-free growth of GaN nanowires. *Journal of Electronic Materials* **35**, 576–580 (2006). Cited on page/s 30.

[89] A. Kikuchi, M. Tada, K. Miwa, and K. Kishino. Growth and characterization of InGaN/-GaN nanocolumn LED. In K. G. Eyink and D. L. Huffaker, editors, *Proc. SPIE 6129, Quantum Dots, Particles, and Nanoclusters III* volume 6129 pages 36–43. International Society for Optics and Photonics SPIE (2006). Cited on page/s 30.

[90] M. A. Reshchikov and H. Morkoc. Luminescence properties of defects in GaN. *Journal of Applied Physics* **97** (6), 061301 (2005). Cited on page/s 30.

[91] K. A. Bertness, N. A. Sanford, and A. V. Davydov. GaN Nanowires Grown by Molecular Beam Epitaxy. *IEEE Journal of Selected Topics in Quantum Electronics* **17** (4), 847–858 (2011). Cited on page/s 30, 31, 32.

[92] J. B. Schlager, K. A. Bertness, P. T. Blanchard, L. H. Robins, A. Roshko, and N. A. Sanford. Steady-state and time-resolved photoluminescence from relaxed and strained GaN nanowires grown by catalyst-free molecular-beam epitaxy. *Journal of Applied Physics* **103** (12), 124309 (2008). Cited on page/s 30, 31.

[93] L. H. Robins, Kris A. Bertness, J. M. Barker, N. A. Sanford, and J. B. Schlager. Optical and structural study of GaN nanowires grown by catalyst-free molecular beam epitaxy. I. Near-band-edge luminescence and strain effects. *Journal of Applied Physics* **101** (11), 113505 (2007). Cited on page/s 30.

[94] M. A. Reshchikov, *et al.* Unusual luminescence lines in GaN. *Journal of Applied Physics* **94** (9), 5623–5632 (2003). Cited on page/s 30.

[95] W. Guo, M. Zhang, A. Banerjee, and P. Bhattacharya. Catalyst-Free InGaN/GaN Nanowire Light Emitting Diodes Grown on (001) Silicon by Molecular Beam Epitaxy. *Nano Letters* **10** (9), 3355–3359 (2010). Cited on page/s 31, 39.

[96] Q. Wang, H. P. T. Nguyen, K. Cui, and Z. Mi. High efficiency ultraviolet emission from $Al_xGa_{1-x}N$ core-shell nanowire heterostructures grown on Si (111) by molecular beam epitaxy. *Applied Physics Letters* **101** (4), 043115 (2012). Cited on page/s 31.

[97] H. P. T. Nguyen, K. Cui, S. Zhang, S. Fathololoumi, and Z. Mi. Full-color InGaN/GaN dot-in-a-wire light emitting diodes on silicon. *Nanotechnology* **22** (44), 445202 (2011). Cited on page/s 31, 39.

[98] H.-M. Kim, Y.-H. Cho, H. Lee, S. I. Kim, S. R. Ryu, D. Y. Kim, T. W. Kang, and K. S. Chung. High-Brightness Light Emitting Diodes Using Dislocation-Free Indium Gallium Nitride/Gallium Nitride Multiquantum-Well Nanorod Arrays. *Nano Letters* **4** (6), 1059–1062 (2004). Cited on page/s 32, 39, 40, 41.

[99] M.-L. Kuo, Y.-J. Lee, T. C. Shen, and S.-Y. Lin. Large enhancement of light-extraction efficiency from optically pumped, nanorod light-emitting diodes. *Optics Letters* **34** (13), 2078–2080 (2009). Cited on page/s 32.

[100] M.-L. Kuo, Y.-S. Kim, M.-L. Hsieh, and S.-Y. Lin. Efficient and Directed Nano-LED Emission by a Complete Elimination of Transverse-Electric Guided Modes. *Nano Letters* **11** (2), 476–481 (2011). Cited on page/s 32.

[101] H.-Y. Ryu. Large enhancement of light extraction efficiency in AlGaN-based nanorod ultraviolet light-emitting diode structures. *Nanoscale Research Letters* **9**, 58 (2014). Cited on page/s 32.

[102] J. Huang, C. Liu, T. Chen, H. Huang, F. Lai, P. Lee, C. Lin, C. Chang, T. S. Kao, and H. Kuo. Enhanced Light Extraction Efficiency of GaN-Based Hybrid Nanorods Light-Emitting Diodes. *IEEE Journal of Selected Topics in Quantum Electronics* **21** (4), 354–360 (2015). Cited on page/s 32.

[103] S. H. Kim, H. H. Park, Y. H. Song, H. J. Park, J. B. Kim, S. R. Jeon, H. Jeong, M. S. Jeong, and G. M. Yang. An improvement of light extraction efficiency for GaN-based light emitting diodes by selective etched nanorods in periodic microholes. *Optics Express* **21** (6), 7125–7130 (2013). Cited on page/s 32.

[104] J. Chesin, X. Zhou, and S. Gradecak. Light extraction in individual GaN nanowires on Si for LEDs. In Nobuhiko P. Kobayashi, A. Alec Talin, and M. Saif Islam, editors, *In Nanoepitaxy: Materials and Devices IV* pages 846703–846703–10. SPIE - International Society for Optical Engineering SPIE - International Society for Optical Engineering (2012). Cited on page/s 32.

[105] Y. Huang, X. Duan, Y. Cui, and C. M. Lieber. Gallium Nitride Nanowire Nanodevices. *Nano Letters* **2** (2), 101–104 (2002). Cited on page/s 32, 39.

[106] H.-Y. Cha, H. Wu, M. Chandrashekhar, Y. C. Choi, S. Chae, G. Koley, and M. G. Spencer. Fabrication and characterization of pre-aligned gallium nitride nanowire field-effect transistors. *Nanotechnology* **17** (5), 1264–1271 (2006). Cited on page/s 32.

[107] L. M. Mansfield, K. A. Bertness, P. T. Blanchard, T. E. Harvey, A. W. Sanders, and N. A. Sanford. GaN Nanowire Carrier Concentration Calculated from Light and Dark Resistance Measurements. *Journal of Electronic Materials* **38**, 495–504 (2009). Cited on page/s 32.

[108] D. Wang, C.-C. Tin, J. R. Williams, M. Park, Y. S. Park, C. M. Park, T. W. Kang, and W.-C. Yang. Raman characterization of electronic properties of self-assembled GaN nanorods grown by plasma-assisted molecular-beam epitaxy. *Applied Physics Letters* **87** (24), 242105 (2005). Cited on page/s 34.

[109] K. Jeganathan, R. K. Debnath, R. Meijers, T. Stoica, R. Calarco, D. Grutzmacher, and H. Luth. Raman scattering of phonon-plasmon coupled modes in self-assembled GaN nanowires. *Journal of Applied Physics* **105** (12), 123707 (2009). Cited on page/s 34.

[110] T. Kozawa, T. Kachi, H. Kano, Y. Taga, M. Hashimoto, N. Koide, and K. Manabe. Raman scattering from LO phonon-plasmon coupled modes in gallium nitride. *Journal of Applied Physics* **75** (2), 1098–1101 (1994). Cited on page/s 34.

[111] Z. Fang, E. Robin, E. Rozas-Jimenez, A. Cros, F. Donatini, N. Mollard, J. Pernot, and B. Daudin. Si Donor Incorporation in GaN Nanowires. *Nano Letters* **15** (10), 6794–6801 (2015). Cited on page/s 34.

[112] A.-M. Siladie, *et al.* Dopant radial inhomogeneity in Mg-doped GaN nanowires. *Nanotechnology* **29** (25), 255706 (2018). Cited on page/s 34.

[113] H. Sun and X. Li. Recent Advances on III-Nitride Nanowire Light Emitters on Foreign Substrates – Toward Flexible Photonics. *Physica Status Solidi A - Applications and Materials Science* **216** (2), 1800420 (2019). Cited on page/s 34, 39.

[114] C. Zhao, N. Alfaraj, R. Chandra Subedi, J. W. Liang, A. A. Alatawi, A. A. Alhamoud, M. Ebaid, M. S. Alias, T. K. Ng, and B. S. Ooi. III-nitride nanowires on unconventional substrates: From materials to optoelectronic device applications. *Progress in Quantum Electronics* **61**, 1–31 (2018). Cited on page/s 34, 39.

[115] S. Zhao, H.P.T. Nguyen, Md. G. Kibria, and Z. Mi. III-Nitride nanowire optoelectronics.

Progress in Quantum Electronics **44**, 14–68 (2015). Cited on page/s 34, 39, 42.

[116] S. Zhao. Molecular Beam Epitaxial Growth, Characterization, and Nanophotonic Device Applications of InN Nanowires on Si Platform. *Doctoral thesis*. McGill University (2013). Cited on page/s 34.

[117] E. F. Schubert, T. Gessmann, and J. K. Kim. Light Emitting Diodes. John Wiley & Sons (2005). Cited on page/s 35, 36, 38.

[118] B. E. A. Saleh and M. C. Teich. Fundamentals of Photonics. Wiley Series in Pure and Appl. Opt. Wiley (2019). Cited on page/s 35.

[119] S. Nakamura. Background Story of the Invention of Efficient InGaN Blue-Light-Emitting Diodes (Nobel Lecture). *Angewandte Chemie* **54** (27), 7770–7788 (2015). Cited on page/s 36, 37.

[120] S. Nakamura, T. Mukai, and M. Senoh. Candela-class high-brightness InGaN/AlGaN double-heterostructure blue-light-emitting diodes. *Applied Physics Letters* **64** (13), 1687–1689 (1994). Cited on page/s 37, 39.

[121] M. Kneissl, J. Han T.-Y. Seong, and Hiroshi Amano. The emergence and prospects of deep-ultraviolet light-emitting diode technologies. *Nature Photonics* **13**, 233–244 (2019). Cited on page/s 39.

[122] A. Kikuchi, M. Kawai, M. Tada, and K. Kishino. InGaN/GaN Multiple Quantum Disk Nanocolumn Light-Emitting Diodes Grown on (111) Si Substrate. *Japanese Journal of Applied Physics* **43** (No. 12A), L1524–L1526 (2004). Cited on page/s 39, 40, 41, 42.

[123] H.-M. Kim, Y.-H. Cho, and T. W. Kang. GaN Nanorods Doped by Hydride Vapor-Phase Epitaxy: Optical and Electrical Properties. *Advanced Materials* **15** (3), 232–235 (2003). Cited on page/s 39.

[124] H. Sekiguchi, K. Kato, J. Tanaka, A. Kikuchi, and K. Kishino. Ultraviolet GaN-based nanocolumn light-emitting diodes grown on n-(111) Si substrates by rf-plasma-assisted molecular beam epitaxy. *Physica Status Solidi A - Applications and Materials Science* **205** (5), 1067–1069 (2008). Cited on page/s 39, 41.

[125] H. Sekiguchi, K. Kishino, and A. Kikuchi. Emission color control from blue to red with nanocolumn diameter of InGaN/GaN nanocolumn arrays grown on same substrate. *Applied Physics Letters* **96** (23), 231104 (2010). Cited on page/s 42.

[126] K. Yamano and K. Kishino. Selective area growth of InGaN-based nanocolumn LED crystals on AlN/Si substrates useful for integrated μ-LED fabrication. *Applied Physics Letters* **112** (9), 091105 (2018). Cited on page/s 42.

[127] K. Kishino and S. Ishizawa. Selective-area growth of GaN nanocolumns on Si(111) substrates for application to nanocolumn emitters with systematic analysis of dislocation filtering effect of nanocolumns. *Nanotechnology* **26** (22), 225602 (2015). Cited on page/s 42.

[128] R. Vadivelu, Y. Igawa, and K. Kishino. 633 nm Red Emissions from InGaN Nanocolumn Light-Emitting Diode by Radio Frequency Plasma Assisted Molecular Beam Epitaxy. *Japanese Journal of Applied Physics* **52** (8S), 08JE18 (2013). Cited on page/s 42.

[129] K. Kishino and K. Yamano. Green-Light Nanocolumn Light Emitting Diodes With Triangular-Lattice Uniform Arrays of InGaN-Based Nanocolumns. *IEEE Journal of Quantum Electronics* **50** (7), 538–547 (2014). Cited on page/s 42.

[130] K. Kishino, K. Nagashima, and K. Yamano. Monolithic Integration of InGaN-Based Nanocolumn Light-Emitting Diodes with Different Emission Colors. *Applied Physics Express* **6** (1), 012101 (2013). Cited on page/s 42.

[131] A. Yanagihara, S. Ishizawa, and K. Kishino. Directional radiation beam from yellow-emitting InGaN-based nanocolumn LEDs with ordered bottom-up nanocolumn array. *Applied Physics Express* 7 (11), 112102 (2014). Cited on page/s 42.

[132] A. Yanagihara and K. Kishino. Red-Emitting InGaN-Based Nanocolumn Light-Emitting

Diodes with Highly Directional Beam Profiles. *Physica Status Solidi A - Applications and Materials Science* **217** (7), 1900771 (2020). Cited on page/s 42.

[133] H. Hayashi, D. Fukushima, T. Noma, D. Tomimatsu, Y. Konno, M. Mizuno, and K. Kishino. Thermally Engineered Flip-Chip InGaN/GaN Well-Ordered Nanocolumn Array LEDs. *IEEE Photonics Technology Letters* **27** (22), 2343–2346 (2015). Cited on page/s 42.

[134] K. Kishino, A. Yanagihara, K. Ikeda, and K. Yamano. Monolithic integration of four-colour InGaN-based nanocolumn LEDs. *Electronics Letters* **51** (11), 852–854 (2015). Cited on page/s 42.

[135] Y.-H. Ra, R. Wang, S. Y. Woo, M. Djavid, S. Md. Sadaf, J. Lee, G. A. Botton, and Z. Mi. Full-Color Single Nanowire Pixels for Projection Displays. *Nano Letters* **16** (7), 4608–4615 (2016). Cited on page/s 42.

[136] K. Kishino, N. Sakakibara, K. Narita, and T. Oto. Two-dimensional multicolor (RGBY) integrated nanocolumn micro-LEDs as a fundamental technology of micro-LED display. *Applied Physics Express* **13** (1), 014003 (2019). Cited on page/s 42.

[137] B. H. Le, S. Zhao, X. Liu, S. Y. Woo, G. A. Botton, and Z. Mi. Controlled Coalescence of AlGaN Nanowire Arrays: An Architecture for Nearly Dislocation-Free Planar Ultraviolet Photonic Device Applications. *Advanced Materials* **28** (38), 8446–8454 (2016). Cited on page/s 42.

CHAPTER 3

Graphene and GaN nanocolumns

During the two decades after the initial works by Yoshizawa *et al.*[1] and Calleja *et al.*[2], the studies on III-nitride nanocolumns, especially GaN, are not only exclusively practiced on crystalline substrates[3–63], but also attempted on amorphous substrates[64–72]. Particularly for fused silica, due to its excellent transparency across UV-visible wavelength regions[73–78], its potential as a host substrate for realizing visible LEDs is promising, despite the fact that leakage current was observed in the devices[79]. Very recently, the investigation of the growth of III-nitride nanocolumns and their application in LEDs on amorphous glass substrates have been demonstrated[80–83]. However, the interlayer and electrode materials, like Ti and GaN deposited or grown on top of these substrates typically absorb UV light, making this method inadequate for short wavelength light emitters, particularly for the bottom emitting LED.

First two sections of this chapter generally discuss various alternative substrates (including graphene) that have been explored for the GaN thin-film growth. At the end, brief updates regarding unusual substrates utilized for GaN nanocolumn growth, with an emphasize on graphene, are presented.

3.1 FROM SAPPHIRE TO UNCONVENTIONAL OXIDE SUBSTRATES

Unlike II-VI and general III-V material systems, the structural quality of grown III-V nitrides are evaluated to be inadequate due to the absence of a native substrate. Even after the usage of a GaN buffer layer in MOCVD-grown GaN on sapphire[84,85], the threading dislocation density was estimated to be as high as $\sim 10^{10}$ cm^{-2}. Such heavily defected GaN material is caused by the large lattice mismatch (16 %) between GaN and sapphire. In contrast, given the very small lattice mismatch between ZnSe and GaAs (0.3 %), ZnSe can be grown with dislocation densities as low as 10^{3} cm^{-2}. This is a key reason why ZnSe received positive reception in the research community as the material of choice for blue LEDs in the 1980s.

Sapphire was used as the substrate for the first synthesis of large area GaN layer by Maruska and Tietjen[86] in 1969, and since then it has become the most extensively utilized substrate for the growth of nitride semiconductors due to the ease in obtaining good quality sapphire material in large area size at low price. Its hexagonal symmetry, ease of handling as well as stability at high temperature make sapphire a favorable template for nitride growth, despite of the significant drawbacks of relatively large mismatches in the lattice constant and CTE with the nitride semiconductor system. The GaN film growth on sapphire is normally accompanied with very high densities of defects, which can act as non-radiative recombination centers and eventually reduce the efficiency of the LEDs[87].

There have been considerable efforts in heteroepitaxial studies of III-nitride semiconductors on a wide variety of substrate materials, including semiconductors, metals and oxides[88,89]. Their lattice mismatches with the III-nitrides are generally smaller compared to sapphire. Among them, most works have been allocated on semiconductors (e.g., Si, GaAs, SiC, GaN, and AlN). Despite the good semiconducting properties and material qualities of Si and GaAs, they have huge disadvantages because of the large mismatch in lattice constant and CTE, along with a phenomenon called melt-back etching (for Si) and low thermal stability (for GaAs). SiC and especially GaN or AlN are the ideal substrate materials for III-nitride growth. Not only do they have very small lattice mismatch, but they also have similar CTE and high thermal conductivity. However, although recent quality improvements of these materials are promising, their availability is limited and cost relatively high.

Metals (e.g., Ag and Cu) on the other hand are very cheap and provide high thermal as well as electrical conductivity. In addition, they have strong light reflection which can be used to reflect light directed toward the substrate and thus increase the LEE of top-emitting LEDs. However, they have large disparity in CTE with III-V nitride materials, and/or this group of materials is particularly unstable at high temperature (not suitable for MBE or MOCVD) causing serious interfacial reactions with the epilayer. While oxide substrates (e.g., $LiGaO_2$ and $MgAl_2O_4$) can have closely matched lattice-CTE with semiconductor III-V nitrides and be suited as potential candidates to obtain a high quality nonpolar GaN structure, they have some drawbacks. Their thermal stability under MBE or MOCVD growth conditions are relatively poor, which can give rise to the formation of an interfacial layer that can lead to high defect densities in the GaN epilayer.

3.2 ALTERNATIVE SUBSTRATE TO GAN FAMILY: GRAPHENE

As the light emitter is designed to work at shorter wavelength (UV region), the only way for generated light to escape is through the bottom, i.e., substrate, due to the absorption at the top metal contact. However, most of the aforementioned substrates also gradually start to absorb light, causing significant reduction in the LEE. Among all, only AlN is known as the semiconductor material to provide good transmission in the wavelength range from from ~210 to ~360 nm (the transparency threshold for GaN is ~364 nm). This is one of the unresolved fundamental problems hampering the development of UV-LEDs based on the GaN/AlGaN semiconductor material system. In this regard, graphene has recently become an emergent potential substrate for GaN/AlGaN semiconductor growth because of its interesting properties which may potentially be used to address this issue.

3.2.1 Graphene and its synthesis

By definition, graphene is a planar monolayer of carbon atoms arranged into a two-dimensional honeycomb lattice (Figure 3.1a) with a carbon-carbon bond length of 0.142 nm[90,91]. Graphene bonding characteristics are sp^2 hybridized with s, p_x and p_y atomic orbitals on each carbon atom forming three strong σ bonds (in-plane) with its nearest neighbors. In contrast, the p_z atomic orbital of each carbon atom (out-of-plane) is weak, and it produces a filled band of π orbital (valence band) and an empty band of π^* orbital (conduction band)[92]. Therefore, this bond provides weak interaction between graphene layers, between graphene and substrate, or between graphene and epilayer. Additionally, it is responsible for the electron conduction of graphene[90].

Charge carriers in graphene behave as massless Dirac fermions, and under ambient conditions they can move with little scattering. Such behaviors give rise to unique phenomena observed in graphene, like the semimetal behavior, an anomalous quantum Hall effect and the absence of localization[90–92]. Furthermore, a variety of intriguing properties have been experimentally reported, including high electron mobility at room-temperature (scattering by the acoustic phonons of graphene gives intrinsic limit up to 200.000 $cm^2\ V^{-1}\ s^{-1}$, whereas scattering by the surface phonons at the SiO_2 substrate gives extrinsic limit up to 40.000 $cm^2\ V^{-1}\ s^{-1}$)[93,94], remarkable optical transmittance[95] across near UV, visible and near infrared regions (Figure 3.1b)[91,96], exceptional thermal conductivity (5000 $W\ m^{-1}\ K^{-1}$)[97], good electrical conductivity[95], superior mechanical properties (Young's modulus of 1 TPa)[98] and complete impermeability to any gases[99]. Note that the absorption peak in Figure 3.1b at ~275 nm is

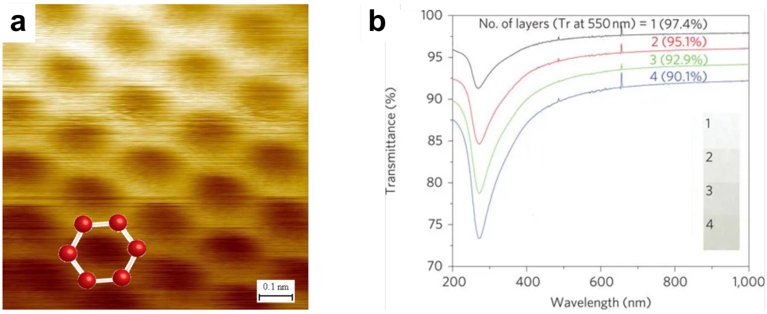

FIGURE 3.1. Structural and optical (transmittance) properties of graphene. a, Scanning tunneling microscopy topographic image of graphene, with a model of the atomic structure (as a guide to the eye) showing six carbon atoms arranged in hexagonal (honeycomb) lattice (adapted with permission from ref. 100 © 2007 National Academy of Sciences, U.S.A.). **b,** Representative transmittance of various numbers of CVD-graphene transferred onto quartz substrates (inset is the optical images for the corresponding number of transferred graphene layers – 1×1 cm^2) (adapted with permission from ref. 96 © 2010 Nature Publishing Group).

related to the interband electronic transition (excitonic Fano resonance) from the unoccupied π^* states[91].

Graphene can be obtained by various methods[101]. The Scotch tape method, to separate graphite into progressively thinner flakes until single-layer graphene is obtained, is called mechanical exfoliation, and this happens owing to the weak van der Waals attraction force between adjacent graphene sheets within the graphite. Although simple and can produce defect-free single-layer graphene, this method results in limited area of graphene flakes (not suitable for mass production).

A synthesis method called chemical vapor deposition (CVD) can deliver high-quality of graphene films in large surface area. To assist the CVD process, the presence of a transition metal is required as a substrate as well as a growth catalyst. These transition metals, for example Ni and Cu, are normally heated to temperatures of around 1000°C in order to decompose a hydrocarbon source (typically methane) into carbon atoms. Following this event, the carbon atoms will dissolve with the metal catalyst (substrate). Here, the solubility property of the metal will determine the formation mechanism of graphene. In case of Cu which has a low carbon solubility, only the adsorbed carbon dissolved in Cu can form graphene, and the growth will terminate once the Cu surface is fully covered with graphene due to the absence of Cu catalyst to decompose methane. In contrast, Ni which has high carbon solubility can dissolve more carbon atoms precipitating on the surface during the cool-down to form extra layers of graphene[91,101,102].

Therefore, the growth of Cu catalyzed CVD (Cu-CVD) graphene is due to a surface adsorption process, whereas the growth of Ni catalyzed CVD (Ni-CVD) graphene occurs by a carbon segregation-precipitation process [103]. Typically, graphene on Cu forms monolayer graphene, while graphene on Ni constitutes multi-layer graphene due to precipitation of extra carbon (thus continuation of graphene layer formation) during the cool-down process of the grown graphene sample to room-temperature. The latter may also lead to non-uniform graphene films [103]. CVD-graphene is shown to be polycrystalline with domain sizes in the range of few microns to hundreds of microns, and these individual domains are stitched together to form a single continuous film. However, recent works listed in ref 102 have shown that the domain size of CVD-graphene can be expanded to the order of one millimeter, and by utilizing oxygen on the Cu surface, one can obtain the growth of centimeter-scale single-crystal graphene domains. Interestingly, wafer-scale epitaxial growth of single-crystalline graphene can be achieved through a thermal decomposition of SiC and more recently using CVD on Ge substrate [101,102]. Transfer of CVD synthesized graphene onto arbitrary substrates can be done after chemically etching the metal substrate (graphene is coated with PMMA layer for the transfer process) [101,102].

3.2.2 *Popular usage of graphene as a transparent conducting electrode*

Of all the described characteristics of graphene, its high transparency across all wavelength, particularly in the UV region, and decent electrical conductivity have attracted considerable amount of attention for the application in optoelectronic devices such as transparent conducting electrodes for LEDs and solar cells. Moreover, the current industry standard for transparent electrode material, namely indium tin oxide (ITO), whereas demonstrating low sheet resistance of ~10 Ω/sq [101], absorbs strongly in UV wavelengths below ~365 nm and is therefore mainly functional for the devices operating in the visible wavelength region. Major general impediments to use ITO are its chemical instability as well as low tolerance towards mechanical stress, as it is not only easily cracked (by mechanical strain > 1%) but also drastically decreases its electrical conductivity [101]. Therefore, the favorable attributes of graphene make this material a feasible contender to substitute ITO as a transparent conductor for specific optoelectronic applications in the near future.

Integration with optoelectronic devices firstly requires adequate area of graphene, and in this respect the CVD method is the feasible (favored) route to fulfill this objective, while at the same time achieving decent electrical and optical properties. However, one significant drawback of the CVD method is that the PMMA used to coat the graphene and aid the transfer, will be the origin of wrinkles and polymer residues on the graphene surface upon its removal [102]. Another challenge [95] is the cracks/tears in the graphene after the transfer caused by small gaps (no full contact) between the graphene and the substrate surface, making the unattached regions to break easily and result in cracks after the PMMA is dissolved. Simultaneously, hard coating of PMMA after curing also tends to stress the graphene. Li *et al.*[95] managed to reduce these graphene imperfections by depositing a second layer of PMMA to mechanically relax the underlying graphene, leading to a better contact with the substrate.

Electron mobility of CVD grown graphene has been found to be as high as 4050 cm^2 V^{-1} s^{-1} at room temperature[104]. This value is orders of magnitude lower compared to mechanically exfoliated graphene[94] due to the line defects induced by grain boundaries[105] and wrinkles[106]. On the other hand, high optical transmittance of at least 90 % at optical wavelength of 550 nm (attenuation coefficient of 2.6% per additional graphene layer) was achieved in the transferred graphene with the method proposed by Li *et al.*[95]. This graphene was characterized with a sheet resistance varying from 350 (four-layer graphene) to 2100 Ω/sq (single-layer graphene). An interesting phenomenon is that the sheet resistance of graphene is likely to be affected by the density of cracks in the graphene films[95], which can act as scattering centers for charge carriers, leading to the degradation of the transport properties of graphene[92].

As schematically shown in Figure 3.2a, Kim *et al.*[107] demonstrated the implementation of large-area few-layer graphene–based transparent conductive electrode as the current spreading layer for GaN-based LEDs emitting at 372 nm. Figure 3.2b demonstrates that higher current at the same voltage bias can be achieved for the LED with graphene-based transparent conductive electrode, which is attributed to the high conductivity of the few-layer graphene. Inset in Figure 3.2b indicates that the electroluminescence emission intensity for the LED with graphene is more homogeneous compared to the LED without graphene, confirming the uniform UV-transparent few-layer graphene as a current-spreading layer. As a note, such graphene-based transparent conductive electrode can be severely degraded during continuous high power operation[107], and this can be caused by various reasons, including generated heat which accelerates the oxidation process in graphene[92].

Large difference in work function between graphene (4.2-4.9 eV) and *p*-GaN (~7.3 eV; presuming the electron affinity of GaN being 4.1 eV)[92,108–110] creates a high potential/contact barrier, which can hinder the movement of carriers across the interface. Consequently, this will increase the contact resistance and can thus lead to a higher operating voltage of the UV-LEDs[92]. High sheet resistance of single-layer graphene[95,107] can have a negative impact on the devices performance, including low efficiency[102], degraded I-V characteristics[108] and limited current spreading around the metal electrode[109]. Reduction of the graphene sheet resistance can be achieved by chemical doping[102] to form *p*-doped graphene, for instance by $AuCl_3$[108] and HNO_3 solutions[109]. This

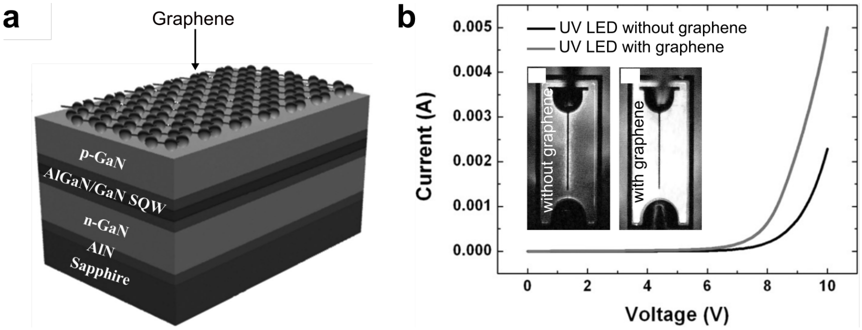

FIGURE 3.2. Graphene top electrode in GaN-based UV-LED. a, Schematic of few-layer graphene as a top transparent conductive electrode for a GaN-based thin-film LED. **b,** The I-V characteristics of the UV-LEDs without and with few-layer graphene based transparent conductive electrode (inset is the optical images of light emission intensity of the UV-LEDs) (adapted with permission from ref. 107 © 2011 AIP Publishing.

results in an improvement in the I-V characteristics and an increased work function of the *p*-doped graphene due to the electron transfer from graphene (5.12[108] and 4.93 eV[109] for $AuCl_3$ and HNO_3, respectively). To lower the sheet resistance at the interface between the *p*-graphene and *p*-GaN, Au (top)/Cr (middle) electrode was introduced above *p*-doped graphene[109]. In this scheme the penetration of Cr into *p*-graphene forms an ohmic contact with *p*-GaN and improves the thermal stability in GaN LEDs. Different metal combinations have been established for graphene, for instance Ni/Au, Cr/Pt/Au, Al/Ti/Au and Ti/Al/Ti/Au[92].

3.2.3 *Opportunity for graphene as a transparent conducting substrate*

That being said, until this point the application of graphene in LEDs is mostly constrained to its functionalization as transparent conducting electrode in the top part of the device. Graphene's unique optoelectronic properties can be beneficial for GaN-based devices if the growth can be carried out on graphene as the semiconductor substrate, so that it at the same time can function as a transparent electrode. The similar hexagonal structural characteristics of graphene with GaN, should theoretically be effective to form an epitaxial relationship, even when the graphene is transferred onto arbitrary non-crystalline substrates having no hexagonal sixfold symmetry[111]. Furthermore, the generic model by Munshi *et al.*[112] predicted that a relatively small lattice mismatch can be generated in the GaN/graphene system, while density functional theory from Gohda and Tsuneyuki[113] showed that a relatively low strain is developed at the GaN/graphene interface.

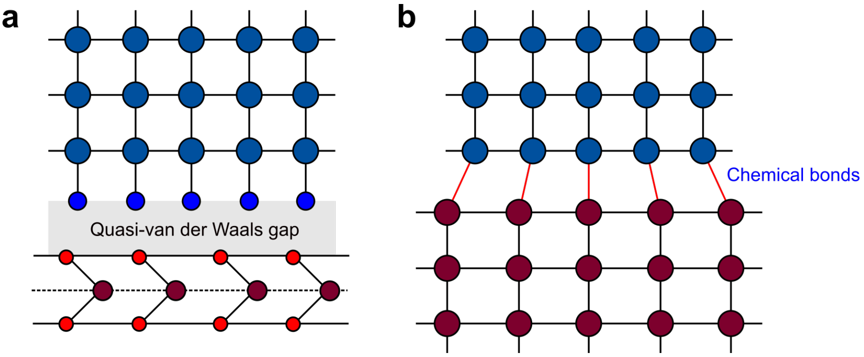

FIGURE 3.3. Illustration of semiconductor-substrate interfaces connected by **a,** quasi-van der Waals and **b,** covalent bonding.

When grown on a graphene surface where the dangling bonds are not present, a reduction of defects in GaN near the interface with graphene can be expected due to the weak quasi-van der Waals relationship[114] between sp^3-bonded GaN and sp^2-bonded graphene, as illustrated in Figure 3.3a. This is different as compared to the growth of GaN on conventional substrates, for instance Si or sapphire, where the epilayer forms a covalent bond with the substrate (Figure 3.3b). As a result, the crystalline quality of the grown material is strongly influenced by the mismatch to the lattice constant of the substrate. The lattice mismatches of GaN/Si(111) (~17%) and GaN/sapphire (~15%) induce crystal defects at the interfaces that can propagate into the epilayer, reducing its crystalline quality and eventually downgrade the performance of devices. Hence, successful growth of GaN semiconductor on graphene can pave a way towards a new approach for UV-LED fabrication where the substrate can be simultaneously utilized as a transparent electrode for the device structure, i.e. creating new types of hybrid 3D/2D heterostructures.

Issues related to high sheet resistance in graphene can be alleviated by doping. Other than chemical doping methods suggested previously[92,102], one can also introduce impurities into the graphene lattice to alter its electronic structure. This approach is known as substitutional doping. Introduction of doping into the graphene can be carried out *in-situ* during the CVD-graphene growth using hetero-atom precursors[101], for example NH_3 as N source or boronic acid as B source to synthesize N-doped (n-type) or B-doped (p-type) graphene, respectively. *Ex-situ* doping[115] is performed by injecting number of heteroatoms through post-synthesis treatment of graphene, for instance annealing processes or plasma treatments. Annealing with C_3N_4 and NH_3 plasma can be used to obtain n-type doping, while arc discharge using B_2H_6 and annealing/plasma treatment with O_2 are employed to produce p-type doping. Consequently, the work function of graphene is changed, which may

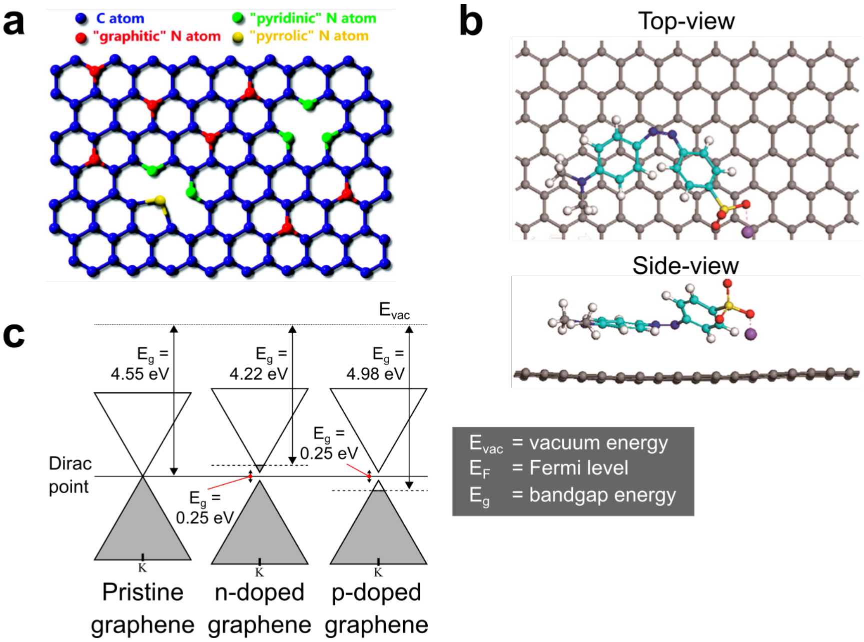

FIGURE 3.4. Doping in graphene. a, b, Schematic representation of the doping introduction in graphene by heteroatom substitution (adapted with permission from ref. 116 © 2009 American Chemical Society) and molecule adsorption (adapted with permission from ref. 117 © 2012 American Chemical Society), respectively. **c,** Simplified band structures of pristine graphene, *n*- and *p*-type doped graphene.

be advantageous to reduce the work function mismatch with that of GaN (~7.5 eV for *p*-GaN; ~4.0 eV for undoped- and *n*-GaN)[92]. Another doping method variation is charge-transfer doping[101], which is generally performed using inorganic acids and metal chlorides.

From the previously mentioned doping methods, substitutional doping is more stable compared to doping incorporation based on physical or chemical adsorption (including chemical doping and charge-transfer doping) because of the covalent bond linkage of the dopant in the graphene lattice[115]. Substitutional doping, however, disturbs the graphene honeycomb structure by inducing defects and disorder in the lattice (Figure 3.4a), which decrease electron mobility and hence cause a degradation in the performance of electrical devices. Such observation in contrast is not observed for the adsorption method since the adsorbed dopants only lead to a local perturbation in graphene (Figure 3.4b). One can then expect the preservation of structural integrity of the lattice; however it should be noted that this doping approach does not guarantee a stable doping system.

Pristine graphene is a zero bandgap semiconductor or semimetal[90,91] in which the conduction band minimum touches the valence band maximum, and they are of conical shape. These two bands intersect at the **K** point of the Brillouin zone, and the Fermi level is located at the Dirac point[118,119]. In this condition, the work function of graphene has been reported in the range from 4.2 to 4.9 eV[108–110,120], and for simplicity, the mean value of 4.55 eV is used for the illustration in Figure 3.4c. Upon the doping (either *n*- or *p*-type doped), the first observation is bandgap opening of graphene. Its energy can be varied from 0.14 to 0.72 eV (in Figure 3.4c the value of ~0.25 eV[118,121] is used for both *n*- and *p*-type doped graphene), depending on the doping methods[101], type of dopants[118,120–122], doping concentrations[118] and number of graphene layers[119,121].

Second observation with the doped graphene is the alteration of Fermi level position relative to the Dirac point, either when the Fermi level is situated (shifted) above or below the Dirac point, assigned as *n*- or *p*-type doping, respectively[115], as illustrated in Figure 3.4c. For *n*-type graphene, the Fermi level is shifted to 0.2-0.7 eV above the Dirac point, and thus the work function is reduced from ~4.55 (undoped) to 3.85-4.35 eV[110,118,119,121–123]. The new Fermi level position is near the conduction band minimum. For *p*-type graphene, the Fermi level is shifted below the Dirac point ranging from 0.19 to 0.7 eV, increasing the work function from ~4.55 eV (pristine) to 4.74-5.25 eV[108,109,118–122]. Now, the Fermi level position is close to the valence band maximum. The average work functions for *n*-type doped and *p*-type doped graphene obtained from the aforementioned references, being 4.22 and 4.98 eV, are used to exemplify work functions for n-type and p-type graphene depicted in Figure 3.4c.

For graphene to be a useful functional 2D material for III-nitride based devices, e.g., LEDs, first of all it is essential to grasp the overall device design concept utilizing graphene as a growth substrate and simultaneously as a transparent electrode. From this perspective, it is established that a so-called flip-chip LED configuration, where the light is emitted through the (transparent) substrate, is a potential device structure fulfilling this role of graphene. When this particular LED device is forward-biased, graphene as an electrode can, in principle, enable vertical current flow from the bottom electrode to the top electrode through the grown nanocolumns, and the generated photons can be emitted through transparent graphene. Here, it should be mentioned that current flow is not strictly vertical provided that the contact to the graphene is on the side of the *p*-GaN contact. In such arrangement, current crowding phenomenon is expected as opposed to the “real” vertical LED devices. The flip-chip LED structures can be more advantageous when it is compared with the traditional top-emitting LED structures, owing to the fact that the latter with lateral current injection suffers from high forward voltage, large series resistance, current crowding and self-heating[124–126].

With light being transmitted through the graphene, the III-V nitride nanostructure formed on top of this single layer of carbon atoms is required to be sufficiently transparent to the photons generated in the active region. This can be achieved by adopting material(s) from the III-V nitride semiconductor system whose energy bandgap is larger than the emitted photon energy. In other words, the material(s) of choice should have as low as possible light absorption coefficient[127–129] in order to obtain optimum LEE. As an example, the UV LEDs emitting light at the wavelength of 365 nm (3.39 eV) ought to consist of III-V nitride semiconductor materials that have energy bandgaps greater than or equal to 3.39 eV. From Figure 1.2, GaN, AlN and their alloy of AlGaN are the standard choices since this material family exhibits the lowest absorption coefficient[128,129] at this particular wavelength (photon energy). For emission wavelengths shorter than 365 nm (or photon energies greater than 3.39 eV) the usage of GaN should be avoided as the absorption coefficient increases rapidly above the GaN bandgap.

Supposing that the *n*-type or *p*-type graphene is in contact with a nitride semiconductor, accordingly the simple interpretations of band diagram of graphene-nitride materials after Fermi level alignment are presented in Figure 3.5. The band diagram of GaN has energy bandgap, electron affinity, along with activation energies of Si donors (*n*-doping) and Mg acceptors (*p*-doping) of respectively 3.39 eV[130], 3.3 eV[131,132], 17 meV[133] and 170 meV[134,135]. While for AlN, its band diagram indicates the energy bandgap of 6.2 eV[135,136], electron affinity of 1.9 eV[131] with Si (*n*-type doping) activation energy of 250 meV[137] and Mg (*p*-type doping) activation energy of 510 meV[135,138]. Concerning InN, the given band diagram displays an energy bandgap, electron affinity, ionization energies of Si (*n*-doping) and Mg (*p*-doping) of 0.65 eV[135,136], 4.6 eV[132], 350 meV[139] and 60 meV[135,140–142], respectively. For InN as a degenerate *n*-type semiconductor, the Fermi level is pinned above the conduction band edge[135,143].

When graphene and a III-nitride semiconductor (as well as semiconductor-semiconductor and metal-semiconductor junctions[144] in general) make contact[145,146] with each other, their Fermi levels have to be at equal level in the absence of an externally applied bias. Because of the different work functions between graphene and III-nitrides, band bending is present in the semiconductor near the interface. Figure 3.5 illustrates the basic schematic band structures when graphene contacts with GaN, AlN along with InN, in their respective *n*- and *p*-type doped versions. In the following examples, the Fermi levels in the semiconductor are pinned at the dopant energy level, i.e., donor or acceptor energy level.

In *n*-graphene/*n*-GaN and *n*-graphene/*n*-AlN, the work function of *n*-

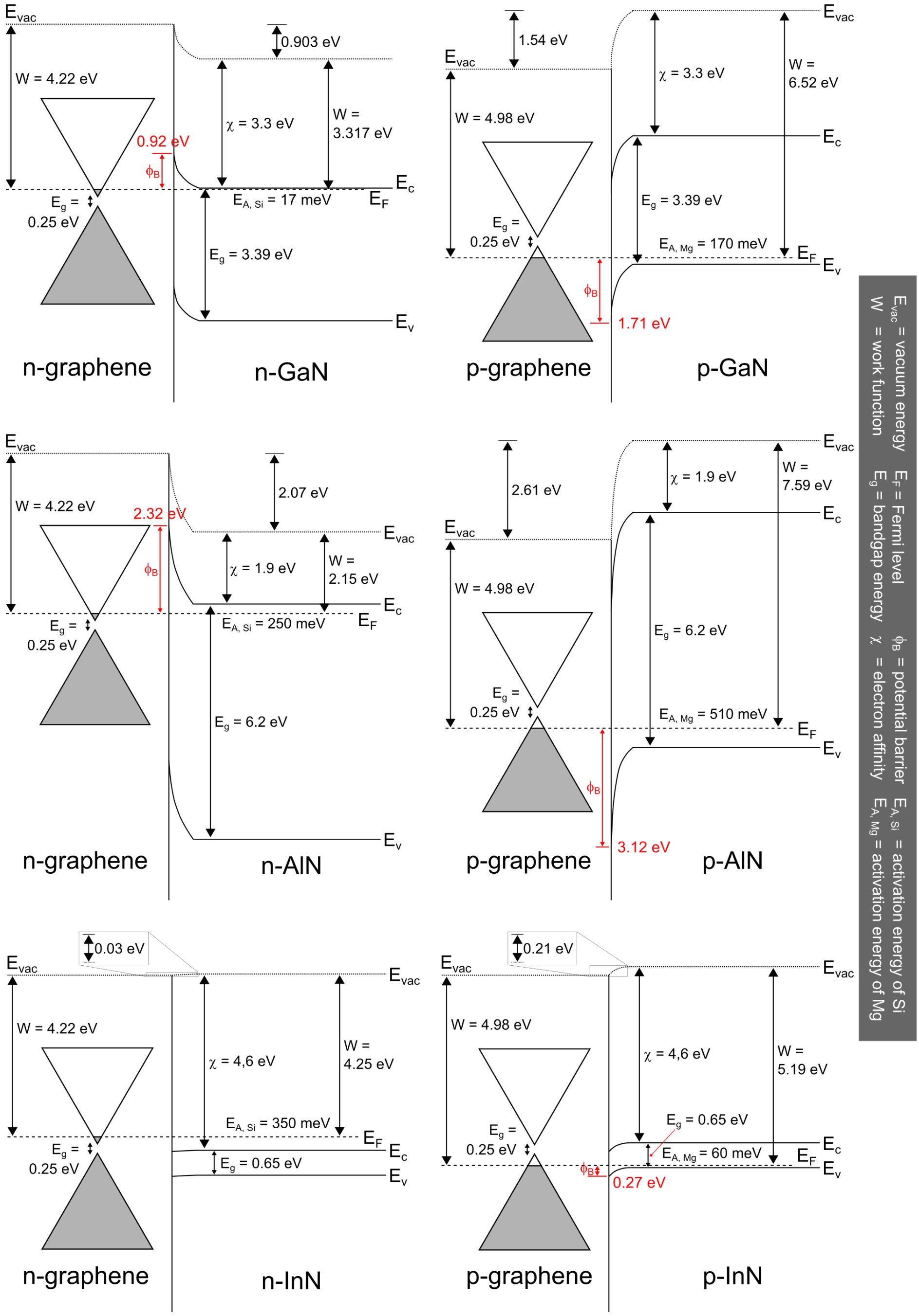

FIGURE 3.5. Band diagram of graphene/nitride semiconductor junctions. Rough sketch of the interface between *n-n* (left) and *p-p* (right) semiconductor heterojunction of graphene-GaN (top), graphene-AlN (middle) and graphene-InN (bottom), after the Fermi level alignment, in the absence of applied bias.

graphene (4.22 eV) is larger than for *n*-GaN (3.317 eV) and *n*-AlN (2.15 eV). If one coincides the vacuum energy level for these two systems, the Fermi levels of *n*-GaN and *n*-AlN are both higher than for *n*-graphene. This will cause a flow of electrons (majority carriers in *n*-type material) from *n*-GaN or *n*-AlN to *n*-graphene until the Fermi level of *n*-graphene is equal with that of *n*-GaN or *n*-AlN. As a result, the conduction and valence bands of *n*-GaN or *n*-AlN bend upward. However, interesting behavior can be seen in *n*-graphene/*n*-InN. The work function of degenerate *n*-InN (4.25 eV) is slightly larger than *n*-graphene, rendering higher Fermi level of *n*-graphene with respect to *n*-InN. Here, electrons flow from the *n*-graphene to *n*-InN until the Fermi level of *n*-InN is equal to the Fermi level of *n*-graphene. This will cause minor downward band bending of the conduction and valence bands for *n*-InN.

On the other hand, for *p*-graphene/*p*-GaN and *p*-graphene/*p*-AlN, the work function of *p*-graphene (4.98 eV) is smaller than for *p*-GaN (6.52 eV) and *p*-AlN (7.59 eV). With respect to the vacuum energy level position, the Fermi level of *p*-graphene is now at a higher level than the Fermi level of *p*-GaN or *p*-AlN. Thus, holes (majority carriers in *p*-type material) will transport from the *p*-GaN or *p*-AlN to *p*-graphene until the Fermi level of *p*-graphene is equal with that of *p*-GaN or *p*-AlN. Consequently, the conduction and valence bands of *p*-GaN or *p*-AlN bend downward. For *p*-graphene/*p*-InN, its behavior is roughly similar with *p*-graphene/*p*-GaN and *p*-graphene/*p*-AlN, only that the downward band bending is not as severe as for the previous two systems due to smaller work function difference between *p*-graphene and *p*-InN (5.19 eV).

Band bending pattern showed by *n*-graphene/*n*-GaN, *n*-graphene/*n*-AlN, *p*-graphene/*p*-GaN and *p*-graphene/*p*-AlN involves potential or Schottky barrier, restricting the movement of majority carriers from graphene to semiconductor. Referring to Figure 3.5, the Schottky barrier is approximately 0.92, 2.32, 1.71, and 3.12 eV for *n*-graphene/*n*-GaN, *n*-graphene/*n*-AlN, *p*-graphene/*p*-GaN and *p*-graphene/*p*-AlN, respectively. In contrast, the potential barrier is absent in *n*-graphene/degenerate *n*-InN (i.e., Ohmic contact), and there is a relatively small potential barrier (0.27 eV) to overcome for holes to be transported from *p*-graphene to *p*-InN. One common way to make a Schottky contact more Ohmic is by annealing, as it can lower the Schottky barrier height. The other is by increasing doping concentrations[147] so that the width of the depletion region is decreased, and thus increase the probability of electrons or holes tunneling through the junction.

Interested reader can check Figure A.1 in Appendix A for the illustration of the band structures when undoped graphene is in contact with *n*- or *p*-type GaN, AlN, or InN. As compared to Figure 3.5, the Schottky barrier heights in Figure A.1 are slightly larger due to increased work function of undoped graphene in comparison with doped graphene.

3.3 CURRENT STATUS: GAN NANOCOLUMN GROWTH ON UNCONVENTIONAL AND GRAPHENE SUBSTRATES

As of 2008, a particular interest in utilizing amorphous substrates has emerged among the nitride nanocolumn community. A number of promising initial works which were mostly done on amorphous SiO_2 [58,59] and Al_xO_y templates [60–63] hint that high-quality nitride nanocolumns can be spontaneously formed although they have little or no epitaxial relationship with the underlying substrate. Furthermore, the ability of nanocolumn to withstand high deformations without plastic relaxation [148] encourages the realization of flexible integrated devices based on nitride nanomaterial [149–155]. However, the fabrication processes demonstrated so far generally involves a transfer method to arbitrary flexible films, which is relatively time-consuming and complicated. Simultaneous growth and fabrication process have been realized by using metallic substrates [67–72], but their instability at high temperature that may lead to interfacial reactions with the nanocolumns remain as one of the serious problems.

Fused silica, another type of non-crystalline material, has been recently re-surfaced [79,156] as an alternative substrate for III-nitride nanocolumns due to a number of advantages [157,158], including excellent transparency across UV-visible wavelength regions and inert property enabling the prevention of impurity defect generations during the growth. In the early attempts, despite the fact that the quality of GaN thin-film was poor, its optical measurements indicated strong excitonic emission with suppressed yellow emission [73–78]. Nearly single-crystalline GaN was later achieved in 2011 by forming GaN pyramid arrays using a Ti pre-orienting layer [79,156], which resulted in an internal quantum efficiency as high as 52%. While visible LEDs based on these nanostructures were able to demonstrate a reliable electroluminescence emission [79,156], a significant amount of leakage current and driving voltage shift was observed.

In 2016, Li *et al.*[80] and Kumaresan *et al.*[81] attempted the growth of III-V nitride nanocolumn on amorphous glass substrate using MOCVD and RF-PAMBE, respectively. Whereas the former growth technique [80] resulted in vertical InN nanocolumns with low growth density (Figure 3.6a), the latter [81] demonstrated dense vertical GaN nanocolumns without using any intentional buffer layer (Figure 3.6b). Similar work with the latter was then later performed by Prabaswara *et al.*[83] but by utilizing Ti as the electrode and pre-orienting layer for GaN/InGaN nanocolumn LEDs emitting at 590 nm. In terms of growth technique, Bae *et al.*[82] have even demonstrated the possibility of selective-area growth using SiO_2 mask on quartz covered with GaN buffer layer. With that being said, both Ti and GaN buffer layers as the bottom contact absorb UV light, and therefore these proposed methods are inadequate for nanocolumn-based UV LEDs.

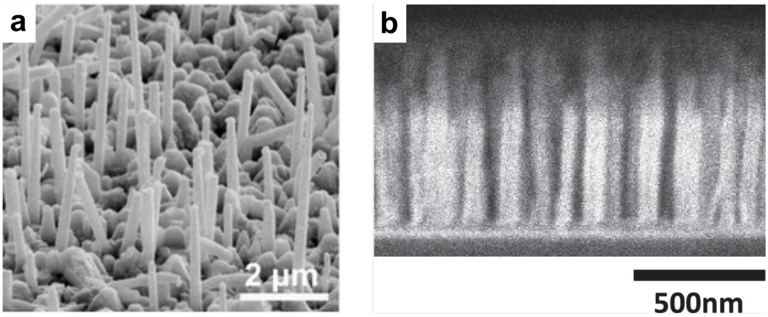

Figure 3.6. III-V nitride nanocolumn on amorphous glass substrate. SEM images of **a,** InN nanorods (bird's eye-view) using high temperature-GaN/Ti interlayer (adapted with permission from ref. 80 © 2016 Springer Nature) and **b,** GaN nanowires (side-view) grown on amorphous glass/fused silica substrates (adapted with permission from ref. 81 © 2016 IOP Publishing Ltd.).

Due to their weak out-of-plane interaction, 2D materials, particularly graphene, boron nitride (BN), tungsten disulfide and molybdenum disulfide (MoS_2) have been lately explored not only as the substrate for semiconductor nitride[159–172] but also as the intermediate layer to assist the transfer process of grown material to foreign substrates, such as plastic, glass or metal. However, the growth on 2D substrates with no dangling bonds often leads to undesired polycrystalline materials[173,174]. For the epitaxial growth of GaN on graphene as an example, one strategy[159] was to grow ZnO nanowalls on oxygen-plasma-treated graphene, which then benefits the nucleation and the growth of a flat GaN layer. Nevertheless, this grown GaN film is characterized with threading dislocation densities similar to the GaN grown on single crystal sapphire substrates, and to alleviate this issue, GaN microrods were employed[175,176]. In both cases, either ZnO nanorods[175] or a GaN buffer layer[176] was utilized in order to prevent poor vertical alignment of GaN microrods.

Compared to BN[162] and MoS_2[161], graphene attracts most of the attentions from III-nitride nanocolumn research groups worldwide as the alternative growth substrate[177–189], due to good transparency across all the wavelength, superior thermal conductivity, high electrical conductivity as well as excellent mechanical properties. In contrast, MoS_2 absorbs UV light[190–194] and along with BN (undoped), they show electrically resistive-like behavior[193–200], making them not universally compatible for the integration with III-nitride-based LEDs. Additionally, MoS_2 can be subjected to degradation due to high substrate temperature as well as exposure to ammonia and hydrogen during the MOVPE-GaN growth[163]. Such MoS_2 degradation after the growth was confirmed as follows: the characteristic signatures of MoS_2 XRD peaks were not observed and TEM measurement did not show MoS_2 at the interface between the SiO_2/Si substrate and GaN layer.

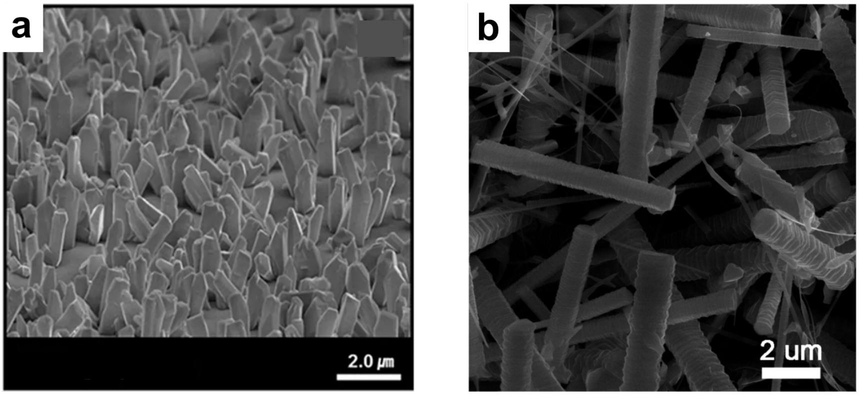

FIGURE 3.7. Early attempts on the GaN nanocolumn growth on graphite and graphene. Bird's eye-view SEM images of GaN nanocolumns grown on **a,** graphene/Si(111) (adapted with permission from ref. 179 © 2015 Springer Nature) and **b,** graphite substrates (adapted with permission from ref. 177 © 2013 American Chemical Society).

Albeit the initial promising results of GaN nanocolumns-on-graphene based UV photoconductive devices[179,180], the growth alignment of GaN nanocolumns is random with respect to the graphene substrate, represented in Figure 3.7a and Figure 3.7b. Possible reasons for this might arise from the fact that the surface of graphene exhibits chemical inertness or its surface profile is not atomically as flat as sapphire[177], causing arbitrary growth direction during GaN nucleation phase. Such random direction nanocolumn formation is not desirable as it can cause few possible issues in terms of structural growth quality and device processing, for example coalescence issue inducing the formation of defects and detrimental luminescence characteristics[201], as well as the difficulty in defining the top contact for nanocolumn semiconductor structure.

In this regard, Heilmann *et al.*[181] successfully showed that vertical GaN micro- and nanorods with well-defined edges and straight sidewall facets can be obtained on graphene transferred onto sapphire and Si substrates[183], as respectively shown in Figure 3.8a and Figure 3.8b (inset shows the clear interface between GaN, graphene and Si). Nevertheless, their uniformity and density are lower compared to those directly grown on sapphire[181]. The lack of chemical reactivity of graphene causes difficulty for the formation of GaN nucleation sites on the surface of graphene, and only at the defects in graphene (orange arrow in Figure 3.8b) can the GaN nanorods naturally be formed due to the availability of dangling bonds enabling the nucleation. Intriguingly, Kumaresan *et al.*[184] managed to solve this issue without any intermediate layer (Figure 3.8c), and surprisingly by utilizing similar growth technique and conditions as on their earlier work on fused silica[81].

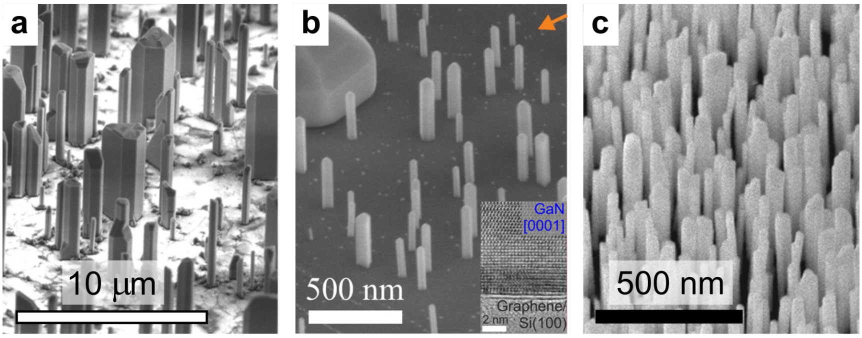

Figure 3.8. **Vertical GaN nanocolumn growths on graphene.** Bird's eye-view SEM images of GaN micro- and nanorods/nanowires grown on graphene transferred on **a,** sapphire (adapted with permission from ref. 181 © 2015 American Chemical Society), **b,** Si(111) (adapted with permission from ref. 183 © 2016 American Chemical Society) and **c,** SiO_2/Si(100) substrates (adapted with permission from ref. 184 © 2016 American Chemical Society). Orange arrow and inset in **b** indicates the position of wrinkles in graphene and shows the TEM cross-sectional image of the interface of GaN with the underlying graphene and SiO_2/Si(100) substrate, respectively.

However, a concern related with the graphene properties after the RF-PAMBE growth was not even discussed, knowing the defects can be generated in the graphene lattice due to exposure of nitrogen plasma [110,123,202]: causing increase of D-D' peaks as depicted in Figure 3.9a. Note that exposure using ammonia plasma [203] shows the reduction of 2D peak. Using the same growth technique, Fernandez-Garrido *et al.* [185] obtained GaN nanocolumns grown along [0001] direction (Figure 3.9b), and revealed that the graphene is damaged after the growth. This finding exposes the challenge for graphene as a substrate and potential built-in bottom contact for RF-PAMBE-grown GaN-based devices. Another important work carried out by Hayashi *et al.* [182] was the utilization of AlN as a buffer layer for high density of vertical GaN nanocolumns on multi-layer graphene (Figure 3.9c), and as possible protection layer for graphene from the direct bombardment of the nitrogen plasma. Inset in Figure 3.9b and Figure 3.9c presents the existence of multi-layer graphene after the GaN growth, where it is characterized as a continuous film.

A common phenomenon in the direct growth of GaN material on 2D materials, either in the thin-film or nanocolumn growth mode, is observed: that the synthesis often results in the formation of sparsely distributed isolated GaN lumps [162]. Similarly, clusters with rough and irregular morphology of GaN are noted in another literature [166]. The non-wetting nature of dangling bond-free 2D materials is presumably the origin of such unintended nanostructure growths [162], which further restricts/suppresses the nucleation of semiconductor nitride and it rather promotes the formation of clusters [189]. All of these works

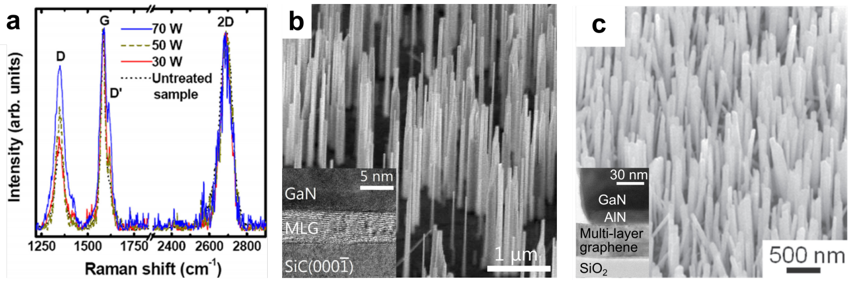

FIGURE 3.9. Raman characterizations of graphene post nitrogen plasma treatment; Vertical GaN nanocolumn growths on graphene. a, Raman spectra of graphene at different nitrogen plasma RF powers (reproduced with permission from ref. 110 © 2014 AIP Publishing). Bird's eye-view SEM images of GaN nanowires/nanocolumns MBE grown on **b,** epitaxial multi-layer graphene/SiC (adapted with permission from ref. 185 © 2017 American Chemical Society) and **c,** CVD-Ni multi-layer graphene transferred onto SiO_2/Si(100) (adapted with permission from ref. 182 © 2015 IOP Publishing Ltd.). Inset in **b** and **c** is the TEM cross-sectional image of the interface of GaN with the underlying graphene and substrate.

indicate that the formation of III-V nitride on graphene or other 2D materials is not as straightforward as the growth on substrates possessing dangling bonds on their surface, due to the lack of chemical activity on the surface of 2D materials[172].

Combination of surface treatment and intermediate layer can be utilized to mitigate the issue of chemical inertness due to the nature of sp^2-bonded structure, i.e., by enabling the creation of numerous nucleation sites for the subsequent van der Waals epitaxy of the III-nitride. In most cases, surface treatment, e.g., by means of O_2[159,169] or N_2 plasma[166,170,171] introduces additional defects for enhancing graphene's chemical reactivity, i.e., the creation of dangling bonds. Intermediate layer, typically consisting either of AlN[166,169–171] or AlGaN[183], plays an important role to improve surface adherence and wetting on graphene or h-BN[162,168]. This is due to the fact that AlN has larger cohesive energy as compared to GaN[204], resulting in much denser AlN island formations[162]. Furthermore, Al atoms on graphene showed higher adsorption energy and lower migration barrier as compared to that of Ga atoms[166,172,183,189]. This suggests that AlN is easier to grow on graphene than GaN, with a tendency to form 3D AlN islands as nucleation sites, especially at high temperatures. In addition to AlN and AlGaN, ZnO nanowalls have been used as an intermediate layer for GaN growth on oxygen plasma-treated graphene[159,172].

Please note that a few works carried out using MOVPE growth technique[162,168,189] disregarded the surface treatment step and utilized only AlN intermediate layer. Apparently during the growth of AlN, the N source (NH_3) can induce defects on graphene surface that accordingly act as nucleation sites for subsequent growth[189].

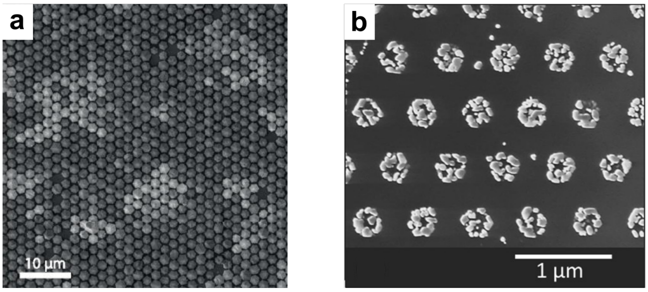

FIGURE 3.10. Position-controlled growth of III-V nitride nanocolumn on graphene. Top-view SEM image of selective area growth of **a,** AlGaN nanopyramid arrays on graphene/Si(100) using Al_xO_y/SiO_x mask (adapted with permission from ref. 205 © 2018 AIP Publishing) and **b,** GaN nanowires on graphene nanodots (adapted with permission from ref. 206 © 2020 American Chemical Society) using SiO_2/Si(100) as a host substrate.

As an additional perspective, selective area growth of III-V nitride nanostructures, namely AlGaN nanopyramid arrays[205] and GaN nanowires[206] has been realized on graphene, as presented in Figure 3.10a and Figure 3.10b, respectively. Interestingly, the position-controlled methods of these two works are different from each other. In the former case, Munshi *et al.*[205] utilized a hole mask pattern of an Al_xO_y/SiO_x stack deposited on the graphene substrate, similar to the established works from Kishino's group[34–41]. On the other hand, the latter case utilized graphene as the template (i.e., graphene nanodots) for the positioned GaN nanowire growth[206]. Such approach has been previously demonstrated by Ishizawa *et al.*[42],[43] who introduced nitrided Al nanopatterns as a guiding nanostructure to promote selective area growth of GaN nanocolumns. Both works[205,206] offer an attractive avenue to address positioned III-V nitride nanostructure growth for future UV LEDs.

The state-of-the-art works related with GaN nanocolumns grown on graphene have shown that the realization of graphene as the fundamental part of a device is not a straightforward task. Moreover, typical graphene substrate carriers that have been used so far, like SiO_2/Si and SiC[181–185] are not transparent in the UV region. Non-crystalline materials like silica glass could be utilized as a host substrate to address this issue. One particular point that until now has yet to be done is the proof-of-concept of the LED based on the direct device integration of GaN nanocolumns on graphene substrate, as the majority of the published works were mainly motivated by the easy removal of the grown III-nitride nanostructures from graphene and transfer to arbitrary foreign substrates. Owing to the merit of the nitride nanocolumn structure and the advantageous properties of graphene, it is therefore of interest to demonstrate that UV-LEDs based on semiconductor nanostructure grown on graphene are possible to achieve.

3.4 REFERENCES

[1] M. Yoshizawa, A. Kikuchi, N. Fujita, K. Kushi, H. Sasamoto, and K. Kishino. Self-organization of GaN/$Al_{0.18}Ga_{0.82}N$ multi-layer nano-columns on (0001) Al_2O_3 by RF molecular beam epitaxy for fabricating GaN quantum disks. *Journal of Crystal Growth* **189-190**, 138–141 (1998). Cited on page/s 53.

[2] E. Calleja, M. A. Sanchez-Garcia, F. J. Sanchez, F. Calleja, F. B. Naranjo, E. Munoz, S. I. Molina, A. M. Sanchez, F. J. Pacheco, and R. Garcia. Growth of III-nitrides on Si(111) by molecular beam epitaxy Doping, optical, and electrical properties. *Journal of Crystal Growth* **201-202**, 296–317 (1999). Cited on page/s 53.

[3] J. Ristic, E. Calleja, S. Fernandez-Garrido, L. Cerutti, A. Trampert, U. J., and K. H. Ploog. On the mechanisms of spontaneous growth of III-nitride nanocolumns by plasma-assisted molecular beam epitaxy. *Journal of Crystal Growth* **310** (18), 4035–4045 (2008). Cited on page/s 53.

[4] R. Calarco, R. J. Meijers, R. K. Debnath, T. Stoica, E. Sutter, and H. Luth. Nucleation and Growth of GaN Nanowires on Si(111) Performed by Molecular Beam Epitaxy. *Nano Letters* 7 (8), 2248–2251 (2007). Cited on page/s 53.

[5] L. Cerutti, J. Ristic, S. Fernandez-Garrido, E. Calleja, A. Trampert, K. H. Ploog, S. Lazic, and J. M. Calleja. Wurtzite GaN nanocolumns grown on Si(001) by molecular beam epitaxy. *Applied Physics Letters* **88** (21), 213114 (2006). Cited on page/s 53.

[6] V. Consonni, M. Knelangen, L. Geelhaar, A. Trampert, and H. Riechert. Nucleation mechanisms of epitaxial GaN nanowires: Origin of their self-induced formation and initial radius. *Physical Review B* **81** (8), 085310 (2010). Cited on page/s 53.

[7] K. A. Bertness, A. Roshko, L. M. Mansfield, T. E. Harvey, and N. A. Sanford. Mechanism for spontaneous growth of GaN nanowires with molecular beam epitaxy. *Journal of Crystal Growth* **310** (13), 3154–3158 (2008). Cited on page/s 53.

[8] M. Knelangen, V. Consonni, A. Trampert, and H. Riechert. In situanalysis of strain relaxation during catalyst-free nucleation and growth of GaN nanowires. *Nanotechnology* **21** (24), 245705 (2010). Cited on page/s 53.

[9] O. Landre, C. Bougerol, H. Renevier, and B. Daudin. Nucleation mechanism of GaN nanowires grown on (111) Si by molecular beam epitaxy. *Nanotechnology* **20** (41), 415602 (2009). Cited on page/s 53.

[10] V. Consonni, M. Knelangen, A. Trampert, L. Geelhaar, and H. Riechert. Nucleation and coalescence effects on the density of self-induced GaN nanowires grown by molecular beam epitaxy. *Applied Physics Letters* **98** (7), 071913 (2011). Cited on page/s 53.

[11] V. Consonni, A. Trampert, L. Geelhaar, and H. Riechert. Physical origin of the incubation time of self-induced GaN nanowires. *Applied Physics Letters* **99** (3), 033102 (2011). Cited on page/s 53.

[12] R. Mata, K. Hestroffer, J. Budagosky, A. Cros, C. Bougerol, H. Renevier, and B. Daudin. Nucleation of GaN nanowires grown by plasma-assisted molecular beam epitaxy: The effect of temperature. *Journal of Crystal Growth* **334** (1), 177–180 (2011). Cited on page/s 53.

[13] V. Consonni. Self-induced growth of GaN nanowires by molecular beam epitaxy: A critical review of the formation mechanisms. *Physica Status Solidi (RRL) – Rapid Research Letters* 7 (10), 699–712 (2013). Cited on page/s 53.

[14] K. Hestroffer, C. Leclere, V. Cantelli, C. Bougerol, H. Renevier, and B. Daudin. In situ study of self-assembled GaN nanowires nucleation on Si(111) by plasma-assisted molecular beam epitaxy. *Applied Physics Letters* **100** (21), 212107 (2012). Cited on page/s 53.

[15] M. D. Brubaker, I. Levin, A. V. Davydov, D. M. Rourke, N. A. Sanford, V. M. Bright, and K. A. Bertness. Effect of AlN buffer layer properties on the morphology and polarity of

GaN nanowires grown by molecular beam epitaxy. *Journal of Applied Physics* **110** (5), 053506 (2011). Cited on page/s 53.

[16] A. Wierzbicka, *et al.* Influence of substrate nitridation temperature on epitaxial alignment of GaN nanowires to Si(111) substrate. *Nanotechnology* **24** (3), 035703 (2012). Cited on page/s 53.

[17] C. Cheze, L. Geelhaar, B. Jenichen, and H. Riechert. Different growth rates for catalyst-induced and self-induced GaN nanowires. *Applied Physics Letters* **97** (15), 153105 (2010). Cited on page/s 53.

[18] C. Cheze, L. Geelhaar, A. Trampert, and H. Riechert. In situ investigation of self-induced GaN nanowire nucleation on Si. *Applied Physics Letters* **97** (4), 043101 (2010). Cited on page/s 53.

[19] F. Furtmayr, M. Vielemeyer, M. Stutzmann, A. Laufer, B. K. Meyer, and M. Eickhoff. Optical properties of Si- and Mg-doped gallium nitride nanowires grown by plasma-assisted molecular beam epitaxy. *Journal of Applied Physics* **104** (7), 074309 (2008). Cited on page/s 53.

[20] M. Tchernycheva, *et al.* Growth of GaN free-standing nanowires by plasma-assisted molecular beam epitaxy: structural and optical characterization. *Nanotechnology* **18** (38), 385306 (2007). Cited on page/s 53.

[21] C. Tessarek, S. Figge, A. Gust, M. Heilmann, C. Dieker, E. Spiecker, and S. Christiansen. Optical properties of vertical, tilted and in-plane GaN nanowires on different crystallographic orientations of sapphire. *Journal of Physics D: Applied Physics* **47** (39), 394008 (2014). Cited on page/s 53.

[22] H. Zhang, *et al.* Comprehensive analyses of core–shell InGaN/GaN single nanowire photodiodes. *Journal of Physics D: Applied Physics* **50** (48), 484001 (2017). Cited on page/s 53.

[23] T. Koukoula, J. Kioseoglou, Th. Kehagias, F. Furtmayr, M. Eickhoff, H. Kirmse, Th. Karakostas, and Ph. Komninou. Interfacial properties of self-assembled GaN nanowires on pre-processed Al_2O_3(0001) surfaces. *Materials Science in Semiconductor Processing* **55**, 46–50 (2016). Cited on page/s 53.

[24] S. Chae, K. Lee, J. Jang, D. Min, J. Kim, and O. Nam. Self-assembled growth of inclined GaN nanorods on (10-10) m-plane sapphire using metal–organic chemical vapor deposition. *Journal of Crystal Growth* **409**, 65–70 (2015). Cited on page/s 53.

[25] X. J. Chen, B. Gayral, D. Sam-Giao, C. Bougerol, C. Durand, and J. Eymery. Catalyst-free growth of high-optical quality GaN nanowires by metal-organic vapor phase epitaxy. *Applied Physics Letters* **99** (25), 251910 (2011). Cited on page/s 53.

[26] X. Wang, S. Li, S. Fundling, H.-H. Wehmann, M. Strassburg, H.-J. Lugauer, U. Steegmuller, and A. Waag. Mechanism of nucleation and growth of catalyst-free self-organized GaN columns by MOVPE. *Journal of Physics D: Applied Physics* **46** (20), 205101 (2013). Cited on page/s 53.

[27] H. Sekiguchi, T. Nakazato, A. Kikuchi, and K. Kishino. Structural and optical properties of GaN nanocolumns grown on (0001) sapphire substrates by rf-plasma-assisted molecular-beam epitaxy. *Journal of Crystal Growth* **300** (1), 259–262 (2007). First International Symposium on Growth of Nitrides. Cited on page/s 53.

[28] S. D. Hersee, X. Sun, and X. Wang. The Controlled Growth of GaN Nanowires. *Nano Letters* **6** (8), 1808–1811 (2006). Cited on page/s 53.

[29] M. Nami, R. F. Eller, S. Okur, A. K. Rishinaramangalam, S. Liu, I. Brener, and D. F. Feezell. Tailoring the morphology and luminescence of GaN/InGaN core–shell nanowires using bottom-up selective-area epitaxy. *Nanotechnology* **28** (2), 025202 (2016). Cited on page/s 53.

[30] K. Lekhal, S.-Y. Bae, H.-J. Lee, T. Mitsunari, A. Tamura, M. Deki, Y. Honda, and H. Amano. Controlled morphology of regular GaN microrod arrays by selective area growth with

HVPE. *Journal of Crystal Growth* **447**, 55–61 (2016). Cited on page/s 53.

[31] Y. Robin, *et al.* Insight into the performance of multi-color InGaN/GaN nanorod light emitting diodes. *Scientific Reports* **8**, 7311 (may 2018). Cited on page/s 53.

[32] Z. Gacevic, D. Gomez Sanchez, and E. Calleja. Formation Mechanisms of GaN Nanowires Grown by Selective Area Growth Homoepitaxy. *Nano Letters* **15** (2), 1117–1121 (2015). Cited on page/s 53.

[33] P. Aseev, Z. Gacevic, A. Torres-Pardo, J. M. Gonzalez-Calbet, and E. Calleja. Improving optical performance of GaN nanowires grown by selective area growth homoepitaxy: Influence of substrate and nanowire dimensions. *Applied Physics Letters* **108** (25), 253109 (2016). Cited on page/s 53.

[34] K. Yamano, K. Kishino, H. Sekiguchi, T. Oto, A. Wakahara, and Y. Kawakami. Novel selective area growth (SAG) method for regularly arranged AlGaN nanocolumns using nanotemplates. *Journal of Crystal Growth* **425**, 316–321 (2015). The 18th International Conference on Molecular Beam Epitaxy (MBE 2014). Cited on page/s 53, 71.

[35] A. Yanagihara, S. Ishizawa, and K. Kishino. Directional radiation beam from yellow-emitting InGaN-based nanocolumn LEDs with ordered bottom-up nanocolumn array. *Applied Physics Express* 7 (11), 112102 (2014). Cited on page/s 53, 71.

[36] H. Sekiguchi, K. Kishino, and A. Kikuchi. Emission color control from blue to red with nanocolumn diameter of InGaN/GaN nanocolumn arrays grown on same substrate. *Applied Physics Letters* **96** (23), 231104 (2010). Cited on page/s 53, 71.

[37] K. Kishino and K. Yamano. Green-Light Nanocolumn Light Emitting Diodes With Triangular-Lattice Uniform Arrays of InGaN-Based Nanocolumns. *IEEE Journal of Quantum Electronics* **50** (7), 538–547 (2014). Cited on page/s 53, 71.

[38] K. Kishino, K. Nagashima, and K. Yamano. Monolithic Integration of InGaN-Based Nanocolumn Light-Emitting Diodes with Different Emission Colors. *Applied Physics Express* **6** (1), 012101 (2013). Cited on page/s 53, 71.

[39] S. Ishizawa, K. Kishino, R. Araki, A. Kikuchi, and S. Sugimoto. Optically Pumped Green (530–560 nm) Stimulated Emissions from InGaN/GaN Multiple-Quantum-Well Triangular-Lattice Nanocolumn Arrays. *Applied Physics Express* **4** (5), 055001 (2011). Cited on page/s 53, 71.

[40] K. Yamano and K. Kishino. Selective area growth of InGaN-based nanocolumn LED crystals on AlN/Si substrates useful for integrated μ-LED fabrication. *Applied Physics Letters* **112** (9), 091105 (2018). Cited on page/s 53, 71.

[41] K. Kishino and S. Ishizawa. Selective-area growth of GaN nanocolumns on Si(111) substrates for application to nanocolumn emitters with systematic analysis of dislocation filtering effect of nanocolumns. *Nanotechnology* **26** (22), 225602 (2015). Cited on page/s 53, 71.

[42] S. Ishizawa, H. Sekiguchi, A. Kikuchi, and K. Kishino. Selective growth of GaN nanocolumns by Al thin layer on substrate. *Physica Status Solidi B - Basic Solid State Physics* **244** (6), 1815–1819 (2007). Cited on page/s 53, 71.

[43] S. Ishizawa, K. Kishino, and A. Kikuchi. Selective-Area Growth of GaN Nanocolumns on Si(111) Substrates Using Nitrided Al Nanopatterns by RF-Plasma-Assisted Molecular-Beam Epitaxy. *Applied Physics Express* **1** (1), 015006 (2008). Cited on page/s 53, 71.

[44] A. Bengoechea-Encabo, S. Albert, D. Lopez-Romero, P. Lefebvre, F. Barbagini, A. Torres-Pardo, J. M. Gonzalez-Calbet, M. A. Sanchez-Garcia, and E. Calleja. Light-Emitting-Diodes based on ordered InGaN nanocolumns emitting in the blue, green and yellow spectral range. *Nanotechnology* **25** (43), 435203 (2014). Cited on page/s 53.

[45] T. Gotschke, T. Schumann, F. Limbach, T. Stoica, and R. Calarco. Influence of the adatom diffusion on selective growth of GaN nanowire regular arrays. *Applied Physics Letters* **98** (10), 103102 (2011). Cited on page/s 53.

[46] C.H. Wu, P.Y. Lee, K.Y. Chen, Y.T. Tseng, Y.L. Wang, and K.Y. Cheng. Selective area growth of high-density GaN nanowire arrays on Si(111) using thin AlN seeding layers. *Journal of Crystal Growth* **454**, 71–81 (2016). Cited on page/s 53.

[47] R. Songmuang, O. Landre, and B. Daudin. From nucleation to growth of catalyst-free GaN nanowires on thin AlN buffer layer. *Applied Physics Letters* **91** (25), 251902 (2007). Cited on page/s 53.

[48] K.A. Bertness, A. Roshko, N.A. Sanford, J.M. Barker, and A.V. Davydov. Spontaneously grown GaN and AlGaN nanowires. *Journal of Crystal Growth* **287** (2), 522–527 (2006). The 16th American Conference on Crystal Growth and Epitaxy The 12th Biennial Workshop on OMVPE. Cited on page/s 53.

[49] R. Meijers, T. Richter, R. Calarco, T. Stoica, H.-P. Bochem, M. Marso, and H. Luth. GaN-nanowhiskers: MBE-growth conditions and optical properties. *Journal of Crystal Growth* **289** (1), 381–386 (2006). Cited on page/s 53.

[50] R. K. Debnath, R. Meijers, T. Richter, T. Stoica, R. Calarco, and H. Luth. Mechanism of molecular beam epitaxy growth of GaN nanowires on Si(111). *Applied Physics Letters* **90** (12), 123117 (2007). Cited on page/s 53.

[51] V. Consonni, M. Hanke, M. Knelangen, L. Geelhaar, A. Trampert, and H. Riechert. Nucleation mechanisms of self-induced GaN nanowires grown on an amorphous interlayer. *Physical Review B* **83** (3), 035310 (2011). Cited on page/s 53.

[52] F. Limbach, R. Caterino, T. Gotschke, T. Stoica, R. Calarco, L. Geelhaar, and H. Riechert. The influence of Mg doping on the nucleation of self-induced GaN nanowires. *AIP Advances* **2** (1), 012157 (2012). Cited on page/s 53.

[53] V. Consonni, V. G. Dubrovskii, A. Trampert, L. Geelhaar, and H. Riechert. Quantitative description for the growth rate of self-induced GaN nanowires. *Physical Review B* **85** (15), 155313 (2012). Cited on page/s 53.

[54] F. Furtmayr, M. Vielemeyer, M. Stutzmann, J. Arbiol, S. Estrade, F. Peiro, J. R. Morante, and M. Eickhoff. Nucleation and growth of GaN nanorods on Si (111) surfaces by plasma-assisted molecular beam epitaxy - The influence of Si- and Mg-doping. *Journal of Applied Physics* **104** (3), 034309 (2008). Cited on page/s 53.

[55] H.-Y. Chen, H.-W. Lin, C.-H. Shen, and S. Gwo. Structure and photoluminescence properties of epitaxially oriented GaN nanorods grown on Si(111) by plasma-assisted molecular-beam epitaxy. *Applied Physics Letters* **89** (24), 243105 (2006). Cited on page/s 53.

[56] S. Fernandez-Garrido, J. Grandal, E. Calleja, M. A. Sanchez-Garcia, and D. Lopez-Romero. A growth diagram for plasma-assisted molecular beam epitaxy of GaN nanocolumns on Si(111). *Journal of Applied Physics* **106** (12), 126102 (2009). Cited on page/s 53.

[57] B. Jenichen, O. Brandt, C. Pfuller, P. Dogan, M. Knelangen, and A. Trampert. Macro- and micro-strain in GaN nanowires on Si(111). *Nanotechnology* **22** (29), 295714 (2011). Cited on page/s 53.

[58] T. Stoica, E. Sutter, R. J. Meijers, R. K. Debnath, R. Calarco, H. Luth, and D. Grutzmacher. Interface and Wetting Layer Effect on the Catalyst-Free Nucleation and Growth of GaN Nanowires. *Small* **4** (6), 751–754 (2008). Cited on page/s 53, 66.

[59] S. Zhao, M. G. Kibria, Q. Wang, H. P. T. Nguyen, and Z. Mi. Growth of large-scale vertically aligned GaN nanowires and their heterostructures with high uniformity on SiO_x by catalyst-free molecular beam epitaxy. *Nanoscale* **5**, 5283–5287 (2013). Cited on page/s 53, 66.

[60] M. Sobanska, V. G. Dubrovskii, G. Tchutchulashvili, K. Klosek, and Z. R. Zytkiewicz. Analysis of Incubation Times for the Self-Induced Formation of GaN Nanowires: Influence of the Substrate on the Nucleation Mechanism. *Crystal Growth & Design* **16** (12), 7205–7211 (2016). Cited on page/s 53, 66.

[61] M. Sobanska, Z. R. Zytkiewicz, G. Calabrese, L. Geelhaar, and S. Fernandez-Garrido.

Comprehensive analysis of the self-assembled formation of GaN nanowires on amorphous Al_xO_y: *in-situ* quadrupole mass spectrometry studies. *Nanotechnology* **30** (15), 154002 (2019). Cited on page/s 53, 66.

[62] M. Sobanska, A. Wierzbicka, K. Klosek, J. Borysiuk, G. Tchutchulashvili, S. Gieraltowska, and Z.R. Zytkiewicz. Arrangement of GaN nanowires grown by plasma-assisted molecular beam epitaxy on silicon substrates with amorphous Al2O3 buffers. *Journal of Crystal Growth* **401**, 657–660 (2014). Proceedings of 17th International Conference on Crystal Growth and Epitaxy (ICCGE-17). Cited on page/s 53, 66.

[63] M. Sobanska, S. Fernandez-Garrido, Z. R. Zytkiewicz, G. Tchutchulashvili, S. Gieraltowska, O. Brandt, and L. Geelhaar. Self-assembled growth of GaN nanowires on amorphous AlxOy: from nucleation to the formation of dense nanowire ensembles. *Nanotechnology* **27** (32), 325601 (2016). Cited on page/s 53, 66.

[64] M. Wolz, C. Hauswald, T. Flissikowski, T. Gotschke, S. Fernandez-Garrido, O. Brandt, H. T. Grahn, L. Geelhaar, and H. Riechert. Epitaxial Growth of GaN Nanowires with High Structural Perfection on a Metallic TiN Film. *Nano Letters* **15** (6), 3743–3747 (2015). Cited on page/s 53.

[65] D. van Treeck, G. Calabrese, J. J. W. Goertz, V. M. Kaganer, O. Brandt, S. Fernandez-Garrido, and L. Geelhaar. Self-assembled formation of long, thin, and uncoalesced GaN nanowires on crystalline TiN films. *Nano Research* **11**, 565–576 (2018). Cited on page/s 53.

[66] G. Calabrese, P. Corfdir, G. Gao, C. Pfuller, A. Trampert, O. Brandt, L. Geelhaar, and S. Fernandez-Garrido. Molecular beam epitaxy of single crystalline GaN nanowires on a flexible Ti foil. *Applied Physics Letters* **108** (20), 202101 (2016). Cited on page/s 53.

[67] A. T. M. G. Sarwar, S. D. Carnevale, F. Yang, T. F. Kent, J. J. Jamison, D. W. McComb, and R. C. Myers. Semiconductor Nanowire Light-Emitting Diodes Grown on Metal: A Direction Toward Large-Scale Fabrication of Nanowire Devices. *Small* **11** (40), 5402–5408 (2015). Cited on page/s 53, 66.

[68] B. J. May, A. T. M. G. Sarwar, and R. C. Myers. Nanowire LEDs grown directly on flexible metal foil. *Applied Physics Letters* **108** (14), 141103 (2016). Cited on page/s 53, 66.

[69] C. Zhao, T. K. Ng, N. Wei, A. Prabaswara, M. S. Alias, B. Janjua, C. Shen, and B. S. Ooi. Facile Formation of High-Quality InGaN/GaN Quantum-Disks-in-Nanowires on Bulk-Metal Substrates for High-Power Light-Emitters. *Nano Letters* **16** (2), 1056–1063 (2016). Cited on page/s 53, 66.

[70] B. Janjua, *et al.* Droop-free $Al_xGa_{1-x}N/Al_yGa_{1-y}N$ quantum-disks-in-nanowires ultraviolet LED emitting at 337 nm on metal/silicon substrates. *Optics Express* **25** (2), 1381–1390 (2017). Cited on page/s 53, 66.

[71] D. Priante, B. Janjua, A. Prabaswara, R. C. Subedi, R. T. Elafandy, S. Lopatin, D. H. Anjum, C. Zhao, T. K. Ng, and B. S. Ooi. Highly uniform ultraviolet-A quantum-confined AlGaN nanowire LEDs on metal/silicon with a TaN interlayer. *Optical Materials Express* **7** (12), 4214–4224 (2017). Cited on page/s 53, 66.

[72] B. J. May, E. C. Hettiaratchy, C. Selcu, B. Wang, B. D. Esser, D. W. McComb, and R. C. Myers. Enhanced uniformity of III-nitride nanowire arrays on bulk metallic glass and nanocrystalline substrates. *Journal of Vacuum Science & Technology B* **37** (3), 031212 (2019). Cited on page/s 53, 66.

[73] H. Asahi, K. Iwata, H. Tampo, R. Kuroiwa, M. Hiroki, K. Asami, S. Nakamura, and S. Gonda. Very strong photoluminescence emission from GaN grown on amorphous silica substrate by gas source MBE. *Journal of Crystal Growth* **201-202**, 371–375 (1999). Cited on page/s 53, 66.

[74] M. Hiroki, H. Asahi, H. Tampo, K. Asami, and S. Gonda. Improved properties of polycrystalline GaN grown on silica glass substrate. *Journal of Crystal Growth* **209** (2), 387–391

(2000). Cited on page/s 53, 66.

[75] H. Tampo, H. Asahi, Y. Imanishi, M. Hiroki, K. Ohnishi, K. Yamada, K. Asami, and S. Gonda. Growth of high-quality polycrystalline GaN on glass substrate by gas source molecular beam epitaxy. *Journal of Crystal Growth* **227-228**, 442–446 (2001). Proceeding of the Eleventh International Conference on Molecular Beam Epitaxy. Cited on page/s 53, 66.

[76] S.-E. Park, D.-J. Kim, S. g. Woo, S.-M. Lim, and Byungsung O. Growth parameters for polycrystalline GaN on silica substrates by metalorganic chemical vapor deposition. *Journal of Crystal Growth* **242** (3), 383–388 (2002). Cited on page/s 53, 66.

[77] J. H. Kim and P. H. Holloway. Room-temperature photoluminescence and electroluminescence properties of sputter-grown gallium nitride doped with europium. *Journal of Applied Physics* **95** (9), 4787–4790 (2004). Cited on page/s 53, 66.

[78] D. P. Bour, N. M. Nickel, C. G. Van de Walle, M. S. Kneissl, B. S. Krusor, Ping Mei, and N. M. Johnson. Polycrystalline nitride semiconductor light-emitting diodes fabricated on quartz substrates. *Applied Physics Letters* **76** (16), 2182–2184 (2000). Cited on page/s 53, 66.

[79] J. H. Choi, *et al.* Nearly single-crystalline GaN light-emitting diodes on amorphous glass substrates. *Nature Photonics* **5**, 763–769 (2011). Cited on page/s 53, 66.

[80] H. Li, G. Zhao, H. Wei, L. Wang, Z. Chen, and S. Yang. Growth of Well-Aligned InN Nanorods on Amorphous Glass Substrates. *Nanoscale Research Letters* **11**, 270 (2016). Cited on page/s 53, 66, 67.

[81] V. Kumaresan, L. Largeau, F. Oehler, H. Zhang, O. Mauguin, F. Glas, N. Gogneau, M. Tchernycheva, and J.-C. Harmand. Self-induced growth of vertical GaN nanowires on silica. *Nanotechnology* **27** (13), 135602 (2016). Cited on page/s 53, 66, 67, 68.

[82] S.-Y. Bae, *et al.* III-nitride core–shell nanorod array on quartz substrates. *Scientific Reports* **7**, 45345 (2017). Cited on page/s 53, 66.

[83] A. Prabaswara, J.-W. Min, C. Zhao, B. Janjua, D. Zhang, A. M. Albadri, A. Y. Alyamani, T. K. Ng, and B. S. Ooi. Direct Growth of III-Nitride Nanowire-Based Yellow Light-Emitting Diode on Amorphous Quartz Using Thin Ti Interlayer. *Nanoscale Research Letters* **13**, 41 (2018). Cited on page/s 53, 66.

[84] S. Nakamura. Background Story of the Invention of Efficient InGaN Blue-Light-Emitting Diodes (Nobel Lecture). *Angewandte Chemie* **54** (27), 7770–7788 (2015). Cited on page/s 53.

[85] S. Nakamura. The Roles of Structural Imperfections in InGaN-Based Blue Light-Emitting Diodes and Laser Diodes. *Science* **281** (5379), 956–961 (1998). Cited on page/s 53.

[86] H. P. Maruska and J. J. Tietjen. THE PREPARATION AND PROPERTIES OF VAPOR-DEPOSITED SINGLE-CRYSTAL-LINE GaN. *Applied Physics Letters* **15** (10), 327–329 (1969). Cited on page/s 54.

[87] K. Ban, J. i. Yamamoto, K. Takeda, K. Ide, M. Iwaya, T. Takeuchi, S. Kamiyama, I. Akasaki, and H. Amano. Internal Quantum Efficiency of Whole-Composition-Range AlGaN Multiquantum Wells. *Applied Physics Express* **4** (5), 052101 (2011). Cited on page/s 54.

[88] L. Liu and J. H. Edgar. Substrates for gallium nitride epitaxy. *Materials Science and Engineering: R: Reports* **37** (3), 61–127 (2002). Cited on page/s 54.

[89] G. Li, W. Wang, W. Yang, Y. Lin, H. Wang, Z. Lin, and S. Zhou. GaN-based light-emitting diodes on various substrates: a critical review. *Reports on Progress in Physics* **79** (5), 056501 (2016). Cited on page/s 54.

[90] X. Huang, Z. Yin, S. Wu, X. Qi, Q. He, Q. Zhang, Q. Yan, F. Boey, and H. Zhang. Graphene-Based Materials: Synthesis, Characterization, Properties, and Applications. *Small* **7** (14), 1876–1902 (2011). Cited on page/s 55, 62.

[91] Graphene based materials: Past, present and future. *Progress in Materials Science* **56** (8), 1178–1271 (2011). Cited on page/s 55, 56, 62.

[92] L. Wang, W. Liu, Y. Zhang, Z.-H. Zhang, S. Tiam Tan, X. Yi, G. Wang, X. Sun, H. Zhu, and H. Volkan Demir. Graphene-based transparent conductive electrodes for GaN-based light emitting diodes: Challenges and countermeasures. *Nano Energy* **12**, 419–436 (2015). Cited on page/s 55, 58, 59, 60, 61.

[93] K.I. Bolotin, K.J. Sikes, Z. Jiang, M. Klima, G. Fudenberg, J. Hone, P. Kim, and H.L. Stormer. Ultrahigh electron mobility in suspended graphene. *Solid State Communications* **146** (9), 351–355 (2008). Cited on page/s 55.

[94] J.-H. Chen, C. Jang, S. Xiao, M. Ishigami, and M. S. Fuhrer. Intrinsic and extrinsic performance limits of graphene devices on SiO_2. *Nature Nanotechnology* **3**, 206–209 (2008). Cited on page/s 55, 58.

[95] X. Li, Y. Zhu, W. Cai, M. Borysiak, B. Han, D. Chen, R. D. Piner, L. Colombo, and R. S. Ruoff. Transfer of Large-Area Graphene Films for High-Performance Transparent Conductive Electrodes. *Nano Letters* **9** (12), 4359–4363 (2009). Cited on page/s 55, 57, 58.

[96] S. Bae, *et al.* Roll-to-roll production of 30-inch graphene films for transparent electrodes. *Nature Nanotechnology* **5**, 574–578 (2010). Cited on page/s 55, 56.

[97] A. A. Balandin, S. Ghosh, W. Bao, I. Calizo, D. Teweldebrhan, F. Miao, and C. N. Lau. Superior Thermal Conductivity of Single-Layer Graphene. *Nano Letters* **8** (3), 902–907 (2008). Cited on page/s 55.

[98] C. Lee, X. Wei, J. W. Kysar, and J. Hone. Measurement of the Elastic Properties and Intrinsic Strength of Monolayer Graphene. *Science* **321** (5887), 385–388 (2008). Cited on page/s 55.

[99] J. S. Bunch, S. S. Verbridge, J. S. Alden, A. M. van der Zande, J. M. Parpia, H. G. Craighead, and P. L. McEuen. Impermeable Atomic Membranes from Graphene Sheets. *Nano Letters* **8** (8), 2458–2462 (2008). Cited on page/s 55.

[100] E. Stolyarova, K. T. Rim, S. Ryu, J. Maultzsch, P. Kim, L. E. Brus, T. F. Heinz, M. S. Hybertsen, and G. W. Flynn. High-resolution scanning tunneling microscopy imaging of mesoscopic graphene sheets on an insulating surface. *Proceedings of the National Academy of Sciences of the United States of America* **104** (22), 9209–9212 (2007). Cited on page/s 56.

[101] T.-H. Han, H. Kim, S.-J. Kwon, and T.-W. Lee. Graphene-based flexible electronic devices. *Materials Science and Engineering: R: Reports* **118**, 1–43 (2017). Cited on page/s 56, 57, 60, 61, 62.

[102] Y. Song, W. Fang, R. Brenes, and J. Kong. Challenges and opportunities for graphene as transparent conductors in optoelectronics. *Nano Today* **10** (6), 681–700 (2015). Cited on page/s 56, 57, 58, 60.

[103] X. Li, W. Cai, L. Colombo, and R. S. Ruoff. Evolution of Graphene Growth on Ni and Cu by Carbon Isotope Labeling. *Nano Letters* **9** (12), 4268–4272 (2009). Cited on page/s 57.

[104] X. Li, *et al.* Large-Area Synthesis of High-Quality and Uniform Graphene Films on Copper Foils. *Science* **324** (5932), 1312–1314 (2009). Cited on page/s 58.

[105] H. S. Song, S. L. Li, H. Miyazaki, S. Sato, K. Hayashi, A. Yamada, N. Yokoyama, and K. Tsukagoshi. Origin of the relatively low transport mobility of graphene grown through chemical vapor deposition. *Scientific Reports* **2**, 337 (2012). Cited on page/s 58.

[106] W. Zhu, T. Low, V. Perebeinos, A. A. Bol, Y. Zhu, H. Yan, J. Tersoff, and P. Avouris. Structure and Electronic Transport in Graphene Wrinkles. *Nano Letters* **12** (7), 3431–3436 (2012). Cited on page/s 58.

[107] B.-J. Kim, C. Lee, Y. Jung, K. Hyeon Baik, M. A. Mastro, J. K. Hite, C. R. Eddy, and J. Kim. Large-area transparent conductive few-layer graphene electrode in GaN-based ultra-violet light-emitting diodes. *Applied Physics Letters* **99** (14), 143101 (2011). Cited on page/s 58, 59.

[108] B.-J. Kim, G. Yang, H.-Y. Kim, K. H. Baik, M. A. Mastro, J. K. Hite, C. R. Eddy, F. Ren, S. J. Pearton, and J. Kim. GaN-based ultraviolet light-emitting diodes with

AuCl3-doped graphene electrodes. *Optics Express* **21** (23), 29025–29030 (2013). Cited on page/s 58, 59, 62.

[109] D.-H. Youn, Y.-J. Yu, H. K. Choi, S.-H. Kim, S.-Y. Choi, and C.-G. Choi. Graphene transparent electrode for enhanced optical power and thermal stability in GaN light-emitting diodes. *Nanotechnology* **24** (7), 075202 (2013). Cited on page/s 58, 59, 62.

[110] J.-J. Zheng and Y.-J. Lin. Tuning the work function of graphene by nitrogen plasma treatment with different radio-frequency powers. *Applied Physics Letters* **104** (23), 233103 (2014). Cited on page/s 58, 62, 69, 70.

[111] T. Araki, *et al.* Radio-frequency plasma-excited molecular beam epitaxy growth of GaN on graphene/Si(100) substrates. *Applied Physics Express* **7** (7), 071001 (2014). Cited on page/s 59.

[112] A. Mazid Munshi, Dasa L. Dheeraj, Vidar T. Fauske, Dong-Chul Kim, Antonius T. J. van Helvoort, Bjørn-Ove Fimland, and Helge Weman. Vertically Aligned GaAs Nanowires on Graphite and Few-Layer Graphene: Generic Model and Epitaxial Growth. *Nano Letters* **12** (9), 4570–4576 (2012). Cited on page/s 59.

[113] Y. Gohda and S. Tsuneyuki. Structural phase transition of graphene caused by GaN epitaxy. *Applied Physics Letters* **100** (5), 053111 (2012). Cited on page/s 59.

[114] A. Koma. Van der Waals epitaxy—a new epitaxial growth method for a highly lattice-mismatched system. *Thin Solid Films* **216** (1), 72–76 (1992). Papers presented at the International Workshop on Science and Technology of Thin Films for the 21st Century, Evanston,IL, USA, July 28-August 2, 1991. Cited on page/s 60.

[115] H. Lee, K. Paeng, and I. S. Kim. A review of doping modulation in graphene. *Synthetic Metals* **244**, 36–47 (2018). Cited on page/s 60, 61, 62.

[116] D. Wei, Y. Liu, Y. Wang, H. Zhang, L. Huang, and G. Yu. Synthesis of N-Doped Graphene by Chemical Vapor Deposition and Its Electrical Properties. *Nano Letters* **9** (5), 1752–1758 (2009). Cited on page/s 61.

[117] N. Peimyoo, J. Li, J. Shang, X. Shen, C. Qiu, L. Xie, W. Huang, and T. Yu. Photocontrolled Molecular Structural Transition and Doping in Graphene. *ACS Nano* **6** (10), 8878–8886 (2012). Cited on page/s 61.

[118] P. Rani and V. K. Jindal. Designing band gap of graphene by B and N dopant atoms. *RSC Advances* **3**, 802–812 (2013). Cited on page/s 62.

[119] S.-O. Guillaume, B. Zheng, J.-C. Charlier, and L. Henrard. Electronic properties and STM images of doped bilayer graphene. *Physical Review B* **85** (3), 035444 (2012). Cited on page/s 62.

[120] C. Klein, D. Cohen-Elias, and G. Sarusi. Controlling graphene work function by doping in a MOCVD reactor. *Heliyon* **4** (E01030) (2018). Cited on page/s 62.

[121] L. S. Panchakarla, K. S. Subrahmanyam, S. K. Saha, Achutharao Govindaraj, H. R. Krishnamurthy, U. V. Waghmare, and C. N. R. Rao. Synthesis, Structure, and Properties of Boron- and Nitrogen-Doped Graphene. *Advanced Materials* **21** (46), 4726–4730 (2009). Cited on page/s 62.

[122] M. Wu, C. Cao, and J. Z. Jiang. Light non-metallic atom (B, N, O and F)-doped graphene: a first-principles study. *Nanotechnology* **21** (50), 505202 (2010). Cited on page/s 62.

[123] M. Rybin, A. Pereyaslavtsev, T. Vasilieva, V. Myasnikov, I. Sokolov, A. Pavlova, E. Obraztsova, A. Khomich, V. Ralchenko, and E. Obraztsova. Efficient nitrogen doping of graphene by plasma treatment. *Carbon* **96**, 196–202 (2016). Cited on page/s 62, 69.

[124] V. Adivarahan, A. Heidari, B. Zhang, Q. Fareed, M. Islam, S. Hwang, K. Balakrishnan, and A. Khan. Vertical Injection Thin Film Deep Ultraviolet Light Emitting Diodes with AlGaN Multiple-Quantum Wells Active Region. *Applied Physics Express* **2** (9), 092102 (2009). Cited on page/s 63.

[125] K. Kawasaki, C. Koike, Y. Aoyagi, and M. Takeuchi. Vertical AlGaN deep ultraviolet light emitting diode emitting at 322 nm fabricated by the laser lift-off technique. *Applied Physics Letters* **89** (26), 261114 (2006). Cited on page/s 63.

[126] L. Zhou, J. E. Epler, M. R. Krames, W. Goetz, M. Gherasimova, Z. Ren, J. Han, M. Kneissl, and N. M. Johnson. Vertical injection thin-film AlGaN/AlGaN multiple-quantum-well deep ultraviolet light-emitting diodes. *Applied Physics Letters* **89** (24), 241113 (2006). Cited on page/s 63.

[127] K. S. A. Butcher and T. L. Tansley. InN, latest development and a review of the band-gap controversy. *Superlattices and Microstructures* **38** (1), 1–37 (2005). Cited on page/s 63.

[128] J. F. Muth, J. H. Lee, I. K. Shmagin, R. M. Kolbas, H. C. Casey, B. P. Keller, U. K. Mishra, and S. P. DenBaars. Absorption coefficient, energy gap, exciton binding energy, and recombination lifetime of GaN obtained from transmission measurements. *Applied Physics Letters* **71** (18), 2572–2574 (1997). Cited on page/s 63.

[129] P. B. Perry and R. F. Rutz. The optical absorption edge of single-crystal AlN prepared by a close-spaced vapor process. *Applied Physics Letters* **33** (4), 319–321 (1978). Cited on page/s 63.

[130] S. Fujita. Wide-bandgap semiconductor materials: For their full bloom. *Japanese Journal of Applied Physics* **54** (3), 030101 (2015). Cited on page/s 63.

[131] C.I. Wu and A. Kahn. Negative electron affinity and electron emission at cesiated GaN and AlN surfaces. *Applied Surface Science* **162-163**, 250–255 (2000). Cited on page/s 63.

[132] S.-C. Lin, C.-T. Kuo, X. Liu, L.-Y. Liang, C.-H. Cheng, C.-H. Lin, S.-J. Tang, L.-Y. Chang, C.-H. Chen, and S. Gwo. Experimental Determination of Electron Affinities for InN and GaN Polar Surfaces. *Applied Physics Express* **5** (3), 031003 (2012). Cited on page/s 63.

[133] W. Gotz, N. M. Johnson, C. Chen, H. Liu, C. Kuo, and W. Imler. Activation energies of Si donors in GaN. *Applied Physics Letters* **68** (22), 3144–3146 (1996). Cited on page/s 63.

[134] W. Gotz, N. M. Johnson, J. Walker, D. P. Bour, and R. A. Street. Activation of acceptors in Mg-doped GaN grown by metalorganic chemical vapor deposition. *Applied Physics Letters* **68** (5), 667–669 (1996). Cited on page/s 63.

[135] J. Wu. When group-III nitrides go infrared: New properties and perspectives. *Journal of Applied Physics* **106** (1), 011101 (2009). Cited on page/s 63.

[136] I. Vurgaftman and J. R. Meyer. Band parameters for nitrogen-containing semiconductors. *Journal of Applied Physics* **94** (6), 3675–3696 (2003). Cited on page/s 63.

[137] B. Borisov, V. Kuryatkov, Y. Kudryavtsev, R. Asomoza, S. Nikishin, D. Y. Song, M. Holtz, and H. Temkin. Si-doped $Al_xGa_{1-x}N(0.56\leqslant x\leqslant 1)$ layers grown by molecular beam epitaxy with ammonia. *Applied Physics Letters* **87** (13), 132106 (2005). Cited on page/s 63.

[138] K. B. Nam, M. L. Nakarmi, J. Li, J. Y. Lin, and H. X. Jiang. Mg acceptor level in AlN probed by deep ultraviolet photoluminescence. *Applied Physics Letters* **83** (5), 878–880 (2003). Cited on page/s 63.

[139] S. Zhao, Z. Mi, M. G. Kibria, Q. Li, and G. T. Wang. Understanding the role of Si doping on surface charge and optical properties: Photoluminescence study of intrinsic and Si-doped InN nanowires. *Physical Review B* **85** (24), 245313 (2012). Cited on page/s 63.

[140] X. Wang, S.-B. Che, Y. Ishitani, and A. Yoshikawa. Growth and properties of Mg-doped In-polar InN films. *Applied Physics Letters* **90** (20), 201913 (2007). Cited on page/s 63.

[141] S. Zhao, X. Liu, and Z. Mi. Photoluminescence properties of Mg-doped InN nanowires. *Applied Physics Letters* **103** (20), 203113 (2013). Cited on page/s 63.

[142] S. Zhao, B. H. Le, D. P. Liu, X. D. Liu, M. G. Kibria, T. Szkopek, H. Guo, and Z. Mi. p-Type InN Nanowires. *Nano Letters* **13** (11), 5509–5513 (2013). Cited on page/s 63.

[143] M. Higashiwaki and T. Matsui. Estimation of band-gap energy of intrinsic InN from photoluminescence properties of undoped and Si-doped InN films grown by plasma-assisted

molecular-beam epitaxy. *Journal of Crystal Growth* **269** (1), 162–166 (2004). Proceedings of the First ONR International Indium Nitride Workshop. Cited on page/s 63.

[144] R. K. Wong. P-type doping of GaN. *Master thesis*. University of California, Berkeley (2000). Cited on page/s 63.

[145] L. Wang, Y. Zhang, X. Li, E. Guo, Z. Liu, X. Yi, H. Zhu, and G. Wang. Improved transport properties of graphene/GaN junctions in GaN-based vertical light emitting diodes by acid doping. *RSC Advances* **3**, 3359–3364 (2013). Cited on page/s 63.

[146] H. Zhong, Z. Liu, J. Wang, A. Pan, G. Xu, and K. Xu. Measuring the local mobility of graphene on semiconductors. *Physical Review Materials* **2** (4), 043801 (2018). Cited on page/s 63.

[147] M. Murakami and Y. Koide. Ohmic Contacts for Compound Semiconductors. *Critical Reviews in Solid State and Materials Sciences* **23** (1), 1–60 (1998). Cited on page/s 65.

[148] H. D. Espinosa, R. A. Bernal, and M. Minary-Jolandan. A Review of Mechanical and Electromechanical Properties of Piezoelectric Nanowires. *Advanced Materials* **24** (34), 4656–4675 (2012). Cited on page/s 66.

[149] M. C. McAlpine, R. S. Friedman, S. Jin, K.-h. Lin, W. U. Wang, and C. M. Lieber. High-Performance Nanowire Electronics and Photonics on Glass and Plastic Substrates. *Nano Letters* **3** (11), 1531–1535 (2003). Cited on page/s 66.

[150] Y. Park, S. Jahangir, Y. Park, P. Bhattacharya, and J. Heo. InGaN/GaN nanowires grown on SiO2 and light emitting diodes with low turn on voltages. *Optics Express* **23** (11), A650–A656 (2015). Cited on page/s 66.

[151] X. Dai, A. Messanvi, H. Zhang, C. Durand, J. Eymery, C. Bougerol, F. H. Julien, and M. Tchernycheva. Flexible Light-Emitting Diodes Based on Vertical Nitride Nanowires. *Nano Letters* **15** (10), 6958–6964 (2015). Cited on page/s 66.

[152] N. Guan, *et al.* Flexible White Light Emitting Diodes Based on Nitride Nanowires and Nanophosphors. *ACS Photonics* **3** (4), 597–603 (2016). Cited on page/s 66.

[153] N. Guan, X. Dai, A. V. Babichev, F. H. Julien, and M. Tchernycheva. Flexible inorganic light emitting diodes based on semiconductor nanowires. *Chemical Science* **8**, 7904–7911 (2017). Cited on page/s 66.

[154] M. Rajan Philip, *et al.* Fabrication of Phosphor-Free III-Nitride Nanowire Light-Emitting Diodes on Metal Substrates for Flexible Photonics. *ACS Omega* **2** (9), 5708–5714 (2017). Cited on page/s 66.

[155] H. Zhang and J. A. Rogers. Recent Advances in Flexible Inorganic Light Emitting Diodes: From Materials Design to Integrated Optoelectronic Platforms. *Advanced Optical Materials* **7** (2), 1800936 (2019). Cited on page/s 66.

[156] J. H. Choi, *et al.* GaN light-emitting diodes on glass substrates with enhanced electroluminescence. *Journal of Materials Chemistry* **22**, 22942–22948 (2012). Cited on page/s 66.

[157] Y. Zhao, X. Li, W. Wang, B. Zhou, H. Duan, T. Shi, X. Zeng, L. Ning, and Y. Wang. Growth and properties of GaAs nanowires on fused quartz substrate. *Journal of Semiconductors* **35** (9), 093002 (2014). Cited on page/s 66.

[158] V. Dhaka, T. Haggren, H. Jussila, H. Jiang, E. Kauppinen, T. Huhtio, M. Sopanen, and H. Lipsanen. High Quality GaAs Nanowires Grown on Glass Substrates. *Nano Letters* **12** (4), 1912–1918 (2012). Cited on page/s 66.

[159] K. Chung, C.-H. Lee, and G.-C. Yi. Transferable GaN Layers Grown on ZnO-Coated Graphene Layers for Optoelectronic Devices. *Science* **330** (6004), 655–657 (2010). Cited on page/s 67, 70.

[160] Y. Kobayashi, K. Kumakura, T. Akasaka, and T. Makimoto. Layered boron nitride as a release layer for mechanical transfer of GaN-based devices. *Nature* **484** (7393), 223–227 (2012). Cited on page/s 67.

[161] C. Zhao, *et al.* InGaN/GaN nanowires epitaxy on large-area MoS_2 for high-performance light-emitters. *RSC Advances* **7**, 26665–26672 (2017). Cited on page/s 67.

[162] S. Sundaram, *et al.* Large-Area van der Waals Epitaxial Growth of Vertical III-Nitride Nanodevice Structures on Layered Boron Nitride. *Advanced Materials Interfaces* **6** (16), 1900207 (2019). Cited on page/s 67, 69, 70.

[163] P. Gupta, *et al.* Layered transition metal dichalcogenides: promising near-lattice-matched substrates for GaN growth. *Scientific Reports* **6**, 23708 (2016). Cited on page/s 67.

[164] Y. Yin, *et al.* Direct van der Waals Epitaxy of Crack-Free AlN Thin Film on Epitaxial WS_2. *Materials* **11** (12), 2464 (2018). Cited on page/s 67.

[165] I. Susanto, C.-Y. Tsai, Fachruddin, T. Rahmiati, Y.-T. Ho, P.-Y. Tsai, and I.-S. Yu. The influence of 2D MoS_2 layers on the growth of GaN films by plasma-assisted molecular beam epitaxy. *Applied Surface Science* **496**, 143616 (2019). Cited on page/s 67.

[166] Z. Chen, *et al.* High-Brightness Blue Light-Emitting Diodes Enabled by a Directly Grown Graphene Buffer Layer. *Advanced Materials* **30** (30), 1801608 (2018). Cited on page/s 67, 69, 70.

[167] Y. Qi, *et al.* Fast Growth of Strain-Free AlN on Graphene-Buffered Sapphire. *Journal of the American Chemical Society* **140** (38), 11935–11941 (2018). Cited on page/s 67.

[168] Y. Li, *et al.* Van der Waals epitaxy of GaN-based light-emitting diodes on wet-transferred multilayer graphene film. *Japanese Journal of Applied Physics* **56** (8), 085506 (2017). Cited on page/s 67, 70.

[169] Q. Wu, *et al.* Growth mechanism of AlN on hexagonal BN/sapphire substrate by metal–organic chemical vapor deposition. *CrystEngComm* **19**, 5849–5856 (2017). Cited on page/s 67, 70.

[170] Z. Chen, *et al.* Improved Epitaxy of AlN Film for Deep-Ultraviolet Light-Emitting Diodes Enabled by Graphene. *Advanced Materials* **31** (23), 1807345 (2019). Cited on page/s 67, 70.

[171] H. Chang, *et al.* Graphene-assisted quasi-van der Waals epitaxy of AlN film for ultraviolet light emitting diodes on nano-patterned sapphire substrate. *Applied Physics Letters* **114** (9), 091107 (2019). Cited on page/s 67, 70.

[172] D. Liang, T. Wei, J. Wang, and J. Li. Quasi van der Waals epitaxy nitride materials and devices on two dimension materials. *Nano Energy* **69**, 104463 (2020). Cited on page/s 67, 70.

[173] T. L. Chu, H. C. Mollenkopf, and S. S. C. Chu. Deposition and Properties of Silicon on Graphite Substrates. *Journal of the Electrochemical Society* **123** (1), 106–110 (1976). Cited on page/s 67.

[174] W. D. Johnston and W. M. Callahan. Properties of Polycrystalline AlAs / GaAs on Graphite Heterojunctions for Solar Cell Applications. *Journal of the Electrochemical Society* **125** (6), 977–983 (1978). Cited on page/s 67.

[175] C.-H. Lee, Y.-J. Kim, Y. J. Hong, S.-R. Jeon, S. Bae, B. H. Hong, and G.-C. Yi. Flexible Inorganic Nanostructure Light-Emitting Diodes Fabricated on Graphene Films. *Advanced Materials* **23** (40), 4614–4619 (2011). Cited on page/s 67.

[176] K. Chung, H. Beak, Y. Tchoe, H. Oh, H. Yoo, M. Kim, and G.-C. Yi. Growth and characterizations of GaN micro-rods on graphene films for flexible light emitting diodes. *APL Materials* **2** (9), 092512 (2014). Cited on page/s 67.

[177] F. Yuan, B. Liu, Z. Wang, B. Yang, Y. Yin, B. Dierre, T. Sekiguchi, G. Zhang, and X. Jiang. Synthesis, Microstructure, and Cathodoluminescence of [0001]-Oriented GaN Nanorods Grown on Conductive Graphite Substrate. *ACS Applied Materials & Interfaces* **5** (22), 12066–12072 (2013). Cited on page/s 67, 68.

[178] Metal catalyst-assisted growth of GaN nanowires on graphene films for flexible photocatalyst applications. *Current Applied Physics* **14** (11), 1437–1442 (2014). Cited on page/s 67.

[179] S. Kang, A. Mandal, J. H. Chu, J.-H. Park, S.-Y. Kwon, and C.-R. Lee. Ultraviolet

photoconductive devices with an n-GaN nanorod-graphene hybrid structure synthesized by metal-organic chemical vapor deposition. *Scientific Reports* **5**, 10808 (2015). Cited on page/s 67, 68.

[180] S. Kang, A. Mandal, J.-H. Park, D.-Y. Um, J. H. Chu, S.-Y. Kwon, and C.-R. Lee. Effects of growth temperatures on the characteristics of n-GaN nanorods–graphene hybrid structures. *Journal of Alloys and Compounds* **644**, 808–813 (2015). Cited on page/s 67, 68.

[181] M. Heilmann, G. Sarau, M. Gobelt, M. Latzel, S. Sadhujan, C. Tessarek, and S. Christiansen. Growth of GaN Micro- and Nanorods on Graphene-Covered Sapphire: Enabling Conductivity to Semiconductor Nanostructures on Insulating Substrates. *Crystal Growth & Design* **15** (5), 2079–2086 (2015). Cited on page/s 67, 68, 69, 71.

[182] H. Hayashi, Y. Konno, and K. Kishino. Self-organization of dislocation-free, high-density, vertically aligned GaN nanocolumns involving InGaN quantum wells on graphene/SiO_2 covered with a thin AlN buffer layer. *Nanotechnology* **27** (5), 055302 (2015). Cited on page/s 67, 69, 70, 71.

[183] M. Heilmann, *et al.* Vertically Oriented Growth of GaN Nanorods on Si Using Graphene as an Atomically Thin Buffer Layer. *Nano Letters* **16** (6), 3524–3532 (2016). Cited on page/s 67, 68, 69, 70, 71.

[184] V. Kumaresan, *et al.* Epitaxy of GaN Nanowires on Graphene. *Nano Letters* **16** (8), 4895–4902 (2016). Cited on page/s 67, 68, 69, 71.

[185] S. Fernandez-Garrido, *et al.* Molecular Beam Epitaxy of GaN Nanowires on Epitaxial Graphene. *Nano Letters* **17** (9), 5213–5221 (2017). Cited on page/s 67, 69, 70, 71.

[186] Y. Wang, D. Dheeraj, Z. Liu, M. Liang, Y. Li, X. Yi, J. Wang, J. Li, and H. Weman. AlGaN Nanowires Grown on SiO_2/Si(100) Using Graphene as a Buffer Layer. *Crystal Growth & Design* **19** (10), 5516–5522 (2019). Cited on page/s 67.

[187] F. Ren, *et al.* Direct Growth of AlGaN Nanorod LEDs on Graphene-Covered Si. *Materials* **11** (12), 2372 (2018). Cited on page/s 67.

[188] S. Nakagawa, T. Tabata, Y. Honda, M. Yamaguchi, and H. Amano. GaN Nanowires Grown on a Graphite Substrate by Radio Frequency Molecular Beam Epitaxy. *Japanese Journal of Applied Physics* **52** (8S), 08JE07 (2013). Cited on page/s 67.

[189] Y. Jia, *et al.* Transferable GaN Enabled by Selective Nucleation of AlN on Graphene for High-Brightness Violet Light-Emitting Diodes. *Advanced Optical Materials* **8** (2), 1901632 (2020). Cited on page/s 67, 69, 70.

[190] S.-S. Kim, J.-W. Lee, J.-M. Yun, and S.-I. Na. 2-Dimensional MoS_2 nanosheets as transparent and highly electrocatalytic counter electrode in dye-sensitized solar cells: Effect of thermal treatments. *Journal of Industrial and Engineering Chemistry* **29**, 71–77 (2015). Cited on page/s 67.

[191] D. Jin-Xiang, Z. Xiao-Kang, Y. Qian, W. Xu-Yang, C. Guang-Hua, and H. De-Yan. Optical properties of hexagonal boron nitride thin films deposited by radio frequency bias magnetron sputtering. *Chinese Physics B* **18** (9), 4013–4018 (2009). Cited on page/s 67.

[192] A. Zunger, A. Katzir, and A. Halperin. Optical properties of hexagonal boron nitride. *Physical Review B* **13** (12), 5560–5573 (1976). Cited on page/s 67.

[193] A. Pakdel, Y. Bando, and D. Golberg. Nano boron nitride flatland. *Chemical Society Reviews* **43**, 934–959 (2014). Cited on page/s 67.

[194] D. Akinwande, N. Petrone, and J. Hone. Two-dimensional flexible nanoelectronics. *Nature Communications* **5**, 5678 (2014). Cited on page/s 67.

[195] X. Li and H. Zhu. Two-dimensional MoS_2: Properties, preparation, and applications. *Journal of Materiomics* **1** (1), 33–44 (2015). Cited on page/s 67.

[196] Y. Zhan, Z. Liu, S. Najmaei, P. M. Ajayan, and J. Lou. Large-Area Vapor-Phase Growth and Characterization of MoS_2 Atomic Layers on a SiO_2 Substrate. *Small* **8** (7), 966–971

(2012). Cited on page/s 67.

[197] Y. Shi, H. Li, and L.-J. Li. Recent advances in controlled synthesis of two-dimensional transition metal dichalcogenides *via* vapour deposition techniques. *Chemical Society Reviews* **44**, 2744–2756 (2015). Cited on page/s 67.

[198] X. Duan, C. Wang, A. Pan, R. Yu, and X. Duan. Two-dimensional transition metal dichalcogenides as atomically thin semiconductors: opportunities and challenges. *Chemical Society Reviews* **44**, 8859–8876 (2015). Cited on page/s 67.

[199] G. R. Bhimanapati, *et al.* Recent Advances in Two-Dimensional Materials beyond Graphene. *ACS Nano* **9** (12), 11509–11539 (2015). Cited on page/s 67.

[200] C. Tan, *et al.* Recent Advances in Ultrathin Two-Dimensional Nanomaterials. *Chemical Reviews* **117** (9), 6225–6331 (2017). Cited on page/s 67.

[201] V. Consonni, M. Knelangen, U. Jahn, A. Trampert, L. Geelhaar, and H. Riechert. Effects of nanowire coalescence on their structural and optical properties on a local scale. *Applied Physics Letters* **95** (24), 241910 (2009). Cited on page/s 68.

[202] M.A Baker, P Hammer, C Lenardi, J Haupt, and W Gissler. Low-temperature sputter deposition and characterisation of carbon nitride films. *Surface and Coatings Technology* **97** (1), 544 – 551 (1997). Cited on page/s 69.

[203] Y.-C. Lin, C.-Y. Lin, and P.-W. Chiu. Controllable graphene N-doping with ammonia plasma. *Applied Physics Letters* **96** (13), 133110 (2010). Cited on page/s 69.

[204] M. Fuchs, J. L. F. Da Silva, C. Stampfl, J. Neugebauer, and M. Scheffler. Cohesive properties of group-III nitrides: A comparative study of all-electron and pseudopotential calculations using the generalized gradient approximation. *Physical Review B* **65** (24), 245212 (2002). Cited on page/s 70.

[205] A. M. Munshi, D.-C. Kim, C. P. Heimdal, M. Heilmann, S. H. Christiansen, P. E. Vullum, A. T. J. van Helvoort, and H. Weman. Selective area growth of AlGaN nanopyramid arrays on graphene by metal-organic vapor phase epitaxy. *Applied Physics Letters* **113** (26), 263102 (2018). Cited on page/s 71.

[206] M. Morassi, *et al.* Selective Area Growth of GaN Nanowires on Graphene Nanodots. *Crystal Growth & Design* **20** (2), 552–559 (2020). Cited on page/s 71.

CHAPTER 4

Growth, characterization and fabrication

The experimental methods that were employed in this thesis will be briefly examined in this chapter. All of the nanocolumn samples were grown by molecular beam epitaxy and investigated by various characterization techniques, namely scanning electron microscopy, transmission electron microscopy, high-resolution X-ray diffraction, photoluminescence, and Raman spectroscopy. Concise description on the UV-LED fabrication process by means of conventional photolithography–metallization and electrical characterization via current-voltage and electroluminescence measurements will be given as well.

4.1 MOLECULAR BEAM EPITAXY

Molecular beam epitaxy (MBE) is a refined form of physical vapor deposition for epitaxial growth for the synthesis of monocrystalline semiconductor materials (with the capability of monolayer-scale control [1]) from the reaction of molecular beams of the constituent elements using a bottom-up approach [1–3]. The grown materials can be in the form of thin-films or nanostructures of high quality and well-controlled dimensions. The concept of a *molecular beam* refers to the long mean free path of evaporated or sublimated elements/species from the sources to the substrate, implying that they do not react/collide with each other until reaching the substrate for the growth [3]. The term of *epitaxy* originates from two ancient Greek words, $\varepsilon\pi\iota$ (*epi*: placed upon) and $\tau\alpha\zeta\iota\zeta$ (*taxis*: arrangement in an ordered manner), referring to extended single-crystal film formation on top of a crystalline substrate [4]. The materials are deposited in an orderly fashion so that their atomic arrangement “accepts” the crystallographic structure of the substrate [1].

Principally, the MBE process builds up the semiconductor crystal one atomic layer at a time, i.e., atom by atom [5–7]. The material beams are very dilute, with partial pressures in the range of $\leqslant 10^{-3}$ Pa [5]. Historically, K. G. Günther laid the foundation of the MBE growth process at Siemens Research Laboratories (Erlangen) in 1958, known as three-temperature method [5,8]. However, the resulting films were not well-ordered (insufficient crystalline quality), triggering limited interest for its use in devices. Later, John R. Arthur Jr. and Alfred Yi Cho at Bell Telephone laboratories in the late 1960s successfully produced high-quality, atomically flat thin-film semiconductor structures using the MBE process[5,9]. Since then, MBE has been widely employed in the manufacture of semiconductor devices, such as transistors, diodes, lasers, and LEDs. It is also considered as one of the most versatile tools for the research and development of nanotechnology materials[10], such as topological insulators[11,12] and 2D materials[13,14].

MBE can be differentiated based on the sources of the reactants: solids, gases, metal–organic compounds, and hydrides[15]. For the MBE utilizing solid sources, its growth technique is commonly called solid source MBE. In such cases, the operation principle of effusion cells as reactant sources is based on the Knudsen mode of evaporation. This name, along with the name of Knudsen cell, comes from Martin Knudsen, a Danish physicist, who discovered that this evaporation occurs as effusion from an isothermal ($\Delta T=0$) enclosure with a small orifice[15]. Effusion is a process in which a gas escapes from a container (enclosure) through a hole (orifice), with a diameter significantly smaller (about one tenth) than the mean free path of the gas molecules at the equilibrium conditions[15]. A Knudsen cell is regarded as a form of conventional effusion cell, and the modified versions of this cell are called dissociation or cracker cells[15]. The essential elements of an MBE system are schematically illustrated in Figure 4.1.

Material depositions are performed by thermally evaporating or sublimating the source materials of highest purity from the carefully shaped crucibles (within the effusion cells)[5] in a chamber maintained under ultra-high vacuum (UHV) condition, between 10^{-7} and 10^{-8} Pa. This UHV condition leads to a few

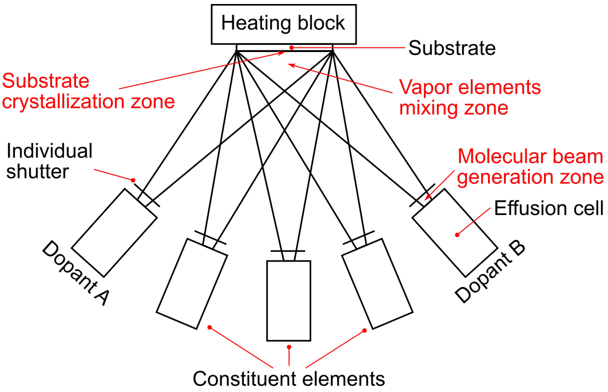

FIGURE 4.1. Simplified schematic of the essential parts of an MBE growth system (adapted with permission from ref. 16 © 1982 Elsevier).

trademarks [3,10] that distinguish MBE from other epitaxial techniques, for instance MOVPE and HVPE. First, incorporation of impurities from the ambient environment are minimized, leading to a grown material with an exceptional purity level. Second, the beam nature of the mass flow toward the substrate is preserved [15]. It maintains source fluxes in the molecular flow regime, i.e., the vaporized high-purity materials form of an evaporated (thermal) beam of atomic or molecular species that can be ballistically projected onto the heated substrate, where these species condense in the solid state. This physical deposition contributes to the growth, while the species that miss or desorb from the substrate tend to be immediately pumped away from the chamber or deposit on cryopanels in the chamber.

Third, an *in-situ* growth characterization method such as RHEED can be performed for real-time monitoring of the crystal growth. Fourth, the thin-film growth rate can be adjusted from hundred nanometers per hour to several micrometers per hour by changing the temperatures of the effusion cells, which can also finely tune the beam flux. Composition and doping levels of the grown material depend on the relative arrival rates of the constituent elements and dopants, which in turn rely on the evaporation rates of the respective sources [1,17,18]. Combined with the ability to rapidly open and close the shutters in front of the cells further enables a better control of the deposited materials, including their chemical compositions, with an atomically sharp interface and precision up to the monolayer level. Additionally, the formation of such interface can be achieved because of the substantial inter-diffusion constraint between layers of different composition, thanks to MBE's relatively low growth temperature [3]. This property is extremely useful for the semiconductor designs that require heterostructures and low-dimensional quantum structures with abrupt junction between the layers of thin-films and nanostructures [10,17].

Based on the MBE arrangement in Figure 4.1, one may categorize different physical phenomena during the growth into three zones [15]. The first zone is *the generation of the molecular beams* from the sources of the Knudsen effusion cell type. The second zone is *the mixing area*, where the beams from different sources intersect each other. Owing to the long mean free path of the molecules belonging to the intersecting beams, it is then assumed that collisions and other kinds of interaction between molecules of different species do not occur here. The third zone is the area where the vaporized elements mix together on the heated substrate surface; that is, where *the crystallization processes* occur. Due to deposition under ultra-high vacuum condition, epitaxial growth events in MBE normally occur under conditions far from thermodynamic equilibrium. Instead, kinetics of the surface processes from the impinging beams that react with the outermost atomic layers of the substrate crystal surface dictate the growth mechanism [1,15].

Upon reaching the outermost atomic layer of the substrate, the atoms undergo two types of adsorption (these atoms are sometimes called adsorbed atoms or adatoms): physical adsorption (*physisorption*) and chemical adsorption (*chemisorption*) [1,15]. Former process refers to when there is no electron transfer between adsorbate and adsorbent, and the bonding is therefore formed via weak van der Waals forces [1,15]. On the other hand, chemisorption involves electron transfer, i.e., by forming a strong covalent bond to the surface atom where it is trapped [1,15]. While physisorption generally shows little or no dependence on the surface site arrangement of the substrate, chemisorption may depend on the crystallographic orientation of the substrate surface, as well as on the nature and spatial distribution of atoms adsorbed on this surface [15].

Compared with the chemisorbed state, the atoms that stick to the surface via physisorption have a higher probability of diffusing or migrating to find an energetically preferred location and forming a stronger chemical bonding [1]. This diffusion process continues until the adatoms either thermally desorb from the surface, nucleate (incorporate) into the crystal lattice of the substrate [15], or aggregate to another existing adatom, forming an island. It is also probable for adatoms to directly impinge on this island, making it to grow further or lead to the next layer growth, depending on the surface potential and energy [1]. The occurrence and magnitude of these surface phenomena [1,15,19] depend not only on the growth conditions [1] that are kinetically (e.g., growth temperature) and/or geometrically (e.g., incidence angle of the impinging atoms) related but also on the nature of the substrate crystal surface whose chemical activity might locally differ from one crystal site to another (dangling bond, vacancy, step edge, etc.).

Furthermore, the occurrence of the different epitaxial growth modes can take place due to binding energy competition between adatoms and adatoms or adatoms and substrate, which is a result of the specific growth conditions. Each growth mode uniquely characterizes the nucleation and growth processes, which directly correspond to the morphology of the grown structures. In case the adatoms preferentially attach to substrate surface sites, this will result in atomically smooth 2D layer, namely *Frank-van der Merwe* (layer-by-layer) growth mode. In contrast, when adatom–adatom interactions are stronger than adatom–substrate interactions, 3D islands are formed, known as *Volmer-Weber* (island) growth mode. A combination (intermediate) between these two is called *Stranski-Krastanov* (layer-plus-island) growth mode, driven by the significant lattice mismatch between epilayer and substrate. As the layer thickness exceeds the critical thickness, dislocations are generated, releasing the accumulated stored elastic strain energy density due to lattice misfit with the substrate (see Subsection 2.3.1), and subsequently the transition from layers growth mode to islands growth mode occurs [1].

Figure 4.2 shows the MBE system built by EpiQuest utilized for the growth of nitride nanocolumns presented in this thesis. It consists of three types of main chambers, as shown in Figure 4.2a, with different vacuum levels: a load-lock chamber, a transfer (preparation) chamber, and two growth chambers. The load-lock chamber, with the help of a rough pump and a turbo molecular pump, can achieve a background pressure in the order of 10^{-5} Pa. It can be exposed to the atmosphere for loading/unloading the samples before/after growth. The transfer chamber, whose background pressure is approximately 10^{-7} Pa with an ion pump, is equipped with a pre-baking station (up to 350°C) for initial thermal desorption of the substrate (a dedicated baking chamber [up to 1200°C] is also available). It serves as a transition chamber between the load-lock and growth chambers and protects the growth chambers from being exposed directly to the load-lock chamber. Each growth chamber has a background pressure in the order of 10^{-8}-10^{-9} Pa, achieved by using a turbo molecular pump, an ion pump, a titanium sublimation pump, and a cryo pump. All of the nanocolumn samples reported in this thesis were grown in the growth chamber E1.

As schematically illustrated in Figure 4.2b, the sample is held in the center of the growth chamber (vertical epitaxy reactor) by the manipulator, which can be heated up to 1250°C (as read by a thermocouple). To ensure the homogeneity in thickness and composition of the grown materials [15]—as well as the flux arrival on the substrate—the substrate has an azimuthal rotation of about 10 RPM (rotations per minute) during the growth. The sources (Knudsen effusion cells and a nitrogen plasma source) are mounted along the arc centered on the sample, with the beam incident angle relative to the normal angle of the substrate surface at ~40° [21]. The material sources are heated in pyrolytic boron nitride crucibles containing ultra-pure group-III materials (Ga, Al, In) and dopants (Si, Mg) with tantalum heat shields, and in front of each effusion cell, a tantalum shutter is mounted. To support high operating temperatures during the growth, every effusion cell is surrounded by a cryo-shield that constantly cools with the flow of liquid nitrogen (77 K). Similarly, the inner part of the growth chamber is also shielded with liquid nitrogen cryo-panel that is used to trap most impurities not removed by pumping.

The flux of individual species is controlled by setting the temperature in the effusion cell (accuracy of 0.1°C), whose beam equivalent pressure is calibrated using a beam flux monitor ion gauge that can be inserted into the growth chamber and placed in the same position as the substrate holder (which must be elevated in order to avoid crashing). N atoms are generated through a radio-frequency (RF) plasma cell supplied by ultra-high purity N2 gas (99.999% or higher). Such cell is utilized to dissociate N_2 molecules via RF electronic discharge, through which its power can be adjusted from 0 to 500 W, and the

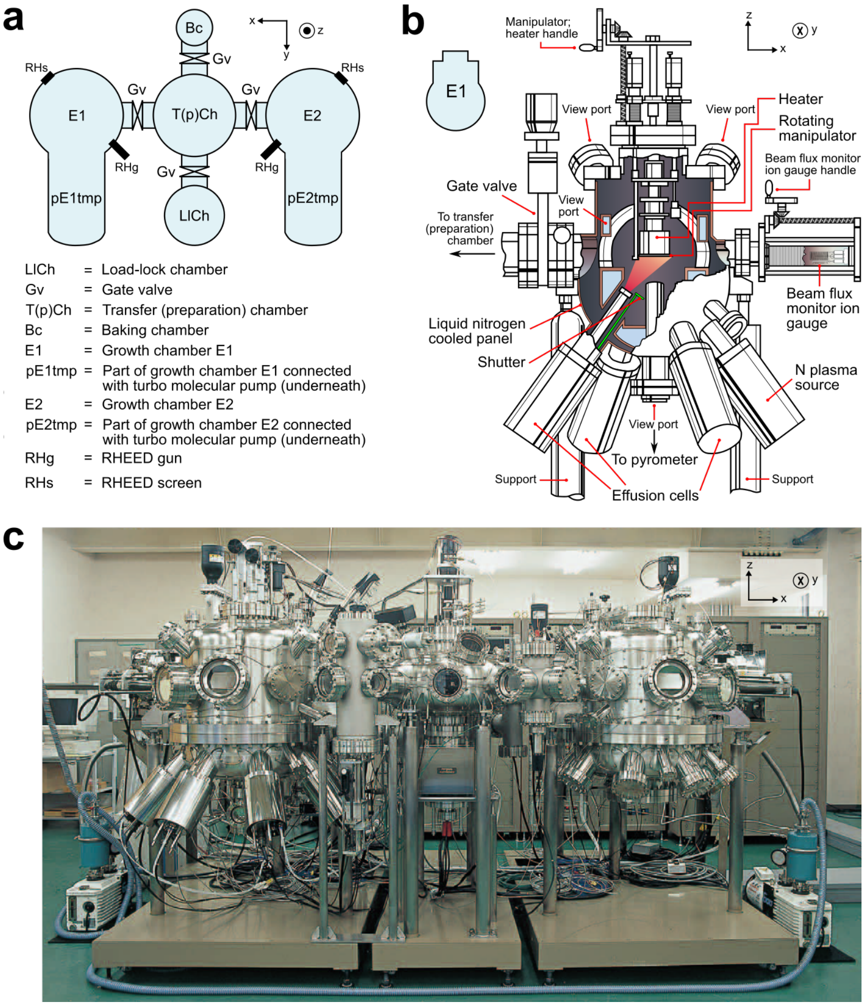

FIGURE 4.2. MBE setup at Sophia University used during the PhD period. a, Top-view sketch of the EpiQuest MBE system consisting of three types of main chambers: load-lock, transfer (preparation) and two growth chambers. **b,** Schematic cross-section diagram of the growth chamber E1 (part of RC2100 RF-PAMBE machine), which was utilized to grow nanocolumn samples for this PhD study. **c,** Photograph of the completed multi-chamber MBE system (RC2100) for GaN growth at Sophia University during its initial installation in 1998. Images in **a**, **b**, and photograph in **c** were adapted with permission from ref. 20 © EpiQuest, Inc.

flow rate can be set from 0.01 to 3.50 standard cubic centimeters per minute (sccm). A tuning box is also used to stabilize the generated plasma in the cavity. Accordingly, the MBE growth technique employing RF for generating plasma is often referred as RF plasma-assisted MBE (RF-PAMBE). The substrate is heated by DC-powered filaments placed behind the substrate in the manipulator, and the temperature of the grown material can be measured from the thermocouple located at a small distance behind the substrate and by the pyrometer placed outside the MBE growth chamber (its location is perpendicular to the substrate).

The III-V nitride MBE system in the Kishino Laboratory, as seen in Figure 4.2c, located at the Department of Engineering and Applied Sciences, Sophia University (Tokyo, Japan), has another growth chamber (E2). The latter is employed mainly for the selective area growth of III-N semiconductor nanocolumns on patterned GaN template/sapphire using Ti as a mask. Activities in the E2 chamber are more focused on the growth of GaN/InGaN nanocolumn structure for visible LEDs. Unfortunately, RHEED characterization technique was not utilized throughout this PhD work because of a malfunction in the RHEED gun. Substrate holders used for growing nanocolumn structures doped with Mg atoms (i.e., *p*-nanocolumn) were/are afterwards baked in the previously mentioned baking chamber. This was/is done to minimize outgassing of Mg atoms in later nanocolumn growths.

4.2 SCANNING ELECTRON MICROSCOPY

Scanning electron microscopy (SEM) is an imaging technique utilizing an electron beam focusing system for the analysis and examination of micro-/nano-structure morphology, topology, and composition with sub-hundred-nanometer resolution by scanning the sample surface in a raster scan pattern. It is a non-destructive, simple, and efficient characterization technique. When the incoming electrons from the electron gun, called the primary electron beam, impinge on the sample's surface, they can penetrate the sample for some distance (up to 10 μm, depending on the electron energy) before they encounter and collide with the atoms from the sample. Figure 4.3a illustrates a wealth of signals that can be generated due to these electron–sample interactions, in which each of them can provide unique information for the analysis of the sample.

The primary electron beam produces a region of primary excitation, causing an ionization of sample atoms. As a result, loosely bound electrons from the outermost atomic shells of the material can be emitted, which are known as *secondary electrons* (inelastic scattering). These electrons have low energy (< 50 eV), and therefore, they can escape from the sample only if they are generated

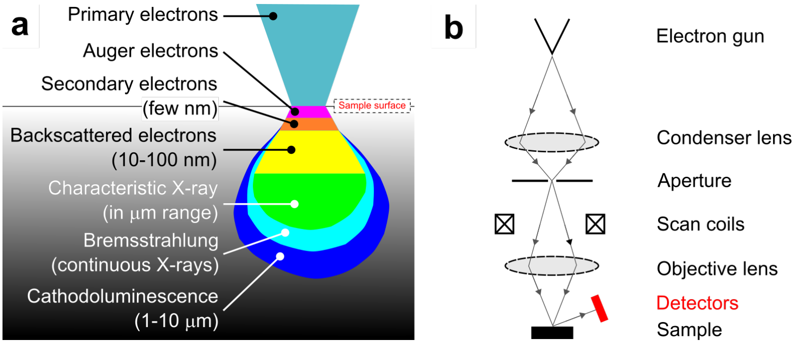

FIGURE 4.3. Scanning electron microscopy. a, Various SEM signals generated upon the interaction of incident electron beam on the sample surface (adapted with permission from ref. 22 © 2013 Sergey Khromov). **b,** Simplified schematic diagram of the SEM apparatus.

approximately a few nanometers from the surface. Since this secondary electron signal originates from the sample surface, it is the most widely used signal for investigation of topographic contrast, emphasizing the visualization of surface texture and roughness.

A group of primary electrons that lose a small amount of energy, called *backscattered electrons*, undergo a single or multiple scattering events and escape from the surface. Their energy are several keV, and they can be the source of another secondary electron. However, this can reduce the overall resolution of the secondary electron image. Since backscattered electrons emerge from deeper locations within the sample, the image resolution is inferior to the secondary electron image. As these backscattering events are strongly dependent on the atomic number (Z) of the constituent atoms, this signal can be used to identify both compositional and topographic information.

Another group of signals that can be exploited for quantitative compositional analysis is *characteristic X-rays*. They are emitted as a result of electron excitation from an inner shell to an outer shell of an atom, followed by electron relaxation filling the vacancy in the inner shell. The technique utilizing characteristic X-rays is called energy-dispersive X-ray spectroscopy (EDS or EDX) or sometimes called particle-induced X-ray emission. An alternative group of signals to characteristic X-rays for surface chemical analysis is *Auger electrons*. The filling of an inner shell vacancy of an atomic orbital by an electron from a higher energy level results in a release of energy, which typically occurs in the form of a photon. However, this energy can also be transferred to another electron, which is then ejected (emitted) from the atom. This technique, utilizing the so-called Auger effect, is referred as Auger electron spectroscopy.

Finally, when the primary electrons can excite electrons in the sample from the valence band to the conduction band, the subsequent de-excitation process will generate a photon emitted as a result of the electron and hole recombination. In this way, a *cathodoluminescence* signal is produced. Material information such as energy bandgap (thus often its composition and crystal structure) and energy levels of impurities and defects can be retrieved from the cathodoluminescence measurement.

Electron beam energy, which is expressed as the acceleration voltage in the SEM graphical user interface, determines the size and shape of the interaction zone within the sample. One can increase (decrease) the penetration depth and interaction volume by increasing (decreasing) the energy of the electron beam. For example, a low acceleration voltage is required to visualize the detailed structural information from the very surface region of the sample using secondary electron signals. This implies that lower acceleration voltage leads to higher resolution. The atomic number (Z) of the atoms in the analyzed material can also influence the penetration depth and interaction volume in such a way that the penetration depth and interaction volume are reduced with the increasing of Z.

A schematic diagram of a SEM is shown in Figure 4.3b. An electron gun generates an electron beam in a high-vacuum chamber (10^{-10} Torr) with an adjustable acceleration voltage in the range of 1-30 kV. Modern SEM utilizes a tungsten field emission source instead of a tungsten or lanthanum hexaboride thermionic emitter to achieve a stable electron beam with high current, a coherent beam, and small spot size. This concentrated beam of electrons is achieved by using a magnetic condenser lens system and an objective lens. Scan coils located between the lens systems are used to produce deflections over the sample in the form of a raster, i.e., by sweeping the focused electron beam over a sample surface one point at a time in a rectangular scanning area—just like the display in previous cathode-ray tube-based television. An aperture can exclude the electrons deviating from the optical axis. Varying signals produced from the bombardment on the sample surface are then identified by using specific detectors, whose output is fed synchronously for visual display.

Note here that the electron lenses in an SEM are not involved in magnification; their function is solely to produce a focused electron beam onto a particular surface region. Achieving a higher magnification can be done only by scanning a much smaller region. This implies that the resolution in an SEM is dependent on the electron probing size on the sample.

The morphological features of the grown GaN and GaN/AlGaN nanocolumns in this thesis were studied using an SII SMI3050SE focused ion beam (FIB)-SEM and a Hitachi SU8000 SEM at the Department of Materials and Life Sciences, Sophia University (Tokyo, Japan). An acceleration voltage of 15 kV for the former and 5-15 kV for the latter was employed for the secondary electron imaging.

4.3 TRANSMISSION ELECTRON MICROSCOPY

Transmission electron microscopy (TEM) is a microscopy technique exploiting the transmitted electrons through a prepared thin sample (< 100 nm) to form an image. With a typical high electron acceleration voltage of 200 kV in TEM, a resolution of 2.7 pm should theoretically be achievable, but due to imperfect lenses (lens aberrations, e.g., spherical and chromatic aberrations, coma, field astigmatism, field curvature, and distortion), the practical resolution is ~ 1 Å. Regardless, this extreme spatial resolution can reveal the crystal phase and defects, as well as determine the lattice constant of semiconductor materials. TEM relies on the detection of primary electrons traversing the sample, either straight or scattered forward into their respective detectors, e.g., a charge-coupled device (CCD) camera, or an electron energy loss spectroscopy (EELS) detector. These direct electron interactions with structure inside the sample can produce higher resolution image than the collection of secondary electrons in SEM. Additionally, TEM is equipped with an EDX detector to detect X-rays that are generated when the electrons inelastically interact with the atoms.

Figure 4.4a presents the general layout of components involved in the TEM[23]. Emitted electrons from the field emission gun are accelerated as they pass through the vacuum column via condenser lenses and aperture, which have the capability to control the beam size (parallel, for conventional TEM imaging, or convergent, for scanning techniques) and intensity upon reaching the sample. Subsequent scan coils are utilized in scanning mode and for tilting the beam in dark-field TEM imaging. The electron beams then interact with the sample ($<$ 100 nm thick): some of the electron beams are transmitted (elastically) through the sample, and some of them are scattered (elastically and inelastically) by the sample into particular directions according to Bragg's law. Subsequently, these scattered beams are brought into focus by the objective lens to a diffraction pattern in the back focal plane and further down to an image in the image plane. Magnification is done via an intermediate lens, and the final electron wave front is projected onto a fluorescent screen or a CCD camera by a projection lens. Resolution in a TEM is primarily dependent on the electron optics, which are limited by aberrations.

Because of the particle/wave duality of high-energy electrons, TEM can provide diverse characterizations and analysis techniques[24]. Figure 4.4b presents the possible interactions that can happen between an incident beam of electrons and a sample. In addition to the signals that have been previously discussed in SEM, accelerated electrons can pass through the sample without interaction (direct beam) or undergo either elastic or inelastic scattering. The coherency features of the elastically scattered electrons—, i.e., phase relationship between scattered electrons—can be used, for example, in high-resolution TEM (co-

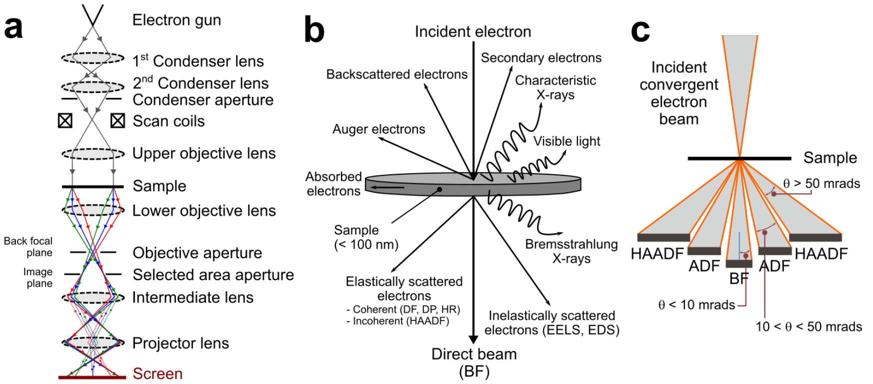

FIGURE 4.4. **Transmission electron microscopy. a,** Schematic diagram of a TEM with its beam paths (adapted with permission from ref. 23 © 2020 Julie Stene Nilsen). The blue lines represent the direct beam, while the green and red lines are associated with scattered electrons at two different directions. Under the intermediate lens: the solid lines illustrate the beam path for imaging mode, the dashed lines depict the beam path for diffraction mode. **b,** Various TEM signals generated upon the traverse of incident electron beam through a thin sample (adapted with permission from ref. 24 © 2014 Takeshi Saito). **c,** Schematic diagram of the STEM and the electron scattering angles with their respective detectors.

herent) and high-angle annular dark field scanning TEM (incoherent). On the other hand, for the inelastically scattered electrons, the loss of incident electron energy due to generation of X-ray can be utilized for EELS and EDS techniques.

Contrast in TEM images is formed from *amplitude contrast* (a combination between mass-thickness and diffraction contrasts) or *phase contrast*[24]. Mass-thickness contrast in the image originates from incoherent elastic scattering. The degree of scattering increases monotonically as a function of Z; high Z (high mass) scatters electrons at an angle that will be blocked by an objective aperture, thus forming darker image. The opposite happens for low Z (low mass), i.e., bright image will be formed. Similarly, a thick region scatters electrons at larger angle than that of a thin region, although they have an identical Z.

Diffraction contrast appears in a situation when the intensity variations arise from differences in diffracting conditions between different regions across the sample. The contrast in this image results from elastic scattering event and it is formed due to the role of atomic planes in the crystal oriented in such a way that leads the electron beam to experience Bragg scattering. When the aperture is positioned to pass only the directly transmitted electrons, a *bright-field* (BF) image is formed. On the other hand, when the aperture is positioned to pass only some diffracted electrons (due to the strongly diffracting regions), a *dark-field* (DF) image is formed.

In BF image, the diffracted beam is blocked, meaning the image is dark in the scattered region, whereas in DF image, the diffracted beam passes through, and thus the image appears bright in the diffracted region. One can select one of these images to be projected onto the detector via an objective aperture by adjusting the incident beam using the scan coils [10,23,24]. DF mode provides inverse and improved contrast relative to BF mode that is useful for capturing smaller features in the crystal, such as crystal stacking order and defects. The contrast provided in this mode is also influenced by the Z, for which a heavy atom gives a brighter contrast, and a light atom gives a darker contrast.

A diffraction pattern [24] is made in the back focal plane of the lower objective lens, where the objective aperture is located. By introducing a selected area aperture (a thin metal strip containing several different hole sizes) into the beam path (image plane), one can block all of the electron beam except for the small fraction that passes through one of the holes. Diffraction pattern from the sample in a specific area down to 100 nm in diameter can be recorded [10], and thus *selected area electron diffraction* (SAED) pattern is obtained. This gives information regarding the local crystallography, orientation, and defects.

TEM, whose image is produced by a *phase contrast* mechanism (another image contrast beside amplitude contrast) is known as high-resolution TEM (HRTEM). This mode can be achieved by selecting a larger objective aperture that allows *both* direct and (several) diffracted electron beams to form an image. The mechanism is based on the interference between these multiple beams, and it originates from the phase shift due to the interaction between the incident electrons and the thin sample [24]. This phenomenon leads to the formation of interference (lattice) fringes containing the information regarding the phase of electron waves scattered throughout a thin sample [25]. The interpretation of these fringes can provide high spatial resolution information for the investigated materials such as the spacing of the lattice planes, i.e., lattice resolution imaging, through which an atomic resolution can be resolved. This technique is very useful for revealing the crystalline stacking order and interface of the heterostructure materials.

Another interesting technique is called scanning TEM (STEM), in which the finely-focused electron probe of TEM (instead of a parallel one) is brought to scan over the sample in a raster method similar to SEM, as illustrated in Figure 4.4c [25]. The transmitted and scattered electrons are subsequently collected by different detectors, namely BF, annular dark-field (ADF), and high-angle annular-dark field (HAADF) detectors. While the BF detector gathers the unscattered electrons (and low-angle scattered electrons, smaller than 10 mrad), the ADF collects scattered electrons (between 10 to 50 mrad) that are mostly thermally diffused scattered electrons. A particular imaging technique, named HAADF-STEM, utilizes elastically scattered electrons resulting from high-angle incoherent scattering (more than 50 mrad) [24]. Such scattering angle is caused by the heavy atoms; the image intensity is proportional to the Z, and thus it is often called “Z-contrast” imaging. Compared to HRTEM, this technique can generate higher atomic resolution images and is more straightforward in interpreting atomic structures.

In this thesis, details of the structural characterization of the GaN nanocolumns on silica glass were studied using different TEM imaging methods (SAED, HRTEM, and HAADF STEM), carried out by means of field emission JEOL-2100F and JEOL JEM-ARM200F systems. The interfaces of GaN nanocolumns/AlN buffer layer on graphene/silica glass and GaN/AlGaN nanocolumns/AlN buffer layer on graphene/silica glass, along with their elemental distributions were studied using HRTEM and STEM EELS/EDS in an emission gun JEOL ARM200F system, equipped with a QuantumER GIF for EELS and a Centurio SDD for EDS. Inelastically scattered electrons for elemental mapping and compositional analysis were measured by EELS, whereas continuous X-rays were analyzed using EDS. These characterizations were carried out by collaborators at TEM Gemini Centre, NTNU.

4.4 HIGH-RESOLUTION X-RAY DIFFRACTION

High-resolution X-ray diffraction (HRXRD) is a non-destructive analytical technique to study the average structural properties and chemical compositions of as-grown crystalline material, based on the information obtained from its diffracted X-ray pattern peak(s) at a specific range of angles. An X-ray beam is incident on the surface of the sample (penetrating several micrometers into the crystal structure), which results in the scattered X-rays from the sample interfering with each other in destructive and constructive fashions. The destructive scattering does not contribute to the output signal. At a particular range of incoming angles, the X-ray beams are scattered constructively by the periodic structure of a crystal that acts as a grating, as illustrated in Figure 4.5a. The particular angles giving rise to the constructive interference is unique for every crystal.

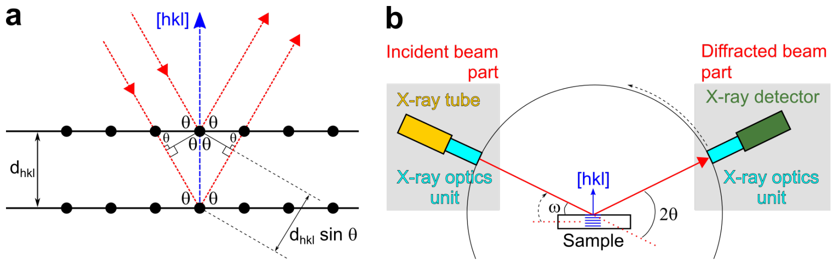

FIGURE 4.5. High-resolution X-ray diffraction. a, Schematic of Bragg diffraction and **b,** the top-view of HRXRD basic configuration for 2θ-ω scan.

The output of XRD signal is determined by the constructive interference at the detector position by waves scattered from atoms of the probed volume of the sample. This means that the size of the receiving slit also matters. Apart from the arrangement of the lattice, the destructive/constructive scattering for a specific reflection is governed by the internal structure of the unit cell (primitive cell to be more precise) via the *structure factor*[26]. The value of the structure factor must be different from 0 for a diffraction to be present.

Constructive interference described earlier can only occur when the path length difference between two reflected waves, as shown in Figure 4.5a, undergoing interferences (given by $2d_{hkl}\sin\theta$) is equal to an integer multiple of the wavelength of the X-ray beam (given by $n\lambda$). This is known as the Bragg condition, and thus the equation of $2d_{hkl}\sin\theta = n\lambda$ is called Bragg's law, where d_{hkl} is the interplanar atomic distance between adjacent (hkl) lattice planes, θ is the incident angle, n is an integer and λ is the X-ray wavelength. Since the incident angle at which constructive interference taking place is measured, and the wavelength of X-ray source is determined, one can use the Bragg equation to precisely calculate the distance between the lattice planes of the material. The result of this HRXRD measurement is expressed with the relation between the X-ray intensity on the y-axis and the incident angle on the x-axis.

Figure 4.5b presents the general HRXRD system, consisting of an X-ray tube, an incident X-ray optics unit, a motorized sample stage, a secondary X-ray optics unit, and an X-ray diffraction detector. The X-ray tube generates X-ray beams by accelerating a focused electron beam at high voltage to bombard a target material, which is typically Cu, resulting in an X-ray wavelength of 1.5406 Å (Kα radiation). An incident X-ray optics unit is composed of a Göbel mirror, a monochromator, and a divergence slit. It has a few specific functions to perform before letting the X-ray beam reach the sample: the Göbel mirror collimates the X-ray beam; the monochromator, made of a channel-cut Ge crystal, enhances the spectral resolution; and the divergence slit limits the divergence of the X-ray beam. Prior to detection, the diffracted X-ray beam goes through the secondary optics unit that has identical parts (with adjustable receiving slits) to those of the previous optics unit.

Two modes were employed in the work presented in this thesis: symmetric 2θ-ω and ω scans (symmetric: crystal planes are parallel to the sample surface). Figure 4.5b virtually illustrates the HRXRD basic configuration for the 2θ-ω scan, where the detector and the sample are rotated simultaneously for 2θ and ω (or θ on the previous notation of Bragg condition), respectively. For the ω scan, also known as the rocking scan, the sample is scanned by rotating ω while keeping the detector stationary. These symmetric scans are capable to reveal the information regarding the lattice constant c, as well as e.g., quantify the crystal quality and strain states (tensile or compressive) of the grown III-V nitride nanocolumns. The 2θ-ω mode is used to provide the crystal structure, orientation, and chemical composition, while the FWHM obtained in rocking mode indicates the orientation quality, i.e., spread of tilt of the nanocolumns. If needed, the lattice constant a can be measured using an additional asymmetric scan.

HRXRD was performed by collaborators using a Bruker D8 Discovery High-Resolution Diffractometer using Cu Kα radiation at the Department of Electronic Systems, NTNU.

4.5 PHOTOLUMINESCENCE SPECTROSCOPY

Photoluminescence spectroscopy is a contactless, non-destructive measurement method for the characterization of optical properties of semiconductors based on the light emission from semiconductors after the absorption of incoming photons from an external source. It can be indirectly employed to study structural properties, like the strain of the materials. The source of excitation is typically a laser, whose beam is incident on a semiconductor sample. When the photon energy of the laser is higher than that of the bandgap of the semiconductor, the absorption of laser light by the semiconductor occurs. (In this section, direct bandgap semiconductor is assumed, unless otherwise stated). At this point, the electrons in the valence band receive energy, enabling their promotion to the conduction band, and they consequently leave behind holes in the valence bands (i.e., electron-hole pairs are created).

However, these excited electrons in the conduction band are unstable. To be able to return to their equilibrium state, they must undergo a few steps (in order to release their excess energy, either via the emission of light or not) before the recombination of electron-hole pairs takes place. The electrons (holes) that are excited at an energy level higher than that of the bandgap will experience a thermal relaxation to release this extra energy in the form of phonons. After that, the electrons (holes) arrive at the minima of the conduction band (maxima of the valence band). Following this, electrons from the minima of the conduction band recombine with the holes at the maxima of the valence band, and this phenomenon is known as the *band-to-band recombination* process. This event leads to the generation of photons, whose energy is related to the difference in energy levels between the excited state and the equilibrium state, i.e., bandgap of the semiconductor material under investigation.

The photon generation mechanism mentioned previously is categorized as the radiative transitions. Radiative transitions in semiconductors can additionally occur via direct or indirect transitions through localized *defect levels* within the bandgap (e.g., in the middle), such as vacancies or interstitials. Their

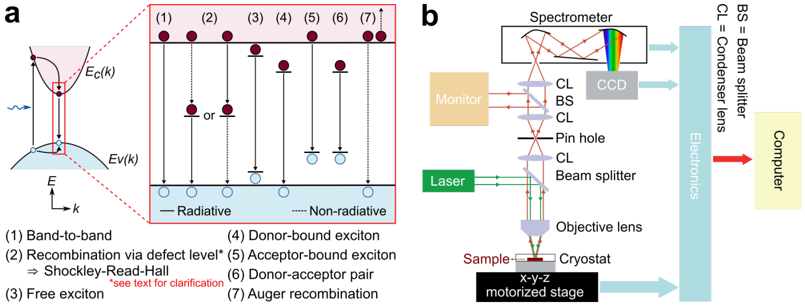

FIGURE 4.6. Photoluminescence spectroscopy. **a,** Recombination processes in a direct bandgap semiconductor. First, electron is excited from the valence band to conduction band using laser. Then it is de-excited to the conduction band minima by emitting optical or acoustic phonons. Various possible photoluminescence processes are followed afterwards as shown in the inset. **b,** Schematic diagram of a micro-photoluminescence setup (adapted with permission from ref. 25 © 2010 Dheeraj Dasa Lakshmi Narayana).

photoluminescence emissions related to these energy levels can be utilized to identify specific defects and possibly to determine their concentrations. Other radiative recombinations can come from *free exciton recombination*, *donor-* and *acceptor-bound excitons*, along with *donor-acceptor pairs*. Figure 4.6a summarizes the aforementioned recombination or transition processes occurring in the semiconductor after excitation. Therefore, analysis of the photoluminescence spectra is useful in revealing the recombination mechanism of a semiconductor material. Corresponding to the energy bandgap measurement, this photo-excitation process can also reveal the information regarding the alloy composition of semiconductor materials.

Photoluminescence intensity is associated with the relative contribution of the radiative processes. In case a semiconductor contains defects, this can influence the optical properties of the semiconductor also as non-radiative recombination centers. The excess energy from electrons transitioning from the conduction band to the defect level (and/or from the defect level to the valence band) can result in a non-radiative, a radiative process (as mentioned in the aforementioned paragraph), or combination of both processes. The third event indicates that one of the transitions could be radiative, depending on materials and/or defects. Another example of non-radiative process is *Auger* recombination, a process where the excess energy is given to a third carrier, i.e., an electron in conduction band. This third carrier is excited to a higher energy level and once it loses its excess energy, it thermalizes back down to the conduction band edge. Non-radiative process can reduce or quench the band-edge luminescence intensity of the semiconductor material, such as in an example given by Geelhaar *et al.*[27]. The nature of the defect in this paragraph is different from the aforementioned defect in that the latter is radiative and can account for additional emission bands. The incorporation of a metal catalyst into the nanocolumns is an example for the defect (as an impurity) that can weaken the GaN photoluminescence intensity[28], whereas stacking fault is an example of the radiative defect[27].

At room-temperature, the recombination process is normally dominated by band-to-band recombination and defect level transitions, if present. Strong electron–phonon interactions at room-temperature broadens the photoluminescence bands, causing an overlap of bands of similar energies. Therefore, it is difficult to analyze the details of a photoluminescence spectrum. At low-temperatures, on the other hand, other recombination processes—in addition to previously mentioned processes at room-temperature—can be observed. For instance, these can include free excitons, donor- or acceptor-bound excitons, and/or donor–acceptor pairs. Moreover, the effect of thermal broadening in the photoluminescence bands is suppressed, so bands that overlap at room-temperature observation are more clearly distinguished at low-temperatures.

Schematic diagram of a micro-photoluminescence setup is presented in Figure 4.6b. The laser is used as an excitation source, with its beam passing through a series of lenses and mirrors, which is then focused using an objective lens that can produce a spot with a diameter from a few to several hundred micrometers on the sample. Subsequently, the photons generated from the sample go through the same objective lens, but now they pass through the beam splitter, collected by condenser optics, converted to a collimated beam by a condenser lens and subsequently focused by another condenser lens to the entrance slit of a spectrometer. Here, the luminescence is dispersed in the spectrometer and then detected by a Si CCD detector. Low-temperature photoluminescence measurement is done by placing the sample in a closed-cycle cryostat, where the temperature of the samples can be controlled from 10 to 300 K.

The first part of the optical studies in this thesis was done at Sophia Nanotechnology Research Center, Sophia University (Tokyo, Japan), using room-temperature and 77 K micro-photoluminescence with a He-Cd laser (325 nm) as the excitation source. Measurement at 77 K was achieved by placing the sample inside the closed-cycle liquid nitrogen cryostat system equipped with a sample heater and thermometer. The second part of the optical studies was conducted by a collaborator at the Nanophotonics Laboratory, Department of Electronic Systems, NTNU. The room-temperature micro-photoluminescence measurements were done using a He-Cd laser (325 nm) and the third harmonics of a tunable, pulsed Ti: Sapphire laser (266 nm) as the excitation source. In addition, the measurement at 4 K was taken by isolating the sample inside a Cryo Industries closed-cycle liquid helium microscopy cryostat system equipped with a sample heater and thermometer for precise sample temperature control.

4.6 RAMAN SPECTROSCOPY

When a monochromatic light is shone on a material, most light will be scattered, with no change in the color of the light. This vast majority of photons (>99.999%) are elastically scattered, meaning that they have the same wavelengths as the incident light. This is known as a *Rayleigh scattering*. However, an insignificant part of the light (<0.001%) will be scattered with a slightly different color. These photons experience an inelastic scattering, a term used for the scattered light that undergoes a wavelength or energy shift either up or down relative to the incoming light. This phenomenon is called *Raman scattering*, and it occurs due to the interaction (energy exchange) between the monochromatic light and atomic vibrations and/or phonons in the material. Simply defined, Raman spectroscopy is a contact-less, non-destructive, spectroscopy-based technique that utilizes the Raman scattering phenomenon for the structural characterization of the semiconductor and graphitic materials, among others.

The electric field of the incident light distorts the electron cloud of the material, triggering electronic transitions to a higher virtual state. In Rayleigh scattering, when a molecule is excited to any virtual state, it relaxes back to its original state by elastically scattering the photon whose energy is the same as that of the incident light energy. However, this is not the case for Raman scattering. In the first situation, the excited molecule in any virtual state is relaxes back to a higher vibrational state than where it originated, making the photon being emitted at lower energy. In the second situation, the molecule from a higher vibrational state is excited to any virtual state, and then it relaxes back to a lower vibrational state than where it originated. Thus, the photon leaves with energy higher than that of the incident photon. Figure 4.7a illustrates all possible scattering in a molecule upon radiation by light.

As a result, the Raman scattering signal in the first situation is shifted toward a lower energy (longer wavelength) than the excitation energy (i.e., *Stokes scattering*), whereas in the second situation, the Raman scattering signal is shifted toward a higher energy (shorter wavelength) than the excitation energy (i.e., *anti-Stokes scattering*). The energy differences (or wavelength shifts) between excitation and scattering recognized in these phenomena are associated with the atomic vibrational transitions. Rayleigh scattering has the strongest signal, followed by Stokes scattering and, finally, anti-Stokes scattering. The signal coming from anti-Stokes scattering is the weakest because only a small fraction of the atoms initially reside at a higher vibrational state (before the photon is incident upon the material). In Raman measurement, the result of interest is the energy difference between the incident and scattered photons—the Raman shift, with the unit expressed in units of wavenumber (number of waves per cm, cm^{-1}). A value of 0 cm^{-1} means that the incident light is scattered without

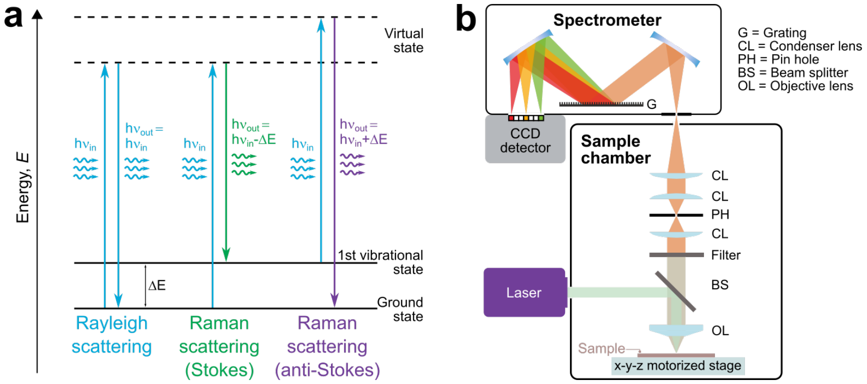

FIGURE 4.7. Raman spectroscopy. a, Energy diagram illustrating Rayleigh and Raman scattering processes. **b,** Schematic of a Raman system (adapted with permission from ref. 29 © 2019 MDPI.

a change (shift) in energy.

Since each material has its unique vibrational fingerprints, Raman spectroscopy is a useful measurement technique for revealing information regarding the identity, structure, thickness, chemical composition, crystallinity, stress state, quality, and even doping level of the materials. Recognition on these features can be achieved by comparing the Raman shifts with the databases of known spectra. Raman spectroscopy is sensitive to small changes in material chemistry and structure, owing to the high sensitivity of vibrational states, which can alter the energy of scattered photons. Moreover, this shift can provide information on the electronic properties that can be derived from LO phonons and coupled plasmon–LO phonon modes [17]. Additionally, the vibration frequency depends on the mass of the atoms and/or the bond strength between them. That is, heavy atoms and/or weak bonds have low Raman shifts (e.g., C-C, ~800 cm^{-1}), while light atoms and/or strong bonds have high Raman shifts (e.g., C-H, ~3000 cm^{-1} or C=C, ~1600 cm^{-1}). Such rules can be used to explain one of many possible features observed in Raman spectra.

A common micro-Raman system presented in Figure 4.7b is similar to that of micro-photoluminescence system in Figure 4.6b. Laser light (focused by a microscope objective lens) illuminating the sample surface generates the scattered light, which is subsequently collected by the same microscope objective lens. It then passes through a lens system and is sent through a spectrometer. Wavelengths near the laser line (due to elastic Rayleigh scattering) are filtered out by using notch and/or edge filters, holographic diffraction gratings, and multiple dispersion stages that can reject laser light at high degrees. In this way, undesired light is blocked (since it would drown out the relatively weak Raman signal), and only those wavelengths in a certain spectral window away from the laser line are dispersed by diffraction grating onto a CCD detector for spectral acquisition.

In this thesis, unpolarized micro-Raman spectroscopy was conducted at room-temperature in backscattering configuration using a Renishaw InVia Reflex Spectrometer System, equipped with a 514.5 nm excitation laser. These measurements were realized at the NTNU NanoLab, and part of the characterization results presented in the subsequent chapters were done by collaborators.

4.7 Device fabrication and electrical measurements

In order to make devices from the nanocolumn samples grown using RF-PAMBE (and generally other growth techniques), it is necessary to first define the contact areas by photolithography. Next, one must deposit the required metals in these predetermined domains by electron-beam (e-beam) evaporation and/or sputtering. Since the graphene used in this PhD work was intended as not only the semiconductor substrate but also the transparent conducting electrode, one of the designated contact areas must be on graphene, not the grown semiconductor layers as in the traditional way. With that being said, the processing and characterization techniques exploited for the LED fabrications are tremendously vast, demanding their own dedicated discussions, which are beyond the scope of this dissertation. Description of the physical phenomena regarding the involved technologies, including atomic layer deposition (ALD), inductively coupled plasma-reactive ion etching (ICP-RIE), photolithography, e-beam evaporation, and sputtering, are available elsewhere. For this reason, the rest of this section emphasizes more on the general procedure of the LED fabrication processes.

The nanocolumn structure that was employed for the device fabrication in this PhD thesis consisted of (from bottom to top) *n*-GaN/*n*-AlGaN/*i*-GaN/*p*-AlGaN/*p*-GaN. In this work, Si-doped *n*-AlN buffer layer was first grown on top of graphene as the nucleation layer for the subsequent nanocolumn formation, enabling a vertical orientation of the *c*-axis growth direction from graphene. Furthermore, this buffer layer alleviates the damage on the graphene surface caused by nitrogen plasma damage during the growth. Simultaneously in this given condition, the doping properties of graphene become *n*-type[30–35]. It is then assumed (and purposely oversimplified) in this study that the graphene-AlN interface in the vicinity of bottom contact area has similar electrical properties, i.e., *n*-*n* semiconductor heterojunction, despite their dissimilarity in work function. Note that the difference in the work function can affect the overall device performance and thus may become a subject of interest for future investigations (see Subsection 3.2.3). Another contact area was defined on the top part of the GaN nanocolumns, which is typically doped with Mg atoms, prompting a *p*-type doped semiconductor.

A stack of metals, usually consisting of 50 nm Ni and 100 nm Au (or 10 nm Ni and 200 nm Au), was utilized as a contact to the top part of the *p*-GaN nanocolumn segment, and 200 nm Au was employed as the bottom contact metal to the graphene. The latter material has been demonstrated to exhibit an ohmic contact to graphene with a low contact resistance [36]. As it might be noticed, the top metal contacts were relatively much thicker compared with other top metal contacts employed in other nanocolumn LED studies, which typically consist of 10 nm Ni and 10 nm Au. The reason for this is that LEDs reported in this thesis are not intended for top emitting devices. Instead, they are designed for flip-chip type devices, in which light can be emitted through the transparent graphene substrate. In this regard, a graphene electrode can *in principle* enable vertical current injection through the nanocolumn LED structures. Please note that as long as the contact formed on graphene is on the side of the LED, lateral current injection and hence current crowding will take place. The latter becomes more pronounced when the sheet resistance of graphene is high. The thick metals at the top are used to ensure uniform connection across the defined contact area of the *p*-GaN nanocolumn segment.

Depending on the geometrical shape of the nanocolumn top, two different approaches can be used for the flip-chip device fabrication. The two approaches share similar processes, but with additional early process steps for one of the fabrication methods.

With the top of nanocolumns merging with each other, i.e., no gap spacing is observed in the *p*-GaN segment of nanocolumns (e.g., Figure 2.15), the following processes, consisting of photolithography and metallization, are described in Figure 4.8. An insulating layer of photoresist was first coated on the sample to define the aperture and bottom contact area. During this first photolithography step, the sample was placed in an oven to resist reflow prior to hard bake, i.e., curing the photoresist. Afterward, a lift-off process (resist reflow and hard bake are now omitted) was carried out to form the Ni/Au top contact area in the vicinity of the aperture. Next, the bottom Au contact area was formed using the same lift-off method mentioned earlier. However, since the nanocolumns covered the graphene surface, it was important to first remove them from the designated bottom contact area by scratching using the tip of a needle. This was the method used throughout this PhD work. Bear in mind that scratching is very likely to damage graphene, and thus dry etching is deemed to be a better approach to remove the nanocolumns. It should be stressed that the use of a dry etching method can damage the graphene as well if it is not controlled well. Finally, Au was deposited as the bottom metal contact to the open graphene area.

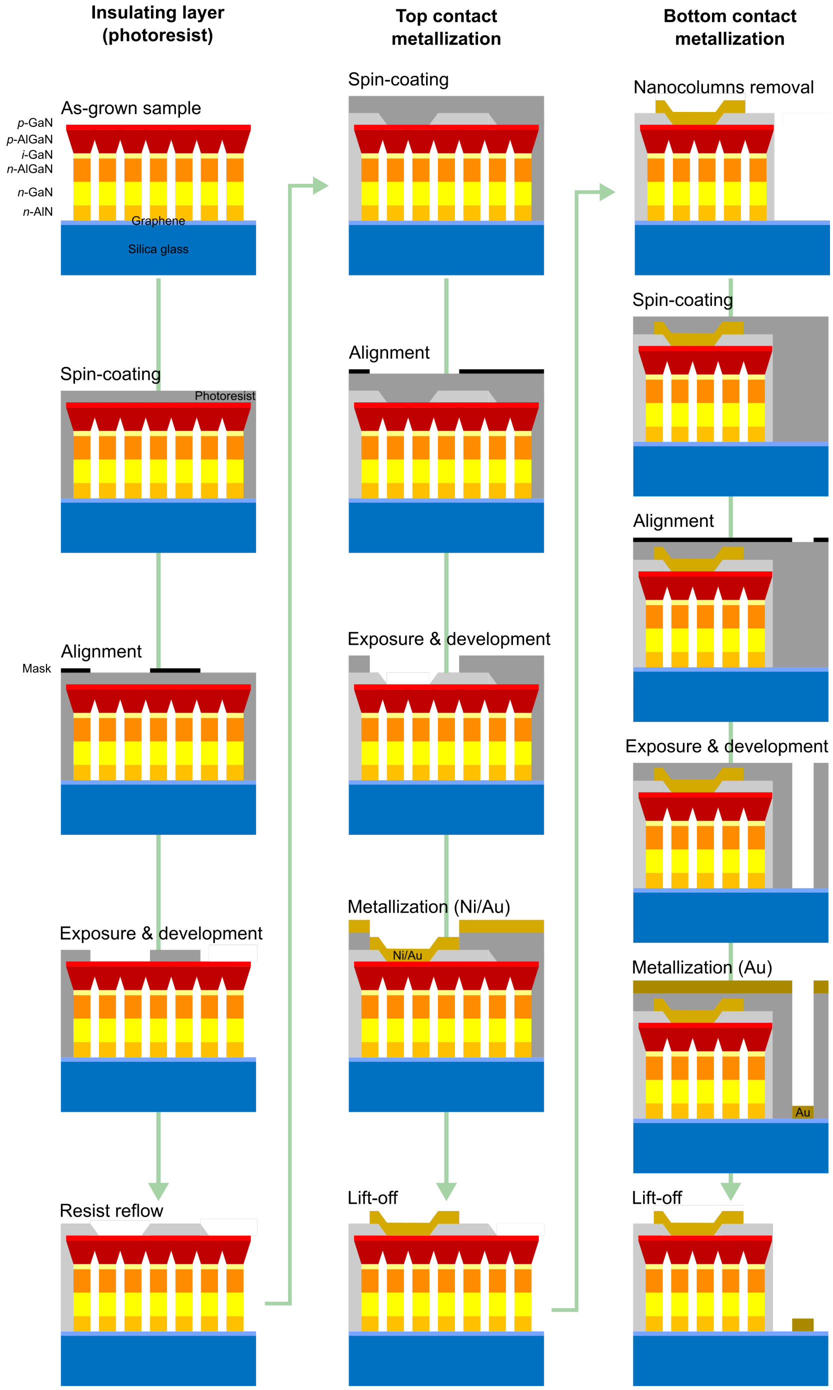

FIGURE 4.8. Illustration of flip-chip nanocolumn-based UV-LED fabrication processes for the nanocolumn structure whose p-GaN segments are coalesced with their proximity.

For nanocolumn LED structures whose *p*-GaN segments do not coalesce with their vicinities, the device fabrication scheme is illustrated in Figure 4.9. Thin aluminium oxide (Al_xO_y), with an approximate thickness of 15 nm, was deposited on the sample using the ALD technique, resulting in a fine conformal coating to the nanocolumn surface and graphene substrate. In this state, Al_xO_y also still covers the *p*-GaN layers, and this coverage should thus be removed prior to the formation of the Ni/Au top contact. To achieve this, a first round of the photolithography process using a diluted photoresist (e.g., S1813 positive photoresist) was realized. Exposing Al_xO_y covering *p*-GaN sections can be accomplished through oxygen plasma etching of the diluted photoresist. The sample was then subjected to an etching process using ICP-RIE to remove the Al_xO_y layer from *p*-GaN. Afterward, this diluted photoresist was washed away, and the same processing methods for the formation of the top and bottom contact metallization described in the previous paragraph were then applied for this sample.

Note that resist reflow was done in both of the aforementioned methods (during the first photolithography stage for the former and the second for the latter) to achieve a V-shaped (inclined) sidewall profile. This particular V-shaped sidewall was used to prevent discontinuity of the metal after the top contact metallization step. Additionally, the extension of metal on top of the cured photoresist can be utilized as a contact (measuring pad) to the top of nanocolumns, where the aperture area was defined. This was beneficial to maintain the stability of device performance, since it was not ideal to directly probe the metal on top of nanocolumns, as any external pressure might damage the nanocolumns beneath this layer. Placing a measuring pad away from the aperture minimizes a possible damage caused by the probing pressure, as it then only affects the nanocolumns that are completely isolated/separated from the nanocolumns in the aperture area.

In the thesis work, the photoresist that was subjected to reflow and hard bake process was intended not only to define the aperture and bottom contact area, but also to isolate the top contact metal from the bottom contact metal. This reduced the possibility for the current to leak through an unintended path with no or very low electrical resistance, which could have resulted in a large leakage current flowing through the device (short circuit). In addition, the current could also leak through the self-assembled nanocolumns—particularly if they are randomly coalesced—as well as through the photoresist itself since it is not a perfect insulator. Therefore, Al_xO_y can be employed as a passivation material to further suppress the leakage path, as shown in Figure 4.9. Furthermore, since it is transparent to the UV light it would have negligible impact on the light extraction from the UV LED. For the studies in the thesis, Al_xO_y was deposited at a relatively slow rate to ensure a conformal layer formation across

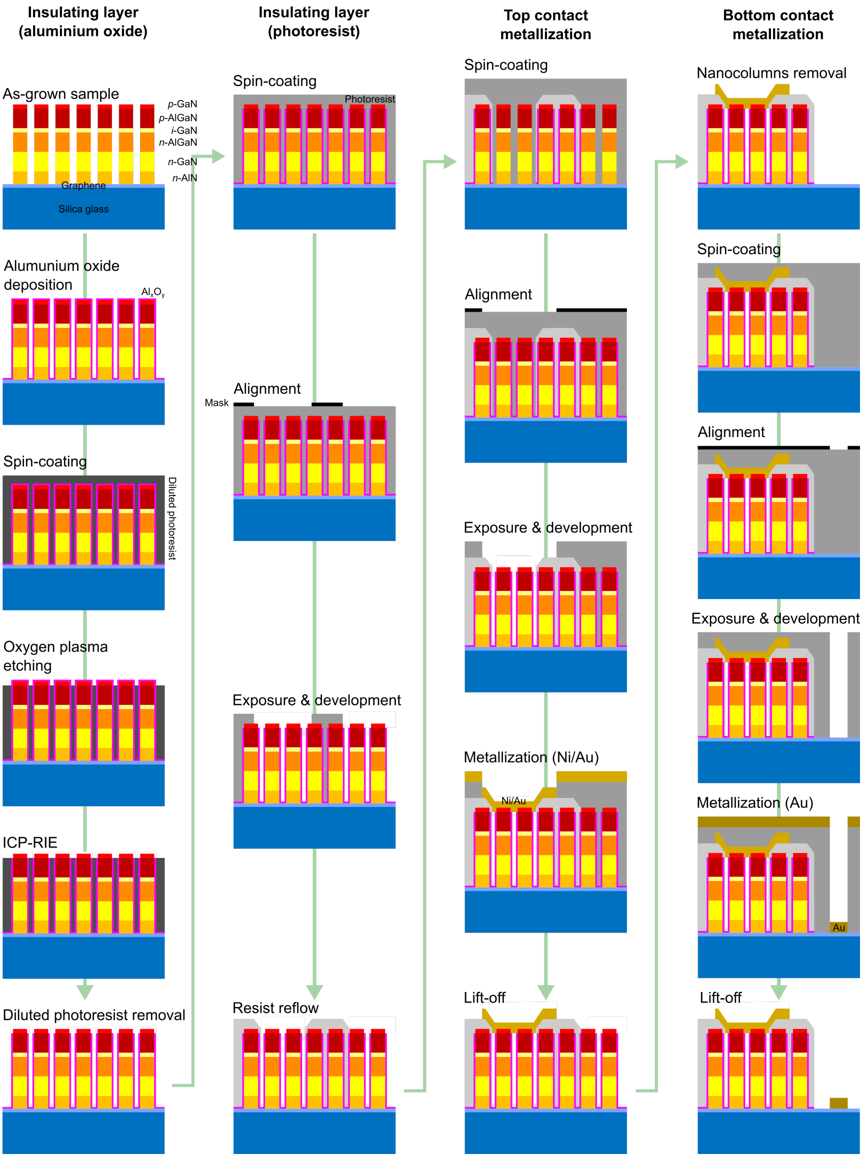

FIGURE 4.9. Schematic diagram of flip-chip nanocolumn-based UV-LED processing flows for the nanocolumn structure whose *p*-GaN segments are separated from each other.

the nanocolumns and graphene surface.

Additionally, the contact annealing step was omitted in both processing approaches because of the presence of photoresist in the final device structure as the insulating layer. Photoresist in general is not suitable to high temperature annealing, due to the creation of bubbles inside the photoresist layer. It is possible as well that the evaporation of photoresist can occur, depending on the resist and temperature. Instead of photoresist and Al_xO_y, a combination of silicon dioxide as an insulating layer and Al_xO_y as a passivation layer is more desirable. This is because such combination allows an annealing process at high temperatures that can improve electrical properties, especially at metal-semiconductor junctions.

The current–voltage (I–V) characteristics of the nanocolumn device structure can be measured by applying a voltage between the metal at the graphene substrate (bottom contact) and the metal at the nanocolumns (top contact). This measurement technique is one of the most common methods for determining the electrical characteristics of optoelectronic devices, which can be further used to extract information such as rectification ratio, series resistance, turn-on voltage, and breakdown voltage. However, one should be aware that excessive applied electric power can lead to Joule heating, which in turn can unintentionally anneal the device during the I–V measurement. Such phenomenon can lead to the degradation of the nanocolumn LED efficiency[37]. Joule heating may have occurred for the device-related work in this PhD thesis.

Furthermore, light emission of the UV-LEDs can be assessed using the electroluminescence measurement technique, which relies on the same principle as the I-V measurement. Applied voltage above the turn-on voltage triggers radiative recombination of injected carriers, which can be measured by a photodetector. The emitted photons have peak wavelength(s) similar to that of the band-to-band recombination observed in photoluminescence. In addition to the electroluminescence spectrum, the EQE of the nanocolumn-based UV-LEDs can also be estimated. Figure 4.10 presents the configuration of the electroluminescence setup (similar to that of the I–V measurement but with light detection capability) for the final UV LED device from each of the previous approaches, as described above. In this arrangement, only nanocolumns within the aperture area contribute to the light generation that is emitted through the graphene/silica glass substrate.

UV-LED processing, I–V, and electroluminescence measurements were made by collaborators at the NTNU NanoLab, I–V Laboratory at the Department of Electronic Systems NTNU, and at CrayoNano AS, respectively.

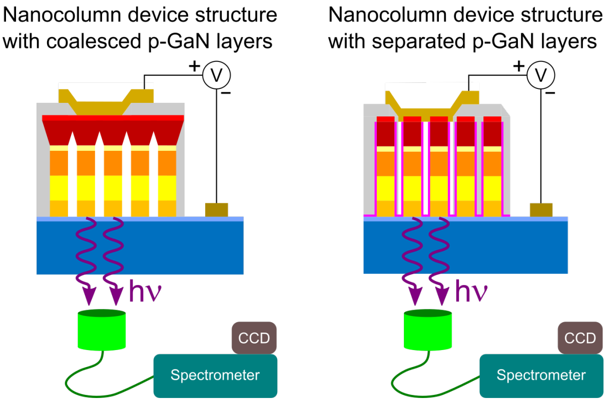

FIGURE 4.10. Sketch for the electroluminescence measurement of the flip-chip UV-LEDs based on nanocolumn structure.

4.8 REFERENCES

[1] T. Al Zoubi. Molecular Beam Epitaxial Growth of III-V Semiconductor Nanostructures on Silicon Substrates. *Doctoral thesis*. University of Kassel (2013). Cited on page/s 85, 87, 88.

[2] K.-Y. Cheng. Molecular beam epitaxy technology of III-V compound semiconductors for optoelectronic applications. *Proceedings of the IEEE* **85** (11), 1694–1714 (1997). Cited on page/s 85.

[3] V. Kumaresan. Novel substrates for growth of III-Nitride materials. *Doctoral thesis*. Universite Pierre et Marie Curie (2016). Cited on page/s 85, 87.

[4] M. Ohring. Chapter 8 - Epitaxy. In Milton Ohring, editor, *Epitaxy, Materials Science of Thin Films (Second Edition)* pages 417–494. Academic Press (2002). Cited on page/s 85.

[5] C. Reichl. MBE growth of ultrahigh-mobility 2DEGs in GaAs/AlGaAs. *Doctoral thesis*. ETH-Zurich (2014). Cited on page/s 85, 86.

[6] D. Laleyan. Molecular Beam Epitaxy of Wide Bandgap Al(Ga)N and h-BN for Deep-Ultraviolet Optoelectronics. *Doctoral thesis*. University of Michigan (2020). Cited on page/s 85.

[7] H. Li. Novel processes for large area gallium nitride single crystal and nanowire growth. *Doctoral thesis*. University of Louisville (2005). Cited on page/s 85.

[8] H. Freller and K.G. Gunther. Three-temperature method as an origin of molecular beam epitaxy. *Thin Solid Films* **88** (4), 291–307 (1982). Cited on page/s 85.

[9] J. R. Arthur. Molecular beam epitaxy. *Surface Science* **500** (1), 189–217 (2002). Cited on page/s 86.

[10] D. Ren. Growth and characterization of self-catalyzed GaAsSb nanowires for optoelectronic applications. *Doctoral thesis*. Norwegian University of Science and Technology (2017). Cited on page/s 86, 87, 96.

[11] L. He, X. Kou, and K. L. Wang. Review of 3D topological insulator thin-film growth by molecular beam epitaxy and potential applications. *Physica Status Solidi (RRL) – Rapid Research Letters* 7 (1-2), 50–63 (2013). Cited on page/s 86.

[12] Y. Ando. Topological Insulator Materials. *Journal of the Physical Society of Japan* **82** (10), 102001 (2013). Cited on page/s 86.

[13] J. M. Wofford, S. Nakhaie, T. Krause, X. Liu, M. Ramsteiner, M. Hanke, H. Riechert, and

J. M. J. Lopes. A hybrid MBE-based growth method for large-area synthesis of stacked hexagonal boron nitride/graphene heterostructures. *Scientific Reports* 7, 43644 (2017). Cited on page/s 86.

[14] F. Presel, H. Tetlow, L. Bignardi, P. Lacovig, C. A. Tache, S. Lizzit, L. Kantorovich, and A. Baraldi. Graphene growth by molecular beam epitaxy: an interplay between desorption, diffusion and intercalation of elemental C species on islands. *Nanoscale* **10**, 7396–7406 (2018). Cited on page/s 86.

[15] M. A. Herman, W. Richter, and H. Sitter. Molecular Beam Epitaxy, in Epitaxy: Physical Principles and Technical Implementation. Springer Series in Materials Science, vol 62. Springer, Berlin, Heidelberg (2004). Cited on page/s 86, 87, 88, 89.

[16] M. A. Herman. Physical problems concerning effusion processes of semiconductors in molecular beam epitaxy. *Vacuum* **32** (9), 555–565 (1982). Cited on page/s 86.

[17] R. K. Debnath. Growth of Undoped and Doped III–Nitride Nanowires and Their Characterization. *Doctoral thesis*. RWTH Aachen (2009). Cited on page/s 87, 103.

[18] M. A. Herman and H. Sitter. Molecular Beam Epitaxy: Fundamentals and Current Status. Springer Series in Materials Science, vol 7. Springer, Berlin, Heidelberg (1996). Cited on page/s 87.

[19] M. Belloeil. Molecular beam epitaxy growth and optical characterization of GaN/AlGaN nanowire heterostructures emitting in the ultraviolet. *Doctoral thesis*. Universite Grenoble Alpes (2017). Cited on page/s 88.

[20] Epiquest Inc. MBE system. Online brochure (2012). Cited on page/s 90.

[21] K. Yamano, K. Kishino, H. Sekiguchi, T. Oto, A. Wakahara, and Y. Kawakami. Novel selective area growth (SAG) method for regularly arranged AlGaN nanocolumns using nanotemplates. *Journal of Crystal Growth* **425**, 316–321 (2015). The 18th International Conference on Molecular Beam Epitaxy (MBE 2014). Cited on page/s 89.

[22] S. Khromov. Doping effects on the structural and optical properties of GaN. *Doctoral thesis*. Linkoping University (2013). Cited on page/s 92.

[23] J. S. Nilsen. Advanced transmission electron microscopy of III-V nanowires. *Doctoral thesis*. Norwegian University of Science and Technology (2020). Cited on page/s 94, 95, 96.

[24] T. Saito. The Effect of Trace Elements on Precipitation in Al-Mg-Si alloys - A Transmission Electron Microscopy Study. *Doctoral thesis*. Norwegian University of Science and Technology (2014). Cited on page/s 94, 95, 96.

[25] D. L. Dheeraj. Growth and structural characterization of III-V nanowires grown by molecular beam epitaxy. *Doctoral thesis*. Norwegian University of Science and Technology (2010). Cited on page/s 96, 100.

[26] T.E. Jenkins. Semiconductor Science: Growth and Characterization Techniques. Prentice Hall (1995). Cited on page/s 98.

[27] L. Geelhaar, *et al.* Properties of GaN Nanowires Grown by Molecular Beam Epitaxy. *IEEE Journal of Selected Topics in Quantum Electronics* **17** (4), 878–888 (2011). Cited on page/s 100, 101.

[28] C. Cheze, *et al.* Direct comparison of catalyst-free and catalyst-induced GaN nanowires. *Nano Research* **3**, 528–536 (2010). Cited on page/s 101.

[29] T. Schmid and P. Dariz. Raman Microspectroscopic Imaging of Binder Remnants in Historical Mortars Reveals Processing Conditions. *Heritage* **2** (2), 1662–1683 (2019). Cited on page/s 103.

[30] J.-J. Zheng and Y.-J. Lin. Tuning the work function of graphene by nitrogen plasma treatment with different radio-frequency powers. *Applied Physics Letters* **104** (23), 233103 (2014). Cited on page/s 104.

[31] S.-O. Guillaume, B. Zheng, J.-C. Charlier, and L. Henrard. Electronic properties and

STM images of doped bilayer graphene. *Physical Review B* **85** (3), 035444 (2012). Cited on page/s 104.

[32] P. Rani and V. K. Jindal. Designing band gap of graphene by B and N dopant atoms. *RSC Advances* **3**, 802–812 (2013). Cited on page/s 104.

[33] M. Wu, C. Cao, and J. Z. Jiang. Light non-metallic atom (B, N, O and F)-doped graphene: a first-principles study. *Nanotechnology* **21** (50), 505202 (2010). Cited on page/s 104.

[34] L. S. Panchakarla, K. S. Subrahmanyam, S. K. Saha, Achutharao Govindaraj, H. R. Krishnamurthy, U. V. Waghmare, and C. N. R. Rao. Synthesis, Structure, and Properties of Boron- and Nitrogen-Doped Graphene. *Advanced Materials* **21** (46), 4726–4730 (2009). Cited on page/s 104.

[35] M. Rybin, A. Pereyaslavtsev, T. Vasilieva, V. Myasnikov, I. Sokolov, A. Pavlova, E. Obraztsova, A. Khomich, V. Ralchenko, and E. Obraztsova. Efficient nitrogen doping of graphene by plasma treatment. *Carbon* **96**, 196–202 (2016). Cited on page/s 104.

[36] A. Gahoi, S. Wagner, A. Bablich, S. Kataria, V. Passi, and M. C. Lemme. Contact resistance study of various metal electrodes with CVD graphene. *Solid-State Electronics* **125**, 234–239 (2016). Extended papers selected from ESSDERC 2015. Cited on page/s 105.

[37] A. A. Efremov, N. I. Bochkareva, R. I. Gorbunov, D. A. Lavrinovich, Yu. T. Rebane, D. V. Tarkhin, and Yu. G. Shreter. Effect of the joule heating on the quantum efficiency and choice of thermal conditions for high-power blue InGaN/GaN LEDs. *Semiconductors* **40**, 605–610 (2006). Cited on page/s 109.

Part II

RESULTS

Chapter 5

Growth study of self-assembled GaN nanocolumns on silica glass by plasma assisted molecular beam epitaxy

Andreas Liudi Mulyo[1,2,a)], Yuta Konno[2], Julie S. Nilsen[3], Antonius T. J. van Helvoort[3], Bjørn-Ove Fimland[1], Helge Weman[1,2], and Katsumi Kishino[2,4]

First published in: *Journal of Crystal Growth* **480**, 67-73 (2017).
DOI: 10.1016/j.jcrysgro.2017.10.009

Contributions

ALM planned the study and performed RF-PAMBE growth under supervision from BOF, HW, and KK. **ALM** conducted SEM and micro-photoluminescence (LT and RT) characterizations. YK assisted **ALM** during the RF-PAMBE experiment, SEM, and micro-photoluminescence measurements. JSN did the HRTEM and HAADF STEM experiments under supervision from ATJvH. **ALM** did all data analysis, drafted the first version of the manuscript, discussed it with other authors, and finalized it.

---

[1] Department of Electronic Systems, Norwegian University of Science and Technology (NTNU), NO-7491, Trondheim, Norway. [2] Department of Engineering and Applied Sciences, Sophia University, 7-1 Kioi-cho, Chiyoda-ku, Tokyo 102-8554, Japan. [3] Department of Physics, Norwegian University of Science and Technology (NTNU), NO-7491 Trondheim, Norway. [4] Sophia Nanotechnology Research Center, Sophia University, 7-1 Kioi-cho, Chiyoda-ku, Tokyo 102-8554, Japan. [a)] e-mail address: andreas.liudi-mulyo@ntnu.no

ABSTRACT

We demonstrate GaN nanocolumn growth on fused silica glass by plasma-assisted molecular beam epitaxy. The effect of the substrate temperature, Ga flux and N_2 flow rate on the structural and optical properties are studied. At optimum growth conditions, GaN nanocolumns are vertically aligned and well separated with an average diameter, height and density of 72 nm, 1.2 μm and 1.6×10^9 cm^{-2}, respectively. The nanocolumns exhibit wurtzite crystal structure with no threading dislocations, stacking faults or twinning and grow in the [0001] direction. At the interface adjacent to the glass, there is a few atom layers thick intermediate phase with *ABC* stacking order (zinc blende). Photoluminescence measurements evidence intense and narrow excitonic emissions, along with the absence of any defect-related zinc blende and yellow luminescence emission.

5.1 INTRODUCTION

Wide band-gap GaN and related ternary III-N semiconductor compounds have been recognized to be among the most important semiconductors for electronic [1,2] and optoelectronic devices [3–5] due to their remarkable optical, electrical and physical properties [1,5]. Nevertheless, the commercialization of GaN-based devices is hampered by the limitation of substrate availability. Si and sapphire (Al_2O_3) have been traditionally employed for the reason of low-cost and good thermal conductivity, despite of having a relatively large lattice- and thermal expansion-mismatch with GaN [6]. This results in a high stacking fault density that affects the efficiency negatively. An alternative could be SiC which offers smaller lattice mismatch for *c*-GaN epitaxy as well as a higher thermal conductivity [6]. However, its poor wetting with GaN, rough surface and high cost [6] inhibit SiC to be fully exploited for GaN-based devices.

The bottom-up growth of nanocolumns (NCs) offers new opportunities to obtain high quality heteroepitaxial material [7–11]. Lattice mismatch is accommodated via the small NC footprint on the substrate, which induces elastic, rather than plastic, strain relaxation at the free surface extending into the NC volume. The generated strain and possible misfit dislocations are confined to the NC/substrate interface and not affecting the bulk of the NC [12]. Thus, the crystal quality of the epitaxial material is nearly independent of the crystalline characteristics of the underlying substrate [13,14]. As a consequence of its large aspect ratio [15–18], possible dislocation lines for NC whose diameter exceeds its critical diameter [7] tend to find its minimum energy by shortening its length in such a way that it bends towards the NC sidewalls instead of propagating vertically along [0001][18]. This explains why the strain relaxation is observed at the lower sidewall facets of NCs[7,19], allowing the upper part of the NC to be free from structural defects[15–18,20]. This merit is exploited in GaN NC growth on various types of substrate material, from crystalline (Si[8,21] and Al_2O_3[8,22,23]), amorphous (SiO_2[24–26], SiN[27], Al_xO_y[28] and TiN[29]) and metal foil (Ti[30,31]). Moreover, high quality GaN NCs have been successfully grown both on multi-layer graphene on SiO_2/Si(100) substrate covered with a thin AlN buffer layer by molecular beam epitaxy (MBE)[32] and directly on single-layer graphene using metal-organic vapor phase epitaxy (MOVPE)[33].

Fused silica glass is an attractive substrate, not only because it is cheap but it also has an excellent optical transparency in the visible and ultraviolet wavelength region[34]. GaN growth on fused silica was demonstrated by Iwata *et al.*[35] already in 1997, but the GaN layers were highly polycrystalline in nature[36]. Despite this, the optical properties showed a favorable indication for the fabrication of large area and low-cost light emitting diodes (LEDs) and solar cells[35–38]. Subsequently, there have been several works investigating morphologies and photoluminescence properties of GaN grown on non-single crystalline or amorphous substrates by either MBE or MOVPE[39–41]. Moreover, fabrication of GaN-based optoelectronic devices[42] exploiting such substrates have been realized with promising performances. Recently, high density and vertically aligned single crystal GaN NCs on fused silica have been demonstrated[13]. To further optimize and utilize this result, it is important to have a detailed understanding on the effect of various growth conditions, in order to optimize the crystalline quality of the GaN NCs and achieve high internal quantum efficiency, which are essential to enhance device efficiency.

This paper presents a growth study of self-assembled GaN NCs on fused silica by plasma-assisted molecular beam epitaxy (PA-MBE). Substrate temperature (T_{sub}), Ga flux (Φ_{Ga}) and N_2 flow rate (Q_N) are varied in order to study their influence upon the structural and optical characteristics of the GaN NCs. The grown GaN NCs are studied using scanning electron microscopy (SEM) and room-temperature (RT) micro-photoluminescence (μ-PL) spectroscopy. Furthermore, the optimized growth of GaN NCs is investigated with lattice-imaging (scanning) transmission electron microscopy (HRTEM and HRSTEM) and μ-PL spectroscopy at 77 K (77 K μ-PL).

5.2 EXPERIMENTS

The GaN NCs were grown on 2” fused silica wafers from Semiwafer (thickness of 0.5 mm with a purity of 99.999 %) using PA-MBE under N-rich conditions.

Standard Knudsen effusion cells were used to supply Ga and Si atoms, while atomic nitrogen was generated from a radio-frequency plasma source operating at 450 W. A 300 nm thick Ti film was evaporated on the backside of the fused silica wafer to ensure a uniform and efficient heat transfer from the heater to the substrate as well as assist pyrometer reading. Prior to loading to the growth chamber, the substrate was thermally cleaned at 350 °C for 1 hour in a preparation chamber. Catalyst-free, self-assembled GaN NCs were then grown directly on fused silica, without deliberately forming any intermediate buffer layer. The growth process was initiated by opening the Ga and N_2 shutters simultaneously, i.e. no intentional nitridation took place on the surface of the substrate prior to NC growth. The GaN NCs were n-type doped with Si using a cell temperature of 1050 °C and a growth time of 90 minutes, identical for all growth series. Si doping has been reported to improve the optical properties of GaN layers[43] based on the capability of Si to decrease dislocation density[44]. Its solubility in GaN films is high, of the order of 10^{20} cm^{-3}, and free carrier concentrations in the range from 10^{17} to 2×10^{19} cm^{-3} have been reported[45]. Table 5.1 lists the growth conditions of each sample grown for this study.

TABLE 5.1. GaN nanocolumn growth conditions for the different samples used in this study.

Sample ID	FS001	FS002	FS003	FS004	FS006	FS007	FS008
T_{sub} (°C)	730	750	760	760	760	760	760
Φ_{Ga} (Pa)	3.0×10^{-4}	3.0×10^{-4}	3.0×10^{-4}	2.0×10^{-4}	2.5×10^{-4}	2.5×10^{-4}	2.5×10^{-4}
Q_N (sccm)	2.75	2.75	2.75	2.75	2.75	2.00	1.50

The structure of the as-grown samples (i.e. without a thin metal coating to reduce charging effects from a high resistivity of the fused silica substrate) was evaluated using a SMI3050SE SEM operating at 15 kV. The optical properties were assessed with RT and 77 K μ-PL using a HeCd laser (325 nm) as excitation source. A commercial GaN bulk substrate grown by hydride vapor phase epitaxy is set as a benchmark reference (HVPE-GaN) of the optical quality, like for previous studies on NC growth on different substrates[15,32]. To verify the crystalline quality of the optimized GaN NCs, different TEM imaging methods (selective area diffraction (SAED), HRTEM, high-angle annular dark field scanning TEM (HAADF STEM)) using a field emission JEOL-2100F and JEOL JEM-ARM200F, both operating at 200 kV, have been used. The TEM specimen was made by a lift-out method utilizing a focused ion beam (FIB). Prior to FIB, the NCs were coated with Au in order to avoid electron charging during the FIB specimen preparation. The TEM lamella was not coated for the TEM analysis.

5.3 Results and Discussion

A summary of the grown GaN NC diameter and density for samples FS001 to FS008 is shown in Figure 5.1. The alteration in NC morphology, diameter and density for each sample corresponds to the given growth conditions as described in Table 5.1.

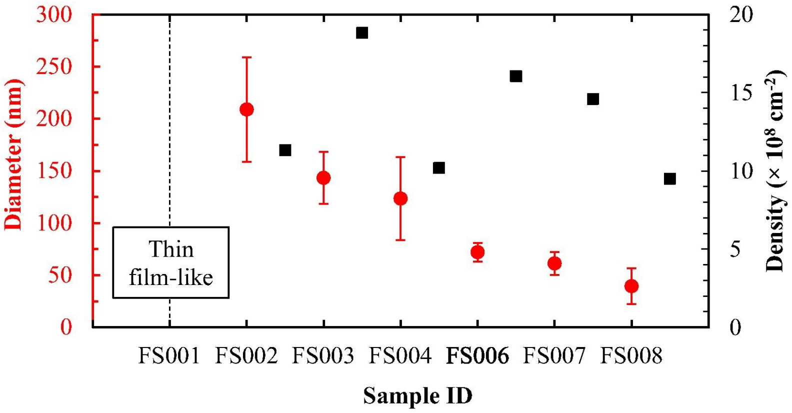

Figure 5.1. Diameter (red dots) and density (black squares) of the grown GaN NCs on samples FS001 to FS004 and FS006 to FS008.

SEM images of the GaN NCs grown at different T_{sub} are presented in Figure 5.2. At 730 °C (sample FS001), the GaN growth resembles a thin film, although it does not cover the whole surface. When T_{sub} is increased to 750 °C (sample FS002), the coalescence is reduced, giving a good indication of further NC isolation. For the sample grown at 760 °C (sample FS003), the formation of NCs becomes clearly visible. Accordingly, the NC density in sample FS003 is increased as its average diameter is decreased relative to sample FS002 (Figure 5.1). Higher T_{sub} increases significantly the likelihood of Ga desorption and GaN decomposition[46]. At the same time, Ga diffusion length is enhanced, which becomes a driving factor for the Ga atoms to have a higher probability in reaching the top of the NC c-plane[47]. The V/III ratio should thus play an important role for the columnar morphology[46].

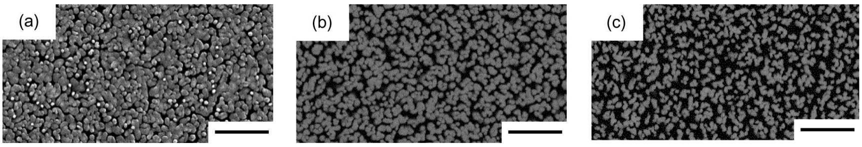

Figure 5.2. Top view SEM images of GaN NC growth at different T_{sub} ((**a**) 730 °C (FS001), (**b**) 750 °C (FS002) and (**c**) 760 °C (FS003)). Φ_{Ga} and Q_N are fixed to 3.0×10^{-4} Pa and 2.75 sccm, respectively. All scale bars are 1 μm.

The dependence of the GaN columnar morphology on Φ_{Ga}, is shown in Figure 5.3. We expect that growth at a reduced Ga supply, especially at a very high T_{sub}, leads to a limited amount of Ga availability on the surface, restricting GaN formation and eventually suppressing the degree of NC coalescence. The growth using Φ_{Ga} of 3.0×10^{-4} Pa is seen to result in coalescence between NCs (sample FS003), whereas the columnar structure becomes more apparent when Φ_{Ga} is reduced to a lower flux. The average diameter has decreased to 72 nm while the density is lowered to 1.6×10^{9} cm^{-2} (Figure 5.1) at Φ_{Ga} of 2.5×10^{-4} Pa (sample FS006). However, larger and more diverse NC diameters (80-160 nm, see Figure 5.1) are observed when Φ_{Ga} is lowered to 2.0×10^{-4} Pa (sample FS004). Further investigation is needed to verify this phenomenon and provide a plausible explanation regarding the inconsistency found for a low Φ_{Ga}.

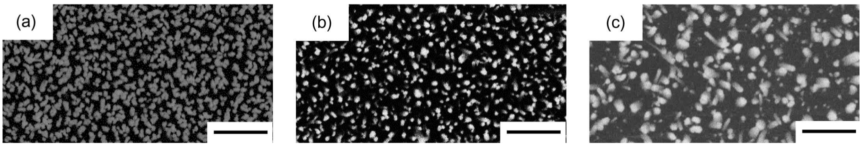

FIGURE 5.3. Top view SEM images of GaN NC growth at different Φ_{Ga} ((**a**) 3.0×10^{-4} Pa (FS003), (**b**) 2.5×10^{-4} Pa (FS006) and (**c**) 2.0×10^{-4} Pa (FS004)). T_{sub} and Q_N, are fixed to 760 °C and 2.75 sccm, respectively. All scale bars are 1 μm.

To investigate the effect of N atoms in contributing to the NCs growth, Q_N is varied and the SEM results are presented in Figure 5.4. In general, a columnar structure can be obtained using Q_N ranging from 1.50 to 2.75 sccm. The electron charging effect due to the high electrical resistivity of fused silica becomes evident in SEM on the sample grown with the lowest Q_N (sample FS008) when it is observed in bird view. This is due to that this sample has a relatively low density of NCs and that the SEM detector in this imaging angle receives information mostly from the charging substrate surface.

It is noticeable from Figure 5.4(a-f) that both the NC density and diameter are reduced with a lower Q_N, implying that Ga desorption is enhanced. There is also a significant variation of the NC height, where the highest NCs are found on FS006 (1220 ± 35 nm), followed by FS007 (870 ± 70 nm) and FS008 (540 ± 100 nm). The radial and axial growth rates are reduced with a lower Q_N, resulting in shorter and thinner NCs. In addition, the distance between NCs become larger, hence the number density is decreased (Figure 5.4(c)-(d), (e)-(f) and Figure 5.1). Compared to FS006, a larger variation in length and diameter (Figure 5.1) is observed for FS007 and FS008 (NCs grown at lower Q_N, Figure 5.4(d), (f)). This indicates that individual GaN NCs experience different nucleation times, similar to what is reported by Wolz *et al.*[29] for GaN NC growth on metallic TiN films. When Q_N is 2.75 sccm, a finer NC structure is

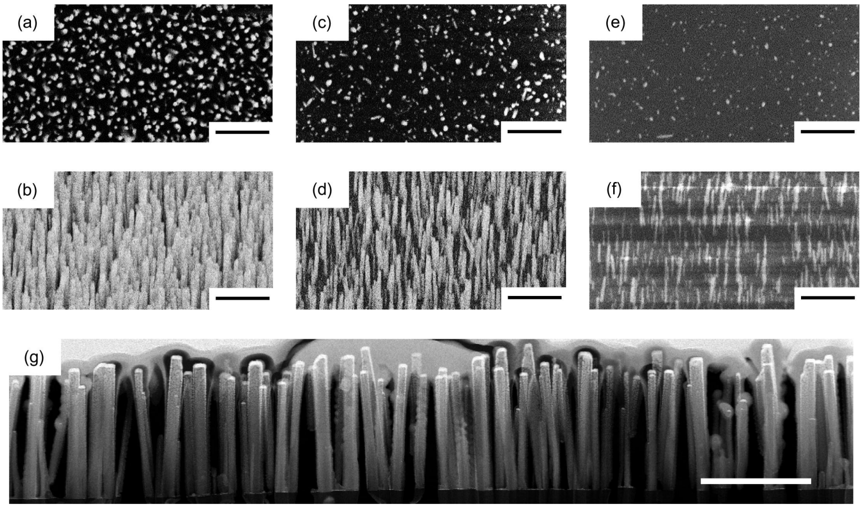

FIGURE 5.4. SEM images (top and bird view at top and middle row, respectively) of GaN NC growth with different Q_N ((**a**, **b**) 2.75 sccm (FS006), (**c**, **d**) 2.00 sccm (FS007) and (**e**, **f**) 1.50 sccm (FS008)). T_{sub} and Φ_{Ga} are fixed to 760 °C and 2.5×10^{-4} Pa, respectively. (**g**) A HAADF STEM overview image of FS006 (a, b). All scale bars are 1 μm.

obtained, confirmed by the uniformity of the NC diameter, density and height (Figure 5.4(a), (b)), implying that the NCs nucleate at an early stage, almost simultaneously. A comprehensive nucleation study is beyond the scope of this work and will be reported elsewhere. A cross-sectional HAADF STEM image of FS006 shows that the ensemble of NCs grow near perpendicular to the fused silica substrate, where each NC has a flat top facet and smooth sidewalls (Figure 5.4(g)).

An overview of the optical quality of all samples is given in Figure 5.5. Overall, the RT μ-PL measured in the range from 340 to 580 nm displays a single emission peak at 364 nm in all samples, due to the wurtzite GaN free exciton emission.

As shown in Figure 5.5, the PL peak intensity of the first four samples (FS001-FS004) are below that of the HVPE-GaN reference sample. However, the PL intensity increases gradually with higher sample ID number, which can be reasoned from that higher T_{sub} (for FS001-FS003, see Table 5.1) aids in effectively decreasing the stacking fault density[48] (coalesced NCs are minimized[20]). A higher light extraction efficiency (LEE) is demonstrated through non-coalescence NC structure by sample FS004 upon reducing Φ_{Ga}. In addition, it has a full width at half maximum (FWHM) of 67.4 meV, which is much narrower than for samples FS001 to FS003 (Figure 5.5). A significant improvement is found in sample FS006, where the PL peak intensity is at least

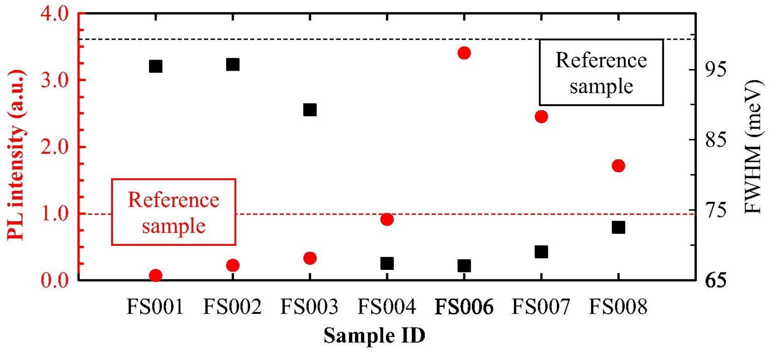

FIGURE 5.5. RT μ-PL maximum peak intensity (red dots) and FWHM (black squares) of grown GaN NCs. The PL peak emission at 364 nm has been normalized to the peak intensity from the HVPE-GaN reference sample. The PL intensity and FWHM of the HVPE-GaN reference sample are indicated by the dashed red and black lines, respectively.

three times higher than for the HVPE-GaN reference sample, demonstrating a similar quality as reported for self-organized GaN NCs on graphene[32]. In addition, it has the lowest FWHM (67 meV) of all samples in this study (Figure 5.5). The PL intensity is further reduced when the Q_N is decreased to 2.00 and 1.50 sccm in sample FS007 and FS008, respectively. The grown NCs in sample FS007 and FS008 are observed to have a larger diameter and height dispersion, as well as lower density compared with FS006 (Figure 5.1 and Figure 5.4(a)-(f)). We expect that these factors are the main reasons for the lower LEE in FS007 and FS008[15]. From structural and optical evaluations, it can thus be deduced that sample FS006 has the highest quality among all grown NCs on fused silica, and its quality is on par with the GaN NCs on different substrates[15,32]. Further detailed examinations by TEM, RT and 77 K μ-PL on this sample are presented below.

The crystallinity of NC and its interface with the fused silica substrate is unveiled by HRTEM, as shown in Figure 5.6(a). The SAED image (inset in Figure 5.6(a)) shows that the NC has a wurtzite crystal structure and the growth direction is [0001]. Even though fused silica is a non-crystalline material, the grown NC is vertical and consistently demonstrates a single crystalline structure with well-defined atomic planes. A darker irregular layer is clearly seen at the interface. This suggests the formation of a thin interfacial layer with a thickness of about 0-4 atomic layers. By aberration corrected HAADF STEM (lower inset in Figure 5.6(b)), the atom columns in the interfacial layer seems less bright compared to the rest of the NC. Assuming an equal specimen thickness, which is reasonable for a FIB specimen, this indicates that this layer has a lower average atomic number, which could indicate that it is Si_xN_y rather than GaN. Due to charging effects, energy-dispersive X-ray spectroscopy could

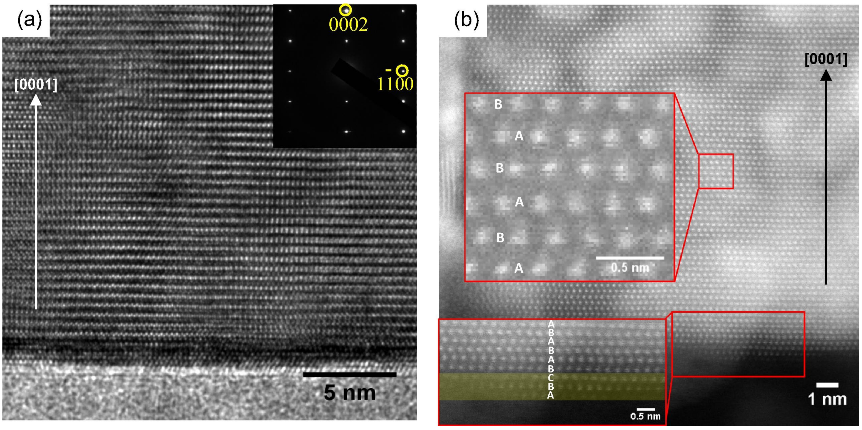

FIGURE 5.6. (**a**) HRTEM and SAED (inset) of a GaN NC (from sample FS006) including its interface with the fused silica substrate, showing a thin interfacial layer (dark contrast). (**b**) Aberration corrected HAADF STEM image of the GaN NC (upper inset: crystal stacking order of wurtzite, lower inset: interface layer).

not be performed to confirm the composition of this layer.

In addition, the fact that Si-N (4.5 eV) has a higher bonding energy compared to Ga-N (2.2 eV), favors SiN rather than GaN as the origin of the interface layer[24]. The layer has a zinc blende crystal structure (*ABC* stacking order, lower inset in Figure 5.6(b)) observed in this interface region. The crystalline interfacial layer with an *ABC* stacking might therefore be Si_xN_y. Due the small and varying layer thickness, i.e. between 0-4 atomic layers, analyzing this layer becomes more challenging. Albeit being inconclusive regarding the exact composition, the variation in stacking order is a clear indication of another phase at the interface. To further study this interfacial layer would require a solution for the charging problem to allow a dedicated advanced TEM study. The stacking otherwise reveals an *ABAB* order (upper inset in Figure 5.6(b)), an evidence of wurtzite crystal structure excluding structural defects, such as threading dislocations and stacking faults. These results serve as a clear evidence of the high structural quality of the GaN NC under investigation (sample FS006), despite it is grown on an amorphous substrate. These results demonstrate the superiority of GaN NC crystal quality over a thin film structure[35,49].

This interfacial layer is generally observed in the grown GaN NCs on Si, both intentionally[27,50,51] and unintentionally grown[14,47,52–54]. However, these reported studies (except[53] which used reflection high energy-electron diffraction and *in situ* grazing incidence X-ray diffraction) on cross-sectional lattice imaging were done solely by HRTEM, making stacking order interpretation of a thin (i.e. a few atomic layers thick) interfacial layer difficult[55], and they did not further discuss the stacking order.

RT μ-PL measurements in the range from 340 to 580 nm of a HVPE-GaN reference sample (black line) and an ensemble GaN NCs (sample FS006, red line) are presented in Figure 5.7(a). Both samples exhibit band edge emission from the GaN wurtzite crystal phase at 364 nm, with a small additional shoulder (grey arrow) observed in the HVPE-GaN reference sample. The NC structure (red line) has an intensity of 3.3 times higher compared to the thin film reference (black line). Zinc blende GaN-related emission, typically occurring at 386 nm [56], is not observed. In addition, the HVPE-GaN reference sample clearly shows PL corresponding to broad yellow luminescence (YL) emission (see insets of Figure 5.7(a)). This infamous broad luminescence in GaN could be caused by the deep acceptor level introduced by the Ga vacancy [57–59] or C substituting Ga (C_{Ga}) [57,60] or C substituting N (C_N) - related defects [60–62]. This type of YL emission is absent in the GaN NCs, indicating that a higher crystalline quality of GaN is obtained in the NC structure.

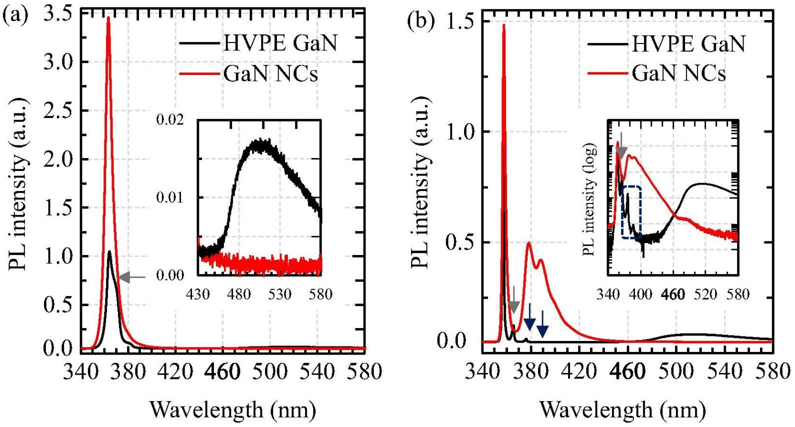

FIGURE 5.7. PL spectra of a HVPE-GaN reference sample (black line) and an ensemble of GaN NCs (sample FS006, red line) measured at (**a**) RT (inset: linear scale in the range from 430 to 580 nm) and (**b**) 77 K (inset: logarithmic scale). In HVPE GaN: grey arrow indicates exciton bound to structural defects [63] and blue arrow (inset: blue dashed box) marks donor acceptor pair recombinations.

Finally, the HVPE-GaN reference sample and sample FS006 were subject to 77 K μ-PL measurements, and the results are shown in Figure Figure 5.7(b). The NC sample demonstrates a strong band edge emission from the GaN wurtzite crystal observed at 357 nm. In addition, the emission peak at 378 nm (3.28 eV) comes from donor-acceptor pairs (DAP) recombinations, while the weaker peak at 388 nm (3.19 eV) is 1-longitudinal optical (LO) phonon replica [64–66]. The DAP recombinations can be observed despite only Si (donor) atoms were used as dopant and probably involve acceptor levels related to carbon impurities, specifically C_N [67].

That GaN material with columnar structure is marked by a prominent intensity of DAP luminescence and their 1-LO phonon replica, as compared to the HVPE GaN reference sample (marked by blue arrows in Figure 5.7(b), might be explained by the presence of unintentional C atoms in the chamber, enforcing incorporation of C into the N sublattice during growth. On the other hand, the halide vapor precursor of the HVPE technique is known to give high purity materials without carbon contamination[68]. Secondary ion mass spectroscopy (SIMS) measurement reveals that in the case of another GaN NC sample, C atoms are present in the n-GaN NCs part at a concentration level of ca. one order of magnitude lower than Si, i.e. 10^{16} C atoms/cm^3 and 10^{17} Si atoms/cm^3. Quantitative SIMS analysis on sample FS006 in particular can be suggested as further research topic. Nevertheless, although the concentration level of unintentional C atoms is relatively high, defects which might originate from C_{Ga}[57,60] or C_N[60–62] are effectively quenched, confirmed from the lacking of YL emission in the GaN with NC structure.

Furthermore, there is a weak PL peak at 365 nm in the HVPE-GaN reference sample (grey arrow) which transforms into a PL shoulder around 369 nm in the RT μ-PL spectrum. This peak is affiliated with an exciton bound to structural defects[63]. The absence of any zinc blende GaN band-edge and YL emission[69] are evidence of the exceptionally high crystal quality of the GaN NCs in sample FS006.

5.4 CONCLUSIONS

The morphology and optical quality of GaN NC structures grown on fused silica glass substrates using PA-MBE have been systematically studied as a function of substrate temperature, Ga flux and N_2 flow rate. Each growth condition gives rise to distinct effects towards the columnar structure. Under optimized conditions, a high density of vertically aligned self-assembled GaN NCs are successfully grown on fused silica without the aid from any external catalyst. TEM confirms a high-quality wurtzite crystal structure with the absence of threading dislocations, stacking faults and twinning defects. A layer with a zinc blende structure/stacking, probably Si_xN_y, and a thickness of a few atomic layers is formed at the interface to the glass. Both RT and 77 K μ-PL measurements show a sharp and intense GaN excitonic emission from an ensemble of NCs with the absence of any deep level related emissions, indicating a very high crystal quality of the free-standing GaN NCs grown on fused silica. These results could facilitate further development of an economical route towards the fabrication of efficient III-nitride NC-based LED devices.

5.5 ACKNOWLEDGEMENTS

We acknowledge T. Oto, I. Matsuyama and Y. Nakagawa for their fruitful discussions on the 77 K μ-PL data. This work was supported by the FRINATEK (Grant No. 214235) and NANO2021 (Grant No. 239206) programs of the Research Council of Norway and by Japan Society for the Promotion of Science KAKENHI (Grant No. 24000013). The Research Council of Norway is also acknowledged for the support to NTNU NanoLab through the Norwegian Micro- and Nano-Fabrication Facility, NorFab (Grant no. 197411), the NORTEM facility (Grant no. 197405), and the Norwegian PhD Network on Nanotechnology for Microsystems (FORSKERSKOLER-221860/F40).

5.6 REFERENCES

[1] X. Liu, *et al.* AlGaN/GaN Metal-Oxide-Semiconductor High-Electron-Mobility Transistor with Polarized P(VDF-TrFE) Ferroelectric Polymer Gating. *Scientific Reports* **5**, 14092 (2015). Cited on page/s 116.

[2] S. J. Pearton and F. Ren. GaN Electronics. *Advanced Materials* **12** (21), 1571–1580 (2000). Cited on page/s 116.

[3] A. Muller, G. Konstantinidis, M. Dragoman, D. Neculoiu, A. Kostopoulos, M. Androulidaki, M. Kayambaki, and D. Vasilache. GaN membrane metal-semiconductor-metal ultraviolet photodetector. *Applied Optics* **47** (10), 1453–1456 (2008). Cited on page/s 116.

[4] S. Nakamura, *et al.* Continuous-wave operation of InGaN/GaN/AlGaN-based laser diodes grown on GaN substrates. *Applied Physics Letters* **72** (16), 2014–2016 (1998). Cited on page/s 116.

[5] S. Nakamura, T. Mukai, and M. Senoh. Candela-class high-brightness InGaN/AlGaN double-heterostructure blue-light-emitting diodes. *Applied Physics Letters* **64** (13), 1687–1689 (1994). Cited on page/s 116.

[6] L. Liu and J. H. Edgar. Substrates for gallium nitride epitaxy. *Materials Science and Engineering: R: Reports* **37** (3), 61–127 (2002). Cited on page/s 116.

[7] F. Glas. Critical dimensions for the plastic relaxation of strained axial heterostructures in free-standing nanowires. *Physical Review B* **74** (12), 121302 (2006). Cited on page/s 116, 117.

[8] K. Kishino, A. Kikuchi, H. Sekiguchi, and S. Ishizawa. InGaN/GaN nanocolumn LEDs emitting from blue to red. In *Proc. SPIE 6473, Gallium Nitride Materials and Devices II* volume 6473 pages 64730T–1. SPIE (2007). Cited on page/s 116, 117.

[9] D. L. Dheeraj, G. Patriarche, H. Zhou, T. B. Hoang, A. F. Moses, S. Gronsberg, A. T. J. van Helvoort, B.-O Fimland, and H. Weman. Growth and Characterization of Wurtzite GaAs Nanowires with Defect-Free Zinc Blende GaAsSb Inserts. *Nano Letters* **8** (12), 4459–4463 (2008). Cited on page/s 116.

[10] D. L. Dheeraj, G. Patriarche, H. Zhou, J. C. Harmand, H. Weman, and B. O. Fimland. Growth and structural characterization of GaAs/GaAsSb axial heterostructured nanowires. *Journal of Crystal Growth* **311** (7), 1847–1850 (2009). Cited on page/s 116.

[11] A. M. Munshi, D. L. Dheeraj, J. Todorovic, A. T. J. van Helvoort, H. Weman, and B.-O. Fimland. Crystal phase engineering in self-catalyzed GaAs and GaAs/GaAsSb nanowires

grown on Si(111). *Journal of Crystal Growth* **372** (Supplement C), 163–169 (2013). Cited on page/s 116.

[12] K. Tomioka, J. Motohisa, S. Hara, and T. Fukui. Control of InAs Nanowire Growth Directions on Si. *Nano Letters* **8** (10), 3475–3480 (2008). Cited on page/s 116.

[13] V. Kumaresan, L. Largeau, F. Oehler, H. Zhang, O. Mauguin, F. Glas, N. Gogneau, M. Tchernycheva, and J.-C. Harmand. Self-induced growth of vertical GaN nanowires on silica. *Nanotechnology* **27** (13), 135602 (2016). Cited on page/s 116, 117.

[14] L. Cerutti, J. Ristic, S. Fernandez-Garrido, E. Calleja, A. Trampert, K. H. Ploog, S. Lazic, and J. M. Calleja. Wurtzite GaN nanocolumns grown on Si(001) by molecular beam epitaxy. *Applied Physics Letters* **88** (21), 213114 (2006). Cited on page/s 116, 123.

[15] K. Kishino and S. Ishizawa. Selective-area growth of GaN nanocolumns on Si(111) substrates for application to nanocolumn emitters with systematic analysis of dislocation filtering effect of nanocolumns. *Nanotechnology* **26** (22), 225602 (2015). Cited on page/s 116, 117, 118, 122.

[16] R. Colby, Z. Liang, I. H. Wildeson, D. A. Ewoldt, T. D. Sands, R. E. García, and E. A. Stach. Dislocation Filtering in GaN Nanostructures. *Nano Letters* **10** (5), 1568–1573 (2010). Cited on page/s 116, 117.

[17] H. Sekiguchi, K. Kishino, and A. Kikuchi. Formation of InGaN quantum dots in regularly arranged GaN nanocolumns grown by rf-plasma-assisted molecular-beam epitaxy. *Physica Status Solidi C - Current Topics in Solid State Physics* **7** (10), 2374–2377 (2010). Cited on page/s 116, 117.

[18] S. D. Hersee, A. K. Rishinaramangalam, M. N. Fairchild, L. Zhang, and P. Varangis. Threading defect elimination in GaN nanowires. *Journal of Materials Research* **26** (17), 2293–2298 (2011). Cited on page/s 116, 117.

[19] X. Zhang, V. G. Dubrovskii, N. V. Sibirev, and X. Ren. Analytical Study of Elastic Relaxation and Plastic Deformation in Nanostructures on Lattice Mismatched Substrates. *Crystal Growth & Design* **11** (12), 5441–5448 (2011). Cited on page/s 117.

[20] V. Consonni, M. Knelangen, U. Jahn, A. Trampert, L. Geelhaar, and H. Riechert. Effects of nanowire coalescence on their structural and optical properties on a local scale. *Applied Physics Letters* **95** (24), 241910 (2009). Cited on page/s 117, 121.

[21] M. Sobanska, A. Wierzbicka, K. Klosek, J. Borysiuk, G. Tchutchulashvili, S. Gieraltowska, and Z.R. Zytkiewicz. Arrangement of GaN nanowires grown by plasma-assisted molecular beam epitaxy on silicon substrates with amorphous Al2O3 buffers. *Journal of Crystal Growth* **401**, 657–660 (2014). Proceedings of 17th International Conference on Crystal Growth and Epitaxy (ICCGE-17). Cited on page/s 117.

[22] M. Yoshizawa, A. Kikuchi, M. Mori, N. Fujita, and K. Kishino. Growth of Self-Organized GaN Nanostructures on Al_2O_3(0001) by RF-Radical Source Molecular Beam Epitaxy. *Japanese Journal of Applied Physics* **36** (Part 2, No. 4B), L459–L462 (1997). Cited on page/s 117.

[23] M. Yoshizawa, A. Kikuchi, N. Fujita, K. Kushi, H. Sasamoto, and K. Kishino. Self-organization of GaN/$Al_{0.18}Ga_{0.82}N$ multi-layer nano-columns on (0001) Al_2O_3 by RF molecular beam epitaxy for fabricating GaN quantum disks. *Journal of Crystal Growth* **189-190**, 138–141 (1998). Cited on page/s 117.

[24] T. Stoica, E. Sutter, R. J. Meijers, R. K. Debnath, R. Calarco, H. Luth, and D. Grutzmacher. Interface and Wetting Layer Effect on the Catalyst-Free Nucleation and Growth of GaN Nanowires. *Small* **4** (6), 751–754 (2008). Cited on page/s 117, 123.

[25] S. Zhao, M. G. Kibria, Q. Wang, H. P. T. Nguyen, and Z. Mi. Growth of large-scale vertically aligned GaN nanowires and their heterostructures with high uniformity on SiO_x by catalyst-free molecular beam epitaxy. *Nanoscale* **5**, 5283–5287 (2013). Cited on page/s 117.

[26] Y. Park, S. Jahangir, Y. Park, P. Bhattacharya, and J. Heo. InGaN/GaN nanowires grown

on SiO2 and light emitting diodes with low turn on voltages. *Optics Express* **23** (11), A650–A656 (2015). Cited on page/s 117.

[27] V. Consonni, M. Hanke, M. Knelangen, L. Geelhaar, A. Trampert, and H. Riechert. Nucleation mechanisms of self-induced GaN nanowires grown on an amorphous interlayer. *Physical Review B* **83** (3), 035310 (2011). Cited on page/s 117, 123.

[28] M. Sobanska, S. Fernandez-Garrido, Z. R. Zytkiewicz, G. Tchutchulashvili, S. Gieraltowska, O. Brandt, and L. Geelhaar. Self-assembled growth of GaN nanowires on amorphous AlxOy: from nucleation to the formation of dense nanowire ensembles. *Nanotechnology* **27** (32), 325601 (2016). Cited on page/s 117.

[29] M. Wolz, C. Hauswald, T. Flissikowski, T. Gotschke, S. Fernandez-Garrido, O. Brandt, H. T. Grahn, L. Geelhaar, and H. Riechert. Epitaxial Growth of GaN Nanowires with High Structural Perfection on a Metallic TiN Film. *Nano Letters* **15** (6), 3743–3747 (2015). Cited on page/s 117, 120.

[30] G. Calabrese, P. Corfdir, G. Gao, C. Pfuller, A. Trampert, O. Brandt, L. Geelhaar, and S. Fernandez-Garrido. Molecular beam epitaxy of single crystalline GaN nanowires on a flexible Ti foil. *Applied Physics Letters* **108** (20), 202101 (2016). Cited on page/s 117.

[31] B. J. May, A. T. M. G. Sarwar, and R. C. Myers. Nanowire LEDs grown directly on flexible metal foil. *Applied Physics Letters* **108** (14), 141103 (2016). Cited on page/s 117.

[32] H. Hayashi, Y. Konno, and K. Kishino. Self-organization of dislocation-free, high-density, vertically aligned GaN nanocolumns involving InGaN quantum wells on graphene/SiO_2 covered with a thin AlN buffer layer. *Nanotechnology* **27** (5), 055302 (2015). Cited on page/s 117, 118, 122.

[33] M. Heilmann, *et al.* Vertically Oriented Growth of GaN Nanorods on Si Using Graphene as an Atomically Thin Buffer Layer. *Nano Letters* **16** (6), 3524–3532 (2016). Cited on page/s 117.

[34] Y. Zhao, X. Li, W. Wang, B. Zhou, H. Duan, T. Shi, X. Zeng, L. Ning, and Y. Wang. Growth and properties of GaAs nanowires on fused quartz substrate. *Journal of Semiconductors* **35** (9), 093002 (2014). Cited on page/s 117.

[35] K. Iwata, H. Asahi, K. Asami, R. Kuroiwa, and S.-I. Gonda. Gas Source Molecular Beam Epitaxy Growth of GaN on C-, A-, R- and M-Plane Sapphire and Silica Glass Substrates. *Japanese Journal of Applied Physics* **36** (6A), L661 (1997). Cited on page/s 117, 123.

[36] K. Iwata, H. Asahi, K. Asami, A. Ishida, R. Kuroiwa, H. Tampo, S. Gonda, and S. Chichibu. Promising characteristics of GaN layers grown on amorphous silica substrates by gas-source MBE. *Journal of Crystal Growth* **189–190**, 218–222 (1998). Cited on page/s 117.

[37] H. Asahi, K. Iwata, H. Tampo, R. Kuroiwa, M. Hiroki, K. Asami, S. Nakamura, and S. Gonda. Very strong photoluminescence emission from GaN grown on amorphous silica substrate by gas source MBE. *Journal of Crystal Growth* **201-202**, 371–375 (1999). Cited on page/s 117.

[38] K. Iwata, H. Asahi, K. Asami, R. Kuroiwa, and S. Gonda. Strong photoluminescence emission from GaN grown on amorphous silica substrates by gas source MBE. *Journal of Crystal Growth* **188** (1–4), 98–102 (1998). Cited on page/s 117.

[39] Y. Sato, A. Fujiwara, S. Ishizaki, S. Nakane, and Y. Murakami. Morphologies and photoluminescence properties of GaN-based thin films grown on non-single-crystalline substrates. *Physica Status Solidi C - Current Topics in Solid State Physics* **14** (1-2), 1600151 (2017). Cited on page/s 117.

[40] S.-Y. Bae, *et al.* III-nitride core–shell nanorod array on quartz substrates. *Scientific Reports* 7, 45345 (2017). Cited on page/s 117.

[41] J. H. Choi, *et al.* Heteroepitaxial Growth of GaN on Unconventional Templates and Layer-Transfer Techniques for Large-Area, Flexible/Stretchable Light-Emitting Diodes. *Advanced Optical Materials* **4** (4), 505–521 (2016). Cited on page/s 117.

[42] D. P. Bour, N. M. Nickel, C. G. Van de Walle, M. S. Kneissl, B. S. Krusor, Ping Mei, and N. M. Johnson. Polycrystalline nitride semiconductor light-emitting diodes fabricated on quartz substrates. *Applied Physics Letters* **76** (16), 2182–2184 (2000). Cited on page/s 117.

[43] H. Peter, M. Atsuyoshi, K. Norikatsu, H. Kazumasa, and S. Nobuhiko. Characterization of the Shallow and Deep Levels in Si Doped GaN Grown by Metal-Organic Vapor Phase Epitaxy. *Japanese Journal of Applied Physics* **33** (12R), 6443 (1994). Cited on page/s 118.

[44] S. Ruvimov, Z. Liliental-Weber, T. Suski, J. W. A. III, J. Washburn, J. Krueger, C. Kisielowski, E. R. Weber, H. Amano, and I. Akasaki. Effect of Si doping on the dislocation structure of GaN grown on the A-face of sapphire. *Applied Physics Letters* **69** (7), 990–992 (1996). Cited on page/s 118.

[45] S. Nakamura, T. Mukai, and M. Senoh. Si- and Ge-Doped GaN Films Grown with GaN Buffer Layers. *Japanese Journal of Applied Physics* **31** (9), 2883–2888 (1992). Cited on page/s 118.

[46] S. Fernandez-Garrido, J. Grandal, E. Calleja, M. A. Sanchez-Garcia, and D. Lopez-Romero. A growth diagram for plasma-assisted molecular beam epitaxy of GaN nanocolumns on Si(111). *Journal of Applied Physics* **106** (12), 126102 (2009). Cited on page/s 119.

[47] J. Ristic, E. Calleja, S. Fernandez-Garrido, L. Cerutti, A. Trampert, U. J., and K. H. Ploog. On the mechanisms of spontaneous growth of III-nitride nanocolumns by plasma-assisted molecular beam epitaxy. *Journal of Crystal Growth* **310** (18), 4035–4045 (2008). Cited on page/s 119, 123.

[48] T. Tabata, J. Paek, Y. Honda, M. Yamaguchi, and H. Amano. Stacking Faults and Luminescence Property of InGaN Nanowires. *Japanese Journal of Applied Physics* **52** (8S), 08JE06 (2013). Cited on page/s 121.

[49] K. Yamada, H. Asahi, H. Tampo, Y. Imanishi, K. Ohnishi, and K. Asami. Strong photoluminescence emission from polycrystalline GaN layers grown on W, Mo, Ta, and Nb metal substrates. *Applied Physics Letters* **78** (19), 2849–2851 (2001). Cited on page/s 123.

[50] F. Furtmayr, M. Vielemeyer, M. Stutzmann, J. Arbiol, S. Estrade, F. Peiro, J. R. Morante, and M. Eickhoff. Nucleation and growth of GaN nanorods on Si (111) surfaces by plasma-assisted molecular beam epitaxy - The influence of Si- and Mg-doping. *Journal of Applied Physics* **104** (3), 034309 (2008). Cited on page/s 123.

[51] A. Wierzbicka, *et al.* Influence of substrate nitridation temperature on epitaxial alignment of GaN nanowires to Si(111) substrate. *Nanotechnology* **24** (3), 035703 (2012). Cited on page/s 123.

[52] E. Calleja, M. A. Sanchez-Garcia, F. J. Sanchez, F. Calleja, F. B. Naranjo, E. Munoz, S. I. Molina, A. M. Sanchez, F. J. Pacheco, and R. Garcia. Growth of III-nitrides on Si(111) by molecular beam epitaxy Doping, optical, and electrical properties. *Journal of Crystal Growth* **201-202**, 296–317 (1999). Cited on page/s 123.

[53] K. Hestroffer, C. Leclere, V. Cantelli, C. Bougerol, H. Renevier, and B. Daudin. In situ study of self-assembled GaN nanowires nucleation on Si(111) by plasma-assisted molecular beam epitaxy. *Applied Physics Letters* **100** (21), 212107 (2012). Cited on page/s 123.

[54] C. Cheze, L. Geelhaar, A. Trampert, and H. Riechert. In situ investigation of self-induced GaN nanowire nucleation on Si. *Applied Physics Letters* **97** (4), 043101 (2010). Cited on page/s 123.

[55] D. B. Williams and C. B. Carter. Transmission Electron Microscopy: A Textbook for Materials Science. Springer (2009). Cited on page/s 123.

[56] D. J. As, F. Schmilgus, C. Wang, B. Schottker, D. Schikora, and K. Lischka. The near band edge photoluminescence of cubic GaN epilayers. *Applied Physics Letters* **70** (10), 1311–1313 (1997). Cited on page/s 124.

[57] J. Neugebauer and C. G. Van de Walle. Gallium vacancies and the yellow luminescence in GaN. *Applied Physics Letters* **69** (4), 503–505 (1996). Cited on page/s 124, 125.

[58] E. Calleja, *et al.* Yellow luminescence and related deep states in undoped GaN. *Physical Review B* **55** (7), 4689–4694 (1997). Cited on page/s 124.

[59] M. A. Reshchikov and H. Morkoc. Luminescence properties of defects in GaN. *Journal of Applied Physics* **97** (6), 061301 (2005). Cited on page/s 124.

[60] M. A. Reshchikov, D. O. Demchenko, A. Usikov, H. Helava, and Yu Makarov. Carbon defects as sources of the green and yellow luminescence bands in undoped GaN. *Physical Review B* **90** (23), 235203 (2014). Cited on page/s 124, 125.

[61] J. L. Lyons, A. Janotti, and C. G. Van de Walle. Carbon impurities and the yellow luminescence in GaN. *Applied Physics Letters* **97** (15), 152108 (2010). Cited on page/s 124, 125.

[62] U. Birkle, M. Fehrer, V. Kirchner, S. Einfeldt, D. Hommel, S. Strauf, P. Michler, and J. Gutowski. Studies on Carbon as Alternative P-Type Dopant for Gallium Nitride. *MRS Proceedings* **537** (2011). Cited on page/s 124, 125.

[63] S. Fischer, *et al.* On the nature of the 3.41 eV luminescence in hexagonal GaN. *Journal of Crystal Growth* **189–190**, 556–560 (1998). Cited on page/s 124, 125.

[64] R. Dingle and M. Ilegems. Donor-acceptor pair recombination in GaN. *Solid State Communications* **9** (3), 175–180 (1971). Cited on page/s 124.

[65] H. G. Grimmeiss and B. Monemar. Low-Temperature Luminescence of GaN. *Journal of Applied Physics* **41** (10), 4054–4058 (1970). Cited on page/s 124.

[66] B. Gil. Low-dimensional Nitride Semiconductors. Oxford University Press (2002). Cited on page/s 124.

[67] C. Tablero. Ionization energy levels in C-doped InxGa1-xN alloys. *Applied Physics Letters* **97** (19), 192102 (2010). Cited on page/s 124.

[68] A. Koukitu and Y. Kumagai. Hydride Vapor Phase Epitaxy of GaN, in Technology of Gallium Nitride Crystal Growth pages 31–60. Springer Series in Materials Science, vol 133. Springer, Berlin, Heidelberg (2010). Cited on page/s 125.

[69] C.-C. Chen, C.-C. Yeh, C.-H. Chen, M.-Y. Yu, H.-L. Liu, J.-J. Wu, K.-H. Chen, L.-C. Chen, J.-Y. Peng, and Y.-F. Chen. Catalytic Growth and Characterization of Gallium Nitride Nanowires. *Journal of the American Chemical Society* **123** (12), 2791–2798 (2001). Cited on page/s 125.

Chapter 6

Vertical GaN nanocolumns grown on graphene intermediated with a thin AlN buffer layer

Andreas Liudi Mulyo[1,2], Mohana K. Rajpalke[1,a)], Haruhiko Kuroe[2], Per-Erik Vullum[3], Helge Weman[1], Bjørn-Ove Fimland[1,b)] and Katsumi Kishino[2,4,b)]

First published in: *Nanotechnology* **30** (1), 015604 (2018).
DOI: 10.1088/1361-6528/aae76b

Contributions

ALM planned the study and performed RF-PAMBE growth under supervision from HW, BOF, and KK. **ALM** conducted SEM, micro-Raman, and micro-photoluminescence characterizations. MKR assisted **ALM** in arranging all the relevant arguments presented in the manuscript (and did XRD measurements and analysis; not shown here). HK provided important preliminary Raman measurement results and examined them with **ALM**. PEV did FIB and TEM experiments. **ALM** interpreted the main results, drafted the first version of the manuscript, discussed it with other authors, and finalized it.

---

[1] Department of Electronic Systems, Norwegian University of Science and Technology (NTNU), NO-7491 Trondheim, Norway. [2] Department of Engineering and Applied Sciences, Sophia University, 102-8554, Tokyo, Japan. [3] SINTEF Industry, NO-7465 Trondheim, Norway. [4] Sophia Nanotechnology Research Center, Sophia University, 102-8554, Tokyo, Japan. [a)] Present address: Center for Quantum Devices, Niels Bohr Institute, University of Copenhagen, 2100 Copenhagen, Denmark. [b)] e-mail: bjorn.fimland@ntnu.no and kishino@sophia.ac.jp

ABSTRACT

We report on the self-assembled growth of high-density and vertically-oriented *n*-doped GaN nanocolumns on graphene by radio-frequency plasma-assisted molecular beam epitaxy. Graphene was transferred to silica glass, which was used as substrate carrier. Using a migration enhanced epitaxy grown AlN buffer layer for the nucleation is found to enable a high density of vertical GaN nanocolumns with *c*-axis growth orientation on graphene. Furthermore, micro-Raman spectroscopy indicates that the AlN buffer reduces damage on the graphene caused by impinging active N species generated by the radio-frequency plasma source during the initial growth stage and nucleation of GaN. In addition, the grown GaN nanocolumns on graphene are found to be virtually stress-free. Micro-photoluminescence measurements show near band-edge emission from wurtzite GaN, exhibiting higher GaN bandgap related photoluminescence intensity relative to a reference GaN bulk substrate and the absence of both yellow luminescence and excitonic defect emission. Transmission electron microscopy reveals the interface of GaN nanocolumns on graphene via thin AlN buffer layer. Even though the first few monolayers of AlN on top of graphene are strained due to in-plane lattice mismatch between AlN and graphene, the grown GaN nanocolumns have wurtzite crystal structure without observable defects. The results of this initial work pave the way towards realizing low-cost and high-performance electronic and optoelectronic devices based on III-N semiconductors grown on graphene.

6.1 INTRODUCTION

For the past two decades, the III-N system has met its high expectations as one of the most promising wide band-gap semiconductors materials for visible, violet and ultraviolet light emitting devices (LEDs)[1–3] and high-power electronics[1,4]. The most commonly used substrates today for III-N materials are Si, SiC and Al_2O_3[5]. However, these substrates have inadequate compatibility with the III-N system as they are characterized by large lattice constant mismatch, large thermal coefficient mismatch, poor thermal conductivity, low thermal stability and/or non-transparent substrate[5]. These issues may be overcome by utilizing graphene[6–9] as a substrate for the epitaxial growth of III-N. In addition, graphene offers an excellent electrical conductivity[10] and thus potentially can become a combined substrate and transparent electrode for improving the performance and functionalities of III-N-based optoelectronic devices. However, the absence of dangling bonds for graphene causes high surface tension, leading to weak nucleation and cluster growth[6,11] which likely generate high-density of stacking faults[11,12] or threading dislocations[13] when GaN thin-film structures are grown on it.

By exploiting the defect-suppressing property of nanowire or nanocolumn structures[14–16], there is a likelihood to overcome these limitations in order to realize high quality GaN on graphene. Additionally, their geometry can provide enhanced light extraction efficiency which is beneficial for LEDs[17]. Number of works have reported the growth of GaN nanocolumns on graphite[18], epitaxial graphene on SiC[19], transferred graphene and multi-layer graphene on various substrate carriers[20–25] such as Si, SiO_2 and Al_2O_3. However, it is generally observed that the grown GaN nanocolumns on graphene have either low density[22–24] or are oriented in non-defined directions[20], which are not desirable for light emitter applications as this can reduce light extraction and emission efficiency. Despite that preferred characteristics of GaN nanowires grown directly on graphene were obtained by Kumaresan *et al.*[21], the graphene's properties after the GaN growth were not evaluated. This issue was addressed by Fernandez-Garrido *et al.*[19] remarking the complete graphene removal after GaN nanowire growth. These findings discourage the graphene's prospective as an integrated part of GaN-based devices as a combined substrate and transparent electrode. Growth of high density and vertically aligned GaN nanocolumns on multi-layer graphene (∼35 nm thick) were successfully demonstrated by Hayashi *et al.*[25]. However, due to the thickness of the multi-layer graphene, it is highly absorbing and cannot be used as a transparent electrode.

Here, we present the growth, structural and optical characterization of GaN nanocolumns grown on transferred (single-layer) graphene on silica glass by radio-frequency plasma-assisted molecular beam epitaxy (RF-PAMBE) utilizing a thin AlN buffer layer. The morphology of the grown GaN nanocolumns was investigated via scanning electron microscopy (SEM). The structural properties of GaN nanocolumns and graphene were analyzed by micro-Raman spectroscopy. The optical quality of the grown GaN nanocolumns was studied by micro-photoluminescence at room temperature (RT). Later, the sample with the optimized growth condition of GaN nanocolumns on graphene is further characterized using transmission electron microscopy (TEM) to examine the structure and chemistry of the grown GaN nanocolumns. We demonstrate the growth of high-density, vertically-aligned and high-quality single crystalline wurtzite (hexagonal) GaN nanocolumns on graphene intermediated with a thin AlN buffer layer. There is a strong impact from the AlN buffer layer, as it serves not only as nucleation sites for the GaN nanocolumn growth, but also alleviates damage of the graphene.

6.2 EXPERIMENTAL METHODS

The substrate was commercially available graphene grown by chemical vapor deposition (CVD) on Cu foil[26] and transferred onto silica glass which was used as the substrate carrier. It should be pointed out that the graphene used in this work refers to the mono (single-) layer of sp^2-bonded carbon atoms tightly packed into a hexagonal two-dimensional lattice, with a theoretical thickness of approximately 0.335 nm. Silica glass was chosen not only because it is cheap, but also due to its excellent optical transparency in the visible and ultraviolet region, which might be useful for flip-chip III-N based LEDs fabrication. In the following, all the values of substrate temperature were based on pyrometer reading. Sample 1 was n-type (Si) doped GaN nanocolumns grown directly on graphene at a substrate temperature of 895 °C for 90 min, using the established growth condition for GaN nanocolumns on silica glass, as described in our previous work[14]. For sample 2, the n-GaN nanocolumns were synthesized identical to sample 1, but with GaN as a buffer layer. This particular buffer layer was formed at a substrate temperature of 690 °C. Ga atoms were first continuously deposited on the graphene for 35 s and then nitrided with N_2 plasma for 60 s. In the case of sample 3, AlN was used as a buffer layer for the n-GaN nanocolumns instead of GaN. This layer was deposited at a substrate temperature of 805 °C using migration-enhanced epitaxy (MEE)[27,28] with alternating supplies of Al atoms and N_2 plasma in a 20-period cycle consisting of: Al supply (4 s), interrupt (5 s), and N_2 plasma (3 s)[25]. Subsequently, GaN nanocolumns were grown under the same conditions as for sample 1.

SEM images were acquired using an SII SMI3050SE focused ion beam-SEM (FIB-SEM) and a Hitachi SU8000 SEM at respective acceleration voltages of 15 kV and 10 kV. Unpolarized Raman spectra were measured at RT in backscattered configuration using a Renishaw InVia Reflex Spectrometer System equipped with a 514.5 nm excitation laser. The laser was focused onto the sample using a 100× objective lens resulting in a spot diameter of ~1.5 μm, and the scattered Raman signal was collected by the same objective lens. Micro-photoluminescence was carried out at RT using a HeCd laser (325 nm) as the excitation source where a 100× objective lens was used to focus the laser beam (spot diameter of ~2 μm) and for the collection of the scattered light. Finally, the TEM analysis was performed with a double Cs corrected cold field emission gun JEOL ARM200F, operated at 200 kV. The TEM images were taken with the nanocolumns oriented along the [1-210] zone axis. The cross-section TEM specimen was prepared with a FEI Helios G4 UX FIB-SEM. Coarse thinning was performed at 30 kV acceleration voltage, while the final thinning was performed at 5 kV and finally 2 kV to minimize surface ion-beam damage.

6.3 RESULTS AND DISCUSSION

SEM images of samples 1, 2 and 3 are presented in Figure 6.1. The grown GaN nanocolumns in sample 1 (Figure 6.1(a) and (b) for bird- and side-view SEM, respectively) are characterized with random growth directions, and exhibit irregular diameters and heights (Figure 6.1(b)). Additionally, the formation of GaN islands are observed (red-circled in Figure 6.1(b)), which might be a result of the high surface tension (low surface energy) caused by the chemical inertness of graphene[6,11]. Furthermore, irradiation of N_2 plasma at the initial growth stage may generate defects in graphene[29–31] or even decompose it[32].

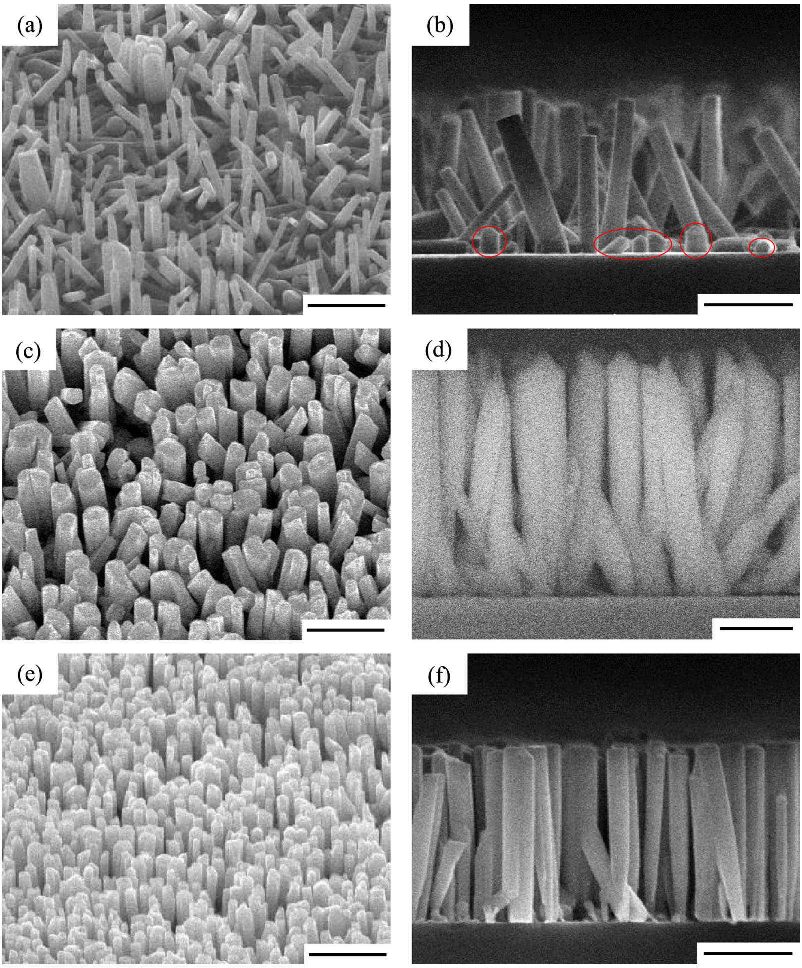

FIGURE 6.1. (**a**, **b**), (**c**, **d**) and (**e**, **f**) are (bird-, side-) view SEM images of samples 1, 2 and 3, respectively. Red circles in (**b**) indicate the formation of GaN islands. Scale bars are 1 μm for (a, c and e) while 500 nm for (b, d and f).

One approach in preventing the direct N_2 plasma on graphene could be to cover the surface area of graphene with continuous Ga atom deposition at low substrate temperature before it is subjected to nitridation to form a GaN buffer layer. For GaN nanocolumn growth on Si(111)[33] it has been shown that this method leads to a high density of dot-like GaN nucleation layers, rather than a thin film, which is crucial to maintain the formation of nanocolumns. In addition, such low temperature (e.g. 690 °C) is expected to reduce graphene's reactivity with the incoming N atoms, thus decreasing the graphene damage upon nitridation, as was the case for a graphene oxidation process[34]. As shown in Figure 6.1(c) and (d) for the bird- and side-view SEM, respectively, the density, diameter uniformity and verticality of the GaN nanocolumns show an improvement compared to sample 1, although they have a tendency to grow in non-perpendicular directions relative to the substrate. Nevertheless, one should consider that the epitaxy of GaN on graphene can partially break the C-C σ bonds of graphene upon expansion of the graphene lattice, where the interface strain is reduced significantly by chemical bonding between C and N atoms, as suggested by Gohda and Tsuneyuki[35]. Compared to samples 1 and 3, sample 2 has the highest vertical nanocolumn length (1750 nm). Additionally, it is noticed from the top facet that the nanocolumns in sample 2 are likely Ga-polar (pyramidal tips[36,37]), whereas samples 1 and 3 are N-polar (flat tips[36,37]), as shown in Figure 6.1(d), (b) and (f), respectively.

To reduce the graphene damage from direct bombardment of active N atoms and alleviate in-plane strain caused by GaN nucleation, an AlN buffer layer was deposited using MEE technique on the graphene surface prior to GaN nanocolumn growth. The MEE technique enhances the surface migration of Al atoms[38], increasing their coverage area on graphene in the absence of N atoms. Due to the polycrystalline nature of CVD grown graphene[39] and its extremely low surface energy[11], AlN tends to form islands[25] instead of a thin-film. Nonetheless, AlN has greater likelihood than GaN to nucleate on graphene via *quasi*-van der Waals forces due to the higher adsorption energy of Al[40] and stronger bonding of Al-N relative to Ga-N[35,41]. Moreover, the graphene lattice is expected to be preserved for AlN grown on graphene due to that the in-plane strain is not large enough to induce structural deformation of the graphene[35]. This is corroborated by the observation of Al Balushi *et al.*[42], where nucleated polycrystalline islands of AlN (grown by metalorganic CVD) on epitaxial graphene did not significantly distort the underlying graphene. We observe that the presence of the AlN buffer layer in sample 3 promotes the perpendicular growth orientation and increases the density of GaN nanocolumns on graphene (Figure 6.1(e) and (f) for bird- and side-view SEM, respectively). The role of the AlN buffer layer as nucleation site leads to a quite uniform morphology of vertically aligned GaN nanocolumns (Figure 6.1(f)) with an average diameter, height and density of 90 nm, 1015 nm and 1.5×10^9 cm^{-2}, respectively. As a note, we manage to obtain almost twice as high density as that of the work of Hayashi *et al.*[25] using the same MEE growth conditions in which multi-layer graphene was employed as the substrate for GaN nanocolumn growth. Having a denser nanocolumn density is more beneficial in further device processing for the fabrication of e.g. nanocolumn-based ultraviolet LEDs, i.e. preventing the usage of a polyimide insulating layer which can degrade light extraction efficiency due to the ultraviolet light absorption by the polyimide.

Structural properties of the nanocolumn samples were further characterized using micro-Raman spectroscopy in the range between 500 and 800 cm^{-1}, where the spectra are shown in Figure 6.2(a). Regardless of the growth conditions, all of these nanocolumn samples have the same wave number for the A_1 (TO), E_1 (TO) and E_2 (high) phonon modes at 531.9, 557.3 and 566.2 cm^{-1}, respectively, all of which are typical values for GaN with a wurtzite crystal structure[43]. These observations are similar to that of self-organized GaN nanocolumns grown on Al_2O_3 and Si substrates[44], as well as to that of regularly arrayed GaN nanostructures[45]. Notably, there is no sign of any TO phonon mode at 554[46] or 555 cm^{-1} [43], suggesting that there is no existence of zinc blende (cubic) GaN in the nanocolumn samples. Moreover, the Raman shift for the obtained E_2 (high) mode is consistent with the reported value for homoepitaxially grown GaN films at a phonon frequency of 566.2 cm^{-1} [47], demonstrating that the GaN nanocolumns in samples 1, 2 and 3 can be considered to be stress-free. In this work, we could not observe an A_1 (LO) phonon mode which is normally detected at 737 cm^{-1} [43–45]. It could be that its weak intensity[44] is overlapped with the broad signal ranging from ~650 to ~750 cm^{-1}. This broad signal might be affiliated to the Fröhlich mode, which is a surface-related vibrational mode[44,45]. Expected Raman-active phonon modes for AlN in sample 3, for instance A_1 (TO) at 614 cm^{-1}, E_2 (high) at 660 cm^{-1} and E_1 (TO) at 673 cm^{-1} [48], are not observed, which could be due to the small excitation volume of the AlN nucleation layer.

To identify the damage of graphene in samples 1, 2 and 3, micro-Raman measurements from 1100 to 3200 cm^{-1} (Figure 6.2(b)) were carried out with pristine graphene transferred onto silica glass as the reference sample. This characterization technique gives rise to well-established first- and second-order Raman scattering mechanisms in undoped graphene[49]. Although graphene is only consisted of one atomic layer of carbon sheet, it exhibits very strong Raman scattering due to the double resonance mechanism in graphene. The first-order Raman band, known as the G band (1588 cm^{-1}), is a doubly degenerate (in-plane transverse optical (iTO) and longitudinal optical (LO)) phonon mode at the Brillouin zone center. On the other hand, the second-order Raman process involves an intervalley double resonance scattering of two iTO phonons

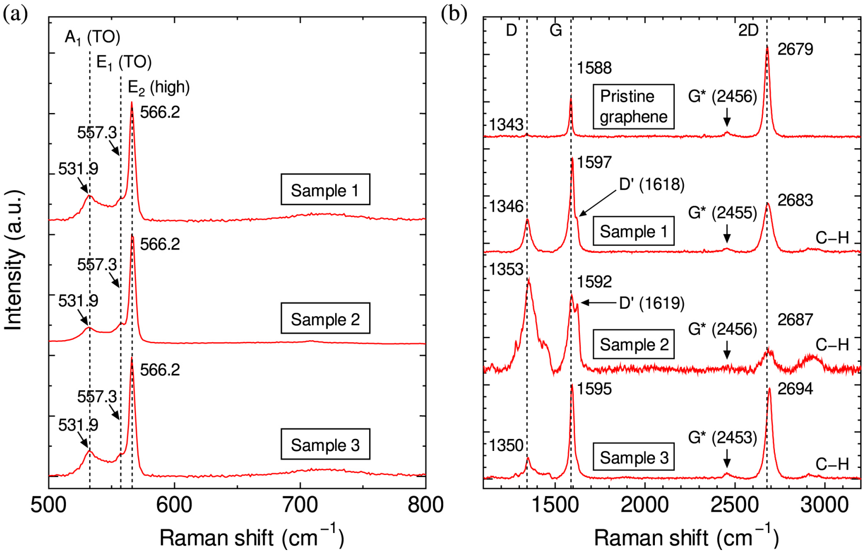

Figure 6.2. Micro-Raman spectra of (**a**) samples 1, 2 and 3 between 500 and 800 cm^{-1} and of (**b**) pristine graphene and samples 1, 2 and 3 between 1100 and 3200 cm^{-1}. The dashed lines in (**b**) indicate the D, G and 2D peak positions of pristine graphene.

near the K point of the Brillouin zone (2D band at 2679 cm^{-1}), and also an intervalley double resonance scattering of one iTO phonon with one defect mode near the K point of the Brillouin zone (D band at 1343 cm^{-1}). A subtle D peak with prominent G and 2D peaks where the intensity ratios of $I_D/I_G \approx 0$ and $I_{2D}/I_G \approx 2$, indicate the high quality of pristine graphene used for the growths reported in this paper. After the GaN nanocolumn growth, sample 1 and moreover sample 2 clearly show higher I_D/I_G and lower I_{2D}/I_G ratios compared to sample 3, implying that the direct exposure of N_2 plasma and GaN nucleation on graphene contribute to a higher degree of damage relative to the graphene which is covered with an AlN buffer layer. In addition, sample 1 exhibits a D' peak in the Raman spectrum (more prominent for sample 2), which is described as a disorder-induced feature in the graphene crystalline lattice[49]. The aggravated graphene damage in sample 2 is possibly caused by the sole irradiation of N_2 plasma following the deposition of Ga atoms on the graphene surface, together with the in-plane strain generated by the subsequent formation of GaN nucleation[42].

Also, the N_2 plasma treatment can modify the chemical properties and electronic structure of graphene, where N atoms form a covalent bonding with C atoms and change the lattice structure of graphene[29,50]. There are mainly three probable bonding configurations for the incorporated N atoms in the graphene network (pyridinic N, pyrrolic N and graphitic N), all of which can influence the electrical properties of graphene[30,31,50–52]. Earlier works have shown that N-doping of graphene by NH_3 plasma[29,30] or N_2 plasma[31] results in *n*-type doping, where the Fermi level is shifted above the Dirac point[53] and the work function becomes smaller than the reported value of undoped graphene[31,51]. Please note that the nitrogen doping in graphene is likely to be inhomogeneous. In the Raman mapping analysis on N-doped graphene performed by Luo *et al.*[54], it was revealed that some spots have high I_D/I_G ratio and some show very low I_D/I_G ratio, which suggests a non-uniform defect distribution induced by inhomogeneous nitrogen incorporation in the graphene. According to the results shown in Figure 6.2(b), the most prominent features in the micro-Raman spectra of graphene (G and 2D bands) in samples 1, 2 and 3, as well as the defect-related D band, are generally shifted to higher wavenumbers relative to the pristine graphene. The blue-shift of the D and G peak can be explained by local electron/hole doping in carbon nanostructures[30,55–57], while the blue-shift of the 2D peak can be the result of doping and/or compressive strain[56,57]. Based on these observations, it is plausible that the nitrogen-treated graphene presented in this paper exhibits an *n*-type semiconductor behavior. To precisely determine the nitrogen content as well as identify the bonding configurations of N atoms in the graphene samples presented in this paper, future studies employing X-ray photoelectron spectroscopy and/or ultraviolet photoelectron spectroscopy measurements are necessary. Apart from the aforementioned peaks, the adsorption of hydrocarbon (C-H) is detected after GaN growth, which is consistent with the work reported by Fernandez-Garrido *et al.*[19] It is also noted that the existence of a G* peak, which originates from the overtone modes (transition from the ground state to the second or higher excited state) of a second-order Raman process involving an intervalley double resonance scattering of two LO phonons near the K point of the Brillouin zone[58], is fairly observable in the pristine graphene, samples 1 and 3, whereas its presence is rather faint for sample 2. Despite being exposed to different growth conditions, the position of the G* peak is relatively stable compared to the earlier discussed D, G and 2D peak positions. Further studies are required to clarify these phenomena, which are beyond the focus of this paper.

Evaluation of the optical properties of samples 1, 2 and 3 was done via micro-photoluminescence at RT using a He-Cd laser (325 nm) as excitation source. A freestanding hydride vapor phase epitaxy (HVPE)-grown GaN bulk substrate with a threading dislocation density of $6\text{-}8 \times 10^6$ cm^{-2} was used as a reference, like for previous studies[14–16,25]. Photoluminescence spectra of sample 1 (blue line), sample 2 (green line), sample 3 (red line), and the reference sample (black line) are presented in Figure 6.3. Here, it is established that there are strong luminescence from GaN in samples 1, 2, 3 and reference sample, whose peak wavelengths are located at 364.6, 364.3, 364.6 and 363.6

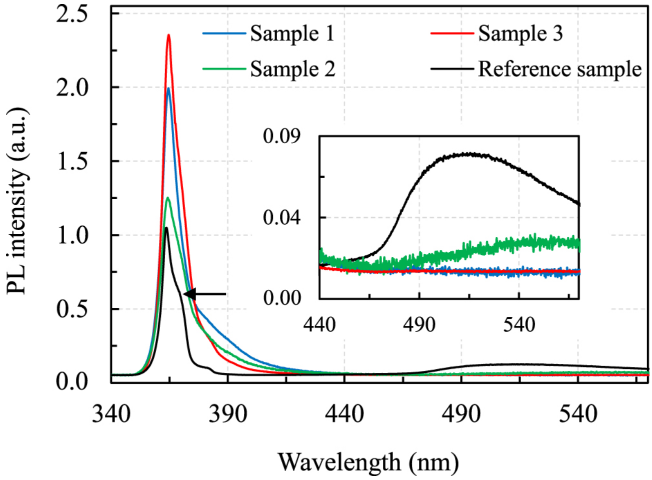

FIGURE 6.3. Photoluminescence spectra of samples 1 (blue line), 2 (green line) and 3 (red line) and a reference GaN bulk sample (black line) measured at RT. Inset shows magnified spectra from 440 to 580 nm. The black arrow pointing to the spectrum of the reference sample highlights the shoulder peak observed at 369 nm related to excitons bound to structural defects[59].

nm, respectively. Although a red-shift of 0.7 to 1.0 nm relative to that of the reference sample is shown by the nanocolumn samples, the observed excitonic emission of near 364 nm can still be related to the wurtzite GaN bandgap. The linewidths in samples 1 and 3 are slightly narrower (full-width at half-maximum (FWHM) of 8.69 and 9.14 nm, respectively) than the reference sample (FWHM of 10.79 nm), whereas for sample 2 it is somewhat wider (FWHM of 11.77 nm). In general, there are not much striking differences in the linewidth between the nanocolumn samples and the reference sample.

It is also noticeable that all of the nanocolumn samples exhibit higher GaN band-edge photoluminescence peak intensity as compared to the reference sample, where the intensity is ∼1.9 times higher for sample 1, ∼1.2 times higher for sample 2 and ∼2.3 times higher for sample 3. Interestingly, GaN nanocolumns in sample 1, which exhibit rather random (non-vertical) growth orientations (Figure 6.1(a) and (b)), demonstrate much higher photoluminescence intensity as compared to GaN nanocolumns in sample 2, where the growth orientation is more defined in terms of verticality (Figure 6.1(c) and (d)). The low photoluminescence intensity could be due to the fact that the lower part of many nanocolumns in sample 2 are coalesced with each other, as can be clearly seen from Figure 6.1(d). On the other hand, the intensity ratio shown by sample 3 should be highlighted, as the optical quality of this sample is similar with that of the GaN nanocolumns grown on other types of substrates, for instance silica glass[14], multi-layer graphene[25] and selective area growth on sputtered

AlN/Si(111) where the diameter of nanocolumn is 200 nm[16] (such comparison is valid here since the same reference sample has also been used for other papers[14–16,25]). Unlike sample 2, the base part of the GaN nanocolumns in sample 3 is less likely to show any coalescence, as shown in Figure 6.1(f).

Furthermore, there are some noteworthy differences in the photoluminescence spectra from the nanocolumn and reference samples that should be mentioned here. First, nanocolumn samples do not exhibit a shoulder peak at 369 nm, which is affiliated with excitons bound to structural defects[59], unlike what is observed in the reference sample (indicated with the black arrow in Figure 6.3). A second distinct difference is the presence of a yellow luminescence band, which is solely observed in the reference sample. In general, all of the nanocolumn samples indicate a strong suppression of this broad emission in the wavelength range from 465 to 570 nm (a magnified spectrum of this yellow luminescence band is shown in the inset of Figure 6.3). For GaN nanocolumns in samples 1 and 3, it is clearly observed that this yellow band is completely eliminated, which indicates that there are no electron transitions from the conduction band to the deep acceptor levels[60,61]. However, a small deviation from this is shown in sample 2, which exhibits a weak emission in the proximity of the yellow luminescence band. Zinc blende GaN-related emission, which typically occurs at ~386 nm[12], is not observed for any of the samples.

According to the SEM, micro-Raman spectroscopy and micro-photoluminescence results on three different growth conditions of GaN nanocolumns on graphene, it is clear that sample 3 represents the best sample. The superior properties of sample 3, being vertically grown GaN nanocolumns exhibiting high photoluminescence peak intensity and reduced graphene damage, are promising for the envisaged nanocolumn/graphene-based devices. For these reasons, further characterizations by TEM were carried out solely based on sample 3.

A cross-section bright field TEM (BF TEM) image (sample 3) from a region covering the top of the silica glass, the graphene, the AlN buffer layer, and the bottom of the GaN nanocolumn is shown in Figure 6.4(a). The graphene layer is observed on top of the silica glass substrate (blue arrows) and interestingly, the contrast from graphene disappears at a few locations (indicated by red arrows). It has been observed that the graphene layer is continuous without any holes in it, as the wrinkles associated with the thermal expansion coefficient difference between Cu and graphene during the synthesis are also found to cross Cu grain boundaries[26]. However, it buckles and bends. The lack of contrast from graphene is likely due to local bending (since silica glass surface is not atomically flat) that makes the graphene deviate from edge-on orientation, and hence the lattice contrast disappears from the TEM image. Since all TEM images are projections that average through the thickness of the TEM lamella,

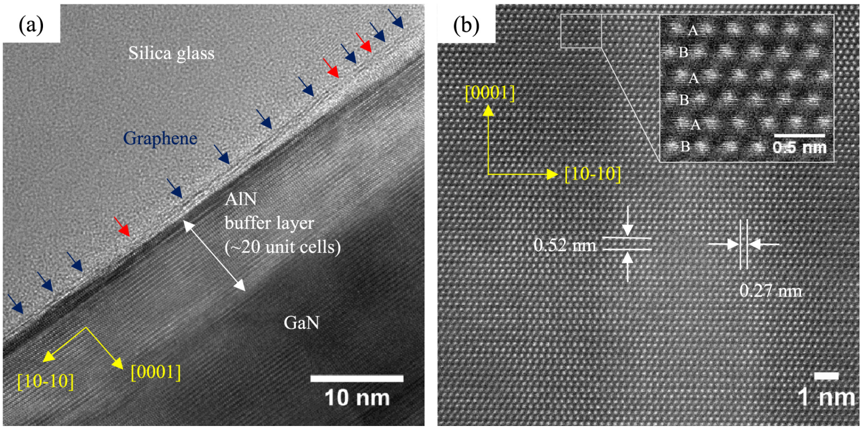

FIGURE 6.4. TEM images of sample 3 taken along the [1-210] zone axis. (**a**) BF TEM image of the interfaces between GaN nanocolumn, AlN buffer layer, graphene and silica glass. The blue arrows point to sites where the presence of graphene is clearly seen in the image, whereas the red arrows point to sites where the presence of graphene is not revealed, probably due to local bending of graphene at those specific sites causing a lack of lattice contrast. (**b**) High resolution HAADF STEM image from the middle of the GaN nanocolumn (inset: crystal stacking order of wurtzite GaN).

local steps or height variations on the silica surface can possibly make a single-layer graphene appear as two or three layers in the TEM images. Similarly, TEM images of the transferred graphene on Si in the work of Heilmann *et al.*[24] show how the graphene is not flat, due to unavoidable formation of amorphous SiO_x layer. In contrast, imaging epitaxial graphene, for example on atomically flat SiC single crystals, results in an unambiguous visualization of the number of graphene layers[6,19,42].

The AlN buffer layer grown on the graphene is found to be of pure wurtzite crystal structure and can be seen in Figure 6.4(a) as an ~20 unit cells (~10 nm) thick layer with predominantly bright contrast. The dark contrast at the bottom (next to the graphene) most likely represents strain contrast due to the in-plane lattice mismatch between AlN and graphene. This strain contrast is only present in the first few monolayers of AlN. However, it is noticed that the strain contrast is not uniform along the interface between AlN and graphene. There are both dark and bright regions close to the graphene interface. The primary reason for this is that the strain is actually inhomogeneously distributed. When dislocations are present, the strain will always vary in the vicinity of a dislocation, i.e. atoms and planes are differently distorted (displaced away from their bulk equilibrium positions) according to the position of the dislocation. The same is also true for point like lattice defects. Nevertheless, no indication of defect propagations, such as stacking faults or threading dislocations, is observed in the GaN nanocolumn (dark contrast) grown on this AlN buffer layer.

High resolution high-angle annular dark field scanning TEM (HAADF STEM) image from the middle of the nanocolumn (Figure 6.4(b)) shows clearly the Ga atomic columns (represented by white dots) which have an *ABAB* stacking order (see inset of Figure 6.4(b) for easier observation). The interplanar spacings of GaN nanocolumns parallel to the [0001] and [10-10] directions, deduced from the image presented in Figure 6.4(b), are approximately 0.52 and 0.27 nm, respectively, in good agreement with the established lattice constant parameters for GaN[5,14,25]. This STEM image demonstrates single crystalline GaN with a perfect wurtzite structure without any observable defects or inversion domain boundaries in the field of view.

6.4 CONCLUSION

In summary, we have demonstrated that growth of high-density and vertically-aligned GaN nanocolumns on graphene/silica glass by RF-PAMBE is feasible using a thin AlN buffer layer. The AlN, grown using MEE technique, does not only serve as nucleation sites for the GaN nanocolumns, but it also provides considerable protection to the graphene from the N_2 plasma source and in-plane strain generated by GaN nucleation. It is proven that when using an AlN buffer layer, the stress-free GaN nanocolumns are grown in the *c*-axis direction with wurtzite structure and exhibit an acceptable verticality. Furthermore, the columnar structure of GaN provides higher photoluminescence intensity and higher structural quality than that of a reference HVPE-grown GaN bulk substrate. TEM of representative GaN nanocolumns demonstrates a high-quality wurtzite crystal structure with the absence of threading dislocations, stacking faults or twinning defects. These findings are therefore very encouraging for further establishing graphene as an alternative substrate to enhance the performance and functionalities of III-N-based semiconductor devices in general.

6.5 ACKNOWLEDGEMENTS

We thank Y. Konno, I. M. Høiaas, D. Ren and A. T. J. v. Helvoort for fruitful discussions. We are also indebted to K. Yamano and I. Matsuyama for dedicated MBE maintenance. This work was supported by the NANO2021 (Grant No. 259553) program of the Research Council of Norway and by Japan Society for the Promotion of Science KAKENHI (Grant No. 24000013). The Research Council of Norway is also acknowledged for the support to

NTNU NanoLab through the Norwegian Micro- and Nano-Fabrication Facility and to the Norwegian PhD Network on Nanotechnology for Microsystems (FORSKERSKOLER-221860). The TEM work was carried out on the NORTEM infrastructure (Grant No. 197405) TEM Gemini Centre, NTNU.

6.6 REFERENCES

[1] S. Fujita. Wide-bandgap semiconductor materials: For their full bloom. *Japanese Journal of Applied Physics* **54** (3), 030101 (2015). Cited on page/s 132.

[2] K. Kishino, A. Yanagihara, K. Ikeda, and K. Yamano. Monolithic integration of four-colour InGaN-based nanocolumn LEDs. *Electronics Letters* **51** (11), 852–854 (2015). Cited on page/s 132.

[3] K. Yamano and K. Kishino. Selective area growth of InGaN-based nanocolumn LED crystals on AlN/Si substrates useful for integrated μ-LED fabrication. *Applied Physics Letters* **112** (9), 091105 (2018). Cited on page/s 132.

[4] M. Kuzuhara, J. T. Asubar, and H. Tokuda. AlGaN/GaN high-electron-mobility transistor technology for high-voltage and low-on-resistance operation. *Japanese Journal of Applied Physics* **55** (7), 070101 (2016). Cited on page/s 132.

[5] G. Li, W. Wang, W. Yang, Y. Lin, H. Wang, Z. Lin, and S. Zhou. GaN-based light-emitting diodes on various substrates: a critical review. *Reports on Progress in Physics* **79** (5), 056501 (2016). Cited on page/s 132, 143.

[6] A. Mazid Munshi, Dasa L. Dheeraj, Vidar T. Fauske, Dong-Chul Kim, Antonius T. J. van Helvoort, Bjørn-Ove Fimland, and Helge Weman. Vertically Aligned GaAs Nanowires on Graphite and Few-Layer Graphene: Generic Model and Epitaxial Growth. *Nano Letters* **12** (9), 4570–4576 (2012). Cited on page/s 132, 133, 135, 142.

[7] J. H. Seol, *et al.* Two-Dimensional Phonon Transport in Supported Graphene. *Science* **328** (5975), 213 (2010). Cited on page/s 132.

[8] K. Kim, W. Regan, B. Geng, B. Aleman, B. M. Kessler, F. Wang, M. F. Crommie, and A. Zettl. High-temperature stability of suspended single-layer graphene. *Physica Status Solidi (RRL) – Rapid Research Letters* **4** (11), 302–304 (2010). Cited on page/s 132.

[9] F. Bonaccorso, Z. Sun, T. Hasan, and A. C. Ferrari. Graphene photonics and optoelectronics. *Nature Photonics* **4**, 611–622 (2010). Cited on page/s 132.

[10] P. Avouris. Graphene: Electronic and Photonic Properties and Devices. *Nano Letters* **10** (11), 4285–4294 (2010). Cited on page/s 132.

[11] Y. Alaskar, S. Arafin, D. Wickramaratne, M. A. Zurbuchen, L. He, J. McKay, Q. Lin, M. S. Goorsky, R. K. Lake, and K. L. Wang. Towards van der Waals Epitaxial Growth of GaAs on Si using a Graphene Buffer Layer. *Advanced Functional Materials* **24** (42), 6629–6638 (2014). Cited on page/s 133, 135, 136.

[12] T. Araki, *et al.* Radio-frequency plasma-excited molecular beam epitaxy growth of GaN on graphene/Si(100) substrates. *Applied Physics Express* **7** (7), 071001 (2014). Cited on page/s 133, 141.

[13] J. Kim, C. Bayram, H. Park, C.-W. Cheng, C. Dimitrakopoulos, J. A. Ott, K. B. Reuter, S. W. Bedell, and D. K. Sadana. Principle of direct van der Waals epitaxy of single-crystalline films on epitaxial graphene. *Nature Communications* **5**, 4836 (2014). Cited on page/s 133.

[14] A. Liudi Mulyo, Y. Konno, J. S. Nilsen, A. T. J. van Helvoort, B.-O. Fimland, H. Weman, and K. Kishino. Growth study of self-assembled GaN nanocolumns on silica glass by plasma assisted molecular beam epitaxy. *Journal of Crystal Growth* **480**, 67–73 (2017). Cited on page/s 133, 134, 139, 140, 141, 143.

[15] K. Kishino and S. Ishizawa. Selective-area growth of GaN nanocolumns on Si(111) substrates for application to nanocolumn emitters with systematic analysis of dislocation filtering effect of nanocolumns. *Nanotechnology* **26** (22), 225602 (2015). Cited on page/s 133, 139, 141.

[16] H. Hayashi, D. Fukushima, D. Tomimatsu, T. Noma, Y. Konno, and K. Kishino. Flip-chip bonding and fabrication of well-ordered nanocolumn arrays on sputter-deposited AlN/Si (111) substrate. *Physica Status Solidi A - Applications and Materials Science* **212** (5), 992–996 (2015). Cited on page/s 133, 139, 141.

[17] Q. Yue, K. Li, F. Kong, J. Zhao, and W. Li. Analysis on the Light Extraction Efficiency of GaN-Based Nanowires Light-Emitting Diodes. *IEEE Journal of Quantum Electronics* **49** (8), 697–704 (2013). Cited on page/s 133.

[18] S. Nakagawa, T. Tabata, Y. Honda, M. Yamaguchi, and H. Amano. GaN Nanowires Grown on a Graphite Substrate by Radio Frequency Molecular Beam Epitaxy. *Japanese Journal of Applied Physics* **52** (8S), 08JE07 (2013). Cited on page/s 133.

[19] S. Fernandez-Garrido, *et al.* Molecular Beam Epitaxy of GaN Nanowires on Epitaxial Graphene. *Nano Letters* **17** (9), 5213–5221 (2017). Cited on page/s 133, 139, 142.

[20] S. Kang, A. Mandal, J. H. Chu, J.-H. Park, S.-Y. Kwon, and C.-R. Lee. Ultraviolet photoconductive devices with an n-GaN nanorod-graphene hybrid structure synthesized by metal-organic chemical vapor deposition. *Scientific Reports* **5**, 10808 (2015). Cited on page/s 133.

[21] V. Kumaresan, *et al.* Epitaxy of GaN Nanowires on Graphene. *Nano Letters* **16** (8), 4895–4902 (2016). Cited on page/s 133.

[22] K. Chung, H. Beak, Y. Tchoe, H. Oh, H. Yoo, M. Kim, and G.-C. Yi. Growth and characterizations of GaN micro-rods on graphene films for flexible light emitting diodes. *APL Materials* **2** (9), 092512 (2014). Cited on page/s 133.

[23] M. Heilmann, G. Sarau, M. Gobelt, M. Latzel, S. Sadhujan, C. Tessarek, and S. Christiansen. Growth of GaN Micro- and Nanorods on Graphene-Covered Sapphire: Enabling Conductivity to Semiconductor Nanostructures on Insulating Substrates. *Crystal Growth & Design* **15** (5), 2079–2086 (2015). Cited on page/s 133.

[24] M. Heilmann, *et al.* Vertically Oriented Growth of GaN Nanorods on Si Using Graphene as an Atomically Thin Buffer Layer. *Nano Letters* **16** (6), 3524–3532 (2016). Cited on page/s 133, 142.

[25] H. Hayashi, Y. Konno, and K. Kishino. Self-organization of dislocation-free, high-density, vertically aligned GaN nanocolumns involving InGaN quantum wells on graphene/SiO_2 covered with a thin AlN buffer layer. *Nanotechnology* **27** (5), 055302 (2015). Cited on page/s 133, 134, 136, 137, 139, 140, 141, 143.

[26] X. Li, *et al.* Large-Area Synthesis of High-Quality and Uniform Graphene Films on Copper Foils. *Science* **324** (5932), 1312–1314 (2009). Cited on page/s 134, 141.

[27] H. Yoshiji, K. Minoru, and Y. Hiroshi. Migration-Enhanced Epitaxy of GaAs and AlGaAs. *Japanese Journal of Applied Physics* **27** (2R), 169 (1988). Cited on page/s 134.

[28] D. Sugihara, A. Kikuchi, K. Kusakabe, S. Nakamura, Y. Toyoura, T. Yamada, and K. Kishino. 2.6 μm/h High-Speed Growth of GaN by RF-Molecular Beam Epitaxy and Improvement of Crystal Quality by Migration Enhanced Epitaxy. *Physica Status Solidi A - Applications and Materials Science* **176** (1), 323–328 (1999). Cited on page/s 134.

[29] M. Rybin, A. Pereyaslavtsev, T. Vasilieva, V. Myasnikov, I. Sokolov, A. Pavlova, E. Obraztsova, A. Khomich, V. Ralchenko, and E. Obraztsova. Efficient nitrogen doping of graphene by plasma treatment. *Carbon* **96**, 196–202 (2016). Cited on page/s 135, 138, 139.

[30] Y.-C. Lin, C.-Y. Lin, and P.-W. Chiu. Controllable graphene N-doping with ammonia plasma. *Applied Physics Letters* **96** (13), 133110 (2010). Cited on page/s 135, 139.

[31] J.-J. Zheng and Y.-J. Lin. Tuning the work function of graphene by nitrogen plasma

treatment with different radio-frequency powers. *Applied Physics Letters* **104** (23), 233103 (2014). Cited on page/s 135, 139.

[32] M.A Baker, P Hammer, C Lenardi, J Haupt, and W Gissler. Low-temperature sputter deposition and characterisation of carbon nitride films. *Surface and Coatings Technology* **97** (1), 544 – 551 (1997). Cited on page/s 135.

[33] K. Kishino, A. Kikuchi, H. Sekiguchi, and S. Ishizawa. InGaN/GaN nanocolumn LEDs emitting from blue to red. In *Proc. SPIE 6473, Gallium Nitride Materials and Devices II* volume 6473 pages 64730T–1. SPIE (2007). Cited on page/s 136.

[34] Y. Zhang, Q. Fu, Y. Cui, R. Mu, L. Jin, and X. Bao. Enhanced reactivity of graphene wrinkles and their function as nanosized gas inlets for reactions under graphene. *Physical Chemistry Chemical Physics* **15** (43), 19042–19048 (2013). Cited on page/s 136.

[35] Y. Gohda and S. Tsuneyuki. Structural phase transition of graphene caused by GaN epitaxy. *Applied Physics Letters* **100** (5), 053111 (2012). Cited on page/s 136.

[36] X. J. Chen, G. Perillat-Merceroz, D. Sam-Giao, C. Durand, and J. Eymery. Homoepitaxial growth of catalyst-free GaN wires on N-polar substrates. *Applied Physics Letters* **97** (15), 151909 (2010). Cited on page/s 136.

[37] A. Urban, J. Malindretos, J. H. Klein-Wiele, P. Simon, and A. Rizzi. Ga-polar GaN nanocolumn arrays with semipolar faceted tips. *New Journal of Physics* **15** (5), 053045 (2013). Cited on page/s 136.

[38] R. G. Banal, M. Funato, and Y. Kawakami. Initial nucleation of AlN grown directly on sapphire substrates by metal-organic vapor phase epitaxy. *Applied Physics Letters* **92** (24), 241905 (2008). Cited on page/s 136.

[39] P. Y. Huang, *et al.* Grains and grain boundaries in single-layer graphene atomic patchwork quilts. *Nature* **469** (7330), 389–392 (2011). Cited on page/s 136.

[40] K. Nakada and A. Ishii. Migration of adatom adsorption on graphene using DFT calculation. *Solid State Communications* **151** (1), 13–16 (2011). Cited on page/s 136.

[41] E. Iliopoulos and T. D. Moustakas. Growth kinetics of AlGaN films by plasma-assisted molecular-beam epitaxy. *Applied Physics Letters* **81** (2), 295–297 (2002). Cited on page/s 136.

[42] Z. Y. Al Balushi, T. Miyagi, Y.-C. Lin, K. Wang, L. Calderin, G. Bhimanapati, J. M. Redwing, and J. A. Robinson. The impact of graphene properties on GaN and AlN nucleation. *Surface Science* **634**, 81–88 (2015). Cited on page/s 136, 138, 142.

[43] A. Tabata, R. Enderlein, J. R. Leite, S. W. da Silva, J. C. Galzerani, D. Schikora, M. Kloidt, and K. Lischka. Comparative Raman studies of cubic and hexagonal GaN epitaxial layers. *Journal of Applied Physics* **79** (8), 4137–4140 (1996). Cited on page/s 137.

[44] T. Sekine, S. Suzuki, H. Kuroe, M. Tada, A. Kikuchi, and K. Kishino. Raman Scattering in GaN Nanocolumns and GaN/AlN Multiple Quantum Disk Nanocolumns. *e-Journal of Surface Science and Nanotechnology* **4**, 227–232 (2006). Cited on page/s 137.

[45] T. Sekine, Y. Komatsu, R. Iwaya, H. Kuroe, A. Kikuchi, and K. Kishino. Surface Phonons Studied by Raman Scattering in GaN Nanostructures. *Journal of the Physical Society of Japan* **86** (7), 074602 (2017). Cited on page/s 137.

[46] M. M. Bulbul, S. R. P. Smith, B. Obradovic, T. S. Cheng, and C. T. Foxon. Raman spectroscopy of optical phonons as a probe of GaN epitaxial layer structural quality. *The European Physical Journal B - Condensed Matter and Complex Systems* **14** (3), 423–429 (2000). Cited on page/s 137.

[47] C. Kisielowski, *et al.* Strain-related phenomena in GaN thin films. *Physical Review B* **54** (24), 17745–17753 (1996). Cited on page/s 137.

[48] L. E. McNeil, M. Grimsditch, and R. H. French. Vibrational Spectroscopy of Aluminum Nitride. *Journal of the American Ceramic Society* **76** (5), 1132–1136 (1993). Cited on page/s 137.

[49] L. M. Malard, M. A. Pimenta, G. Dresselhaus, and M. S. Dresselhaus. Raman spectroscopy in graphene. *Physics Reports* **473** (5–6), 51–87 (2009). Cited on page/s 137, 138.

[50] D. Wei, Y. Liu, Y. Wang, H. Zhang, L. Huang, and G. Yu. Synthesis of N-Doped Graphene by Chemical Vapor Deposition and Its Electrical Properties. *Nano Letters* **9** (5), 1752–1758 (2009). Cited on page/s 138, 139.

[51] T. Schiros, *et al.* Connecting Dopant Bond Type with Electronic Structure in N-Doped Graphene. *Nano Letters* **12** (8), 4025–4031 (2012). Cited on page/s 139.

[52] Z. Jin, J. Yao, C. Kittrell, and J. M. Tour. Large-Scale Growth and Characterizations of Nitrogen-Doped Monolayer Graphene Sheets. *ACS Nano* **5** (5), 4112–4117 (2011). Cited on page/s 139.

[53] M. Wu, C. Cao, and J. Z. Jiang. Light non-metallic atom (B, N, O and F)-doped graphene: a first-principles study. *Nanotechnology* **21** (50), 505202 (2010). Cited on page/s 139.

[54] Z. Luo, S. Lim, Z. Tian, J. Shang, L. Lai, B. MacDonald, C. Fu, Z. Shen, T. Yu, and J. Lin. Pyridinic N doped graphene: synthesis, electronic structure, and electrocatalytic property. *Journal of Materials Chemistry* **21** (22), 8038–8044 (2011). Cited on page/s 139.

[55] J. Liu, Q. Li, Y. Zou, Q. Qian, Y. Jin, G. Li, K. Jiang, and S. Fan. The Dependence of Graphene Raman D-band on Carrier Density. *Nano Letters* **13** (12), 6170–6175 (2013). Cited on page/s 139.

[56] G. Sarau, M. Heilmann, M. Bashouti, M. Latzel, C. Tessarek, and S. Christiansen. Efficient Nitrogen Doping of Single-Layer Graphene Accompanied by Negligible Defect Generation for Integration into Hybrid Semiconductor Heterostructures. *ACS Applied Materials & Interfaces* **9** (11), 10003–10011 (2017). Cited on page/s 139.

[57] Z. H. Ni, W. Chen, X. F. Fan, J. L. Kuo, T. Yu, A. T. S. Wee, and Z. X. Shen. Raman spectroscopy of epitaxial graphene on a SiC substrate. *Physical Review B* 77 (11), 115416 (2008). Cited on page/s 139.

[58] T. Shimada, *et al.* Origin of the 2450 cm^{-1} Raman bands in HOPG, single-wall and double-wall carbon nanotubes. *Carbon* **43** (5), 1049–1054 (2005). Cited on page/s 139.

[59] M. A. Reshchikov, D. Huang, F. Yun, H. Morkoç, R. J. Molnar, and C. W. Litton. Excitons bound to structural defects in GaN. *MRS Proceedings* **693**, I6.28.1 (2011). Cited on page/s 140, 141.

[60] I. Shogo, N. Taihei, S. Nobuhiko, A. Hyung Soo, I. Masashi, H. Toshiki, H. Yoshio, Y. Masahito, and A. Hiroshi. Nature of yellow luminescence band in GaN grown on Si substrate. *Japanese Journal of Applied Physics* **53** (11S), 11RC02 (2014). Cited on page/s 141.

[61] D. O. Demchenko, I. C. Diallo, and M. A. Reshchikov. Yellow Luminescence of Gallium Nitride Generated by Carbon Defect Complexes. *Physical Review Letters* **110** (8), 087404 (2013). Cited on page/s 141.

Chapter 7

The influence of AlN buffer layer on the growth of self-assembled GaN nanocolumns on graphene

Andreas Liudi Mulyo[1,2], Mohana Krishnappa Rajpalke[1,5], Per Erik Vullum[3], Helge Weman[1], Katsumi Kishino[2,4,6*] and Bjørn-Ove Fimland[1*]

First published in: *Scientific Reports* **10**, 853 (2020).
DOI: 10.1038/s41598-019-55424-z

Contributions

HW conceived the initial research idea and **ALM** planned the study. **ALM** performed RF-PAMBE growth under supervision from HW, KK and BOF. **ALM** conducted SEM characterizations. PEV carried out TEM experiments. MR performed HRXRD measurements. **ALM** conducted RT micro-photoluminescence and micro-Raman characterizations. **ALM** prepared all the figures and wrote the first version of the manuscript. All authors have discussed the results, commented on them and given approval to the final version of the manuscript.

---

[1] Department of Electronic Systems, Norwegian University of Science and Technology (NTNU), NO-7491, Trondheim, Norway. [2] Department of Engineering and Applied Sciences, Sophia University, 102-8554, Tokyo, Japan. [3] SINTEF Industry, NO-7465, Trondheim, Norway. [4] Sophia Nanotechnology Research Center, Sophia University, 102-8554, Tokyo, Japan. [5] Present address: Microsoft Quantum Materials Lab, Niels Bohr Institute, University of Copenhagen, 2100, Copenhagen, Denmark. [6] Present address: Sophia University, 102-8554, Tokyo, Japan. [*] e-mail: kishino@sophia.ac.jp; bjorn.fimland@ntnu.no

ABSTRACT

GaN nanocolumns were synthesized on single-layer graphene via radio-frequency plasma-assisted molecular beam epitaxy, using a thin migration-enhanced epitaxy (MEE) AlN buffer layer as nucleation sites. Due to the weak nucleation on graphene, instead of an AlN thin-film we observe two distinguished AlN formations which affect the subsequent GaN nanocolumn growth: (i) AlN islands and (ii) AlN nanostructures grown along line defects (grain boundaries or wrinkles) of graphene. Structure (i) leads to the formation of vertical GaN nanocolumns regardless of the number of AlN MEE cycles, whereas (ii) can result in random orientation of the nanocolumns depending on the AlN morphology. Additionally, there is a limited amount of direct GaN nucleation on graphene, which induces non-vertical GaN nanocolumn growth. The GaN nanocolumn samples were characterized by means of scanning electron microscopy, transmission electron microscopy, high-resolution X-ray diffraction, room temperature micro-photoluminescence, and micro-Raman measurements. Surprisingly, the graphene with AlN buffer layer formed using less MEE cycles, thus resulting in lower AlN coverage, has a lower level of nitrogen plasma damage. The AlN buffer layer with lowest AlN coverage also provides the best result with respect to high-quality and vertically-aligned GaN nanocolumns.

7.1 INTRODUCTION

Recent progresses in the growth of GaN thin-film on graphene [1–6] increasingly justify the possibility for graphene to be a good alternative substrate over the available conventional substrates, for instance Si [7,8], SiC [9] and sapphire [10]. It is also reported that GaN thin-film is achievable on sapphire or amorphous substrates by employing either multi-layer or single-layer graphene as buffer layer [11–14]. Such exploitations can be realized by taking advantage of the weak quasi-van der Waals binding [15–17] which can drastically relax the lattice matching condition to be satisfied by constituent materials. That being said, the lack of chemical reactivity of graphene and its extremely low surface energy [18] greatly disrupt the nucleation process of GaN, resulting in a low nucleation density [19] and difficulty in controlling the stacking sequence of the GaN growth [3]. The latter issue, which often manifests in the form of stacking faults [3,5] or threading dislocations [1,4,17], can possibly be suppressed by growing nanowire or nanocolumn structures [16,20–25]. Nevertheless, because of the absence of dangling bonds in graphene, nanocolumns are often aligned in non-vertical directions [26–28] and/or have low density [27,29]. Both problems are required to be addressed in order to demonstrate that the growth of III-N semiconductor nanostructures, particularly nanocolumns, utilizing graphene as the substrate can be further considered as an alternative platform in enabling the advancement of optoelectronic device performance and functionality, for instance light-emitting diodes[30].

In this regard, the introduction of defects in graphene by means of plasma treatments could alleviate the issue of absence of dangling bonds in graphene. In case of GaN grown by metal-organic vapor phase epitaxy (MOVPE), the creation of dangling bonds in graphene by this method has been achieved via *ex-situ* manner[4,14]. However, the plasma treatments to prepare the growth of GaN on graphene in radio-frequency plasma-assisted molecular beam epitaxy (RF-PAMBE), which is typically done *in-situ*, often lead to the generation of more severe plasma-induced damage of graphene[28,31]. Moreover, it has been evidenced that the GaN nanocolumns may be randomly oriented if the growth is done directly on graphene[27,28]. The use of a thin AlN buffer layer can provide substantial protection to the graphene from the direct bombardment of nitrogen plasma and enable the growth of high-density, vertically-aligned GaN nanocolumns on graphene[27,28]. Therefore, it is now perceived that the understanding of AlN as an intermediate layer in the GaN/graphene system is necessary to grasp the growth behavior of the GaN nanocolumns in relation to the graphene properties at a given growth condition. Furthermore, it is expected that the insight towards these aspects can shed light on the preference of certain growth conditions over others, which later can be utilized for growing device structures.

In the present work, we concentrate on the RF-PAMBE synthesis of self-assembled GaN nanocolumns on transferred single-layer graphene on silica glass for different AlN growth conditions. An insight towards the relation between the AlN migration-enhanced epitaxy (MEE) cycles and the morphology of the AlN buffer layer, as well as the resulting structural and optical properties of the grown GaN nanocolumns on graphene with AlN used as an intermediate layer, is reported. Additionally, the impact of the AlN buffer layer growth on graphene structural properties is presented.

7.2 RESULTS AND DISCUSSION

The morphology of the thin AlN buffer layer formed on the graphene surface using MEE by RF-PAMBE technique was studied as a function of the amount of AlN deposited, defined by the number of MEE cycles. Details concerning the growth parameters for the AlN buffer layer are outlined in Methods. Three different AlN samples, namely A1, A2 and A3, with respectively 20, 40 and

80 MEE cycles, were grown and characterized. Figure 7.1(a,d), (b,e) and (c,f) depict top- and bird's eye-view scanning electron microscopy (SEM) images of samples A1, A2 and A3, respectively. In sample A1 there are still numerous areas of exposed graphene (marked with yellow dashed outline). These areas are reduced with the increasing number of MEE cycles, as shown in sample A2 and further A3. We note that there are two distinct arrangements of AlN on graphene. The *first feature* is the nucleation of high-density and irregular AlN nanostructures along the line defects of graphene (e.g., marked with the yellow lines), which is similar to the cases of AlGaN nucleation by MOVPE on graphene[29]. Commonly, line defects observed in chemical vapor deposition (CVD)-graphene are wrinkles and grain boundaries[32–34]. In addition to the surface morphology of the copper foil and the transfer process[34], the wrinkles are often related with the compressive stress caused by the difference in thermal expansion coefficients between graphene and the copper foil during cooling from CVD growth temperature to room temperature (RT)[35]. The grain boundaries are formed as a result of coalesced graphene grains which are grown on the different copper facets during the CVD growth process[36]. These areas of graphene likely contain defects, which can eventually create dangling bonds to support covalent/chemical bonding of atoms, resulting in a high nucleation density of AlN nanostructures on those particular graphene sites. From bird's eye-view SEM images, one clearly sees how the nucleation of AlN nanostructures spreads further away from the line defects with the increase of MEE cycles (e.g., marked with the yellow arrows). This will eventually cover the graphene surface, as shown in sample A2, and furthermore in sample A3.

The *second feature* is the formation of individual AlN islands (e.g., marked with the yellow contours). Unlike the high-density AlN nanostructures along the graphene line defects described above, their size are quite significant, with average diameters of approximately 70, 120 and 200 nm for samples A1, A2 and A3, respectively. In addition to the formation of individual AlN islands, it is also possible for the AlN islands to merge with their nearest vicinity to form coalesced AlN islands (e.g., marked with the orange contours). A tendency for AlN to form an island (and its cluster formation) instead of a thin-film could be caused by the extremely low surface energy (lack of dangling bonds/chemical inertness) of graphene[18], which promotes the high surface tension on graphene surface. In addition, the lack of dangling bonds in these graphene surface areas hampers the AlN nucleation process to form a continuous thin-film structure, contrary to the formation of high-density AlN nanostructures in which the dangling bonds are provided by the defects along the graphene line defects. As opposed to this, when the MEE technique was applied to grow AlN on a sapphire substrate at a similar substrate temperature, it resulted in large island sizes and good coverage on the substrate surface[37].

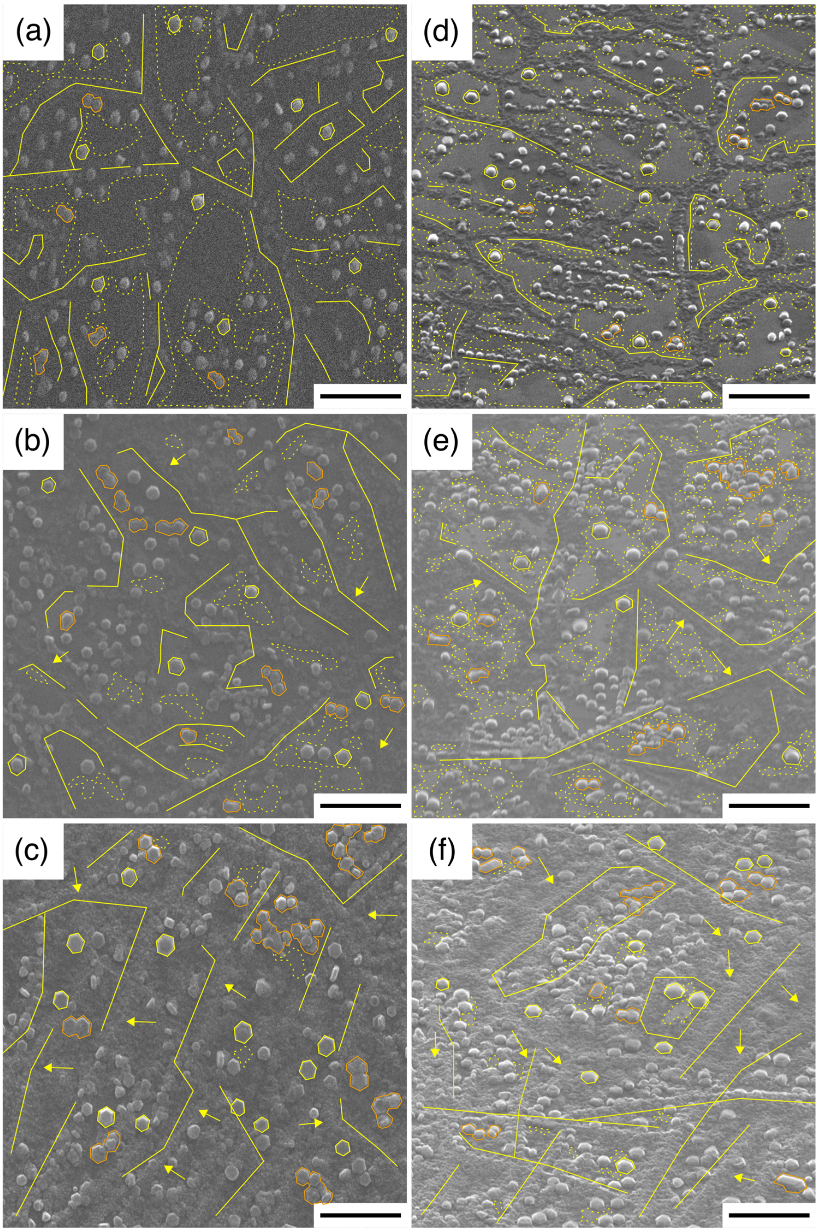

Figure 7.1. SEM images of AlN on graphene formed via different MEE cycles. (**a**,**d**), (**b**,**e**) and (**c**,**f**) are (top-, bird's eye-view) SEM images of samples A1, A2 and A3, respectively. Scale bars are 1 μm. Features marked with yellow lines, yellow (orange) contours and yellow dashed outlines are high-density AlN nanostructures grown along line defects of graphene, individual (coalesced) AlN islands and areas of exposed graphene, respectively. Yellow arrows in samples A2 and A3 show the lateral growth of AlN nanostructures that initially nucleate at the line defects of graphene in sample A1.

Further RF-PAMBE growth of GaN nanocolumns was then carried out on samples A1, A2 and A3, after which they were re-named as G1, G2 and G3, respectively. In order to gain insight into the influence of the AlN buffer layer on the formation of GaN nanocolumns, the growth conditions of GaN nanocolumns on samples G1, G2 and G3 were kept the same (described in Methods). The representative top- and bird's eye-view SEM images for samples G1, G2 and G3 are given in Figure 7.2(a,d), (b,e) and (c,f), respectively. We notice that the nanocolumns follow a particular arrangement which resembles the previously grown AlN buffer layer. The *first group of features* is the row of high-density vertical GaN nanocolumn growth (e.g., marked with the yellow lines), where nanocolumn diameters vary from 50 to 70 nm. More often, these nanocolumns are found to be grown very close to their neighbor, which is very likely to form coalesced nanocolumn structures, rather than single isolated nanocolumns. Such formation of coalesced GaN nanocolumn structures is clearly visible in sample G1. When formed on 40 MEE cycles AlN buffer (sample G2), it becomes more difficult to discern the rows of vertical GaN nanocolumns, since the density of the nanocolumn structures in general is increased. However, this unique pattern is still observable if one follows the GaN nanocolumns lining with each other, where the nanocolumns have a tendency to coalesce with their vicinity. Interestingly, GaN nanocolumns in sample G3, which has the highest number of AlN MEE cycles, do not meet the expectation of being the most coalesced nanocolumns, forming GaN nanowall-like structures, but rather display nanocolumn structures with identical diameters to those of sample G1.

The *second group of features* is the individual vertical GaN nanocolumns (e.g., marked with the yellow circles). It appears that the number of MEE cycles during AlN formation affects the diameter of the grown nanocolumns, where less cycles give smaller diameter. It is found that the GaN nanocolumns in samples G1, G2 and G3 show average diameters of 90, 130 and 210 nm, respectively. Additionally, it is discovered that there are certain nanocolumns (e.g., marked with the orange contours) whose diameter is considerably larger than the mentioned average values. Some of them seem to result from single nanocolumn growth which eventually merges with other nanocolumns in its proximity forming an irregular shape, while there are also circular-shaped nanocolumns where the coalescence process likely starts immediately from the nucleation stage. It should be remarked that GaN nanotubular-like structures (white outlines) can also be formed[38] because the edge of the AlN islands can initiate GaN nanocolumn growth[39]. The *third group of features* is the formation of tilted nanocolumns (see areas marked with yellow dashed outlines in Figure 7.2) that have an average diameter of 70 nm for all three G-samples. Overall, samples G1 and G2 exhibit less tilted nanocolumns compared to sample G3, where tilted nanocolumns dominate over the vertical ones. Representative

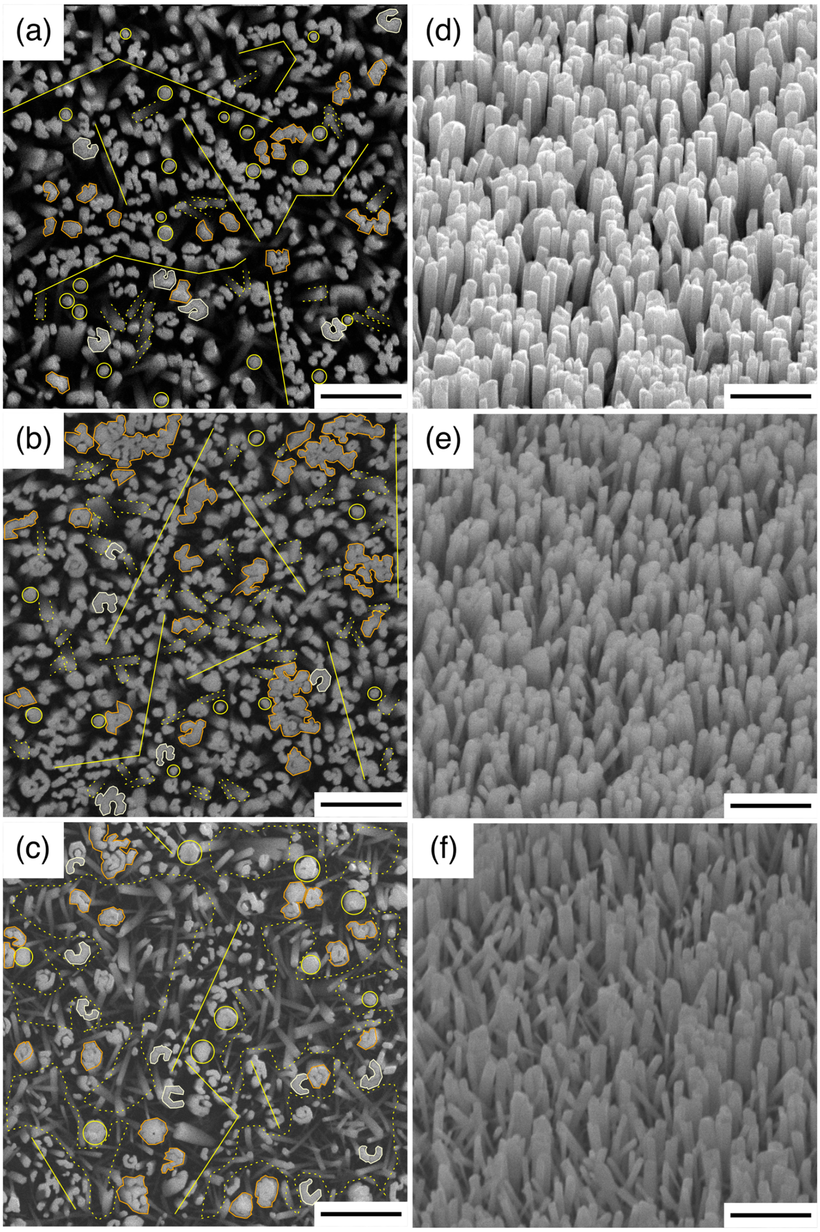

FIGURE 7.2. SEM images of GaN nanocolumns on graphene formed via different AlN MEE cycles. (**a**,**d**), (**b**,**e**) and (**c**,**f**) are (top-, bird's eye-view) SEM images of samples G1, G2 and G3, respectively. Scale bars are 1 μm. Yellow lines, yellow circles (orange contours) and yellow dashed outlines indicate row of high-density vertical GaN nanocolumns, individual (coalesced) vertical GaN nanocolumns and areas with individual tilted GaN nanocolumns, respectively. White outlines in sample G3 indicate the GaN nanotubular-like structures.

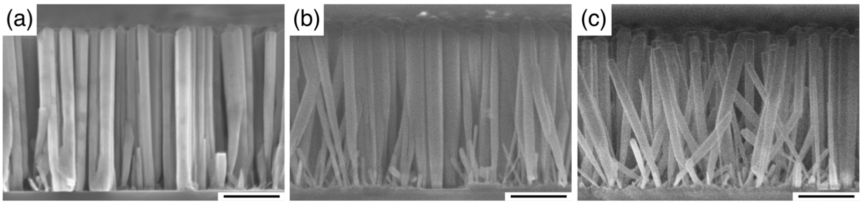

FIGURE 7.3. Cross-sectional SEM images of GaN nanocolumns on graphene formed via different AlN MEE cycles. Samples (**a**) G1, (**b**) G2, and (**c**) G3. Scale bars are 500 nm.

cross-sectional SEM images of samples G1, G2 and G3 in Figure 7.3(a–c), respectively, also show this. The average length (height) of the vertical GaN nanocolumns (first and second group) is around 1400 nm, while the length of tilted nanocolumns (third group) varies from 175 to 1400 nm. The large variation noticed in the latter group of nanocolumns is possibly caused by a shadowing effect during the GaN growth. With increased number of MEE cycles, the AlN surface turns rougher and the tilted nanocolumns in the G-samples become more discernible.

Based on the SEM observations in Figure 7.1-Figure 7.3, an illustrative representation of the AlN buffer layer and GaN nanocolumn growth on graphene is presented in Figure 7.4. The MEE growth of an AlN buffer layer in sample A1 results in the formation of AlN islands and a high density of AlN nanostructures (growing along the graphene line defects). A higher number of MEE cycles generally increases the lateral size and the density of these AlN features, which could lead to coalesced structures. This will eventually reduce the area of exposed graphene, until it is finally almost absent in sample A3 (Figure 7.1(c,f)). For the subsequent GaN growth, it is likely that the single vertical GaN nanocolumn structures (indicated by white color in Figure 7.4) nucleated on the AlN islands, as the average GaN nanocolumn diameter is comparable to that of the AlN islands. The same applies to those grown on the coalesced AlN islands, resulting in coalesced nanocolumns (indicated by green color in Figure 7.4). Next, the row of high-density GaN nanocolumns (indicated by purple color in Figure 7.4) most likely forms on the high-density AlN nanostructures. Vertical nanocolumns are expected to form here, however it is possible to get tilted ones as well due to the misalignment of the AlN lattice formed on defective graphene areas[40], including graphene line defects. The latter becomes more pronounced with a higher number of AlN MEE cycles, especially in sample G3 (Figure 7.4(c)). Indeed, randomly-aligned nanocolumn growth could be also due to limited direct nucleation of GaN on exposed graphene (indicated by the cyan color in Figure 7.4(a,b)), however this is not likely for sample G3 since the AlN covers nearly the whole graphene surface. It might be that the rough surface

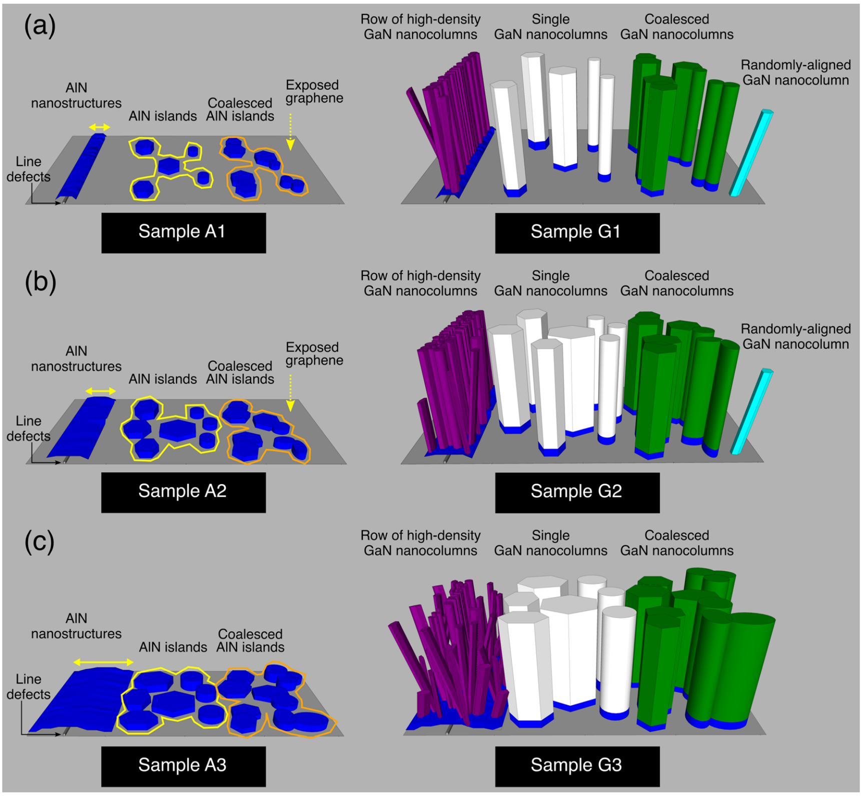

Figure 7.4. Simplified schematics of the AlN buffer structures and GaN nanocolumn formation on graphene. Samples (**a**) A1-G1, (**b**) A2-G2 and (**c**) A3-G3. There are two possible AlN (blue) nanostructures forming on graphene: 1) AlN islands and 2) AlN nanostructures along the line defects of graphene (the yellow arrows indicate their lateral growth spread further away from the line defects). Single (white) and coalesced (green) vertical GaN nanocolumn structures are nucleated from the AlN islands, while row of high-density nanocolumns (purple) form on the AlN nanostructures that spread from the line defects. Additional tilted nanocolumns (cyan) are likely to grow on exposed graphene.

(many crystallites of irregular shape) of AlN nanostructures, which are formed near (but away) from the graphene line defects induces the deterioration of GaN nanocolumn growth orientation.

A separate nanocolumn sample was synthesized with nominally the same growth conditions as sample G1 for transmission electron microscopy (TEM) measurements. The cross-sectional high-angle annular dark field scanning TEM (HAADF STEM) image of Figure 7.5(a) depicts that most of the observed nanocolumns exhibit a perpendicular growth direction with respect to the substrate (exemplified by star-marked and purple arrows). The average height of the nanocolumns is 400 nm shorter than for the nanocolumns in sample

G1. This difference could be caused by a reduced growth rate (after chamber maintenance) during the growth of the sample for the TEM measurements. Additionally, the image reveals irregular GaN nanostructures like short inclined GaN nanocolumns (red arrows) and GaN islands/crystallites (brown arrows). Two GaN nanocolumns with star symbol (yellow frame in Figure 7.5(a)) are closely examined in Figure 7.5(b). At the base there is an area of darker contrast, attributed to AlN owing to the atomic number difference between Al and Ga (the intensity contrast in HAADF STEM images scales approximately with Z^2, where Z = the atomic number). Simultaneous energy dispersive spectroscopy (EDS) and electron energy-loss spectroscopy (EELS) were carried out on the same area to map all present elements. The Ga, Al and O element maps are combined into a color map in Figure 7.5(c), which clearly shows that Al (blue) appears at the base of nanocolumns (with a measured height and diameter of ~10 and ~65 nm, respectively), and Ga (green) is identified at the nanocolumn regions. Interestingly, no trace of any Al signal is detected in between the GaN nanocolumns or in the region outside the area where the vertical GaN nanocolumns are successfully synthesized. O (red) is detected in the silica glass substrate, as expected. Before this discussion is continued, we would like to point out that the vertical GaN nanocolumns marked by purple arrows in Figure 7.5(a) have a top diameter of 50–70 nm, which is smaller than for the GaN nanocolumns marked with star symbol (average diameter of 90 nm). Based on the SEM observations explained in Figure 7.2(a), there is a high probability that this group of GaN nanocolumns is grown on AlN nanostructures on or near line defects of the graphene.

A higher magnification of the GaN nanocolumn interface area (green frame in Figure 7.5(b)) is presented in Figure 7.5(d) together with six different element maps (Ga, Al, N, C, Si and O) of the blue framed area. Here, one can clearly distinguish that the AlN island acts as a nucleation site for the GaN nanocolumn. Three things to note from the elemental mapping observation: 1) A sharp interface separates Ga in the GaN nanocolumn and Al in the AlN island with no severe intermixing between them; 2) N is distributed evenly in the GaN nanocolumn regions and AlN island; 3) A distinct signal from C, implying the existence of graphene between the silica glass (Si, O) and the AlN island. Figure 7.5(e) presents a close-up image from the light-blue framed area in Figure 7.5(a). Whereas intensity contrasts reveal the presence of AlN islands within the cyan frames, no indication of an AlN island is observed at the base of the inclined GaN nanocolumn marked with a yellow-dashed line. Moreover, its diameter of 50 nm is similar to the dimensions of the tilted GaN nanocolumns described in Figure 7.2. Next to this tilted GaN nanocolumn, there are broken parts of other GaN nanocolumns (red frame) which are nucleated on the same AlN island. The GaN nanocolumn that appears to be on top of these parts (dark-yellow dashed

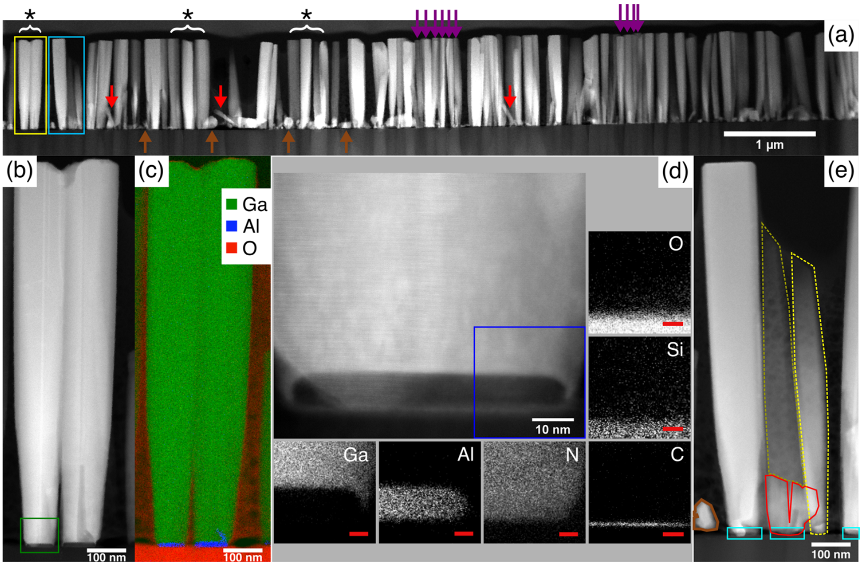

Figure 7.5. TEM image of GaN nanocolumn sample synthesized with nominally the same growth conditions as sample G1. (**a**) Overview cross-sectional HAADF STEM image, showing vertical GaN nanocolumns (star-marked and purple arrows), inclined GaN nanocolumns (red arrows) and GaN crystallites (brown arrows). (**b**) HAADF STEM image of two GaN nanocolumns within yellow frame in **a**. (**c**) Combined color map of the Ga (green), Al (blue) and O (red) elemental distributions (EDS/EELS) on the corresponding region in **b**. (**d**) Magnified image of the lower part of the GaN nanocolumn near the interface of the left GaN nanocolumn in **b** (green frame), with the elemental mapping near the interfaces between the GaN nanocolumn, AlN island, graphene and silica glass (blue frame) by EDS (Ga, Al, Si) and EELS (N, O, C). The red scale bars are 5 nm. (**e**) HAADF STEM image of the GaN nanocolumns that is light-blue framed in **a**. The inclined GaN nanocolumn (yellow-dashed line) is possibly directly nucleated on graphene (indicated by the absence of any AlN layer [cyan frames] at the base). There are two broken GaN nanocolumns (red framed area) sharing the same AlN island and another inclined GaN nanocolumn (dark-yellow dashed line) in the background. An irregular GaN crystallite (brown outline) likely grown directly on graphene is also observed.

line) is a different GaN nanocolumn located in the background. Notice as well the irregular GaN crystallite to the left (brown outline) which also does not have AlN underneath it. In similar fashion, other inclined GaN nanocolumns (red arrows) and GaN crystallites (brown arrows) shown in Figure 7.5(a) could have had their nucleation occurring directly on the graphene.

From the intense peak observed at 34.56° in the 2θ-ω high-resolution X-ray diffraction (HRXRD) scans presented in Figure 7.6(a), it is confirmed that all the GaN nanocolumn samples demonstrate growth orientation along the *c*-axis of the wurtzite GaN structure. Aside from this peak, a weak peak detected at ~36° is assigned to wurtzite AlN with the same crystal orientation as the GaN. Despite of these similarities, we find that the AlN buffer layer

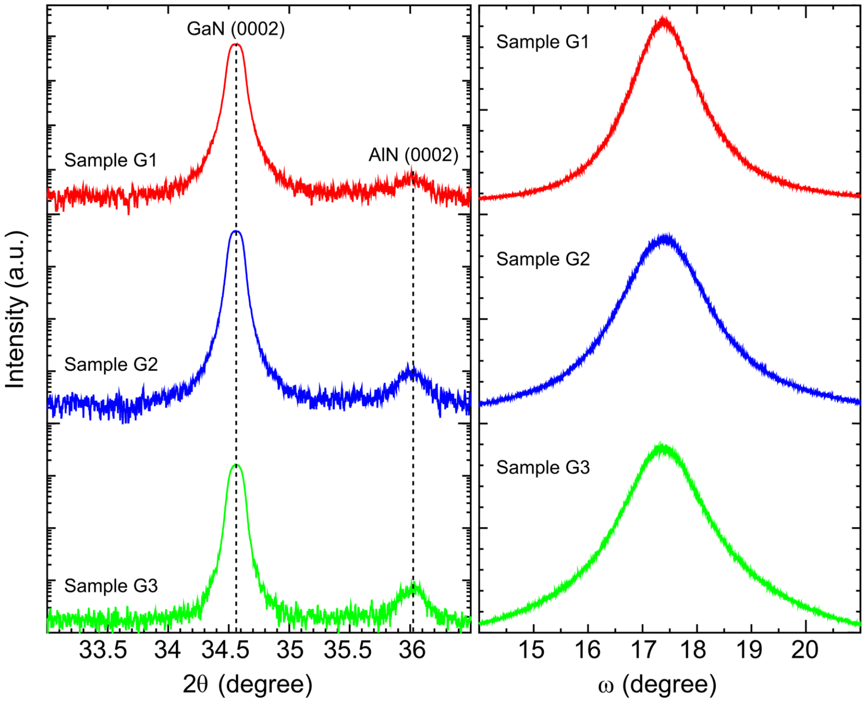

FIGURE 7.6. HRXRD measurements of the nanocolumns. (**a**) 2θ-ω scanning curve and (**b**) ω scanning curve of samples G1, G2 and G3.

formed using different number of MEE cycles influences the GaN signals. The peak intensity of the 0002 diffraction of GaN is found to be highest for sample G1 and lowest for sample G3. Since this peak only represents signal from the planes normal to the *c*-axis (i.e. the 0002 reflection) of the GaN crystal, it indicates that sample G1 with 20 AlN MEE cycles has the highest density of vertical nanocolumns (since the SEM characterization presented above show that G1 has the lowest average GaN nanocolumn diameter [90 nm] among the G-samples). We note that whereas the peak intensity of the AlN 0002 reflection is higher for sample G2 than for sample G1, there is not much difference in this peak between sample G2 and sample G3, despite higher number of AlN MEE cycles for sample G3 and improved graphene coverage surface area (Figure 7.1). It is possibly mostly reflection from AlN islands that contributes significantly to this peak, since the crystalline quality of AlN nanostructures grown on graphene defects is most likely polycrystalline[40]. (We should here point out that the 2θ-ω scans presented in Figure 7.6(a) were recorded with a wider receiving slit than the normal [0.6 mm vs. 0.1 mm, respectively], in order to record the weak signal from the AlN buffer. Using the wider slit causes the peaks to be slightly broadened, as is seen by the "rounded out" top of the peak.)

The ω (rocking) scans of the GaN, shown in Figure 7.6(b) with peaks centered at 17.28°, reveal that the full-width at half-maximum (FWHM) broadens with the higher number of AlN MEE cycles, increasing from 1.6 to 2.3 and 2.4° for samples G1, G2 and G3, respectively. The larger FWHM shown by the GaN nanocolumns in samples G2 and G3 relative to G1 indicates poorer orientation, i.e. larger GaN nanocolumn tilt distribution in samples G2 and G3. (0.1 mm receiving slit width was used for recording the rocking curves presented in Figure 7.6(b)).

Room temperature micro-photoluminescence measurements from the reference sample, samples G1, G2 and G3 clearly show distinguished emission peaks at 363.6, 364.6, 364.5 and 364.5 nm, respectively (Figure 7.7), and can be associated with wurtzite GaN. In terms of linewidths, GaN nanocolumns in samples G1, G2 and G3 demonstrate narrower FWHM compared to the freestanding hydride vapor-phase epitaxy (HVPE)-GaN bulk substrate reference sample, being respectively 9.02, 10.17 and 8.62 nm, against 10.79 nm. The peak intensity of the GaN near band-edge emission among the GaN nanocolumn samples is highest for sample G1, which is almost two times more intense than that of the reference sample. Unlike for sample G1, emissions of GaN nanocolumns in samples G2 and G3 exhibit approximately similar peak intensity with the reference sample. Such unexpected low emission peak intensity from the GaN nanocolumn structure in these two samples is possibly caused by two separate driving factors. GaN nanocolumns in sample G2 (Figure 7.2(b)) are shown to have a higher degree of coalescence relative to that of samples G1 and G3 (Figure 7.2(a,c)), which can lead to the degradation of crystalline quality via formation of defects or dislocations[24]. For sample G3, the grown GaN nanocolumns characterized with lower density (Figure 7.2(c)), and shorter nanocolumn height compared to sample G1 (Figure 7.3(c)), thus inducing smaller excitation volume[41], could potentially reduce the photoluminescence intensity.

None of the G-samples show any emission at 386 nm which is related to the GaN zinc blende crystal phase[3,42]. Unlike the reference sample, the GaN nanocolumn samples G1 and G3 do not display any shoulder peak at 369 nm, which is attributed to excitons bound to structural defects[43]. Apparently there is a faint “bump” in the spectrum of sample G2 related to dislocation-related emission, which is likely correlated with the higher defect density due to more nanocolumns being coalesced as to that of nanocolumns formed in samples G1 and G3. The distinct presence of green and yellow luminescence bands[44] in the reference sample covering the wavelengths from 465 to 570 nm (emphasized in the inset of Figure 7.7) is associated to isolated defects involving Ga vacancies and to the same defect bound to structural defects[45]. The absence of these broad bands in the GaN nanocolumn samples can also be an indication that

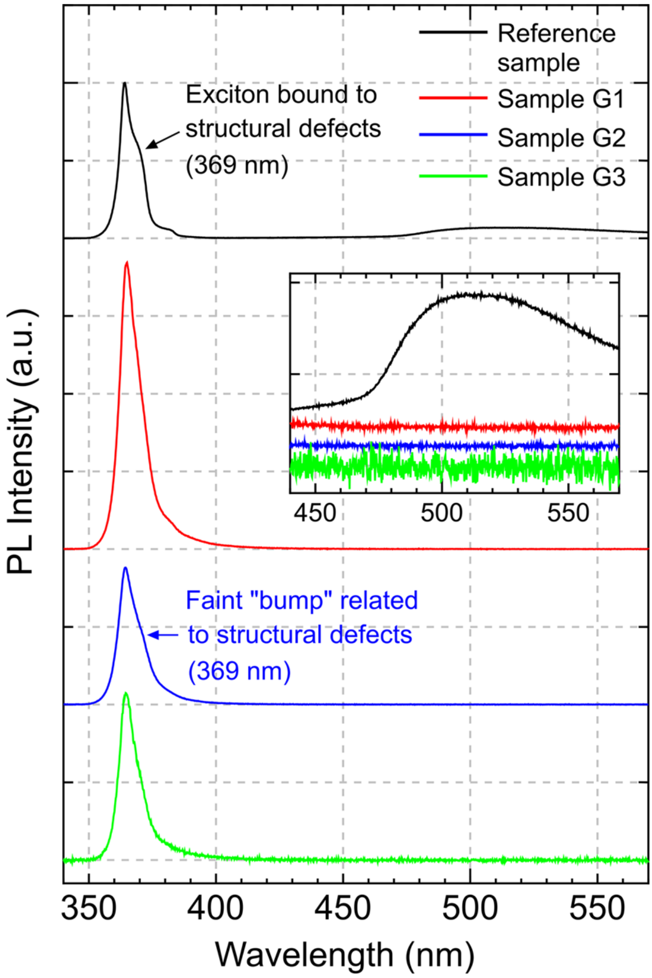

FIGURE 7.7. RT micro-photoluminescence spectra of reference sample (HVPE-freestanding GaN), samples G1, G2 and G3. Inset shows the magnified spectra in the wavelength range from 440 to 570 nm, highlighting the presence of broad green and yellow emission band in the reference sample.

the grown nanocolumns are free from threading edge dislocations[46].

Raman spectra of previously studied GaN nanocolumns, either grown in self-assembled manner with an AlN buffer layer on sapphire or Si substrates[47,48] or synthesized selectively using a Ti mask on GaN template/sapphire[49], demonstrate features at (531.5 ± 0.5), (557.9 ± 0.9) and (566 ± 1.0) cm^{-1}. These wave numbers correspond well to the established A_1 (transverse optical (TO)), E_1 (TO) and E_2 (high) phonon modes of wurtzite GaN, respectively[50–53]. In line with the former results, the as-grown GaN nanocolumns in samples G1, G2 and G3 likewise exhibit almost identical spectra. As presented in Figure 7.8(a), they

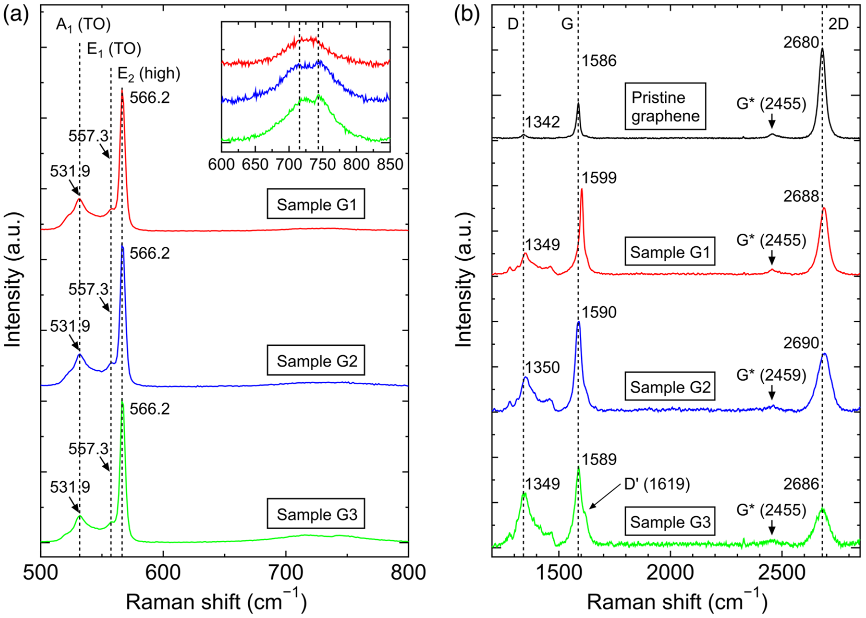

FIGURE 7.8. Micro-Raman spectroscopy of the nanocolumn samples, including the graphene for each respective sample. Raman spectra of (**a**) samples G1, G2 and G3 between 500 and 800 cm^{-1}, with the peak frequencies of the A$_1$ (TO), E$_1$ (TO) and E$_2$ (high) modes indicated by vertical dashed lines (inset: magnification from 600 to 850 cm^{-1}, with the identified peak frequencies at 715 and 743 cm^{-1} of the possible SO and LPP modes, respectively[48,52], indicated by vertical dashed lines), and (**b**) pristine graphene, samples G1, G2 and G3 between 1100 and 3200 cm^{-1}. The dashed lines indicate D, G and 2D peak positions of pristine graphene.

show the peaks at 531.9, 557.3 and 566.2 cm^{-1}. In addition, the E$_2$ (low) phonon mode (not shown in Figure 7.8(a)) is observed at 144 cm^{-1} [48,50]. Notice that the identified peak of E$_2$ (high) mode at 566.2 cm^{-1} and its small FWHM (~4.9 cm^{-1}, comparable to that of GaN nanocolumns on Si(001) and Si(111)[54]) correspond to the FWHM of a fully relaxed thick free-standing GaN layer[55], which can be an indicator of the high crystalline quality of the GaN nanocolumns. Furthermore, the TO phonon mode at 555 cm^{-1} related to zinc blende GaN[50,51] is not detected in any of the GaN nanocolumn samples. However, expected A$_1$ (longitudinal optical, LO) and E$_1$ (LO) phonon modes of GaN[50,51] at 734 and 741 cm^{-1} are not visible in any of the GaN nanocolumn samples, similar to the results obtained by Robins *et al.*[48] and Jeganathan *et al.*[52]. Instead, we notice very weak peaks at 715 cm^{-1} and 743 cm^{-1} (inset in Figure 7.8(a)) which might be related to the existence of surface optical (SO) and single LO or longitudinal phonon-plasmon (LPP) modes, respectively, whose frequencies and line widths are dependent on GaN carrier concentrations[48,52,53]. Further study is required to confirm this phenomenon.

In comparison with the pristine graphene reference sample (i.e. sample before any III-V growth), graphene structural properties after the GaN nanocolumn growth demonstrate quite significant alterations, as can be seen in Figure 7.8(b). A typical Raman spectrum of the pristine graphene[56] is strongly characterized with two main peaks, namely the G band (1586 cm^{-1}) and the 2D band (2680 cm^{-1}) with an intensity ratio of $I_{2D}/I_G \approx 2$, while the disorder-induced D band (1342 cm^{-1}) is barely seen, making the intensity ratio of I_D/I_G almost negligible. Changes to the aforementioned intensity ratios, peak positions and possible generation of another band are observed in all of the GaN nanocolumn samples (whereas a faint G* band at ~2456 cm^{-1} is unaffected). Firstly, the most prominent changes are the decline of the I_{2D}/I_G ratio along with an increasing I_D/I_G ratio from sample G1 to G2 and G3, implying that graphene becomes more defective as the number of AlN MEE cycles increases from 20 to 80. Secondly, another defect-related signature in graphene at 1619 cm^{-1}, known as D' band[56], is noticed only in sample G3. Finally, the peak positions of the D, G and 2D bands experience slight blue shifts, indicating a compressive strain and/or a modification of the carbon atoms in the graphene network by the incorporation of nitrogen atoms which could lead to an n-type doping[57]. Such blue-shifting peaks have been observed when an intentional plasma nitridation of graphene using either nitrogen[58] or ammonia[59] causes the introduction of defects as well as changes in the chemical and electronic properties of graphene. Indeed, in this work such nitridation process is an inevitable part of the GaN nanocolumn growth in RF-PAMBE, although during the AlN buffer layer formation the exposure of nitrogen plasma is intended for the nitridation of Al. As shown in Figure 7.1, one can evidently notice that the deposited Al could not form a continuous layer, particularly at lower numbers of MEE cycles. Thus, we cannot rule out the possibility of graphene being nitrided although it only occurs for three seconds per MEE cycle. With that in mind, it can be assumed that the higher number of MEE cycles could extend the duration of graphene being exposed to nitridation process.

7.3 CONCLUSION

From the growth observation on the synthesis of GaN nanocolumns on graphene utilizing AlN buffer layers grown via MEE technique with 20, 40 and 80 cycles, it can be suggested that their morphology and orientation are restrained by the AlN structures on graphene. The high surface tension of graphene creates AlN islands on the graphene surface, beneficial for nucleation of GaN nanocolumns. Along with the islands, AlN nanostructures are densely formed along line defects (grain boundaries or wrinkles) of graphene due to the existence of defects which provides dangling bonds. Vertical GaN nanocolumns can be consistently obtained from the AlN islands independent of the number of AlN MEE cycles, whereas the GaN nanocolumns formed on AlN nanostructures can be randomly oriented when they are grown with higher number of AlN MEE cycles. There is also a likelihood of limited direct growth of GaN nanocolumns on graphene, resulting most likely in random growth orientations. Although higher number of MEE cycles produce wider AlN coverage on graphene, the subsequent GaN nanocolumns as well as the graphene property turn out to be not ideal. The structural characterizations and optical measurements present that GaN nanocolumn formation utilizing AlN buffer layer formed with 20 MEE cycles is the most preferable growth condition to obtain overall good quality and vertical alignment of GaN nanocolumns while maintaining the least damage on graphene.

7.4 METHODS

Radio-frequency plasma-assisted molecular beam epitaxial growth. Commercially available 10 × 10 mm^2 CVD-graphene grown on copper foil[34] and transferred onto the center of a 2-inch supporting silica glass wafer (thickness of 0.5 mm) by Graphene Platform Corp. (Tokyo, Japan) was used as growth substrates. All the graphene substrates used in this work refer to an atomic layer of sp^2 hybridized carbon atoms arranged in a hexagonal structure with an approximate thickness of 0.335 nm. The samples were grown by an EpiQuest RF-PAMBE system (at Sophia University) equipped with an RF nitrogen plasma source to generate active nitrogen and standard solid-source effusion cells (Knudsen cells) to provide Al, Ga and Si atoms.

In general, the growth was started by depositing the AlN buffer layer using the MEE technique[37,60] at 805 °C, with expectation that the migration length of the supplied atoms on the substrate surface becomes longer than when using the conventional MBE method. Stated substrate temperatures were measured by a pyrometer [ref. 21]. MEE was executed by supplying Al and N atoms alternately to the graphene surface using an Al flux of 8.0×10^{-5} Pa, a N_2 flow rate of 2.0 sccm and an RF power of 450 W. Each MEE cycle (or MEE period) of AlN consists of four seconds with Al atom supply, five seconds of interruption (resting time) and three seconds with N atom supply[27]. To investigate the effect of the AlN buffer layer, we grew AlN buffer layer samples A1, A2 and A3 with different layer thicknesses by employing 20, 40 and 80 MEE cycles, respectively. After SEM characterization, these samples were re-loaded into the RF-PAMBE growth chamber and further growth of GaN nanocolumns was performed with conventional MBE method using the following growth parameters[28]: a Ga flux of 2.5×10^{-4} Pa and a N_2 flow rate of 2.75 sccm (RF power of 450 W) at a substrate temperature of 895 °C with a growth duration of 90 minutes. After the growth of GaN nanocolumns on samples A1, A2 and A3, the samples were re-labeled as G1, G2 and G3, respectively.

Scanning electron microscopy. SEM images were obtained using an SII SMI3050SE focused ion beam-SEM and a Hitachi SU8000 SEM at acceleration voltages of 15 and 10 kV, respectively.

Transmission electron microscopy. The interface of nanocolumn/buffer layer/graphene/silica glass and their element distribution were studied by high-resolution TEM and STEM-EELS in a double Cs-corrected cold field emission gun JEOL ARM200F operating at 200 kV, equipped with a QuantumER GIF for EELS. Details on the TEM specimen preparation can be found in ref. 28.

X-ray diffraction. HRXRD was performed with a Bruker D8 Discovery High-Resolution Diffractometer using Cu Kα radiation (1.5406 Å).

RT micro-photoluminescence measurements. Optical studies were done using RT micro-photoluminescence with a He-Cd laser (325 nm) as the excitation source. A freestanding HVPE-grown GaN bulk substrate (threading dislocation density of $6–8 \times 10^6$ cm^{-2}) was used as the reference sample like for previous studies[21,24].

Micro-Raman spectroscopy. Unpolarized micro-Raman spectroscopy was conducted at RT in backscattering configuration using a Renishaw InVia Reflex Spectrometer System equipped with a 514.5 nm excitation laser. A pristine graphene transferred onto silica glass was utilized as a comparison to graphene samples after RF-PAMBE growth.

7.5 ACKNOWLEDGEMENTS

The authors thank Yuta Konno, Haruhiko Kuroe and Rany Miranti for fruitful discussions. We are also grateful to Koji Yamano and Isamu Matsuyama for dedicated MBE maintenance.

We acknowledge the financial support from the Research Council of Norway (NANO2021 program grant no. 259553, NORTEM infrastructure grant no. 197405 and FORSKERSKOLER program grant no. 221860) and the Japan Society for the Promotion of Science KAKENHI (Grant No. 24000013).

7.6 REFERENCES

[1] J.-K. Choi, *et al.* One-step graphene coating of heteroepitaxial GaN films. *Nanotechnology* **23** (43), 435603 (2012). Cited on page/s 150.

[2] D.-H. Mun, H. Bae, S. Bae, H. Lee, J.-S. Ha, and S. Lee. Stress relaxation of GaN microstructures on a graphene-buffered Al_2O_3 substrate. *Physica Status Solidi (RRL) – Rapid Research Letters* **8** (4), 341–344 (2014). Cited on page/s 150.

[3] T. Araki, *et al.* Radio-frequency plasma-excited molecular beam epitaxy growth of GaN on graphene/Si(100) substrates. *Applied Physics Express* 7 (7), 071001 (2014). Cited on page/s 150, 161.

[4] S. J. Chae, *et al.* Direct growth of etch pit-free GaN crystals on few-layer graphene. *RSC Advances* **5**, 1343–1349 (2015). Cited on page/s 150, 151.

[5] E. Zhao, Y. Xu, B. Cao, Z. Li, S. Yang, J. Wang, C. Wang, and K. Xu. Microstructural and optical properties of GaN buffer layers grown on graphene. *Japanese Journal of Applied Physics* **57** (8), 085502 (2018). Cited on page/s 150.

[6] T. Li, *et al.* Understanding the Growth Mechanism of GaN Epitaxial Layers on Mechanically Exfoliated Graphite. *Nanoscale Research Letters* **13** (1), 130 (2018). Cited on page/s 150.

[7] X. Pan, M. Wei, C. Yang, H. Xiao, C. Wang, and X. Wang. Growth of GaN film on Si (111) substrate using AlN sandwich structure as buffer. *Journal of Crystal Growth* **318** (1), 464–467 (2011). Cited on page/s 150.

[8] W. Wang, H. Wang, W. Yang, Y. Zhu, and G. Li. A new approach to epitaxially grow high-quality GaN films on Si substrates: the combination of MBE and PLD. *Scientific Reports* **6**, 24448 (2016). Cited on page/s 150.

[9] Z. Sun, P. Song, S. Nitta, Y. Honda, and H. Amano. A-plane GaN growth on (11-20) 4H-SiC substrate with an ultrathin interlayer. *Journal of Crystal Growth* **468**, 866–869 (2017). Cited on page/s 150.

[10] S. S. Kushvaha, M. S. Kumar, M. Maheshwari, A. K. Shukla, P. Pal, and K. K. Maurya. Structural and electronic properties of epitaxial GaN layer grown on sapphire (0001) using laser molecular beam epitaxy. *Materials Research Express* **1** (3), 035903 (2014). Cited on page/s 150.

[11] J. W. Shon, J. Ohta, K. Ueno, A. Kobayashi, and H. Fujioka. Structural properties of GaN films grown on multilayer graphene films by pulsed sputtering. *Applied Physics Express* 7 (8), 085502 (2014). Cited on page/s 150.

[12] T. H. Seo, A. H. Park, S. Park, Y. H. Kim, G. H. Lee, M. J. Kim, M. S. Jeong, Y. H. Lee, Y.-B. Hahn, and E.-K. Suh. Direct growth of GaN layer on carbon nanotube-graphene hybrid structure and its application for light emitting diodes. *Scientific Reports* **5**, 7747 (2015). Cited on page/s 150.

[13] Y. Li, *et al.* Van der Waals epitaxy of GaN-based light-emitting diodes on wet-transferred multilayer graphene film. *Japanese Journal of Applied Physics* **56** (8), 085506 (2017). Cited on page/s 150.

[14] Z. Chen, *et al.* High-Brightness Blue Light-Emitting Diodes Enabled by a Directly Grown Graphene Buffer Layer. *Advanced Materials* **30** (30), 1801608 (2018). Cited on page/s 150, 151.

[15] A. Koma. Van der Waals epitaxy for highly lattice-mismatched systems. *Journal of Crystal Growth* **201-202**, 236–241 (1999). Cited on page/s 150.

[16] A. Mazid Munshi, Dasa L. Dheeraj, Vidar T. Fauske, Dong-Chul Kim, Antonius T. J. van Helvoort, Bjørn-Ove Fimland, and Helge Weman. Vertically Aligned GaAs Nanowires on Graphite and Few-Layer Graphene: Generic Model and Epitaxial Growth. *Nano Letters* **12** (9), 4570–4576 (2012). Cited on page/s 150.

[17] J. Kim, C. Bayram, H. Park, C.-W. Cheng, C. Dimitrakopoulos, J. A. Ott, K. B. Reuter, S. W. Bedell, and D. K. Sadana. Principle of direct van der Waals epitaxy of single-crystalline films on epitaxial graphene. *Nature Communications* **5**, 4836 (2014). Cited on page/s 150.

[18] C. D. van Engers, N. E. A. Cousens, V. Babenko, J. Britton, B. Zappone, N. Grobert, and S. Perkin. Direct Measurement of the Surface Energy of Graphene. *Nano Letters* **17** (6), 3815–3821 (2017). Cited on page/s 150, 152.

[19] T. Journot, V. Bouchiat, B. Gayral, J. Dijon, and B. Hyot. Self-Assembled UV Photodetector Made by Direct Epitaxial GaN Growth on Graphene. *ACS Applied Materials & Interfaces* **10** (22), 18857–18862 (2018). Cited on page/s 150.

[20] K. Yamano, K. Kishino, H. Sekiguchi, T. Oto, A. Wakahara, and Y. Kawakami. Novel selective area growth (SAG) method for regularly arranged AlGaN nanocolumns using nanotemplates. *Journal of Crystal Growth* **425**, 316–321 (2015). The 18th International Conference on Molecular Beam Epitaxy (MBE 2014). Cited on page/s 150.

[21] A. Liudi Mulyo, Y. Konno, J. S. Nilsen, A. T. J. van Helvoort, B.-O. Fimland, H. Weman, and K. Kishino. Growth study of self-assembled GaN nanocolumns on silica glass by plasma assisted molecular beam epitaxy. *Journal of Crystal Growth* **480**, 67–73 (2017). Cited on page/s 150, 165, 166.

[22] A. T. M. G. Sarwar, S. D. Carnevale, F. Yang, T. F. Kent, J. J. Jamison, D. W. McComb, and R. C. Myers. Semiconductor Nanowire Light-Emitting Diodes Grown on Metal: A Direction Toward Large-Scale Fabrication of Nanowire Devices. *Small* **11** (40), 5402–5408 (2015). Cited on page/s 150.

[23] M. Sobanska, K. P. Korona, Z. R. Zytkiewicz, K. Klosek, and G. Tchutchulashvili. Kinetics of self-induced nucleation and optical properties of GaN nanowires grown by plasma-assisted molecular beam epitaxy on amorphous $\mathrm{Al_xO_y}$. *Journal of Applied Physics* **118** (18), 184303 (2015). Cited on page/s 150.

[24] K. Kishino and S. Ishizawa. Selective-area growth of GaN nanocolumns on Si(111) substrates for application to nanocolumn emitters with systematic analysis of dislocation filtering effect of nanocolumns. *Nanotechnology* **26** (22), 225602 (2015). Cited on page/s 150, 161, 166.

[25] B. Janjua, *et al.* Droop-free $\mathrm{Al_xGa_{1\text{-}x}N/Al_yGa_{1\text{-}y}N}$ quantum-disks-in-nanowires ultraviolet LED emitting at 337 nm on metal/silicon substrates. *Optics Express* **25** (2), 1381–1390 (2017). Cited on page/s 150.

[26] S. Kang, A. Mandal, J.-H. Park, D.-Y. Um, J. H. Chu, S.-Y. Kwon, and C.-R. Lee. Effects of growth temperatures on the characteristics of n-GaN nanorods–graphene hybrid structures. *Journal of Alloys and Compounds* **644**, 808–813 (2015). Cited on page/s 150.

[27] H. Hayashi, Y. Konno, and K. Kishino. Self-organization of dislocation-free, high-density, vertically aligned GaN nanocolumns involving InGaN quantum wells on graphene/$\mathrm{SiO_2}$ covered with a thin AlN buffer layer. *Nanotechnology* **27** (5), 055302 (2015). Cited on page/s 150, 151, 165.

[28] A. Liudi Mulyo, M. K. Rajpalke, H. Kuroe, P.-E. Vullum, H. Weman, B.-O. Fimland, and K. Kishino. Vertical GaN nanocolumns grown on graphene intermediated with a thin AlN buffer layer. *Nanotechnology* **30** (1), 015604 (2018). Cited on page/s 150, 151, 165, 166.

[29] M. Heilmann, *et al.* Vertically Oriented Growth of GaN Nanorods on Si Using Graphene as an Atomically Thin Buffer Layer. *Nano Letters* **16** (6), 3524–3532 (2016). Cited on page/s 150, 152.

[30] I. M. Høiaas, A. Liudi Mulyo, P. E. Vullum, D.-C. Kim, L. Ahtapodov, B.-O. Fimland, K. Kishino, and H. Weman. GaN/AlGaN Nanocolumn Ultraviolet Light-Emitting Diode Using Double-Layer Graphene as Substrate and Transparent Electrode. *Nano Letters* **19** (3), 1649–1658 (2019). Cited on page/s 151.

[31] S. Fernandez-Garrido, *et al.* Molecular Beam Epitaxy of GaN Nanowires on Epitaxial

Graphene. *Nano Letters* **17** (9), 5213–5221 (2017). Cited on page/s 151.

[32] S. U. Yu, B. Park, Y. Cho, S. Hyun, J. K. Kim, and K. S. Kim. Simultaneous Visualization of Graphene Grain Boundaries and Wrinkles with Structural Information by Gold Deposition. *ACS Nano* **8** (8), 8662–8668 (2014). Cited on page/s 152.

[33] F. Long, P. Yasaei, R. Sanoj, W. Yao, P. Kral, A. Salehi-Khojin, and R. Shahbazian-Yassar. Characteristic Work Function Variations of Graphene Line Defects. *ACS Applied Materials & Interfaces* **8** (28), 18360–18366 (2016). Cited on page/s 152.

[34] N. Liu, Z. Pan, L. Fu, C. Zhang, B. Dai, and Z. Liu. The origin of wrinkles on transferred graphene. *Nano Research* **4** (10), 996 (2011). Cited on page/s 152, 165.

[35] A. N. Obraztsov, E. A. Obraztsova, A. V. Tyurnina, and A. A. Zolotukhin. Chemical vapor deposition of thin graphite films of nanometer thickness. *Carbon* **45** (10), 2017–2021 (2007). Cited on page/s 152.

[36] P. Zhao, A. Kumamoto, S. Kim, X. Chen, B. Hou, S. Chiashi, E. Einarsson, Y. Ikuhara, and S. Maruyama. Self-Limiting Chemical Vapor Deposition Growth of Monolayer Graphene from Ethanol. *The Journal of Physical Chemistry C* **117** (20), 10755–10763 (2013). Cited on page/s 152.

[37] D. V. Nechaev, P. A. Aseev, V. N. Jmerik, P. N. Brunkov, Y. V. Kuznetsova, A. A. Sitnikova, V. V. Ratnikov, and S. V. Ivanov. Control of threading dislocation density at the initial growth stage of AlN on c-sapphire in plasma-assisted MBE. *Journal of Crystal Growth* **378**, 319–322 (2013). Cited on page/s 152, 165.

[38] S. Ishizawa, K. Kishino, and A. Kikuchi. Selective-Area Growth of GaN Nanocolumns on Si(111) Substrates Using Nitrided Al Nanopatterns by RF-Plasma-Assisted Molecular-Beam Epitaxy. *Applied Physics Express* **1** (1), 015006 (2008). Cited on page/s 154.

[39] H. Sekiguchi, T. Nakazato, A. Kikuchi, and K. Kishino. Structural and optical properties of GaN nanocolumns grown on (0001) sapphire substrates by rf-plasma-assisted molecular-beam epitaxy. *Journal of Crystal Growth* **300** (1), 259–262 (2007). First International Symposium on Growth of Nitrides. Cited on page/s 154.

[40] Z. Y. Al Balushi, T. Miyagi, Y.-C. Lin, K. Wang, L. Calderin, G. Bhimanapati, J. M. Redwing, and J. A. Robinson. The impact of graphene properties on GaN and AlN nucleation. *Surface Science* **634**, 81–88 (2015). Cited on page/s 156, 160.

[41] E. Calleja, M. A. Sánchez-García, F. J. Sánchez, F. Calle, F. B. Naranjo, E. Muñoz, U. Jahn, and K. Ploog. Luminescence properties and defects in GaN nanocolumns grown by molecular beam epitaxy. *Physical Review B* **62** (24), 16826–16834 (2000). Cited on page/s 161.

[42] S. A. Church, *et al.* Photoluminescence studies of cubic GaN epilayers. *Physica Status Solidi B - Basic Solid State Physics* **254** (8), 1600733 (2017). Cited on page/s 161.

[43] M. A. Reshchikov, D. Huang, F. Yun, H. Morkoç, R. J. Molnar, and C. W. Litton. Excitons bound to structural defects in GaN. *MRS Proceedings* **693**, I6.28.1 (2011). Cited on page/s 161.

[44] H. Fujikura, T. Konno, T. Yoshida, and F. Horikiri. Hydride-vapor-phase epitaxial growth of highly pure GaN layers with smooth as-grown surfaces on freestanding GaN substrates. *Japanese Journal of Applied Physics* **56** (8), 085503 (2017). Cited on page/s 161.

[45] M. A. Reshchikov, H. Morkoç, S. S. Park, and K. Y. Lee. Yellow and green luminescence in a freestanding GaN template. *Applied Physics Letters* **78** (20), 3041–3043 (2001). Cited on page/s 161.

[46] B. Liu, F. Yuan, B. Dierre, T. Sekiguchi, S. Zhang, Y. Xu, and X. Jiang. Origin of Yellow-Band Emission in Epitaxially Grown GaN Nanowire Arrays. *ACS Applied Materials & Interfaces* **6** (16), 14159–14166 (2014). Cited on page/s 162.

[47] T. Sekine, S. Suzuki, H. Kuroe, M. Tada, A. Kikuchi, and K. Kishino. Raman Scattering in GaN Nanocolumns and GaN/AlN Multiple Quantum Disk Nanocolumns. *e-Journal of*

Surface Science and Nanotechnology **4**, 227–232 (2006). Cited on page/s 162.

[48] L. H. Robins, E. Horneber, N. A. Sanford, K. A. Bertness, M. D. Brubaker, and J. B. Schlager. Raman spectroscopy based measurements of carrier concentration in n-type GaN nanowires grown by plasma-assisted molecular beam epitaxy. *Journal of Applied Physics* **120** (12), 124313 (2016). Cited on page/s 162, 163.

[49] T. Sekine, Y. Komatsu, R. Iwaya, H. Kuroe, A. Kikuchi, and K. Kishino. Surface Phonons Studied by Raman Scattering in GaN Nanostructures. *Journal of the Physical Society of Japan* **86** (7), 074602 (2017). Cited on page/s 162.

[50] H. Harima. Properties of GaN and related compounds studied by means of Raman scattering. *Journal of Physics: Condensed Matter* **14** (38), R967–R993 (2002). Cited on page/s 162, 163.

[51] A. Tabata, R. Enderlein, J. R. Leite, S. W. da Silva, J. C. Galzerani, D. Schikora, M. Kloidt, and K. Lischka. Comparative Raman studies of cubic and hexagonal GaN epitaxial layers. *Journal of Applied Physics* **79** (8), 4137–4140 (1996). Cited on page/s 162, 163.

[52] K. Jeganathan, R. K. Debnath, R. Meijers, T. Stoica, R. Calarco, D. Grutzmacher, and H. Luth. Raman scattering of phonon-plasmon coupled modes in self-assembled GaN nanowires. *Journal of Applied Physics* **105** (12), 123707 (2009). Cited on page/s 162, 163.

[53] T. Kozawa, T. Kachi, H. Kano, Y. Taga, M. Hashimoto, N. Koide, and K. Manabe. Raman scattering from LO phonon-plasmon coupled modes in gallium nitride. *Journal of Applied Physics* **75** (2), 1098–1101 (1994). Cited on page/s 162, 163.

[54] L. Cerutti, J. Ristic, S. Fernandez-Garrido, E. Calleja, A. Trampert, K. H. Ploog, S. Lazic, and J. M. Calleja. Wurtzite GaN nanocolumns grown on Si(001) by molecular beam epitaxy. *Applied Physics Letters* **88** (21), 213114 (2006). Cited on page/s 163.

[55] Y. Tian, Y. Shao, Y. Wu, X. Hao, L. Zhang, Y. Dai, and Q. Huo. Direct growth of freestanding GaN on C-face SiC by HVPE. *Scientific Reports* **5**, 10748 (2015). Cited on page/s 163.

[56] R. Beams, L. G. Cancado, and L. Novotny. Raman characterization of defects and dopants in graphene. *Journal of Physics: Condensed Matter* **27** (8), 083002 (2015). Cited on page/s 164.

[57] G. Sarau, M. Heilmann, M. Bashouti, M. Latzel, C. Tessarek, and S. Christiansen. Efficient Nitrogen Doping of Single-Layer Graphene Accompanied by Negligible Defect Generation for Integration into Hybrid Semiconductor Heterostructures. *ACS Applied Materials & Interfaces* **9** (11), 10003–10011 (2017). Cited on page/s 164.

[58] J.-J. Zheng and Y.-J. Lin. Tuning the work function of graphene by nitrogen plasma treatment with different radio-frequency powers. *Applied Physics Letters* **104** (23), 233103 (2014). Cited on page/s 164.

[59] Y.-C. Lin, C.-Y. Lin, and P.-W. Chiu. Controllable graphene N-doping with ammonia plasma. *Applied Physics Letters* **96** (13), 133110 (2010). Cited on page/s 164.

[60] Y. Takano, M. Lopez, T. Torihata, T. Ikei, Y. Kanaya, K. Pak, and H. Yonezu. Realization of mirror surface in (111)- and (110)-oriented GaAs by migration-enhanced epitaxy. *Journal of Crystal Growth* **111** (1), 216–220 (1991). Cited on page/s 165.

Chapter 8

GaN/AlGaN nanocolumn ultraviolet light-emitting diode using double-layer graphene as substrate and transparent electrode

Ida Marie Høiaas[1,*]**Andreas Liudi Mulyo**[1,2,*], Per Erik Vullum[3], Dong-Chul Kim[1], Lyubomir Ahtapodov[1], Bjørn-Ove Fimland[1], Katsumi Kishino[2,4,#] and Helge Weman[1,#] *[*]IMH and **ALM** contributed equally to this study.*

First published in: *Nano Letters* **19** (3), 1649-1658 (2019).
DOI: 10.1021/acs.nanolett.8b04607

Contributions

ALM planned the study with IMH under the supervision of BOF, KK and HW. **ALM** performed the nanowire growth by MBE and SEM imaging, while IMH performed the experimental work related to device fabrication and characterization. PEV did the TEM/STEM/EDX/EELS imaging in discussion with **ALM** and IMH. LA performed the photoluminescence measurements. **ALM** drafted the manuscript together with IMH. All authors contributed to the discussion of results and preparations of the manuscript.

---

[1] Department of Electronic Systems, Norwegian University of Science and Technology (NTNU), NO-7491 Trondheim, Norway. [2] Department of Engineering and Applied Sciences, Sophia University, 102-8554 Tokyo, Japan. [3] SINTEF Industry, NO-7465 Trondheim, Norway. [4] Sophia Nanotechnology Research Center, Sophia University, 102-8554 Tokyo, Japan. [#] e-mail: kishino@sophia.ac.jp and helge.weman@ntnu.no

ABSTRACT

The many outstanding properties of graphene have impressed and intrigued scientists for the last few decades. Its transparency to light of all wavelengths combined with a low sheet resistance makes it a promising electrode material for novel optoelectronics. So far, no one has utilized graphene as both the substrate and transparent electrode of a functional optoelectronic device. Here, we demonstrate the use of double-layer graphene as a growth substrate and transparent conductive electrode for an ultraviolet light-emitting diode in a flip-chip configuration, where GaN/AlGaN nanocolumns are grown as the light-emitting structure using plasma-assisted molecular beam epitaxy. Although the sheet resistance is increased after nanocolumn growth compared with pristine double-layer graphene, our experiments show that the double-layer graphene functions adequately as an electrode. The GaN/AlGaN nanocolumns are found to exhibit a high crystal quality with no observable defects or stacking faults. Room-temperature electroluminescence measurements show a GaN related near bandgap emission peak at 365 nm and no defect-related yellow emission.

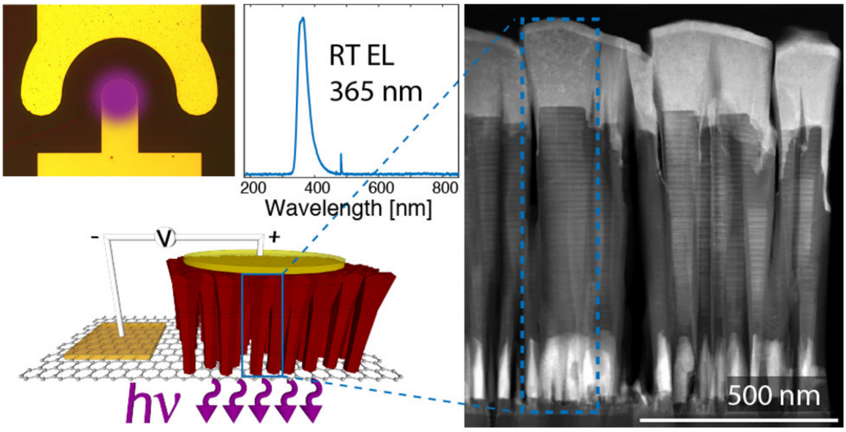

8.1 INTRODUCTION

With the emergence of new semiconductor nanomaterials and heterostructures, new possibilities for optoelectronics arise. The semiconductor materials most commonly used for optoelectronics today, such as Si[1], GaAs, InAs[2], ZnO[3], and GaN with its alloys[2], exhibit structural imperfections when grown as heteroepitaxial thin-films, for instance twinning defects, threading dislocations and stacking faults. This is due to a large lattice mismatch between these materials as well as with conventional substrates. By nanostructuring the semiconductor materials in the forms of columns or pyramids, new combinations of materials can be explored, and new substrates can be employed for the epitaxial growth.

An intriguing potential substrate for epitaxial growth of semiconductors is graphene, the single-layer form of carbon, as it can not only act as an atomically thin crystalline growth template, but also has outstanding functional properties when it comes to strength, flexibility, electron and thermal conductivity [4,5]. Hybrid systems based on the growth of semiconductor nanocolumns on different graphitic substrates have been intensively studied in the past decade, with the aim of developing new functionalities and higher efficiency optoelectronic devices as for example solar cells, photodetectors, light-emitting diodes (LEDs) and lasers. Such hybrid systems have been demonstrated for GaAs [6], InAs [7–9], InAsSb [10], In(Ga)As [11,12], ZnO [13,14], and GaN. With regards to the growth of GaN nanocolumns, different graphitic forms have been used as growth substrate, for instance graphite [15], transferred chemical vapor deposition (CVD) graphene (single- and multilayer) [16–25], and epitaxial graphene [26]. However, these studies mostly focused on the growth of the nanocolumns, without further demonstration of a hybrid device realization.

In addition to the attributes already mentioned, graphene has the attractive property of being transparent in all parts of the electromagnetic spectrum and has been demonstrated as a top-emitting transparent conductive electrode (TCE) for GaN [27,28] and InGaN LEDs [29–31]. In contrast to the traditional TCE in optoelectronic devices, indium tin oxide, graphene is transparent in the whole UV region of the electromagnetic spectrum (100-350 nm) [32], offering a potential solution for devices operating in this region.

Recently, our group showed GaN/AlGaN nanocolumn growth with a single-layer graphene substrate as the bottom electrode [25]. However, so far there has been no realization of utilizing graphene simultaneously as the growth substrate and the TCE of a semiconductor device. Here, we demonstrate a UV-A LED using transferred double-layer graphene (DLG) both as the substrate for GaN/AlGaN nanocolumn growth and as the TCE in the processed device. Along with the reduced sheet resistance of DLG compared to single-layer graphene [33], it is expected that the additional top layer of graphene will protect the bottom layer of graphene from plasma nitridation damage during growth. The electric current is thus injected directly from the conducting DLG substrate in a *vertical* flip-chip device configuration, which can be advantageous when compared to traditional mesa LED structures with lateral current injection that suffer from current crowding [34–36].

8.2 NANOCOLUMN GROWTH AND STRUCTURAL CHARACTERIZATION

In this work, we have grown catalyst-free, self-assembled $Al_xGa_{1-x}N$/GaN nanocolumn heterostructures on transferred DLG on amorphous silica glass by radio-frequency plasma-assisted molecular beam epitaxy (RF-PAMBE) under N-rich conditions (see Methods for the detailed information on the growth). The intended LED structure is shown schematically in Figure B.1a in the Appendix B, where each nanocolumn is designed to consist of 40 nm n-AlN, 140 nm n-GaN, 550 nm n-$Al_{0.25}Ga_{0.75}N$, 27 nm undoped GaN, 200 nm p-$Al_{0.25}Ga_{0.75}N$, and 20 nm p-GaN. Here, we would like to emphasize that the length of each aforementioned segment is based on nominal values. In addition, the indicated Al and Ga compositions are nominal compositions, i.e., based on the ratio between the Al and Ga fluxes (see Table B.1 in Appendix B). To verify these values, further transmission electron microscopy (TEM) investigations were carried out and will be discussed in the following paragraphs. A thin AlN buffer layer does not only serve as a nucleation site for n-GaN [17,23–25], but it also reduces damage to the graphene induced by impinging active N species generated by the RF plasma source [17,23–26,37] and in-plane strain generated by GaN nucleation [23,38]. To achieve even higher density of nanocolumns, the AlN deposition method is modified [25] from the migration enhanced epitaxy (MEE) technique which was utilized to obtain 1 μm long vertically aligned GaN nanocolumns on single-layer [23,24] and multi-layer graphene [17]. In addition, a higher probability of vertical growth of n-GaN nanocolumns on graphene was achieved, which is important for the subsequent vertical n-AlGaN nanocolumn growth [39,40].

Shown in Figure 8.1a-b are the top- and bird-view scanning electron microscopy (SEM) images of the self-assembled GaN/AlGaN nanocolumns grown on DLG. It can be seen that the nanocolumns coalesce with each other, forming an almost continuous film-like layer in the top part of the nanocolumns. The top-view SEM image from the center area of the sample (Figure 8.1a) shows that the geometry of some of the uncoalesced nanocolumns exhibits near-perfect hexagonal morphology. In addition, there are a few small gaps (less than 50 nm) between some nanocolumns and their neighbors. From some of the nanocolumns with distinguished hexagonal cross-sectional geometrical shape, the average top diameter is found to be about 220 nm. Figure 8.1b shows a bird-view SEM image, indicating that the nanocolumns are highly dense and vertically oriented with respect to the graphene/glass substrate, as well as demonstrating a relatively uniform height distribution. Figure B.1b in the Appendix B is a representative side-view SEM image of the grown GaN/AlGaN nanocolumns, where the average height and average bottom- and top-diameter of the grown nanocolumns, as derived from 20 SEM images, are found to be 1070, 35 and 220 nm, respectively. It is evident that the nanocolumn geometry exhibits a highly inverse-tapered structure due to the abrupt growth temperature reduction by 200 - 220 °C starting from the p-AlGaN segment, forming a champagne glass-like structure, similar to the work reported by Sekiguchi *et al.*[39]. As a result of the low growth temperature (675 – 695 °C), the nanocolumns tend to grow faster in the radial direction, causing the top part of the nanocolumns to coalesce with each other. Such coalesced nanocolumns are used in order to ensure a uniform and continuous metal contact to the top p-GaN segment in the subsequent LED processing, preventing discontinuous metal deposition on p-GaN as shown in previous work[25]. Furthermore, metal can be deposited without the use of any insulating filler material between nanocolumns. The reasons for lowering the growth temperature during growth of the p-AlGaN and p-GaN segments of the device structure are explained in more detail in the Appendix B.

Detailed structural characterization was further carried out by TEM. Figure 8.1c shows a bright-field (BF) TEM overview image of the self-assembled GaN/AlGaN nanocolumns. All nanocolumns grow in the [0001]-direction, which was observed by electron diffraction for more than 20 nanocolumns and is exemplified in the diffraction pattern in Figure B.2a in the Appendix B. This is consistent with previous reports of GaN nanocolumns grown on single-layer[16,18,23,24] and multi-layer graphene[17,26]. The darker contrast nanocolumns shown in Figure 8.1c are oriented with the electron beam parallel to the $[\bar{2}110]$-direction, i.e., they possess a very similar in-plane orientation. Tilting the sample to different in-plane orientations reveals several clusters of identically oriented nanocolumns on the μm-scale. Since the CVD DLG used as a substrate is polycrystalline, the observed preferred in-plane orientation of the nanocolumns is an indication that they adopt an epitaxial orientation related to the graphene lattice and thus follow the orientation of a particular graphene grain[6]. The DLG can be distinguished in Figure 8.1d as indicated by the red arrows. The exact number of layers cannot be confirmed by this image, as the graphene layers are buckled and the two-dimensional image of the TEM lamella thus indicates more than two layers[23]. The nanocolumns exhibit a pure wurtzite crystal structure and no interfacial layer, which is identical with our observation in the growth of n-GaN nanocolumns on graphene using an MEE-AlN buffer layer[23] but different from n-GaN nanocolumns grown directly on silica glass[41]. No dislocations, stacking faults or other defects are found in the GaN- and AlGaN-nanocolumn segments. The AlN buffer layer, however, is found to have some dislocations and point defects. Using high-angle annular dark-field scanning TEM (HAADF STEM) to get a Z-contrast image of the nanocolumns in Figure 8.1c, the different segments of the GaN/AlGaN nanocolumns can be distinguished, as shown in Figure 8.1e.

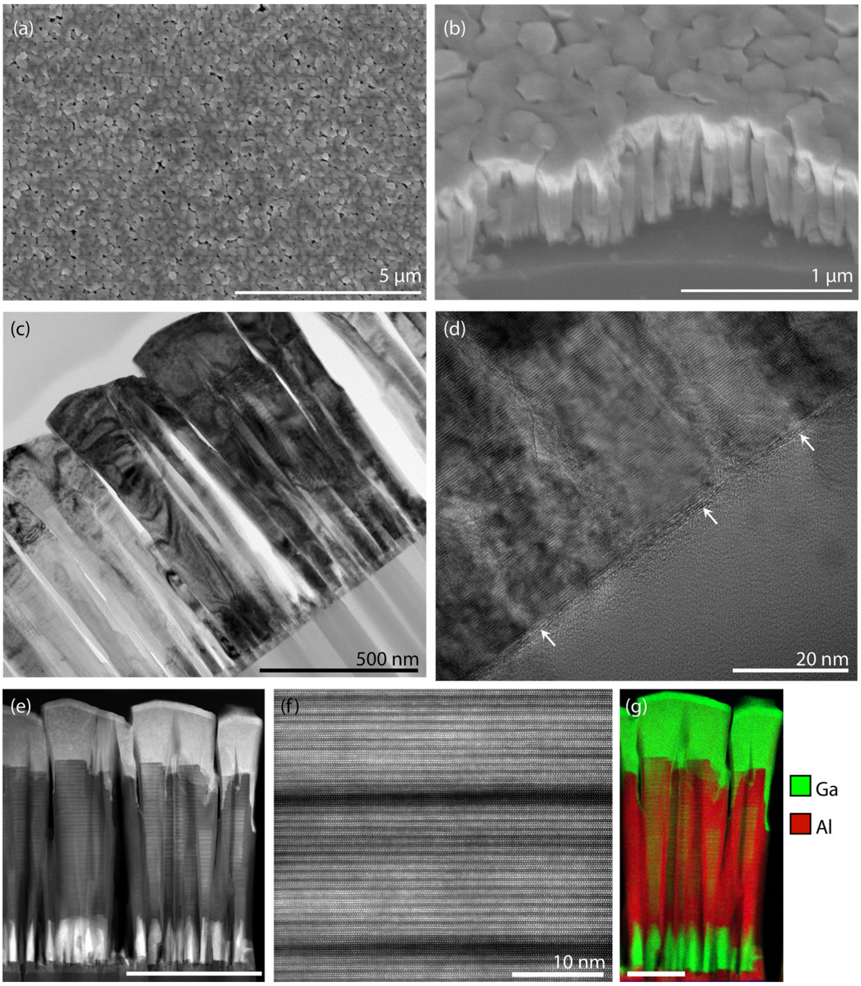

FIGURE 8.1. Overview of self-assembled GaN/AlGaN nanocolumns by SEM and their structural details by TEM. (**a**,**b**) Top- and bird-view SEM images of nanocolumns grown on DLG transferred onto amorphous silica glass. (**c**) BF TEM image of the nanocolumns shows local preferential orientation as several neighboring nanocolumns are simultaneously on-axis, indicating epitaxy with the graphene substrate. The nanocolumns grow in the [0001]-direction. (**d**) High-resolution BF TEM image showing the DLG (white arrows) between the amorphous silica glass support and the crystalline nanocolumns. (**e**) A superlattice-like structure can be observed by HAADF STEM (scale bar 500 nm). (**f**) High-resolution HAADF STEM image of alternating Al-rich/Ga-rich layers in the superlattice-like n-AlGaN nanocolumn segment. (**g**) Compositional mapping by EDS and EELS of the different GaN/AlGaN segments shows an actual nanocolumn heterostructure consisting of n-AlN/n-GaN/n-$Al_{0.76}Ga_{0.24}N$/p-$Al_{0.42}Ga_{0.58}N$/p-GaN (scale bar 200 nm).

The AlN buffer layer, seen in the base of the nanocolumns, tends to assemble as a continuous layer, although there are a few AlN islands as well. Short stems consisting of n-GaN are clearly visible below the n-AlGaN nanocolumn segments. A slight oscillation of the Ga/Al-ratio in the n-AlGaN segment is noticeable, forming a superlattice-like structure as is more evident in the HAADF STEM image in Figure 8.1f (the line scan can be seen in Figure B.2b in the Appendix B). The main reason for such composition inhomogeneity could be kinetical [42]; as a consequence of a difference in sticking coefficients and diffusion lengths for Al and Ga adatoms as well as a competition between Al and Ga incorporation during the nanocolumn growth. This would be the case for both the direct impingement on the top of the nanocolumns and for diffusion along the nanocolumn sidewalls [42,43]. As the higher Al-content barriers in the superlattice-like structure in the n-AlGaN segment are only ~2-3 nm thick, it is unlikely that they will affect the electronic properties of the nanocolumns. From Figure B.2c in the Appendix B, a higher Al-content nanocolumn shell-layer can be seen surrounding the AlGaN nanocolumn core, which might act as a self-passivation layer for the nanocolumn side facets. No intrinsic GaN segment is observed in the TEM images, which is likely caused by the complete desorption of this layer during the growth interruption needed to reduce the temperature for the subsequent p-AlGaN growth, as the Ga desorption rate is very high at these substrate temperatures [44]. The p-AlGaN segment and thin p-GaN contact layer grow highly inverse-tapered (as desired for the subsequent process of top contact metallization), indicating a switch from N-polar to Ga-polar growth mode (for improvement of p-type doping efficiency) [45], which is further evidenced by a switch from planar to inclined interfaces at the top of the nanocolumns.

The elemental composition of the different segments is estimated by combining X-ray electron dispersive spectroscopy (EDS) with electron energy loss spectroscopy (EELS), using the pure AlN and GaN layers at the bottom and top of the nanocolumns as references, respectively. The results shown in Figure 8.1g indicate that the n-AlGaN segment has a composition of 76% Al close to the p-n junction, while the p-AlGaN segment has a composition of 42% Al (more detailed in Figure B.2c in the Appendix B). These values may have contributions from the Al-rich shell leading to an overestimation of the Al-content in the n- and p-AlGaN segments. However, most of the large deviation from the designed n- and p-AlGaN segment composition of 25% Al is most likely caused by the higher Ga desorption rate as explained above.

8.3 GRAPHENE ELECTRODE

The nitrogen plasma sources utilized during RF-PAMBE growth of III-N nanocolumns are known to have a damaging effect to graphene[23–26,37]. To assess the extent of the possible damage, the DLG was characterized by micro-Raman spectroscopy and sheet resistance measurements before and after nanocolumn growth. Figure 8.2a shows the average micro-Raman spectrum from 1600 measurements of DLG before and after nanocolumn growth. The graphene is notably damaged after growth, as evidenced by the increase in the defect-related D-peak at ∼1350 cm^{-1}, the reduction in the G- and 2D-peaks at ∼1600 cm^{-1} and ∼2700 cm^{-1} and the appearance of the D'-peak at ∼1620 cm^{-1}. Mapping the peak intensity ratio of the D- and G-peaks in Figure 8.2b reveals that the defect distribution is non-uniform in graphene after the nanocolumn growth, with some areas resembling the pre-growth graphene quality while others are extensively damaged. The increased presence of defects in graphene may lead to an increase in carrier scattering and therefore an increase in the graphene sheet resistance. This is confirmed by van der Pauw measurements, where the sheet resistance is found to increase from 329 Ω/□ before nanocolumn growth to 2326 Ω/□ after growth for the DLG. For single-layer graphene, the sheet resistance increases more severely, from 779 Ω/□ before nanocolumn growth to 86869 Ω/□ after growth. It is worth to mention that the nitrogen plasma emission during nanocolumn growth is two times higher and the total growth time is two times longer than for our previous work[25] (see Table B.1 in Appendix B), resulting in more defective graphene and consequently a larger sheet resistance, especially for the single-layer graphene. However, for the case of DLG, the limited increase in sheet resistance shows that the top layer of graphene protects the bottom layer and thus limits the extent of the damage in the bottom layer. The UV transparency of transferred DLG on silica glass is reduced by an additional ∼3% compared to that of transferred single-layer graphene on the same substrate carrier, retaining a total transmission of more than 80%[46].

Table 8.1 shows the D, G and 2D peak positions, intensities and ratios of the micro-Raman spectroscopy mapping, and maps of these parameters can be found in Figure B.3 in the Appendix B. The apparent blue-shift of the G- and 2D-peaks for the DLG could be due to doping and/or strain in graphene after the nanocolumn growth[47]. It is known that exposure to nitrogen plasma may n-type dope graphene[37]. Using the correlation analysis developed by Lee *et al.*[48], one can untangle how much strain and doping contributes to the Raman shift, but as there is a notable occurrence of defects in the DLG after nanocolumn growth, it is not possible to conclude on the exact origin of the peak-shifts.

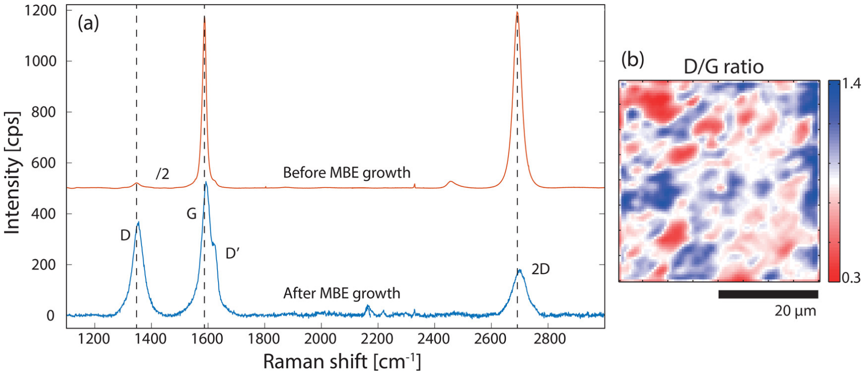

FIGURE 8.2. Micro-Raman characterization of DLG before and after RF-PAMBE GaN/AlGaN nanocolumn growth. (**a**) Averaged micro-Raman spectra from a 40 × 40 μm area with a 1 μm step size before (offset by 500 cps for clarity) and after nanocolumn growth, respectively. The intensity of the spectra taken before nanocolumn growth have been divided by two, and peak positions are indicated by the dashed lines. (**b**) Map of the same area shows the spatial variation of defects as represented by D/G peak intensity ratio.

TABLE 8.1. Micro-Raman peak positions, intensities and ratios

Sample	Median D/G ratio	Median G Position [cm^{-1}]	Median G Intensity [cps]	Median 2D Position [cm^{-1}]	Median 2D Intensity [cps]	Median 2D FWHM [cm^{-1}]	Median 2D/G ratio
DLG before MBE growth	0.04	1587	1003	2692	1314	37	1.31
DLG after MBE growth	0.9	1597	532	2698	169	58	0.32

8.4 LED FABRICATION AND ELECTRICAL CHARACTERIZATION

The graphene-nanocolumn LED devices were fabricated as shown schematically in Figure 8.3. After nanocolumn growth, Ti was removed from the backside by mechanical removal and etching the sample in a buffered oxide etch, where hydrofluoric acid dissolves the Ti (Figure 8.3a). Contact areas to the graphene and nanocolumns were defined by photolithography (Figure 8.3b), and the metal contacts were deposited by electron beam evaporation (Figure 8.3c). A Ni/Au metal stack of 50/100 nm thickness was used as a top contact to the thin-film like p-GaN surface layer of the nanocolumns. To avoid deposition on the graphene, the top contact metals were deposited at an ∼30° angle with regards to the substrate plane. For the bottom metal contact to the graphene, 200 nm Au was used, which is known to give an ohmic contact to

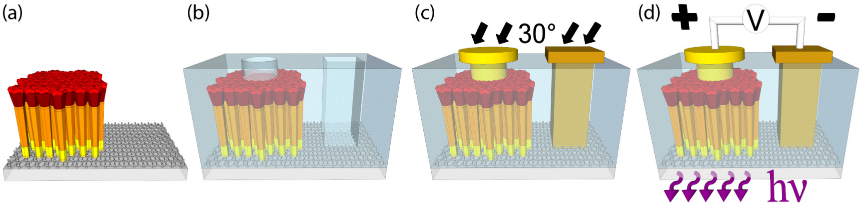

FIGURE 8.3. Schematic of the fabrication steps of the flip-chip UV LED device. (**a**) The nanocolumns are grown by RF-PAMBE on a DLG/silica glass substrate. (**b**) An insulating polymer is deposited and separate areas of graphene and nanocolumns are opened for the bottom and top metal contacts, respectively. (**c**) A Ni/Au metal stack contacts the top layer of p-GaN of the nanocolumns (deposited at an angle of 30° with the substrate plane), while Au contacts the graphene at the bottom. (**d**) The LED device is biased between the two contacts, and light is emitted through the graphene/silica glass substrate in a flip-chip configuration.

graphene with a low contact resistance[49]. In this configuration, light can be emitted through the transparent graphene/silica glass substrate of the sample as a flip-chip type device (Figure 8.3d), and the continuous graphene electrode allows for vertical current injection through the nanocolumns. Figure 8.4a shows an optical microscopy image of the LED device, with the graphene-Au contact at the top of the image and p-GaN nanocolumn-Ni/Au contact at the bottom. The LED devices have apertures of 75 or 150 μm diameter, and the distances between the top and bottom metal contacts were fixed at ~100 μm.

Figure 8.4b shows the current-voltage (I-V) curves measured for six different LED devices on the same sample, and Figure 8.4c shows the same data in a semi-logarithmic scale. The different curves are from devices with different LED apertures. Devices with the same size show similar diode characteristics, indicating uniform nanocolumn growth and junction formation. For the same bias voltage, one would expect a quadrupled current level for the device with a doubled diameter, but as the current only increases by a factor of ~2, it is evident that the injection current does not scale with the aperture area. This could be an effect of the defect generation in the graphene layers caused by nanocolumn growth, which also causes a relatively large sheet resistance, as was discussed above. The turn-on voltage is found to be 7.7 V (by intersecting the semi-linear region of the I-V curve between 10 V and 12 V and the voltage axis), somewhat larger than expected for a GaN/AlGaN nanocolumn LED[50], but considering the high Al-content of the n-AlGaN and p-AlGaN layers a higher turn-on voltage is more reasonable. However, the high resistance of the device makes it difficult to define an exact turn-on voltage, as multiple semi-linear regions could possibly be used to find different intersections. In the semilog-plot in Figure 8.4c, two voltage regions can be distinguished. A less steep slope below ~3.5 V can be seen, and the current below this value is attributed to leakage due to acceptor level recombination and electron overshoot[51].

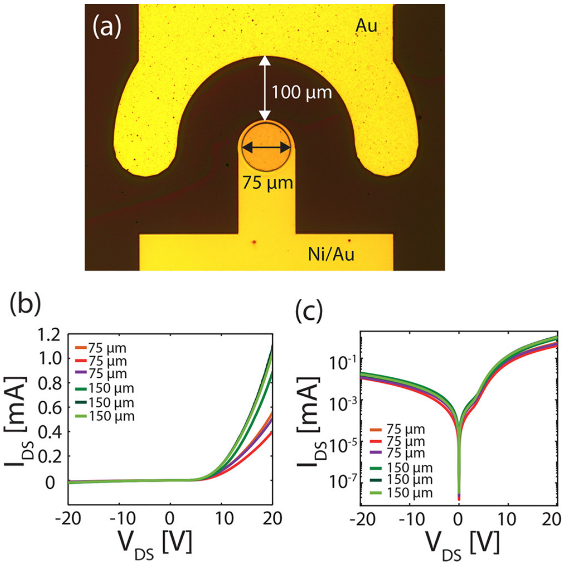

FIGURE 8.4. Processed LED device and I-V characteristics. (**a**) Optical microscope image from the p-GaN side of a 75 μm diameter aperture LED device (before flip-chip). (**b**,**c**) Linear and logarithmic I-V characteristics, respectively, from six LED devices with aperture sizes of 75 and 150 μm diameters.

Using the elemental compositions measured by combined EDS and EELS for the $Al_xGa_{1-x}N$ segments, the band gaps can be calculated by a model using local density approximation (LDA-1/2)[52]. The band gap of AlN is 6.28 eV and GaN 3.44 eV, so using a bowing parameter of 0.8 eV yields band gaps of 5.45 eV (227 nm) and 4.44 eV (279 nm) for the n-$Al_{0.76}Ga_{0.24}N$ and p-$Al_{0.42}Ga_{0.58}N$ segments, respectively[52]. The higher Al-composition at the n-doped side will increase electron leakage to the p-AlGaN side of the p-n junction.

8.5 LED EMISSION AND OPTICAL POWER OUTPUT

Low temperature photoluminescence (PL) measurements show a main emission peak at 360 nm (3.44 eV), in addition to two weaker and less defined bands at 368 nm (3.37 eV) and 382 nm (3.25 eV), as shown in Figure 8.5. The latter band, typically referred to as the blue luminescence band, originating from donor-acceptor-pair recombination, in conjunction with the absence of a yellow luminescence band, strongly indicates that the PL emission originates from the top p-type GaN nanocolumn layer. The main emission peak at 360 nm (365 nm at room temperature (RT)) is most likely attributable to Mg_{Ga} acceptor bound excitons, as commonly done in the literature[53]. The internal quantum efficiency (IQE) at RT is estimated from the ratio of the integrated PL intensity

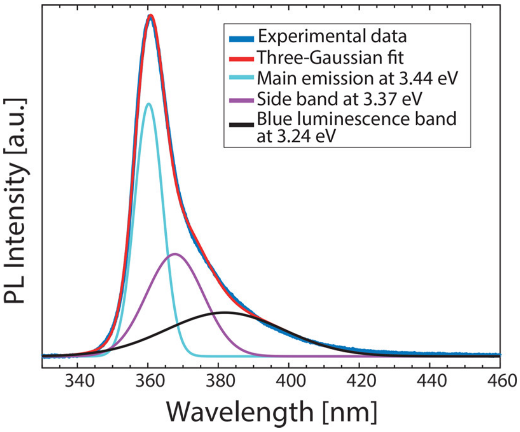

FIGURE 8.5. Low-temperature 10 K photoluminescence spectrum of the LED device. The main PL emission is at 360 nm (3.44 eV), with two side bands at 368 nm (3.37 eV) and 382 nm (3.24 eV). For an interpretation of the PL spectrum see main text.

at RT to the interpolated value at T = 0 K (see Figure B.4 in Appendix B for further details). The obtained IQE is dependent on the excitation power density used[54], and the maximum value determined in our experiments was ~46 % at an excitation power of 5.5 mW.

The LED device performance was further investigated by RT continuous current injection electroluminescence (EL) measurements, where the EL is detected either by a UV sensitive detector inside an integrating sphere for power measurements, or a spectrometer for spectral information. Figure 8.6a-b shows the measured light under different current injection conditions, with a main peak emission at 365 nm with a full width at half maximum (FWHM) of 37 nm at 20 V, which is slightly broader than near-UV GaN/AlGaN nanocolumn LEDs grown on Si substrates[55]. As already discussed above in relation with the TEM images in Figure 8.1e and Figure 8.1g, there is no intrinsic GaN layer observed between the n-$Al_{0.76}Ga_{0.24}N$ and p-$Al_{0.42}Ga_{0.58}N$ nanocolumn segments. In addition, the main EL emission measured at 365 nm resembles closely the main PL emission band at RT, with the exception of the weak UV and blue-luminescence defect-related PL bands and a shorter-wavelength shoulder in the EL spectra appearing at high forward bias, as illustrated in Figure 8.6c. Therefore, it is most likely that similarly to the PL recombination, the EL recombination also occurs in the p-GaN nanocolumn layer. Several peaks contribute to the EL emission around 365 nm, indicating some local inhomogeneity in the thin p-GaN nanocolumn contact layer. There is no notable EL peak shift with increasing injection currents up to 1.1 mA. EL emission is detected from ~4.5 V, and the intensity is seen to increase linearly with the injected current at lower voltages before saturating at higher voltages > 18 V. No defect-related

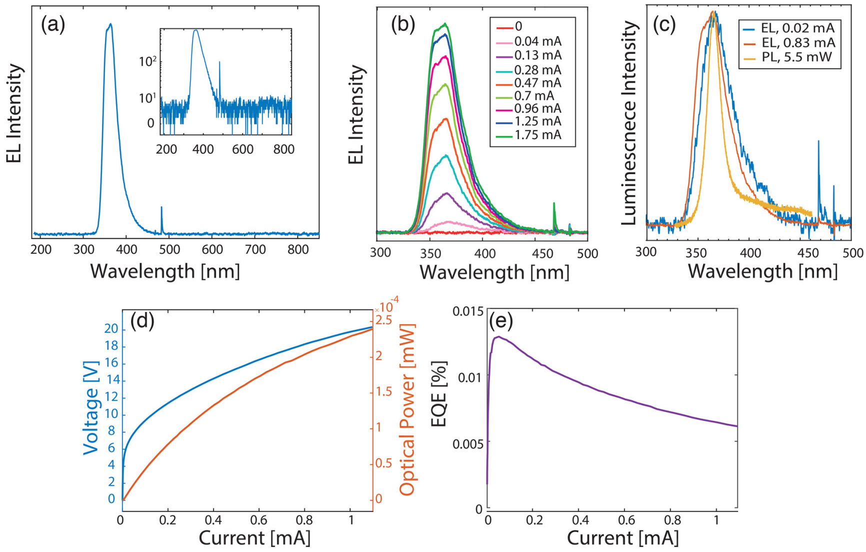

FIGURE 8.6. Room-temperature electroluminescence measurements and LED device efficiency. (**a**) Electroluminescence spectrum measured for a 150 μm diameter aperture LED device under a bias of 20 V, with the logarithmic plot in the inset, showing a peak emission at 365 nm. (**b**) EL spectra at different injection currents. (**c**) Comparison between RT PL and EL spectra normalized to their respective maximum intensity. (**d**) Voltage and optical output power dependency on injection current. (**e**) External quantum efficiency (EQE) at varying injection current measured using an integrating sphere.

yellow EL emission was detected[56], as evidenced by the semi-logarithmic data representation of the inset in Figure 8.6a.

The external quantum efficiency (EQE) of the LED is a product of the IQE, the current injection efficiency (CIE) and the light extraction efficiency (LEE). Figure 8.6d shows the measured optical power with respect to the injected current. The slope of the dependence gradually decreases as the current increases due to droop[57], which can be more clearly seen by calculating the EQE as a function of injection current. The EQE is defined as the ratio of emitted photons over the number of injected electrons as given by the expression

$$EQE = \frac{q \times P_{opt}}{I \times h\nu} \tag{8.1}$$

where q is the electron charge, P_{opt} is the measured optical power, I is the injected current and $h\nu$ is the energy of the emitted photons. The measured EQE is shown in Figure 8.6e, and it is clear that the LED device is most efficient at current injections around 0.05 mA for a 150 μm diameter aperture device, with a continuous decrease in the EQE with increasing forward bias. A major factor for the low EQE of this LED is believed to be the low effective hole doping in especially the p-AlGaN segment causing hole-blocking at the p-GaN/p-AlGaN interface. Because of this, the holes cannot reach the middle of the p-n junction and instead the EL recombination occurs in the thin p- GaN contact layer which is intrinsically a region with a low EQE. The absorption of the 140 nm long n-GaN segment at the emission wavelength of 365 nm can be considered to be negligible. However, one must design a shorter n-GaN segment for UV LEDs emitting below 365 nm as the absorption coefficient increases abruptly above the GaN band gap[58]. In this study, the nanocolumns are randomly positioned (by self-assembly) across the graphene substrate. However, controlling the nanocolumn diameter and spacing by e.g., selective area growth with a hole-patterned mask can potentially increase the EQE by enabling coupling of the light emission into guided modes along the nanocolumns, as demonstrated in AlGaN- and InGaN-based nanocolumn/nanopyramid arrays[50,59–62]. Furthermore, one can reduce EQE droop by inserting an electron blocking layer on the p-side of the active layer, preventing electrons from overshooting the recombination region[63]. By incorporating quantum wells in the active layers, the efficiency can be further improved as the probability of radiative recombination increases[64]. Reducing the sheet resistance of graphene would lower the operating voltage of the LED, and there are several methods to achieve this. The reduction of plasma-damage has already been discussed, but in addition conducting elements can be deposited on the graphene if the LED is delaminated from the glass substrate[65]. Examples of conducting elements are Ag nanowires[66] and Au dots[67].

8.6 CONCLUSIONS

To summarize and conclude, we have shown that DLG can be used as a substrate for RF-PAMBE growth of GaN/AlGaN nanocolumns, and subsequently as the transparent electrode in a fabricated UV-A LED device. Although graphene gets damaged by plasma-activated nitrogen during the nanocolumn RF-PAMBE growth, the DLG retains its prominent characteristics and functions as a transparent electrode. Electroluminescence emission is achieved during continuous biasing at a wavelength of 365 nm with no defect-related yellow emission. On the basis of temperature-dependent PL, an IQE of ~46 % is estimated, confirming the high crystal quality of the nanocolumns. These results indicate that graphene can be used as a functional substrate and electrode for III-nitride-based device technology. Furthermore, we have indicated several possible steps for growth and device design optimization to improve the EQE, now that this platform has been established.

8.7 METHODS

Substrate preparation. The DLG is formed by two successive transfers of single-layer graphene. In this work, we used commercially available DLG as a substrate which was synthesized using CVD on Cu foil[33] and transferred to a substrate carrier of amorphous silica glass by Graphene Platform Corp. (Tokyo, Japan). The backside of the substrate was coated with an approximately 300 nm thick Ti layer for efficient and uniform absorption of thermal radiation from the heater to the substrate, as well as assisting the pyrometer reading during nanocolumn growth.

Growth of GaN/AlGaN nanocolumns. The catalyst-free and self-assembled GaN/$Al_xGa_{1-x}N$ nanocolumn heterostructures were grown in an EpiQuest RF-PAMBE system under N-rich conditions[17,39]. Standard effusion cells were used to supply Al, Ga, Mg (p-type dopant), and Si (n-type dopant) atoms, while atomic nitrogen was supplied from an RF plasma source operating at 450 W. Growth temperatures were recorded both from thermocouple readings near the Ti-coated backside of the silica glass substrate carrier and from pyrometer readings, in order to obtain as good as possible control over the substrate temperature. For the purpose of consistency, the growth temperatures stated hereafter refer to the pyrometer readings. The length/thickness for each segment/layer mentioned in the next paragraph are nominal values based on the ratio between the Al and Ga fluxes (see Table B.1 in Appendix B).

To start the nanocolumn growth, an Al seeding layer with Si atoms were deposited at 805 °C before the graphene substrate was exposed to N plasma. After that, the Si, Al and N shutters were opened simultaneously to form an n-AlN buffer layer with a thickness of approximately 40 nm[25]. Afterwards, a segment of about 140 nm[25] high n-GaN nanocolumn segments were formed at 895 °C, acting as a template for n-AlGaN[39], minimizing the chance of coalescence and/or quasi-film-like structures[40]. Subsequently, 550 nm long n-$Al_{0.25}Ga_{0.75}N$ nanocolumn segments were grown at 915 °C, followed by an active region of 27 nm thick intrinsic GaN segment grown at 895 °C. Radial nanocolumn development is anticipated, increasing the chance of achieving champagne-glass structure for the following nanocolumn segments[39]. Using this method, one can increase the diameter of nanocolumns and thus coverage without introducing a higher Al flux[25]. Next, a 200 nm thick p-$Al_{0.25}Ga_{0.75}N$ segment was grown at 695 °C, and finally, 20 nm thick p-GaN grown at 675 °C was used as a p-type contact layer. Each nanocolumn segment has its own distinctive growth condition with respect to Al, Ga, Si, and Mg beam equivalent pressures, N_2 flow rate and growth time, as summarized in Table B.1 in the Appendix B.

Micro-Raman measurements. A Renishaw inVia Reflex system with a 100 mW 532 nm laser, a 50× confocal objective and a spectral resolution of less than 1 cm^{-1} was used to map 40 × 40 μm areas on the samples. 10 mW laser power with a dwell time of 10 s was used for the acquisitions, and spectra shown in Figure 8.2a are averaged from 1600 individual measurements.

SEM imaging. Secondary electron images were taken with a Hitachi SU8000 system at an acceleration voltage of 5 kV.

TEM imaging. The cross-section TEM lamella was prepared by a FEI Helios G4 UX dual-beam FIB-SEM. Two protection layers of carbon, the first one made by e-beam assisted deposition and the second by ion-beam assisted deposition, were deposited on the surface of the selected area prior to milling. Coarse thinning was performed at 30 kV ion-beam acceleration voltage, while the final thinning was performed at 5 and finally 2 kV to minimize Ga implantation and surface amorphization.

TEM characterization was performed with a double Cs-corrected cold-FEG JEOL ARM 200CF, operated at 200 kV and equipped with a 100 mm^2 (0.98 sr solid angle) Centurio SDD for X-ray energy dispersive spectroscopy (EDS) and a Quantum ER GIF for electron energy loss spectroscopy (EELS). In order to remove surficial hydrocarbons, the TEM lamella was gently plasma cleaned with a shielding holder 2 × 10 s prior to TEM characterization. Simultaneous EDS and dual-EELS were performed in scanning TEM (STEM) mode for chemical compositional analysis.

Electrical measurements. For van der Pauw measurements, Au contacts to graphene were made in the corners of a quadratic 0.5 × 0.5 cm^2 sample. The voltage was measured on opposite sides of the bias current path for both polarities to find the corresponding resistance, giving a total of eight measurements. These values were then inserted into the van der Pauw formula and the equation was solved for R_s numerically. The current-voltage measurements were done on a two-probe station connected to a Keithley 2636A sourcemeter.

Photoluminescence measurements. Continuous-wave (CW) excitation was achieved with a Kimmon Koha He-Cd laser operating at 325 nm. The excitation beam was focused on the sample using a 5 mm lens, achieving a spot size of ~0.42 mm. The sample was placed inside a Cryo Industries closed-cycle liquid He microscopy cryostat system equipped with a sample heater and thermometer for precise sample temperature control. PL detection was achieved with an Andor Shamrock 303i imaging spectrograph, using a 600 lines/mm grating blazed at 500 nm, dispersing the signal onto an Andor Newton electron multiplying charge-coupled device (EMCCD).

Electroluminescence spectral measurements. For LED electroluminescence measurements, a StellarNet EPP2000 UV-VIS (185 nm - 850 nm) compact spectrometer with a resolution between 0.4 nm (UV) and 0.25 nm (VIS), 2048 channels, was used with a UV-transparent fiber.

Electroluminescence integrating sphere measurements. The integrating sphere measurement system consists of a 50 cm diameter integrating sphere ($BaSO_4$ coating) and a spectrometer consisting of a grating monochromator with step motor and photomultiplier tube. The optical resolution of the entire system is about 1.2 nm. According to the manufacturer, the minimum spectroradiometric accuracy of the system is ±1% in the UVA and visible spectral region for each individual wavelength step. The LED sample is positioned in the center of the integrating sphere and contacted via contact probes. The LED is electrically driven and measured using a Keithley 2400 sourcemeter.

8.8 ACKNOWLEDGMENTS

We acknowledge financial supports from the Research Council of Norway via the NANO2021 (259553) program and the Japan Society for the Promotion of Science KAKENHI (24000013). We would also like to acknowledge the Research Council of Norway for the support to the Micro and Nano-Fabrication Facility, NorFab (245963/F50). The TEM work was carried out on the NORTEM infrastructure (Grant No. 197405) TEM Gemini Centre, NTNU. We would like to thank Alain Ferber at SINTEF-Oslo, Michael Kneissl, Tim Wernicke and Martin Guttman of TU Berlin for their help in acquiring electroluminescence data. We are also indebted to Koji Yamano and Isamu Matsuyama of Sophia University for dedicated RF-PAMBE maintenance and insightful suggestions. Shunsuke Ishizawa, Yohei Nakagawa and Yuzo Matsui of Sophia University are appreciated for fruitful discussions.

8.9 REFERENCES

[1] R. A. Soref. Silicon-Based Optoelectronics. *Proceedings of the IEEE* **81** (12), 1687–1706 (1993). Cited on page/s 172.

[2] S. Mokkapati and C. Jagadish. III-V Compound SC for Optoelectronic Devices. *Materials Today* **12** (4), 22–32 (2009). Cited on page/s 172.

[3] Y. Kozuka, A. Tsukazaki, and M. Kawasaki. Challenges and Opportunities of ZnO-Related Single Crystalline Heterostructures. *Applied Physics Reviews* **1** (1), 011303 (2014). Cited on page/s 172.

[4] A. K. Geim and K. S. Novoselov. The Rise of Graphene. *Nature Materials* **6**, 183–191 (2007). Cited on page/s 173.

[5] A. A. Balandin, S. Ghosh, W. Bao, I. Calizo, D. Teweldebrhan, F. Miao, and C. N. Lau. Superior Thermal Conductivity of Single-Layer Graphene. *Nano Letters* **8** (3), 902–907 (2008). Cited on page/s 173.

[6] A. Mazid Munshi, Dasa L. Dheeraj, Vidar T. Fauske, Dong-Chul Kim, Antonius T. J. van Helvoort, Bjørn-Ove Fimland, and Helge Weman. Vertically Aligned GaAs Nanowires on Graphite and Few-Layer Graphene: Generic Model and Epitaxial Growth. *Nano Letters* **12** (9), 4570–4576 (2012). Cited on page/s 173, 175.

[7] Y. J. Hong, J. W. Yang, W. H. Lee, R. S. Ruoff, K. S. Kim, and T. Fukui. Van der Waals Epitaxial Double Heterostructure: InAs/Single-Layer Graphene/InAs. *Advanced Materials* **25** (47), 6847–6853 (2013). Cited on page/s 173.

[8] J. Wallentin, D. Kriegner, J. Stangl, and M. T. Borgstrom. Au-Seeded Growth of Vertical and in-Plane III-V Nanowires on Graphite Substrates. *Nano Letters* **14** (4), 1707–1713 (2014). Cited on page/s 173.

[9] E. A. Anyebe, I. Sandall, Z. M. Jin, A. M. Sanchez, M. K. Rajpalke, T. D. Veal, Y. C. Cao, H. D. Li, R. Harvey, and Q. D. Zhuang. Optimization of Self-Catalyzed InAs Nanowires on Flexible Graphite for Photovoltaic Infrared Photodetectors. *Scientific Reports* 7, 46110 (2017). Cited on page/s 173.

[10] E. A. Anyebe, A. M. Sanchez, S. Hindmarsh, X. Chen, J. Shao, M. K. Rajpalke, T. D. Veal, B. J. Robinson, O. Kolosov, and F. Anderson. Realization of Vertically Aligned, Ultrahigh Aspect Ratio InAsSb Nanowires on Graphite. *Nano Letters* **15** (7), 4348–4355 (2015). Cited on page/s 173.

[11] P. K. Mohseni, A. Behnam, J. D. Wood, X. Zhao, K. J. Yu, N. C. Wang, A. Rockett, J. a. Rogers, J. W. Lyding, and E. Pop. Monolithic III-V Nanowire Solar Cells on Graphene via Direct van der Waals Epitaxy. *Advanced Materials* **26** (22), 3755–3760 (2014). Cited on page/s 173.

[12] Y. Tchoe, J. Jo, M. Kim, and G.-C. Yi. Catalyst-Free Growth of InAs/InxGa1−xAs Coaxial Nanorod Heterostructures on Graphene Layers Using Molecular Beam Epitaxy. *NPG Asia Materials* 7, e206 (2015). Cited on page/s 173.

[13] R. K. Biroju, N. Tilak, G. Rajender, S. Dhara, and P. K. Giri. Catalyst Free Growth of ZnO Nanowires on Graphene and Graphene Oxide and Its Enhanced Photoluminescence and Photoresponse. *Nanotechnology* **26** (14), 145601 (2015). Cited on page/s 173.

[14] C.-H. Lee, Y.-J. Kim, Y. J. Hong, S.-R. Jeon, S. Bae, B. H. Hong, and G.-C. Yi. Flexible Inorganic Nanostructure Light-Emitting Diodes Fabricated on Graphene Films. *Advanced Materials* **23** (40), 4614–4619 (2011). Cited on page/s 173.

[15] S. Nakagawa, T. Tabata, Y. Honda, M. Yamaguchi, and H. Amano. GaN Nanowires Grown on a Graphite Substrate by Radio Frequency Molecular Beam Epitaxy. *Japanese Journal of Applied Physics* **52** (8S), 08JE07 (2013). Cited on page/s 173.

[16] M. Heilmann, G. Sarau, M. Gobelt, M. Latzel, S. Sadhujan, C. Tessarek, and S. Christiansen. Growth of GaN Micro- and Nanorods on Graphene-Covered Sapphire: Enabling Conductivity to Semiconductor Nanostructures on Insulating Substrates. *Crystal Growth & Design* **15** (5), 2079–2086 (2015). Cited on page/s 173, 175.

[17] H. Hayashi, Y. Konno, and K. Kishino. Self-organization of dislocation-free, high-density, vertically aligned GaN nanocolumns involving InGaN quantum wells on graphene/SiO_2 covered with a thin AlN buffer layer. *Nanotechnology* **27** (5), 055302 (2015). Cited on page/s 173, 174, 175, 185.

[18] M. Heilmann, *et al.* Vertically Oriented Growth of GaN Nanorods on Si Using Graphene as an Atomically Thin Buffer Layer. *Nano Letters* **16** (6), 3524–3532 (2016). Cited on page/s 173, 175.

[19] S. R. Ryu, S. D. G. Ram, S. J. Lee, H. Cho, S. Lee, T. W. Kang, S. Kwon, W. Yang, S. Shin, and Y. Woo. Vertical Current-Flow Enhancement via Fabrication of GaN Nanorod p-n Junction Diode on Graphene. *Applied Surface Science* **347**, 793–798 (2015). Cited on page/s 173.

[20] S. Kang, A. Mandal, J.-H. Park, D.-Y. Um, J. H. Chu, S.-Y. Kwon, and C.-R. Lee. Effects of growth temperatures on the characteristics of n-GaN nanorods–graphene hybrid structures. *Journal of Alloys and Compounds* **644**, 808–813 (2015). Cited on page/s 173.

[21] V. Kumaresan, *et al.* Epitaxy of GaN Nanowires on Graphene. *Nano Letters* **16** (8), 4895–4902 (2016). Cited on page/s 173.

[22] K. Chung, H. Beak, Y. Tchoe, H. Oh, H. Yoo, M. Kim, and G.-C. Yi. Growth and characterizations of GaN micro-rods on graphene films for flexible light emitting diodes. *APL Materials* **2** (9), 092512 (2014). Cited on page/s 173.

[23] A. Liudi Mulyo, M. K. Rajpalke, H. Kuroe, P.-E. Vullum, H. Weman, B.-O. Fimland, and K. Kishino. Vertical GaN nanocolumns grown on graphene intermediated with a thin AlN buffer layer. *Nanotechnology* **30** (1), 015604 (2018). Cited on page/s 173, 174, 175, 178.

[24] A. Liudi Mulyo *et al.* The Influence of AlN Buffer Layer on the Growth of Self-Assembled GaN Nanocolumns on Graphene. *Unpublished* (n.d). Cited on page/s 173, 174, 175, 178.

[25] A. Liudi Mulyo *et al.* Utilization of Graphene as Substrate and Bottom Electrode for High-Density and Vertically-Aligned GaN/AlGaN Nanocolumns. *Unpublished* (n.d). Cited on page/s 173, 174, 175, 178, 185.

[26] S. Fernandez-Garrido, *et al.* Molecular Beam Epitaxy of GaN Nanowires on Epitaxial Graphene. *Nano Letters* **17** (9), 5213–5221 (2017). Cited on page/s 173, 174, 175, 178.

[27] B.-J. Kim, C. Lee, Y. Jung, K. Hyeon Baik, M. A. Mastro, J. K. Hite, C. R. Eddy, and J. Kim. Large-area transparent conductive few-layer graphene electrode in GaN-based ultra-violet light-emitting diodes. *Applied Physics Letters* **99** (14), 143101 (2011). Cited on page/s 173.

[28] B.-J. Kim, G. Yang, H.-Y. Kim, K. H. Baik, M. A. Mastro, J. K. Hite, C. R. Eddy, F. Ren, S. J. Pearton, and J. Kim. GaN-based ultraviolet light-emitting diodes with AuCl3-doped graphene electrodes. *Optics Express* **21** (23), 29025–29030 (2013). Cited on page/s 173.

[29] J. Kang, Z. Li, H. Li, Z. Liu, X. Li, X. Yi, P. Ma, H. Zhu, and G. Wang. Pyramid Array InGaN/GaN Core-Shell Light Emitting Diodes with Homogeneous Multilayer Graphene Electrodes. *Applied Physics Express* **6** (7), 072102 (2013). Cited on page/s 173.

[30] G. Jo, M. Choe, C. Y. Cho, J. H. Kim, W. Park, S. Lee, W.-K. Hong, T.-W. Kim, S.-J. Park, and B. H. Hong. Large-Scale Patterned Multi-Layer Graphene Films as Transparent Conducting Electrodes for GaN Light-Emitting Diodes. *Nanotechnology* **21** (17), 175201 (2010). Cited on page/s 173.

[31] B. Fu, Y. Cheng, Z. Si, T. Wei, X. Zeng, G. Yuan, Z. Liu, H. Lu, X. Yi, and J. Li. Phosphor-Free InGaN Micro-Pyramid White Light Emitting Diodes with Multilayer Graphene Electrode. *RSC Advances* **5** (122), 100646–100650 (2015). Cited on page/s 173.

[32] F. Bonaccorso, Z. Sun, T. Hasan, and A. C. Ferrari. Graphene photonics and optoelectronics. *Nature Photonics* **4**, 611–622 (2010). Cited on page/s 173.

[33] J. W. Suk, A. Kitt, C. W. Magnuson, Y. Hao, S. Ahmed, J. An, A. K. Swan, B. B. Goldberg, and R. S. Ruoff. Transfer of CVD-Grown Monolayer Graphene onto Arbitrary Substrates. *ACS Nano* **5** (9), 6916–6924 (2011). Cited on page/s 173, 185.

[34] L. Zhou, J. E. Epler, M. R. Krames, W. Goetz, M. Gherasimova, Z. Ren, J. Han, M. Kneissl, and N. M. Johnson. Vertical injection thin-film AlGaN/AlGaN multiple-quantum-well deep ultraviolet light-emitting diodes. *Applied Physics Letters* **89** (24), 241113 (2006). Cited on page/s 173.

[35] K. Kawasaki, C. Koike, Y. Aoyagi, and M. Takeuchi. Vertical AlGaN deep ultraviolet light emitting diode emitting at 322 nm fabricated by the laser lift-off technique. *Applied Physics Letters* **89** (26), 261114 (2006). Cited on page/s 173.

[36] V. Adivarahan, A. Heidari, B. Zhang, Q. Fareed, M. Islam, S. Hwang, K. Balakrishnan, and A. Khan. Vertical Injection Thin Film Deep Ultraviolet Light Emitting Diodes with AlGaN Multiple-Quantum Wells Active Region. *Applied Physics Express* **2** (9), 092102 (2009).

Cited on page/s 173.

[37] J.-J. Zheng and Y.-J. Lin. Tuning the work function of graphene by nitrogen plasma treatment with different radio-frequency powers. *Applied Physics Letters* **104** (23), 233103 (2014). Cited on page/s 174, 178.

[38] Y. Gohda and S. Tsuneyuki. Structural phase transition of graphene caused by GaN epitaxy. *Applied Physics Letters* **100** (5), 053111 (2012). Cited on page/s 174.

[39] H. Sekiguchi, K. Kato, J. Tanaka, A. Kikuchi, and K. Kishino. Ultraviolet GaN-based nanocolumn light-emitting diodes grown on n-(111) Si substrates by rf-plasma-assisted molecular beam epitaxy. *Physica Status Solidi A - Applications and Materials Science* **205** (5), 1067–1069 (2008). Cited on page/s 174, 175, 185.

[40] S. Zhao, S. Y. Woo, S. M. Sadaf, Y. Wu, A. Pofelski, D. A. Laleyan, R. T. Rashid, Y. Wang, G. A. Botton, and Z. Mi. Molecular Beam Epitaxy Growth of Al-Rich AlGaN Nanowires for Deep Ultraviolet Optoelectronics. *APL Materials* **4** (8), 086115 (2016). Cited on page/s 174, 185.

[41] A. Liudi Mulyo, Y. Konno, J. S. Nilsen, A. T. J. van Helvoort, B.-O. Fimland, H. Weman, and K. Kishino. Growth study of self-assembled GaN nanocolumns on silica glass by plasma assisted molecular beam epitaxy. *Journal of Crystal Growth* **480**, 67–73 (2017). Cited on page/s 175.

[42] A. Pierret, C. Bougerol, M. den Hertog, B. Gayral, M. Kociak, H. Renevier, and B. Daudin. Structural and Optical Properties of $Al_xGa_{1-x}N$ Nanowires. *Physica Status Solidi (RRL) – Rapid Research Letters* **7** (10), 868–873 (2013). Cited on page/s 177.

[43] A. Pierret, C. Bougerol, S. Murcia-Mascaros, A. Cros, H. Renevier, B. Gayral, and B. Daudin. Growth, Structural and Optical Properties of AlGaN Nanowires in the Whole Composition Range. *Nanotechnology* **24** (11), 115704 (2013). Cited on page/s 177.

[44] S. Fernandez-Garrido, G. Koblmuller, E. Calleja, and J. S. Speck. In Situ GaN Decomposition Analysis by Quadrupole Mass Spectrometry and Reflection High-Energy Electron Diffraction. *Journal of Applied Physics* **104** (3), 033541 (2008). Cited on page/s 177.

[45] L. K. Li, M. J. Jurkovic, W. I. Wang, J. M. van Hove, and P. P. Chow. Surface Polarity Dependence of Mg Doping in GaN Grown by Molecular-Beam Epitaxy Surface. *Applied Physics Letters* **76** (13), 1740–1742 (2000). Cited on page/s 177.

[46] B. Wu, H. M. Tuncer, A. Katsounaros, W. Wu, M. T. Cole, K. Ying, L. Zhang, W. I. Milne, and Y. Hao. Microwave Absorption and Radiation from Large-Area Multilayer CVD Graphene. *Carbon* 77, 814–822 (2014). Cited on page/s 178.

[47] G. Sarau, M. Heilmann, M. Bashouti, M. Latzel, C. Tessarek, and S. Christiansen. Efficient Nitrogen Doping of Single-Layer Graphene Accompanied by Negligible Defect Generation for Integration into Hybrid Semiconductor Heterostructures. *ACS Applied Materials & Interfaces* **9** (11), 10003–10011 (2017). Cited on page/s 178.

[48] J. E. Lee, G. Ahn, J. Shim, Y. S. Lee, and S. Ryu. Optical Separation of Mechanical Strain from Charge Doping in Graphene. *Nature Communications* **3**, 1024 (2012). Cited on page/s 178.

[49] A. Gahoi, S. Wagner, A. Bablich, S. Kataria, V. Passi, and M. C. Lemme. Contact resistance study of various metal electrodes with CVD graphene. *Solid-State Electronics* **125**, 234–239 (2016). Extended papers selected from ESSDERC 2015. Cited on page/s 180.

[50] B. H. Le, S. Zhao, X. Liu, S. Y. Woo, G. A. Botton, and Z. Mi. Controlled Coalescence of AlGaN Nanowire Arrays: An Architecture for Nearly Dislocation-Free Planar Ultraviolet Photonic Device Applications. *Advanced Materials* **28** (38), 8446–8454 (2016). Cited on page/s 180, 184.

[51] M. Qi, K. Nomoto, M. Zhu, Z. Hu, Y. Zhao, V. Protasenko, B. Song, X. Yan, G. Li, and J. Verma. High Breakdown Single-Crystal GaN p-n Diodes by Molecular Beam Epitaxy. *Applied Physics Letters* **107** (23), 232101 (2015). Cited on page/s 180.

[52] R. R. Pela, C. Caetano, M. Marques, L. G. Ferreira, J. Furthmüller, and L. K. Teles. Accurate

Band Gaps of AlGaN, InGaN, and AlInN Alloys Calculations Based on LDA-1/2 Approach. *Applied Physics Letters* **98** (15), 151907 (2011). Cited on page/s 181.

[53] M. A. Reshchikov and H. Morkoc. Luminescence properties of defects in GaN. *Journal of Applied Physics* **97** (6), 061301 (2005). Cited on page/s 181.

[54] S. Watanabe, N. Yamada, M. Nagashima, Y. Ueki, C. Sasaki, Y. Yamada, T. Taguchi, K. Tadatomo, H. Okagawa, and H. Kudo. Internal Quantum Efficiency of Highly-Efficient InxGa1-xN-Based near-Ultraviolet Light-Emitting Diodes. *Applied Physics Letters* **83** (24), 4906–4908 (2003). Cited on page/s 182.

[55] Q. Wang, A. T. Connie, H. P. T. Nguyen, M. G. Kibria, S. Zhao, S. Sharif, I. Shih, and Z. Mi. Highly Efficient, Spectrally Pure 340 nm Ultraviolet Emission from $Al_xGa_{1-x}N$ Nanowire Based Light Emitting Diodes. *Nanotechnology* **24** (34), 345201 (2013). Cited on page/s 182.

[56] I. Lee, I. Choi, C. R. Lee, and S. K. Noh. Evolution of Stress Relaxation and Yellow Luminescence in GaN/Sapphire by Si Incorporation. *Applied Physics Letters* **71** (10), 1359–1361 (1997). Cited on page/s 183.

[57] W. Sun, M. Shatalov, J. Deng, X. Hu, J. Yang, A. Lunev, Y. Bilenko, M. Shur, and R. Gaska. Efficiency Droop in 245–247 nm AlGaN Light-Emitting Diodes with Continuous Wave 2 mW Output Power. *Applied Physics Letters* **96** (6), 061102 (2010). Cited on page/s 183.

[58] J. F. Muth, J. H. Lee, I. K. Shmagin, R. M. Kolbas, H. C. Casey, B. P. Keller, U. K. Mishra, and S. P. DenBaars. Absorption coefficient, energy gap, exciton binding energy, and recombination lifetime of GaN obtained from transmission measurements. *Applied Physics Letters* **71** (18), 2572–2574 (1997). Cited on page/s 184.

[59] M. Djavid and Z. Mi. Enhancing the light extraction efficiency of AlGaN deep ultraviolet light emitting diodes by using nanowire structures. *Applied Physics Letters* **108** (5), 051102 (2016). Cited on page/s 184.

[60] A. M. Munshi, D.-C. Kim, C. P. Heimdal, M. Heilmann, S. H. Christiansen, P. E. Vullum, A. T. J. van Helvoort, and H. Weman. Selective area growth of AlGaN nanopyramid arrays on graphene by metal-organic vapor phase epitaxy. *Applied Physics Letters* **113** (26), 263102 (2018). Cited on page/s 184.

[61] K. Kishino and S. Ishizawa. Spectrally-Broadened Multimode Lasing Based on Structurally Graded InGaN Nanocolumn Photonic Crystals Suitable for Reduction of Speckle Contrast. *Applied Physics Letters* **109** (7), 071106 (2016). Cited on page/s 184.

[62] K. Yamano and K. Kishino. Selective area growth of InGaN-based nanocolumn LED crystals on AlN/Si substrates useful for integrated μ-LED fabrication. *Applied Physics Letters* **112** (9), 091105 (2018). Cited on page/s 184.

[63] H. P. T. Nguyen, K. Cui, S. Zhang, M. Djavid, A. Korinek, G. A. Botton, and Z. Mi. Controlling Electron Overflow in Phosphor-Free InGaN/GaN Nanowire White Light-Emitting Diodes. *Nano Letters* **12** (3), 1317–1323 (2012). Cited on page/s 184.

[64] J. Han, M. H. Crawford, R. J. Shul, J. J. Figiel, M. Banas, L. Zhang, Y. K. Song, H. Zhou, and A. V. Nurmikko. AlGaN/GaN Quantum Well Ultraviolet Light Emitting Diodes. *Applied Physics Letters* **73** (12), 1688–1690 (1998). Cited on page/s 184.

[65] L. Wang, W. Liu, Y. Zhang, Z.-H. Zhang, S. Tiam Tan, X. Yi, G. Wang, X. Sun, H. Zhu, and H. Volkan Demir. Graphene-based transparent conductive electrodes for GaN-based light emitting diodes: Challenges and countermeasures. *Nano Energy* **12**, 419–436 (2015). Cited on page/s 184.

[66] Z. Li, J. Kang, Z. Liu, C. Du, X. Lee, X. Li, L. Wang, X. Yi, H. Zhu, and G. Wang. Enhanced Performance of GaN-Based Light-Emitting Diodes with Graphene/Ag Nanowires Hybrid Films. *AIP Advances* **3** (4), 042134 (2013). Cited on page/s 184.

[67] M. Choe, C.-Y. Cho, J.-P. Shim, W. Park, S. K. Lim, W.-K. Hong, B. H. Lee, D.-S. Lee, S.-J. Park, and T. Lee. Au Nanoparticle-Decorated Graphene Electrodes for GaN-Based Optoelectronic Devices. *Applied Physics Letters* **101** (3), 031115 (2012). Cited on page/s 184.

CHAPTER 9

Graphene as transparent conducting substrate for GaN/AlGaN nanocolumn flip-chip ultraviolet light-emitting diode

---

Andreas Liudi Mulyo[1,2], Anjan Mukherjee[1,*], Ida Marie Høiaas[1,*], Lyubomir Ahtapodov[1], Tron Arne Nilsen[1], Håvard Hem Toftevaag[1], Per Erik Vullum[3,4], Katsumi Kishino[2,5,#], Helge Weman[1,#] and Bjørn-Ove Fimland[1]
**AM and IMH contributed equally to this study.*

Manuscript under review, submitted on the 3rd of February 2021

The title and content of this chapter are based on the submitted manuscript version.

Contributions

ALM planned the experiments under the supervision of BOF, HW and KK. **ALM** performed the nanocolumn growth by MBE and SEM imaging. IMH and HHT conducted Raman spectroscopy and mapping and analyzed the data, in collaboration with **ALM**. IMH and AM carried out preliminary device fabrication and I-V measurements, while AM fabricated the final LED device together with HHT and did I-V/EL measurements. TAN did XRD characterization, simulation and analysis. PEV performed TEM/STEM/EDX/EELS imaging and spectroscopy. LA conducted the photoluminescence measurements and analysis. **ALM** drafted the manuscript. All authors contributed to the discussion of results and preparations of the manuscript.

---

[1] Department of Electronic Systems, Norwegian University of Science and Technology (NTNU), NO-7491 Trondheim, Norway. [2] Department of Engineering and Applied Sciences, Sophia University, 102-8554 Tokyo, Japan. [3] SINTEF Industry, NO-7465 Trondheim, Norway. [4] Department of Physics, Norwegian University of Science and Technology (NTNU), NO-7491 Trondheim, Norway. [5] Sophia Nanotechnology Research Center, Sophia University, 102-8554 Tokyo, Japan. [#] e-mail: kishino@sophia.ac.jp and bjorn.fimland@ntnu.no

Part III

EPILOGUE

Chapter 10

Closing remarks

With nitride semiconductor/graphene-based material growth and device technology being at an initial phase of research, the results presented in this study add to the understanding of growth, as well as provide the proof-of-concept of UV LEDs based on GaN/AlGaN nanocolumns using graphene as substrate and transparent electrode. This last chapter of this dissertation contains a summary and conclusions of the present work, including potential directions for future work. The latter section could be viewed as an entry point to further advance the growth method and improve the device performance presented in this PhD thesis.

10.1 Summary

Two different kinds of materials, namely GaN nanocolumns and graphene , have developed as favorable contenders for the realization of the hybrid system for nano-optoelectronic devices, for instance UV LEDs, due to their respective complementary properties. GaN, along with its alloys, is inherently endowed with a direct wide bandgap, and being in the nanocolumn form, a structure with reduced stacking faults and threading dislocation densities can be obtained due to the effective radial strain relaxation. Such relaxation also suppresses the piezoelectric polarization field, as well as the resulting QCSE [1]. These unique nanocolumn features have been utilized to obtain high structural quality of III-nitride materials on virtually any substrate [2–4]. Graphene exhibits many interesting properties, a few of which are quite beneficial for GaN-based UV LED devices when graphene is employed as a substrate material, especially if it is utilized as a transparent conductive electrode [5–7].

That said, the integration of a GaN nanocolumn-based device with graphene employed as a transparent conductive substrate has not been demonstrated *prior* to this thesis work. Knowing that the full exploitation of graphene could improve the functionalities of optoelectronic devices based on III-V nitride semiconductors, especially LED devices working at deep UV range, this could turn out to be a very promising route. An equally important topic that has not been sufficiently addressed in the literature is the investigation of GaN nanocolumn synthesis on graphene. Understanding the general mechanism of the growth behavior of GaN nanocolumns on graphene could elucidate the adequate approach to obtain a GaN/AlGaN nanocolumn device structure using the RF-PAMBE technique and advance the development of optoelectronic device fabrication based on III-V nitride semiconductors grown on graphene in general.

Growth study of GaN and GaN/AlGaN nanocolumns on graphene substrate and their attempted use in UV LED fabrication have been central topics in this PhD thesis. A preliminary study (Chapter 5) on self-assembled GaN nanocolumns grown on fused silica demonstrated that these nanocolumns are grown preferentially along the *c*-axis direction, and their structural and optical qualities are comparable to those of the GaN nanocolumns on silicon and sapphire substrates, despite the absence of a global epitaxial relationship between GaN and the fused silica substrate. More importantly, it was further demonstrated (Chapter 6) that highly dense and vertical GaN nanocolumns can be obtained on CVD grown graphene transferred to silica glass, owing to the presence of a thin AlN buffer (intermediate) layer. Later in Chapter 7, it was identified that the AlN buffer layer has the capability to affect the growth morphology of GaN nanocolumns, as well as to alter the graphene properties.

These findings facilitate the progress on realizing the GaN nanocolumn device structure (with AlGaN as the cladding layer) on double-layer graphene (Chapter 8) and subsequently single-layer graphene substrates (Chapter 9). In both situations, the first evidence on graphene being used simultaneously as a substrate and a transparent conducting electrode for the GaN/AlGaN nanocolumn device structure has been provided. The absence of defects, such as stacking faults and/or threading dislocations in the grown nanocolumns, indicates that high-quality single crystalline wurtzite GaN/AlGaN nanocolumns can be grown on graphene. More interestingly, these initial attempts successfully demonstrate the achievement of electroluminescence emissions in LEDs working at the UV-A wavelength range, with no observation of defect-related yellow luminescence emission. These results hint at the opportunity that graphene could be exploited as a functional substrate for nitride semiconductor-based optoelectronic and electronic device technology in the future.

10.2 PERSPECTIVE

The reader might notice that the active area of GaN/AlGaN nanocolumn device structures shown in Chapter 8 consists of a GaN bulk region with a nominal thickness of around 30 nm. One suggestion to improve the LED efficiency of the present work is via the exploitation of a quantum well structure as the active layer, as briefly demonstrated and discussed in Chapter 9. This could effectively trap the injected charge carriers, i.e., electrons and holes, enhancing the carrier confinement and electron-hole wavefunction overlap in the nanocolumn active region. In this way, the probability for electrons and holes to undergo radiative recombination processes is increased. A multi-quantum well structure and an electron blocking layer could be used to further improve the luminescence efficiency of UV LEDs as is typically done for thin film based UV LEDs.

One coefficient that is normally included to calculate the IQE of GaN-based nanocolumn LEDs, namely the Auger recombination coefficient, is measured to be much smaller compared with those measured in GaN-based planar LEDs [1,8]. This reduced Auger recombination is assumed to have a direct consequence, with a negligible droop in LEDs utilizing nanocolumn structures. It could be that the suppressed defect density in nanocolumn-based LEDs plays a major role in lowering the Auger recombination coefficient, which benefits the device performance.

Despite the fact that lowered Auger recombination can be obtained, the geometry of the nanocolumn itself contains some potential drawbacks [3], which should be considered to be improved in future work. One drawback is the enhancement of non-radiative surface recombination, namely Shockley-Read-Hall recombination associated with the presence of surface states, due to the large surface-to-volume ratio in the nanocolumn structure. Consequently, this high density of surface states will severely reduce the current injection efficiency in LEDs [2]. In addition, nanocolumns suffer from band bending caused by surface Fermi-level pinning, which reduces the recombination probability of electron-hole pairs. The less active volume per unit area of nanocolumn arrays also prompts less light-emitting media than a comparable thin-film structure does. It should be noted as well that the coalescence of self-organized III-nitride nanocolumns during the growth generates defects and they can result in degradation of the crystal quality that further reduces the IQE.

One proposal to reduce the total density of surface states, and thus to minimize the non-radiative surface recombination rate, is to use surface passivation techniques [2], which can be achieved via *in-situ* growth of nanocolumn core-shell structures. In this case, the shell typically consists of III-V nitride material with larger energy bandgap than that of the III-V nitride material in the core, e.g., visible InGaN/GaN dot-in-a-wire as a core structure and AlGaN as a shell [9]. In the latter case, the AlGaN shell was shown to be effective in reducing surface non-radiative recombination and enhancing the carrier injection efficiency, which in turn improved the LED device performance. Apart from that, *p*-type modulation doping techniques [10] or *p*-AlGaN electron blocking layers [8,11] can be implemented to mitigate the electron overflow across the active region. Such measures should be taken owing to the poor hole doping and mobility as well as inhomogeneous distribution of holes within the *p*-side of the nanocolumns, which can cause a significantly enhanced Auger recombination and increased electron overflow.

Particularly for AlGaN nanocolumns with high Al-content, one should consider the presence of a spontaneous polarization field [2], as the implementation of a *p*-AlGaN electron blocking layer alone might not completely resolve the electron overflow issue. The potential problem here originates from the polarization mismatch between layers in the LED active region, i.e., *p*-(Al)GaN barrier and *p*-AlGaN electron blocking layer. At the interface between these two layers, there is a presence of positive sheet charge (which is attractive to electrons) that can pull down the conduction band of the electron blocking layer, thus reducing the effective barrier height for electrons. As a result, electron leakage from the active region is enhanced at this heterointerface. Reducing carrier leakage stemming from the polarization mismatch can be achieved by employing a polarization-matched AlGaInN barrier instead of an (Al)GaN barrier. In the application of visible LEDs, this method has been proven to be effective in increasing the EQE [12]. For high Al-content in AlGaN LEDs, one can consider employing a monolayer GaN embedded in an AlN matrix, as this structure can exhibit transverse electric (instead of transverse magnetic) polarized emission in deep UV wavelengths [13].

With relation to spontaneous polarization fields due to the ionic character of the AlGa-N bonds combined with their non-centrosymmetric wurtzite crystal structure, one can utilize this property to achieve efficient AlGaN *p*-type doping. Compositional grading of a thin-film or nanocolumn of a non-centrosymmetric crystal along the direction of the dipole can lead to a positive- or negative-polarization bound charge. The former induces the formation of a mobile 3D electron gas, whereas the latter results in a mobile 3D hole gas, which makes an *n*- or *p*-type semiconductor, respectively [14]. Using this principle, Carnevale *et al.* [15] demonstrated working UV LEDs based on a polarization-induced AlGaN nanocolumn whose *p*-*n* junction was formed without impurity doping. This technique offers an interesting approach to the *p*-doping with Mg, which, due to its large activation energy, can lead to a highly resistive *p*-GaN, and even more resistive *p*-AlGaN.

In line with the attempts to find alternatives for the high-resistance *p*-type Mg doping of the GaN and AlGaN layers, a nanocolumn with a tunnel junction structure has been proposed. Compared with conventional *p*-*i*-*n* AlGaN nanocolumn LEDs, the incorporation of a tunnel junction in nanocolumn-based UV LEDs can reduce the device resistance by one order of magnitude and increase the light output power by two orders of magnitude[16]. This result can be obtained due to the tunnel junction device structure arranged in such a way that the top contact layer can consist of a low resistance *n*-GaN, instead of a resistive *p*-GaN. Laleyan *et al.*[17] reported that the *p*-type characteristics of B vacancies in h-BN can be used for efficient *p*-type conduction to replace Mg-doped GaN and AlGaN in nanocolumn LEDs. Their findings using this structure include better electrical performance compared with conventional LEDs whose *p*-AlGaN/*p*-GaN is based on Mg doping.

The self-organized GaN nanocolumn growth on graphene substrates demonstrated in this dissertation nucleate and grow non-uniformly in terms of length, diameter, and position. Similarly, the self-assembly process of AlGaN nanocolumns can additionally introduce an inhomogeneity in the spatial distribution of the Al composition for each nanocolumn, possibly due to fluctuations in the nanocolumn geometry and position[18]. Moreover, the random distribution of nanocolumns leads to a light-trapping effect and reduces the LEE[19]. Selective area growth of the nanocolumns[18–20] on hole masked graphene can be employed to mitigate these issues. Here, nanocolumns are only formed in the defined apertures of the mask placed on top of the graphene substrate due to the growth selectivity. The mask itself, typically composed of Ti or SiO_x, could be also utilized as a protection layer against the nitrogen plasma, thus reducing the graphene damage.

Employing more layers of graphene as a growth substrate can be considered as well, since it has lower sheet resistance compared with single- and double-layer graphene although this comes with the trade-off of reduced transparency. Additionally, it is presumed that the top layer(s) of graphene could take the damage from the plasma nitridation (i.e., as a sacrificial layer), allowing the graphene layer(s) below to retain their electrical properties as a bottom contact electrode. Furthermore, one can utilize interlayer materials placed between graphene and *p*-GaN, such as Au nanoparticles or Ag nanowires[6], in order to reduce the operating voltage of the LEDs. These conducting elements can also be deposited on the graphene once the nanocolumn/graphene is delaminated from the silica glass host substrate. Nevertheless, this method comes with an expense of reducing the light output of flip-chip type UV LEDs.

Regarding the issue of the number of graphene layers for the realization of nitride nanocolumn-based UV LEDs, particularly for the flip-chip type devices, ideally, many graphene layers should be chosen based on the reasoning mentioned in the previous paragraph. However, one should realize that extra graphene layers will increasingly absorb more of the generated UV light, which correspondingly limits the light output in flip-chip UV LEDs. Therefore, the emphasis should be placed on the balance between the optical transparency, structural property, and electrical property of the graphene, as these characteristics play a significant role in graphene as a transparent conducting substrate in this particular type of device. Within the nanocolumn structure itself, a GaN nanocolumn as the growth template for the following AlGaN nanocolumn should be avoided because of GaN's ability to absorb UV light for wavelengths shorter than 365 nm.

Different approaches for growing intermediate nanocolumn buffer layers on graphene could benefit future devices. Indeed, the *n*-AlN buffer layer proposed in this PhD thesis has been proven to significantly reduce the formation of tilted nanocolumns and demonstrate vertical nanocolumn growth to an extent that is acceptable for further devices. However, as *n*-AlN becomes a part of the device, its nature of being highly electrically insulating (reflected in its high energy bandgap of 6.2 eV) makes this material inherently unsuitable to achieve high device performance. It is expected as well that the interface between graphene and the *n*-AlN buffer layer forms a Schottky barrier, which can severely reduce the flow of electrons from graphene to *n*-AlN, as discussed in Subsection 3.2.3. Therefore, the utilization of an *n*-AlGaN buffer layer with sufficiently low Al-content (depending on the emission wavelength of the UV LED) could be an interesting alternative to achieve the same benefits as with *n*-AlN, e.g., retrieving vertical nanocolumns, and in addition provide a better electrical path for current transport from the graphene to the nanocolumns.

As a final remark, considering that Auger recombination and defects can be alleviated by growing GaN/AlGaN nanocolumn structures, the issues of poor hole transport, electron and hole leakage, electron overflow, and polarization field can be regarded as the main challenges (besides high sheet resistance of graphene after nanocolumn growth) that need to be addressed to improve the performance of UV LEDs achieved in the current study. They have been identified as the most probable causes for the underlying *efficiency droop* phenomenon in the UV LEDs, where the increasing injection current causes a decrease in the EQE. Moreover, the dominance of large densities of defects/surface states along the nanocolumn surface can cause unintentional carrier leakage, making the performance of such nanoscale LEDs fall short compared with conventional planar thin-film heterostructures[2,11]. Nonetheless, by implementing various possible approaches suggested in the closing section of this Doctoral thesis, it is expected that future UV light emitters based on GaN/AlGaN nanocolumns using graphene as a growth substrate and transparent conducting electrode could exhibit significantly enhanced efficiency.

10.3 REFERENCES

[1] W. Guo, M. Zhang, P. Bhattacharya, and J. Heo. Auger Recombination in III-Nitride Nanowires and Its Effect on Nanowire Light-Emitting Diode Characteristics. *Nano Letters* **11** (4), 1434–1438 (2011). Cited on page/s 219, 221.

[2] S. Zhao, H.P.T. Nguyen, Md. G. Kibria, and Z. Mi. III-Nitride nanowire optoelectronics. *Progress in Quantum Electronics* **44**, 14–68 (2015). Cited on page/s 219, 221, 222, 224.

[3] C. Zhao, N. Alfaraj, R. Chandra Subedi, J. W. Liang, A. A. Alatawi, A. A. Alhamoud, M. Ebaid, M. S. Alias, T. K. Ng, and B. S. Ooi. III-nitride nanowires on unconventional substrates: From materials to optoelectronic device applications. *Progress in Quantum Electronics* **61**, 1–31 (2018). Cited on page/s 219, 221.

[4] H. Sun and X. Li. Recent Advances on III-Nitride Nanowire Light Emitters on Foreign Substrates – Toward Flexible Photonics. *Physica Status Solidi A - Applications and Materials Science* **216** (2), 1800420 (2019). Cited on page/s 219.

[5] D. Liang, T. Wei, J. Wang, and J. Li. Quasi van der Waals epitaxy nitride materials and devices on two dimension materials. *Nano Energy* **69**, 104463 (2020). Cited on page/s 219.

[6] L. Wang, W. Liu, Y. Zhang, Z.-H. Zhang, S. Tiam Tan, X. Yi, G. Wang, X. Sun, H. Zhu, and H. Volkan Demir. Graphene-based transparent conductive electrodes for GaN-based light emitting diodes: Challenges and countermeasures. *Nano Energy* **12**, 419–436 (2015). Cited on page/s 219, 223.

[7] Y. Song, W. Fang, R. Brenes, and J. Kong. Challenges and opportunities for graphene as transparent conductors in optoelectronics. *Nano Today* **10** (6), 681–700 (2015). Cited on page/s 219.

[8] H. P. T. Nguyen, M. Djavid, K. C., and Z. Mi. Temperature-dependent nonradiative recombination processes in GaN-based nanowire white-light-emitting diodes on silicon. *Nanotechnology* **23** (19), 194012 (2012). Cited on page/s 221, 222.

[9] H. P. T. Nguyen, S. Zhang, A. T. Connie, M. G. Kibria, Q. Wang, I. Shih, and Z. Mi. Breaking the Carrier Injection Bottleneck of Phosphor-Free Nanowire White Light-Emitting Diodes. *Nano Letters* **13** (11), 5437–5442 (2013). Cited on page/s 221.

[10] H. P. T. Nguyen, S. Zhang, K. Cui, X. Han, S. Fathololoumi, M. Couillard, G. A. Botton, and Z. Mi. p-Type Modulation Doped InGaN/GaN Dot-in-a-Wire White-Light-Emitting Diodes Monolithically Grown on Si(111). *Nano Letters* **11** (5), 1919–1924 (2011). Cited on page/s 222.

[11] H. P. T. Nguyen, K. Cui, S. Zhang, M. Djavid, A. Korinek, G. A. Botton, and Z. Mi. Controlling Electron Overflow in Phosphor-Free InGaN/GaN Nanowire White Light-Emitting Diodes. *Nano Letters* **12** (3), 1317–1323 (2012). Cited on page/s 222, 224.

[12] M. F. Schubert, J. Xu, J. K. Kim, E. F. Schubert, M. H. Kim, S. Yoon, S. M. Lee, C. Sone, T. Sakong, and Y. Park. Polarization-matched GaInN/AlGaInN multi-quantum-well light-emitting diodes with reduced efficiency droop. *Applied Physics Letters* **93** (4), 041102 (2008). Cited on page/s 222.

[13] Y. Wu, X. Liu, P. Wang, D. A. Laleyan, K. Sun, Y. Sun, C. Ahn, M. Kira, E. Kioupakis, and Z. Mi. Monolayer GaN excitonic deep ultraviolet light emitting diodes. *Applied Physics Letters* **116** (1), 013101 (2020). Cited on page/s 222.

[14] J. Simon, V. Protasenko, C. Lian, H. Xing, and D. Jena. Polarization-Induced Hole Doping in Wide–Band-Gap Uniaxial Semiconductor Heterostructures. *Science* **327** (5961), 60–64 (2010). Cited on page/s 222.

[15] S. D. Carnevale, T. F. Kent, P. J. Phillips, M. J. Mills, S. Rajan, and R. C. Myers. Polarization-Induced pn Diodes in Wide-Band-Gap Nanowires with Ultraviolet Electroluminescence. *Nano Letters* **12** (2), 915–920 (2012). Cited on page/s 222.

[16] S. Zhao, S. M. Sadaf, S. Vanka, Y. Wang, R. Rashid, and Z. Mi. Sub-milliwatt AlGaN nanowire tunnel junction deep ultraviolet light emitting diodes on silicon operating at 242 nm. *Applied Physics Letters* **109** (20), 201106 (2016). Cited on page/s 223.

[17] D. A. Laleyan, S. Zhao, S. Y. Woo, H. N. Tran, H. B. Le, T. Szkopek, H. Guo, G. A. Botton, and Z. Mi. AlN/h-BN Heterostructures for Mg Dopant-Free Deep Ultraviolet Photonics. *Nano Letters* **17** (6), 3738–3743 (2017). Cited on page/s 223.

[18] H. Sekiguchi, K. Kishino, and A. Kikuchi. Emission color control from blue to red with nanocolumn diameter of InGaN/GaN nanocolumn arrays grown on same substrate. *Applied Physics Letters* **96** (23), 231104 (2010). Cited on page/s 223.

[19] M. Djavid and Z. Mi. Enhancing the light extraction efficiency of AlGaN deep ultraviolet light emitting diodes by using nanowire structures. *Applied Physics Letters* **108** (5), 051102 (2016). Cited on page/s 223.

[20] X. Liu, B. H. Le, S. Y. Woo, S. Zhao, A. Pofelski, G. A. Botton, and Z. Mi. Selective area epitaxy of AlGaN nanowire arrays across nearly the entire compositional range for deep ultraviolet photonics. *Optics Express* **25** (24), 30494–30502 (2017). Cited on page/s 223.

* * *

APPENDIX A

Additional figure for chapter 3

In the subsequent page, the illustration of the band structures when undoped graphene is in contact with *n*- or *p*-type GaN, AlN, or InN, is presented. The Fermi levels in the semiconductors in Figure A.1 are pinned at the dopant energy level, i.e., donor or acceptor energy level. It is appearant that the potential barrier ϕ_B is larger compared to that of doped graphene in Figure 3.5.

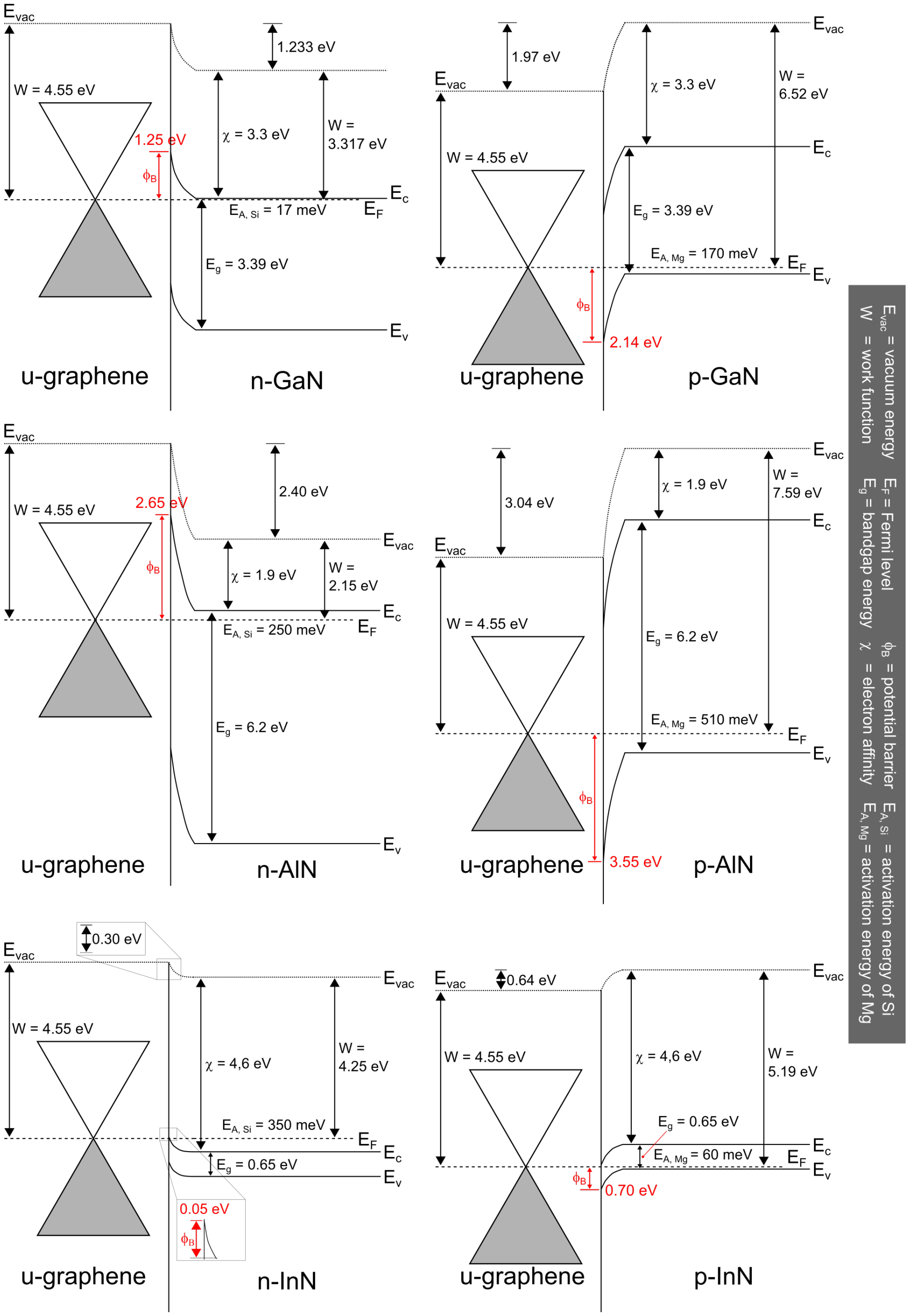

FIGURE A.1. The energy band diagram of undoped graphene/nitride semiconductor junctions. Rough sketch of the interface between undoped graphene—*n*/*p*-GaN (top), —*n*/*p*-AlN (middle), and —*n*/*p*-InN (bottom) after Fermi level alignment in the absence of an externally applied bias. See how the band diagram looks like in case for doped graphene in Figure 3.5.

Appendix B

Supporting information for chapter 8

B.1 Illustrative diagram and additional SEM image

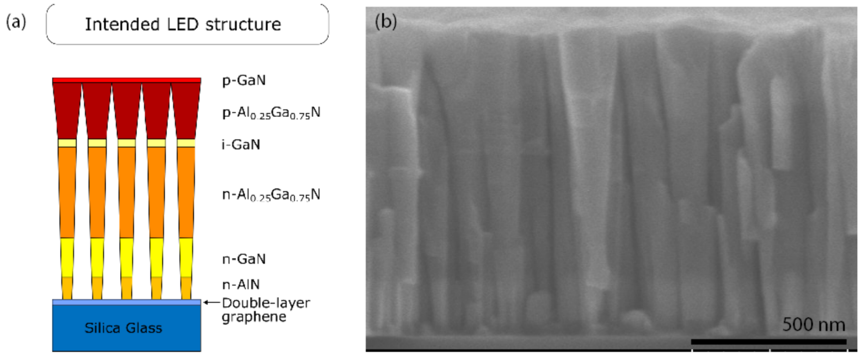

Figure B.1. Nanocolumn design and SEM image of grown nanocolumns. (**a**) Schematic of the intended GaN/AlGaN nanocolumn device structure. (**b**) Side-view SEM image of self-assembled GaN/AlGaN nanocolumns grown on double-layer graphene transferred onto silica glass, where the nanocolumn dimensions are found to be ~1070, ~35 and ~220 nm for the length, bottom- and top-diameter, respectively.

B.2 DETAILED GROWTH INFORMATION

TABLE B.1. Growth conditions of the GaN/AlGaN nanocolumns

Nanocolumn segment/layer	Growth temperature, pyrometer reading (°C)	Beam equivalent pressure (Pa)			Si cell temperature (°C)	N_2 flow rate/ plasma emission (sccm/mV)	Growth time (sec)
		Al	Ga	Mg			
Al seeding with Si	805	8.0×10^{-5}	-	-	1050	-	35
Nitridation	805	-	-	-	-	2.00/10.13	60
n-AlN	805	8.0×10^{-5}	-	-	1050	2.00/10.13	200
n-GaN	895	-	2.5×10^{-4}	-	1050	2.75/10.08	600
n-$Al_{0.25}Ga_{0.75}N$	915	6.7×10^{-5}	2.0×10^{-4}	-	1050	1.00/8.715	3600
i-GaN	895	-	2.5×10^{-4}	-	-	2.75/10.025	30
p-$Al_{0.25}Ga_{0.75}N$	695	2.7×10^{-5}	8.0×10^{-5}	6.0×10^{-6}	-	2.00/10.075	1500
p-GaN	675	-	8.0×10^{-5}	6.0×10^{-6}	-	3.00/9.94	300

B.3 EXPLANATION FOR USING LOW GROWTH TEMPERATURE DURING P-TYPE DOPING OF THE NANOCOLUMNS

At a growth temperature slightly below 700 °C, it is expected that Mg atoms are reasonably incorporated into the p-AlGaN and p-GaN layers [1–3]. If grown at a similar temperature as the n-AlGaN layers, the high vapor pressure of Mg could lead to a reduced Mg incorporation efficiency and an enhancement of Mg segregation [4]. However, further reduction of the growth temperature below 675 °C for the p-AlGaN and p-GaN layers may induce polarity inversion from Ga-polar to N-polar, leading to undesirable consequences such as a low Mg doping efficiency [3,5], which is accompanied with highly resistive or semi-insulating behavior [6]. Another important parameter to control in order to improve the efficiency of the p-type doping is the flux of supplied Mg. In GaN thin films grown under extreme Ga-rich conditions, an excessive Mg flux has been found to induce polarity inversion from Ga-polar to N-polar [7]. An increase of the growth temperature avoids this inversion, however then the Mg flux needs to be increased to compensate the strong desorption rate [1,2], suggesting that a balance between these two parameters has to be reached. This is further complicated by the very narrow Mg cell temperature window that can be used to achieve optimized nanocolumn growth [2,8]. For this work, the value of Mg flux being used is based on a previous study on GaN/AlGaN-based nanocolumn LEDs [9].

B.4 TEM ANALYSIS

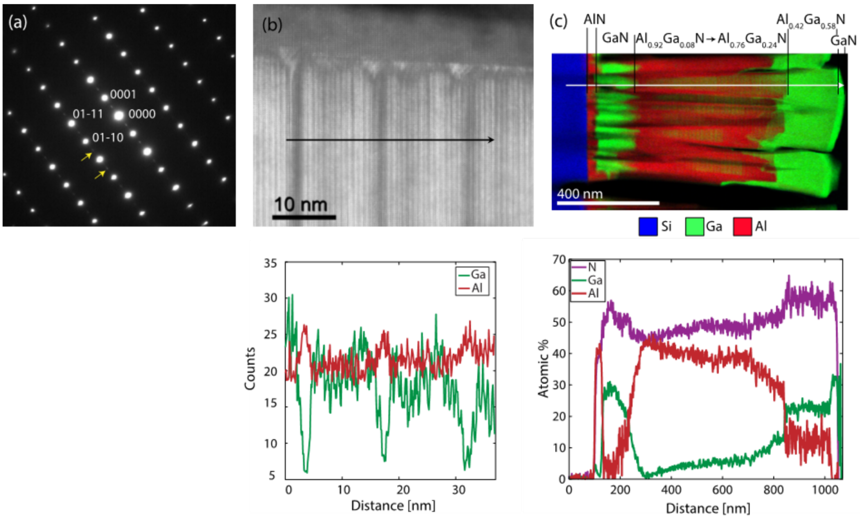

Figure B.2. Transmission electron microscopy diffraction data and line scans. (**a**) Diffraction pattern taken from n-AlGaN segment of nanocolumns shown in Figure 8.1c in the main text confirms that they grow along the hexagonal *c*-axis. Diffraction from the semi-periodic superlattice-like structure can also be observed in the pattern, as marked by yellow arrows. (**b**) HAADF STEM image and line scan across the superlattice-like structure in the n-AlGaN segment. (**c**) Compositional nanocolumn EDS and EELS mapping presented together with its line scan in the bottom.

B.5 RAMAN MEASUREMENTS

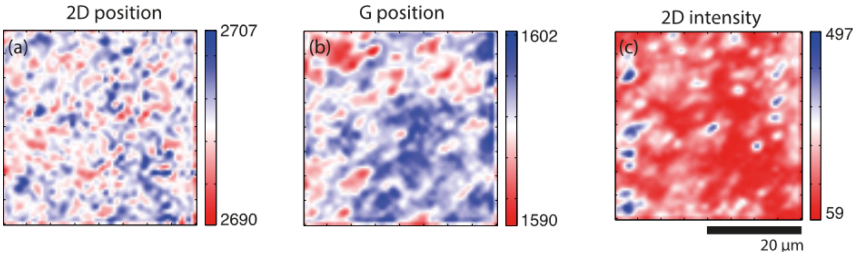

Figure B.3. Micro-Raman maps of peak positions and intensities of the double-layer graphene after the GaN/AlGaN nanocolumn growth. Maps taken from same area as shown in Figure 8.2 in the main text. (**a**, **b**) Peak positions of 2D- and G-peak. (**c**) 2D peak intensity.

B.6 IQE MEASUREMENTS

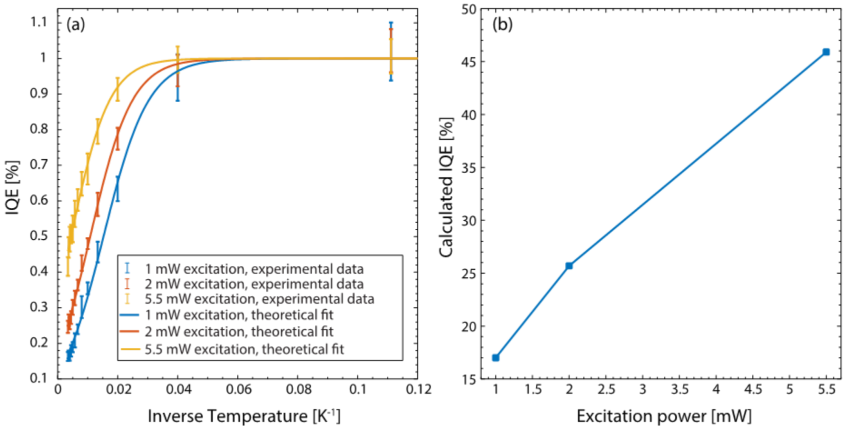

FIGURE B.4. Power and temperature dependence of the IQE. (**a**) Temperature dependence of the IQE for three different excitation powers. Experimental points correspond to the average integrated intensity of the main emission peak over ten randomly selected spots per temperature step, and error bars represent the standard deviation. Theoretical fits were obtained using the model equation I(T)=I(0)/(1+α.exp(-E_a/kT)), with I(0), α and E_a as fitting parameters. (**b**) Excitation power dependence of the IQE at room temperature.

B.7 REFERENCES

[1] E. Haus, I.P. Smorchkova, B. Heying, P. Fini, C. Poblenz, T. Mates, U.K. Mishra, and J.S. Speck. The role of growth conditions on the p-doping of GaN by plasma-assisted molecular beam epitaxy. *Journal of Crystal Growth* **246** (1), 55–63 (2002). Cited on page/s A-5.

[2] F.B. Naranjo, E. Calleja, Z. Bougrioua, A. Trampert, X. Kong, and K.H. Ploog. Efficiency optimization of p-type doping in GaN:Mg layers grown by molecular-beam epitaxy. *Journal of Crystal Growth* **270** (3), 542–546 (2004). Cited on page/s A-5.

[3] A. Feduniewicz, *et al.* Control of Mg doping of GaN in RF-plasma molecular beam epitaxy. *Journal of Crystal Growth* **278** (1), 443–448 (2005). 13th International Conference on Molecular Beam Epitaxy. Cited on page/s A-5.

[4] E. Monroy, T. Andreev, P. Holliger, E. Bellet-Amalric, T. Shibata, M. Tanaka, and B. Daudin. Modification of GaN(0001) growth kinetics by Mg doping. *Applied Physics Letters* **84** (14), 2554–2556 (2004). Cited on page/s A-5.

[5] A. J. Ptak, T. H. Myers, L. T. Romano, C. G. Van de Walle, and J. E. Northrup. Magnesium incorporation in GaN grown by molecular-beam epitaxy. *Applied Physics Letters* **78** (3), 285–287 (2001). Cited on page/s A-5.

[6] L. K. Li, M. J. Jurkovic, W. I. Wang, J. M. van Hove, and P. P. Chow. Surface Polarity Dependence of Mg Doping in GaN Grown by Molecular-Beam Epitaxy Surface. *Applied Physics Letters* **76** (13), 1740–1742 (2000). Cited on page/s A-5.

[7] V. Ramachandran, R. M. Feenstra, W. L. Sarney, L. Salamanca-Riba, J. E. Northrup, L. T. Romano, and D. W. Greve. Inversion of wurtzite GaN(0001) by exposure to magnesium. *Applied Physics Letters* **75** (6), 808–810 (1999). Cited on page/s A-5.

[8] H. Okumura, D. Martin, M. Malinverni, and N. Grandjean. Backward diodes using heavily Mg-doped GaN growth by ammonia molecular-beam epitaxy. *Applied Physics Letters* **108** (7), 072102 (2016). Cited on page/s A-5.

[9] H. Sekiguchi, K. Kato, J. Tanaka, A. Kikuchi, and K. Kishino. Ultraviolet GaN-based nanocolumn light-emitting diodes grown on n-(111) Si substrates by rf-plasma-assisted molecular beam epitaxy. *Physica Status Solidi A - Applications and Materials Science* **205** (5), 1067–1069 (2008). Cited on page/s A-5.

APPENDIX C

Supporting information for chapter 9

C.1 ADDITIONAL SCANNING ELECTRON MICROSCOPY (SEM) IMAGES

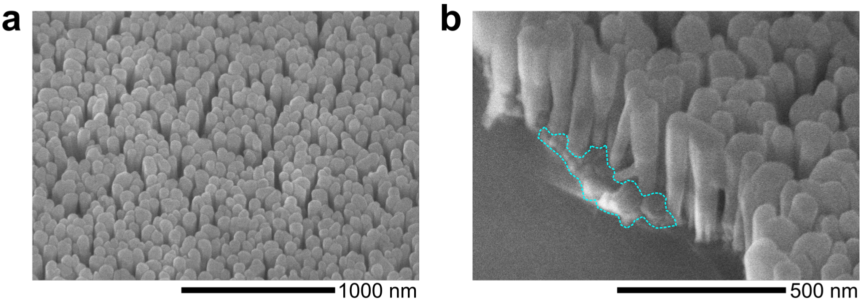

FIGURE C.1. **a** and **b,** Representative bird eye's-view SEM images (taken at an angle of 30° from substrate normal) of the GaN/AlGaN nanocolumn LED structure grown on graphene/silica glass, at the center and at the edge of the sample, respectively, using a two-stage *n*-AlN buffer layer deposition method. In **b**, one can see the protruding of a continuous structure at the base of the nanocolumns (marked with aqua dashed contours), which could be the AlN buffer layer. It seems that the nanocolumns grown on top of the protruding part of this layer were removed during wafer cutting (using laser).

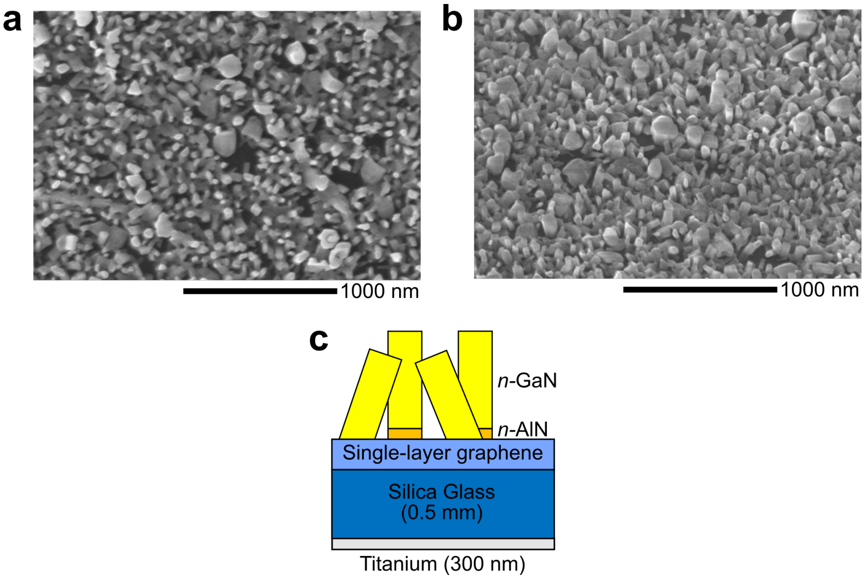

FIGURE C.2. **a** and **b,** Representative top- and bird eye's-view (latter taken at an angle of 30° from substrate normal) SEM images of the short *n*-GaN nanocolumns grown on graphene/silica glass using an *n*-AlN buffer layer formed using 40 migration-enhanced epitaxy (MEE) cycles[1]. With MEE, Al and N atoms are alternately supplied to the graphene surface with an interruption time φ in-between. **c,** Schematic diagram of the *n*-GaN nanocolumns grown on graphene.

Since there is only a short time for Al to diffuse on the graphene before it reacts with N, it was assumed that island-like growth formation is preferred. Later it was discovered that this deposition method results in the formation of *n*-AlN islands[1,2] and *n*-AlN nanostructures grown along line defects of graphene[1], leaving exposed areas of graphene. The short, vertical *n*-GaN nanocolumns are likely grown on *n*-AlN islands and *n*-AlN nanostructures, whereas tilted ones are grown directly on various defects in graphene[1]. This growth shows undesirable high density of non-vertical nanocolumn growth directions, and also leads to a non-uniform size of the vertical nanocolumns (due to the coalescence with the nearest vertical and non-vertical nanocolumns).

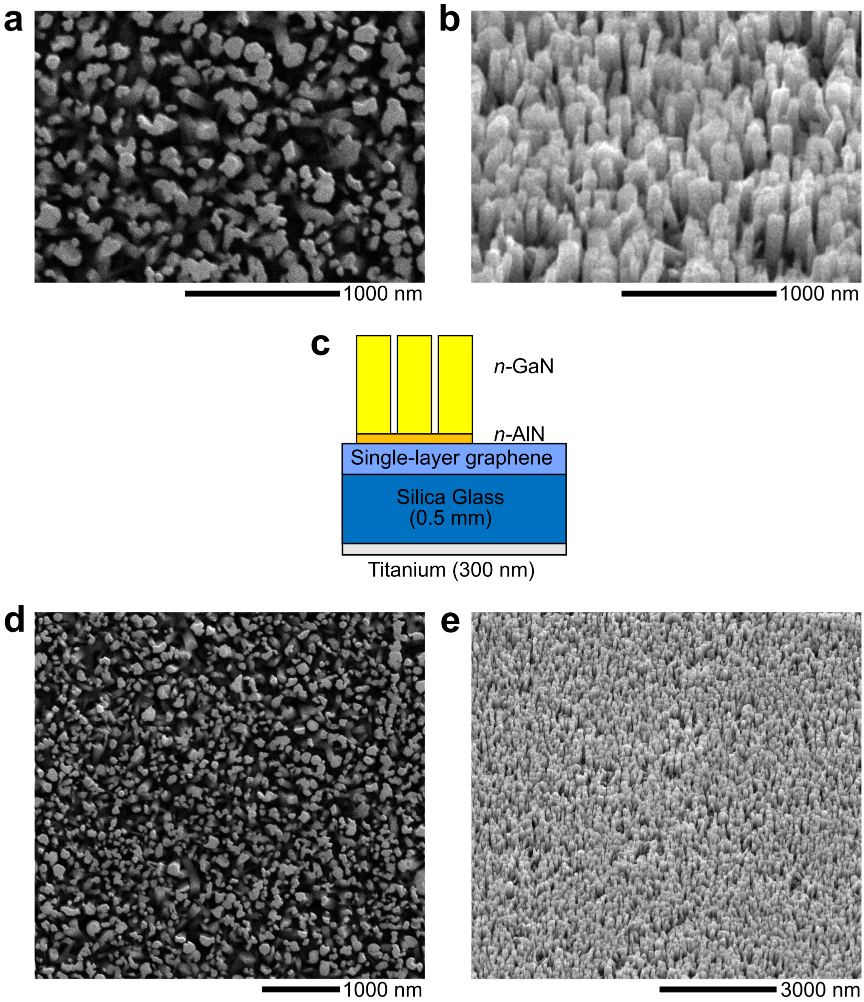

FIGURE C.3. **a** and **b,** Representative top- and bird eye's-view (latter taken at an angle of 30° from substrate normal) SEM images of the short *n*-GaN nanocolumns grown on graphene/silica glass using a two-stage *n*-AlN buffer layer deposition method. This deposition method is described as follows: First 35 seconds of Al and Si deposition on the graphene surface was carried out prior to a 60-seconds nitridation process. Afterwards, the Si, Al and N atoms were deposited at the same time for 200 seconds. **c,** Schematic diagram of the short *n*-GaN nanocolumns grown on graphene. **d** and **e,** Low magnification SEM images from the same area as **a** and **b**, respectively.

Since Al has a longer time to diffuse on the graphene surface before it reacts with N for the first time compared with in the MEE-AlN deposition method (35 seconds vs. 4 seconds[1]), it is hypothesized that this deposition method suppresses the growth of *n*-AlN islands, and rather promotes a larger coverage of *n*-AlN buffer layer on graphene. This will further prompt the direct nucleation of *n*-GaN on *n*-AlN (instead of on graphene), thus leading to vertical nanocolumn growth.

C.2 Additional transmission electron microscopy (TEM) images

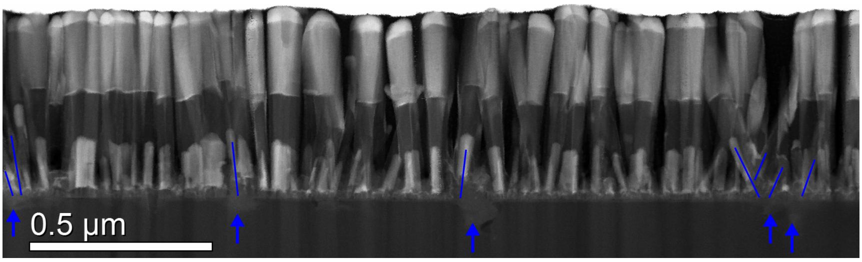

Figure C.4. High-angle annular dark-field scanning TEM (HAADF STEM) images of the GaN/AlGaN nanocolumns grown on graphene/silica glass using a two-stage n-AlN buffer layer deposition method. Blue arrows point out the diffuse interface areas between the nanocolumns and the graphene/silica glass substrate, while blue lines show the non-vertical growth direction of the nanocolumns stemming from the diffuse interface area.

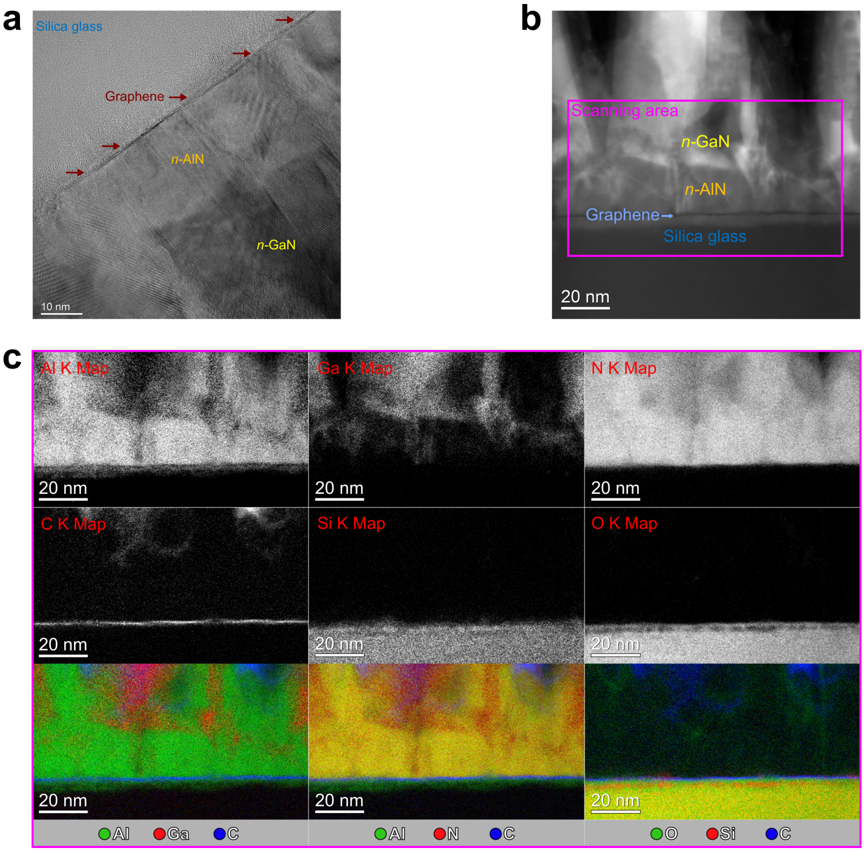

FIGURE C.5. **a,** High-magnification bright-field TEM image of the interface between the *n*-AlN buffer layer, graphene and silica glass. Similar interface region investigated using **b,** HAADF STEM combined with **c,** energy-dispersive X-ray spectroscopy (EDS) and electron energy loss spectroscopy (EELS). The Al, Ga and Si maps are taken from EDS, while the N, C and O maps are from EELS. The yellow color seen in bottom middle and bottom right is the mixture between green color and red color, representing Al-N and O-Si, respectively.

From the 3 × 3 images in Figure C.5c, the presence of graphene can be clearly noticed in the C map (middle left image). Below the graphene layer, aluminium oxide (expected to be in amorphous state owing to the fact that no crystalline contrast is observed under graphene [from Figure C.5a]) has formed at the top of the silica glass substrate (top left and middle right images). Additionally, large amounts of Al signal is unexpectedly observed above the AlN buffer layer (top left image), mixing with the nominally grown GaN nanocolumn (Ga signal, shown in top middle image). As it has been discussed in the main text and further shown in Figure C6[B], this Al signal originates from the (unintentional) AlGaN grown on AlN buffer layer during the initial formation of the *n*-AlGaN nanocolumn section, due to moderate GaN nanocolumn density. Other than those, N signal, shown in top right image (O and Si signals, shown in middle right and middle images, respectively), is not detected below (above) the graphene layer. The relative position of Al, O, Ga, N, and Si signals with respect to C signal is easily assessed from the three images in the bottom panel.

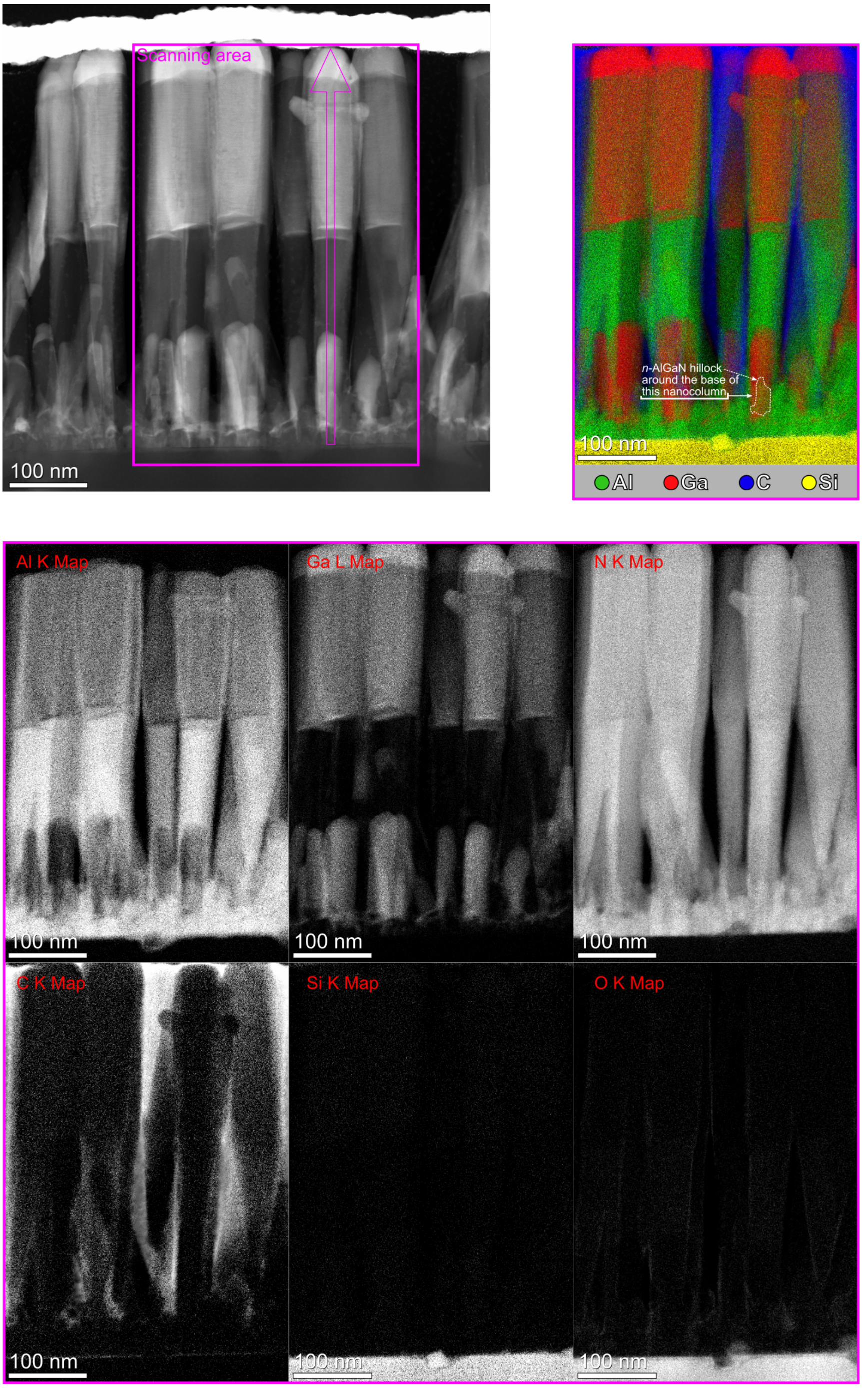

Figure C6A. HAADF STEM image of GaN/AlGaN nanocolumns and element maps from EDS-EELS (Al, Ga, N, C, Si, and O). Note that the nanocolumn marked with purple arrow in top left image seems to have two *i*-GaN quantum disk layers, but this likely comes from two nanocolumns with slightly different heights (possibly one of them is somewhat tilted) superposed on each other in the STEM image.

In the combined elemental map (top right image), the signal from the base of the same nanocolumn overlaps with the signal from part of an *n*-AlGaN hillock (within the white dashed countour) either from behind the nanocolumn or from thin remainings (after the focused ion beam thinning) in front of the nanocolumn.

With the *n*-AlGaN nanocolumn segment getting longer, a shadowing effect takes place that limits the deposition of a rough *n*-AlGaN structure on the *n*-AlN buffer layer: the Al signal in the overlapped region (Figure C6^{B}) is gradually reduced along the growth direction, but only to certain extent because of the formation of an *n*-AlGaN shell enveloping the *n*-GaN core nanocolumn. After about 50 nm (end of the overlapped region in Figure C6^{B}), the Al signal increases as the influence of high Al flux during the growth of *n*-AlGaN nanocolumns becomes stronger.

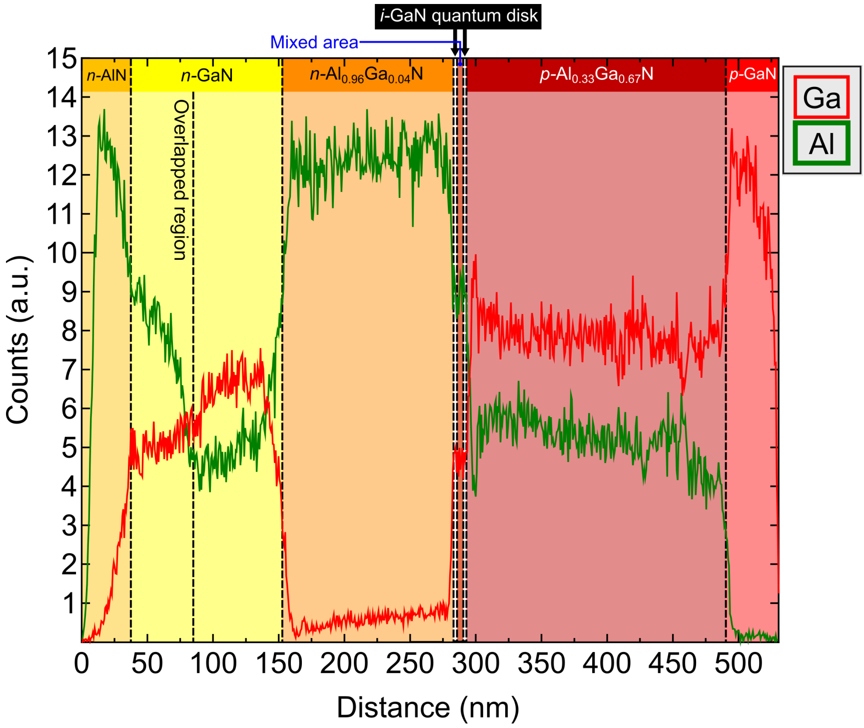

FIGURE C6^B^. EDS line scan plot of Ga (red) and Al (green) measured along the nanocolumn marked with a purple arrow symbol in Figure C6^A. It is noticed that the bottom *n*-GaN / *n*-AlGaN core-shell nanocolumn segment does not have an abrupt change from the *n*-AlN buffer layer (overlapped region) due to a suspected overlapping with an *n*-AlGaN hillock (Al composition of 96 %) behind (or thin remaining in front of) the base of the nanocolumn (part of same hillock that can be observed on the right side of the investigated nanocolumn base). We believe there is also some contribution from a partially sliced nanocolumn behind the nanocolumn marked with a purple arrow symbol in Figure C6^A.

As pointed out in Figure C6^A, two *i*-GaN quantum disk regions are detected between *n*-$Al_{0.96}Ga_{0.04}N$ and *p*-$Al_{0.33}Ga_{0.67}N$ cladding segments. In addition, signals from the distance interval between the two *i*-GaN quantum disk positions are likely a mix of signals from *n*-$Al_{0.96}Ga_{0.04}N$ and *p*-$Al_{0.33}Ga_{0.67}N$ segments of the two nanocolumns with slightly differing heights.

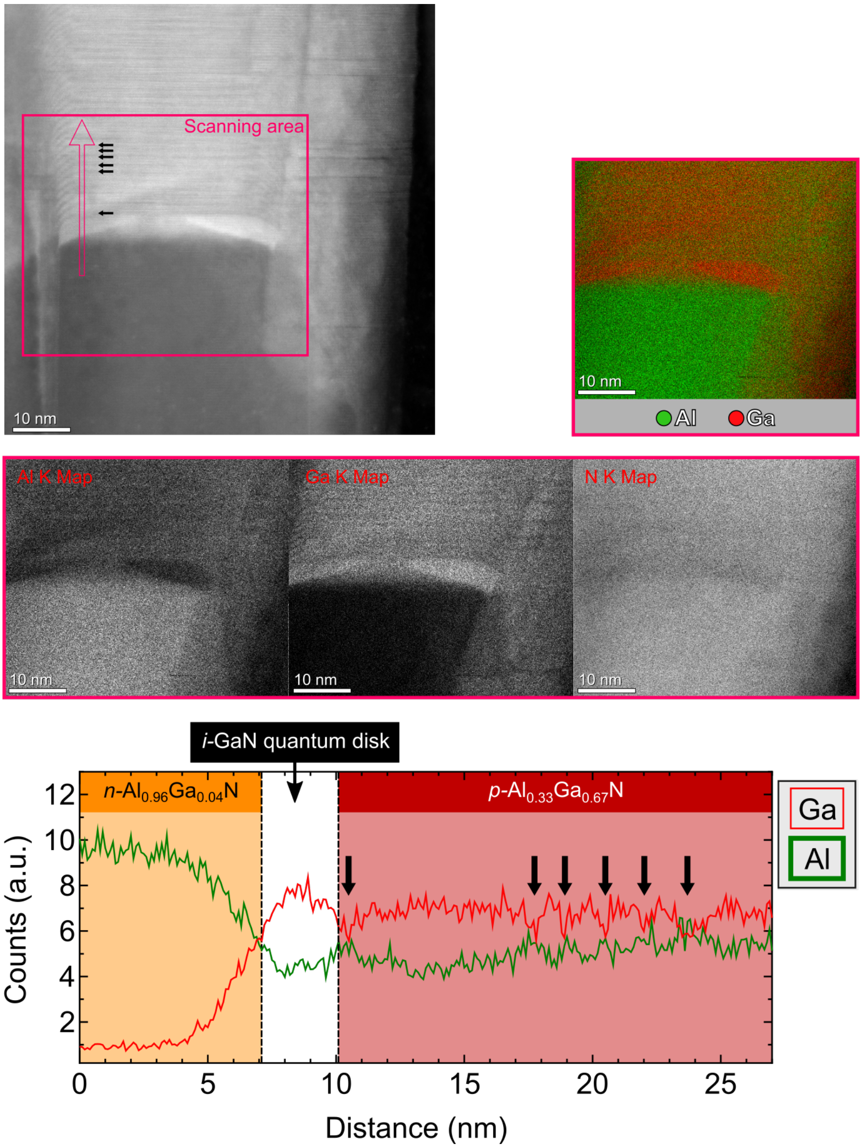

FIGURE C.7. HAADF STEM image of the *i*-GaN quantum disk region, its individual elemental mapping via EDS-EELS (Al and Ga) and EDS line scan plot of Ga (red) and Al (green) in the square area marked in pink along the direction of the pink arrow. Faint compositional variations in the Ga to Al ratio are seen in the *p*-AlGaN nanocolumn segment, with the black arrows in two of the figures demonstrating slightly lower Ga-content than the average.

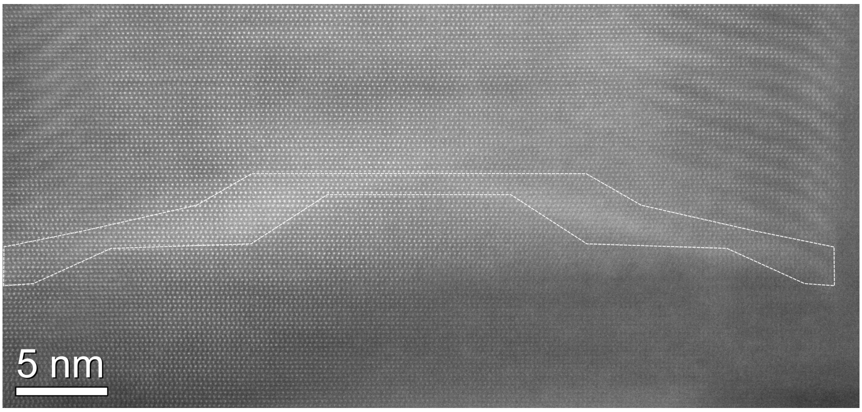

FIGURE C.8. High-magnification HAADF STEM image of the *i*-GaN quantum disk region (marked with white dashed contour) of the GaN/AlGaN nanocolumn. Layers above and below are the *p*-$Al_{0.33}Ga_{0.67}N$ and *n*-$Al_{0.96}Ga_{0.04}N$ nanocolumn segments surrounding the *i*-GaN quantum disk. The figure shows the apparent lattice fringe for the area under observation, and it is confirmed that the *p*-AlGaN, *i*-GaN quantum disk and *n*-AlGaN have wurtzite lattice crystal structure.

C.3 ADDITIONAL PHOTOLUMINESCENCE MEASUREMENTS

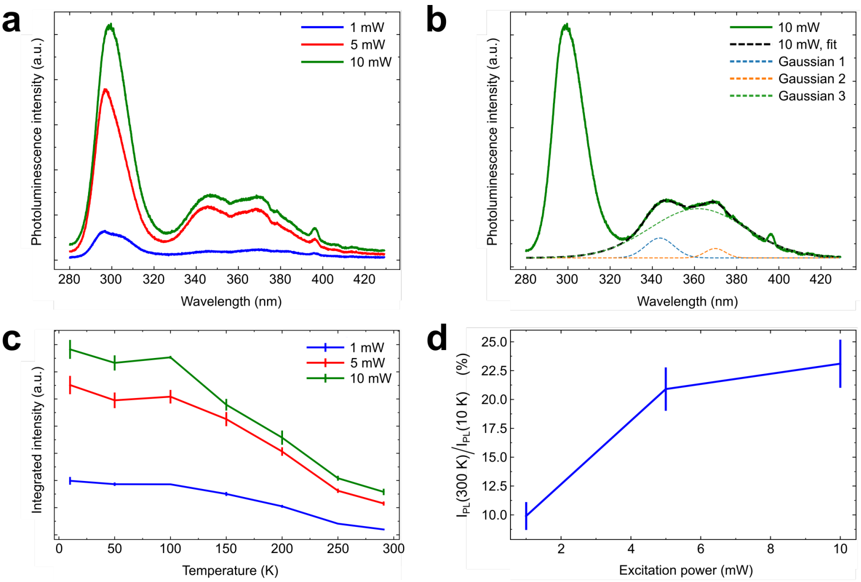

FIGURE C.9. Optical characterizations of the as-grown GaN/AlGaN nanocolumn sample. **a,** Laser excitation power dependent room-temperature photoluminescence spectra and **b,** the respective three-Gaussian least-square fit of the emission bands between 325 and 420 nm for 10 mW laser excitation power. **c,** Integrated photoluminescence intensity in the range of 325-420 nm as a function of temperature. For each temperature, five areas of the sample were selected, and error bars represent the standard deviation. **d,** Integrated photoluminescence intensity at room-temperature (300 K) to that at low-temperature (10 K), $I_{PL}(300\ K)/I_{PL}(10\ K)$, as a function of excitation power.

High N_2 flow rate[3] used during the growth of the *p*-AlGaN segment could be the origin of the local variations in Al composition across the *p*-AlGaN growth axis. One thus can speculate that the two-peak emission band in the region around 300 nm (similar to photoluminescence band broadening in the work of Zhao *et al.*[3]) at low power spectrum (1 mW) in Figure C.9a could be associated with the atomic scale Ga/Al compositional modulations in the *p*-AlGaN segment (Figure C.7). However, as the carriers would normally diffuse and recombine in the position where the Al-content is the lowest (smallest energy bandgap), the local variations in Al composition have low probability to be the cause of two-peak emission band. Hence, it is more likely that this two-peak emission band has a contribution from defect-related levels in the *p*-AlGaN, in analogy with the photoluminescence from *p*-GaN[4].

C.4 Additional micro-Raman spectroscopy measurements

Table C.1. Summary of micro-Raman spectroscopy measurements for the as-grown GaN/AlGaN nanocolumn sample carried out in different areas (of the same sample) from what is presented in Figure 9.4. Referring to optical image within the marked square in Figure C.10a, the table shows the median values of the D peak, G peak, and 2D peak, for the entire mapping (865 measurements), from the green patches (50 measurements), and from the purple areas (50 measurements). In these additional Raman mapping measurements, the acquisition time was longer and we did more accumulations than in the measurements presented in Figure 9.4a, which consequently escalates the Raman signal, e.g. 2D peak intensity

Median value	Area (number of measurements)	Position [cm^{-1}]	Intensity [cps]	FWHM [cm^{-1}]	Intensity ratio to G peak
D peak	Green patches (50)	1345.5	4742.6	36.2	1.09
	Full map (865)	1339.9	1763.7	60.7	1.23
	Purple areas (50)	1337.6	1605.7	63.3	1.28
G peak (*)	Green patches (50)	1586.6	4342.8	-	-
	Full map (865)	1585.5	1433.2	-	-
	Purple areas (50)	1586.6	1248.2	-	-
2D peak	Green patches (50)	2692.1	2935.5	55.9	0.68
	Full map (865)	2686.6	272.8	75.3	0.19
	Purple areas (50)	2674.8	163.8	129.4	0.13
D’ peak (**)	Green patches (50)	1619.3	2830.6	-	0.65

(*) Due to interference of the D’ peak, the FWHM of the G peak could not be obtained.

(**) The median D’ peak position and peak intensity (height) are only shown for the green patches since this peak is only clearly resolved in these regions. For purple areas however, the D’ peak is almost completely merged with the G peak, appearing as a shoulder peak and is thus neglected in the table.

As the graphene quality increases, i.e., the green patches, we observe the following (relative to full map/purple areas):

- Higher intensities of D, G and 2D peaks.
- D peak position is shifted towards higher cm^{-1}, along with smaller FWHM and D/G ratio.
- G peak position is not shifted.
- 2D peak position is shifted towards higher cm^{-1}, along with smaller FWHM and larger 2D/G peak ratio.

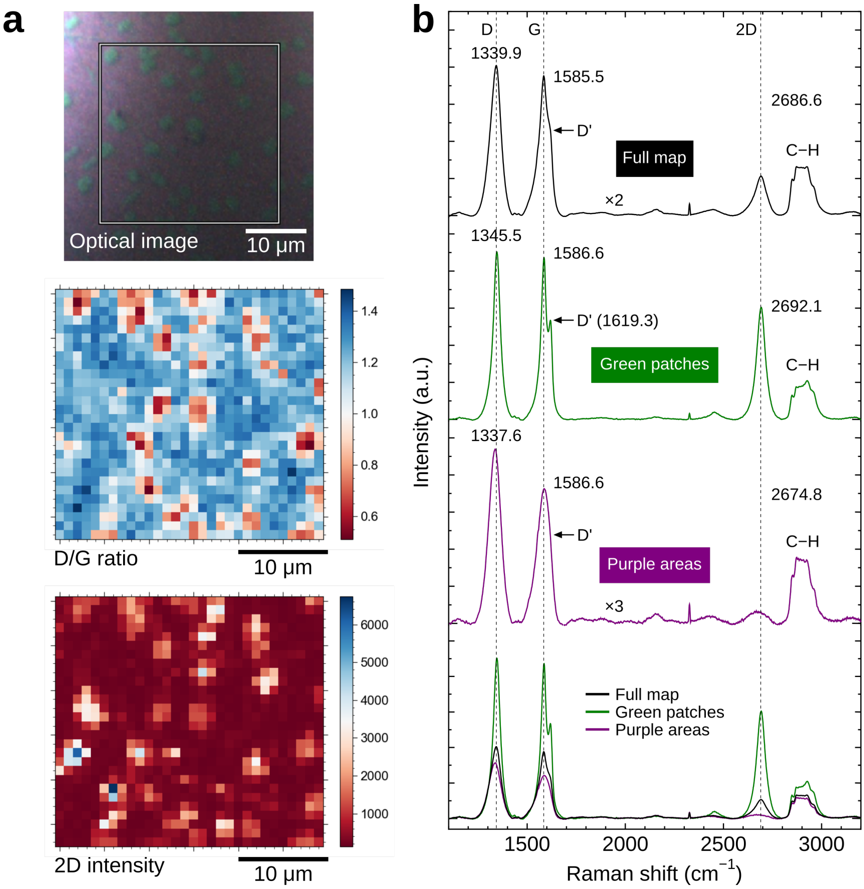

FIGURE C.10. **a,** Optical image and its corresponding micro-Raman D/G ratio and 2D intensity maps (from the area within the square) of the graphene after the nanocolumn growth. **b,** Averaged Raman spectra of the graphene after the nanocolumn growth (based on Table C.1).

C.5 Additional current-voltage (I-V) measurements

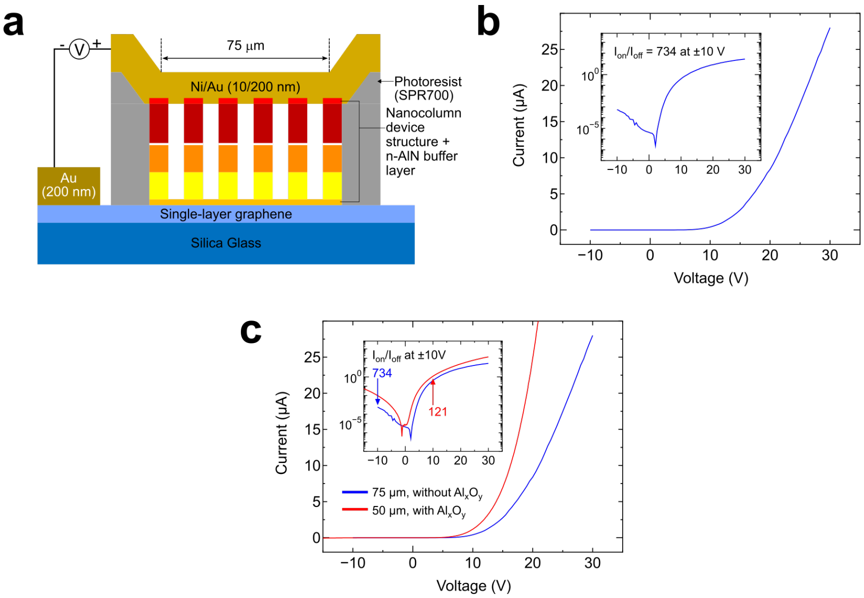

Figure C.11. **a,** Schematic diagram of a fabricated GaN/AlGaN nanocolumn LED, without aluminium oxide (Al_xO_y) passivation layer. **b,** I-V characteristic from a measured GaN/AlGaN nanocolumn device of 75 μm aperture diameter. **c,** Comparison of I-V characteristics between LED devices with aperture diameter of 75 μm (without Al_xO_y) and 50 μm (with Al_xO_y). Inset in **b** and **c** shows the respective I-V plot in a log scale with its respective I_{on}/I_{off} ratios at ± 10 V.

Please note that although different aperture sizes are compared, one should expect that the larger device (75 μm, without Al_xO_y) should exhibit higher current level compared to the smaller device (50 μm, with Al_xO_y). Here, however, the smaller device demonstrates higher current level at the same input voltage.

C.6 REFERENCES

[1] A. Liudi Mulyo, M. K. Rajpalke, P. E. Vullum, H. Weman, K. Kishino, and B.-O. Fimland. The influence of AlN buffer layer on the growth of self-assembled GaN nanocolumns on graphene. *Scientific Reports* **10** (1), 853 (2020). Cited on page/s A-10, A-11.

[2] H. Hayashi, Y. Konno, and K. Kishino. Self-organization of dislocation-free, high-density, vertically aligned GaN nanocolumns involving InGaN quantum wells on graphene/SiO_2 covered with a thin AlN buffer layer. *Nanotechnology* **27** (5), 055302 (2015). Cited on page/s A-10.

[3] S. Zhao, S. Y. Woo, S. M. Sadaf, Y. Wu, A. Pofelski, D. A. Laleyan, R. T. Rashid, Y. Wang, G. A. Botton, and Z. Mi. Molecular Beam Epitaxy Growth of Al-Rich AlGaN Nanowires for Deep Ultraviolet Optoelectronics. *APL Materials* **4** (8), 086115 (2016). Cited on page/s A-21.

[4] I. M. Høiaas, A. Liudi Mulyo, P. E. Vullum, D.-C. Kim, L. Ahtapodov, B.-O. Fimland, K. Kishino, and H. Weman. GaN/AlGaN Nanocolumn Ultraviolet Light-Emitting Diode Using Double-Layer Graphene as Substrate and Transparent Electrode. *Nano Letters* **19** (3), 1649–1658 (2019). Cited on page/s A-21.

CURRICULUM VITAE

Andreas Liudi Mulyo

PERSONAL INFORMATION

Family name, given name	:	Liudi Mulyo, Andreas
Nationaliy	:	Indonesia
Place, date of birth	:	Jember (Indonesia), September 2nd, 1988
Current address	:	Loholt Alle 4B, 7049 Trondheim, NO

EDUCATIONAL BACKGROUND AND RESEARCH EXPERIENCE

Doctor of Philosophy (Ph.D.) in Electronic Systems
Norwegian University of Science and Technology (NTNU), Trondheim, NO
March 2014 - March 2021

- Thesis title: Molecular Beam Epitaxy of GaN/AlGaN Nanocolumns on Graphene: for Potential Application in Ultraviolet Light-Emitting Diodes
- Advisors: Professor Bjørn-Ove Fimland and Professor Helge Weman
- Collaborative researcher in the Kishino Laboratory (Professor Katsumi Kishino) at Sophia University, Tokyo, Japan for total of 21 months

Master of Science (M.Sc.) in Condensed Matter Physics
Norwegian University of Science and Technology (NTNU), Trondheim, NO
August 2011 - August 2013

- Thesis title: Characterisation of quantum dot-intermediate band solar cells with optical spectroscopy
- Advisors: Professor Morten Kildemo, Associate Professor Turid Worren, and Dr. Lars Martin Sandvik Aas

Bachelor of Engineering (B.Eng.) in Engineering Physics
Sepuluh Nopember Institute of Technology (ITS), Surabaya, ID
August 2006 - July 2010

- Thesis title: Identification of the Intrinsic Spectrum of Star Using Line Spread Function of Deep Space Spectrograph-7 in Bosscha Observatory, Bandung Institute of Technology
- Advisors: Professor Sekartedjo and Professor Hakim L. Malasan

Teaching experience

Laboratory assistant for various courses, at **NTNU**: Nanoelectronics 2 (spring 2020 & 2021), Semiconductor Physics with Lab (spring 2017-2020), Physical Methods for Nanostructuring and Characterization (autumn 2015, 2017 & 2018), Chemical Methods for Synthesis and Characterization of Nanomaterial (autumn 2017 & 2018), Semiconductor manufacturing technology (spring 2015); at **ITS**: Optics (spring 2009 & 2010).

Awards

➤ Norges tekniske høgskoles fond, a travel grant for ISSLED 2017	2017
➤ NorFab travel grant for MBE 2016 and CSW 2017	2016-2017
➤ NorFab project support, for research visit in Sophia University	2016-2017
➤ PhD scholarship, NTNU	2014-2019
➤ Norwegian Quota Scheme, a scholarship for master degree	2011-2013
➤ PPA scholarship (Academic Achievement Improvement)	2009

Skills

Scientific (laboratory) competency

- Experienced with the growth of semiconductor using molecular beam epitaxy technique.
- Skilled for material characterization techniques using scanning electron microscopy, photoluminescence, and Raman spectroscopy.
- Familiar with device fabrication tools, including mask/maskless aligner, e-beam/sputter deposition, plasma-enhanced chemical vapor deposition, wet etching, and inductively-coupled plasma reactive ion etching.
- Basic knowledge of e-beam lithography and X-ray diffraction.

Computer literacy

- Microsoft Windows, MacOS, and Debian-based Linux (competent)
- Microsoft Office, Inkscape, ImageJ, Ngraph, and LaTeX (intermediate)
- SketchUp, Blender, Python, MatLab, C++, HTML, and LabView (beginner)

Language fluency

- Indonesia (native)
- English (full professional)
- Japanese (elementary)
- Norwegian (elementary)

Contact information

E-mail : liudimulyo@outlook.com
Homepage : https://andreasliudimulyo.github.io

Dissemination of research

PUBLICATIONS IN PEER REVIEWED JOURNALS

[1] **A. Liudi Mulyo**, Y. Konno, J. S. Nilsen, A. T. J. van Helvoort, B.-O. Fimland, H. Weman, and K. Kishino. Growth study of self-assembled GaN nanocolumns on silica glass by plasma assisted molecular beam epitaxy. *Journal of Crystal Growth* **480**, 67-73 (2017).

[2] **A. Liudi Mulyo**, M. K. Rajpalke, H. Kuroe, P. E. Vullum, H. Weman, B.-O. Fimland, and K. Kishino. Vertical GaN nanocolumns grown on graphene intermediated with a thin AlN buffer layer. *Nanotechnology* **30** (1), 015604 (2018).
*This article was chosen as **cover image/featured article**, see Figure D.1.*

[3] I. M. Høiaas*, **A. Liudi Mulyo***, P. E. Vullum, D.-C. Kim, L. Ahtapodov, B.-O. Fimland, K. Kishino, and H. Weman. GaN/AlGaN Nanocolumn Ultraviolet Light-Emitting Diode Using Double-Layer Graphene as Substrate and Transparent Electrode. *Nano Letters* **19** (3), 1649-1658 (2019).
***equal contributions**

[4] **A. Liudi Mulyo**, M. K. Rajpalke, P. E. Vullum, H. Weman, K. Kishino, and B.-O. Fimland. The influence of AlN buffer layer on the growth of self-assembled GaN nanocolumns on graphene. *Scientific Reports* **10**, 853 (2020).

MANUSCRIPT UNDER REVIEW

[1] **A. Liudi Mulyo**, A. Mukherjee*, I. M. Høiaas*, L. Ahtapodov, T. A. Nilsen, H. H. Toftevaag, P. E. Vullum, K. Kishino, H. Weman, and B.-O. Fimland. Graphene as *Transparent Conducting Substrate* for GaN/AlGaN Nanocolumn Flip-chip Ultraviolet Light-Emitting Diode.
*equal contributions

ISSN 0957–4484

NANOTECHNOLOGY

VOLUME 30 NUMBER 1 4 JANUARY 2019

iopscience.org/nano

Featured article

Vertical GaN nanocolumns grown on graphene intermediated with a thin AlN buffer layer

Andreas Liudi Mulyo, Mohana Krishnappa Rajpalke, Haruhiko Kuroe, Per-Erik Vullum, Helge Weman, Bjørn-Ove Fimland and Katsumi Kishino

IOP Publishing

FIGURE D.1. Our work published in Nanotechnology was selected as a cover image/featured article for the first issue of 2019 (4 January).

CONFERENCE PARTICIPATION (PRESENTATIONS)

Name of the author with † indicates the presenter. Half of the past meeting records (i.e., conference websites or pdf files of the conference programs) are still accessible online, and unfortunately half of them are no longer active (as of December 03 2020). For the latter, reader might notice that they are linked via Internet Archive or my personal website.

[1] **A. Liudi Mulyo**†, Y. Konno, H. Weman, and K. Kishino. *Self-Organized GaN Nanocolumns Grown on Silica Glass by RF-Molecular Beam Epitaxy*. Contributed talk at The 63rd Japanese Society of Applied Physics, Spring Meeting 2016, Tokyo, Japan, March 19-22 2016.

[2] **A. Liudi Mulyo**†, Y. Konno, B.-O. Fimland, H. Weman, and K. Kishino. *Self-Organized Vertical GaN Nanocolumns Grown on Silica Glass by RF-Molecular Beam Epitaxy*. Contributed talk at The 19th International Conference on Molecular Beam Epitaxy (MBE 2016), Montpellier, France, September 04-09 2016.

[3] **A. Liudi Mulyo**, Y. Konno, B.-O. Fimland, H. Weman, and K. Kishino†. *Growth of Self-Organized Vertical GaN Nanocolumns Utilizing AlN as Nucleation Sites on Single Layer Graphene/Silica Glass by Molecular Beam Epitaxy*. Contributed talk at International Workshop on Nitride Semiconductors, Orlando (Florida), USA, October 02-07 2016.

[4] **A. Liudi Mulyo**†, A. T. J. van Helvoort, B.-O. Fimland, H. Weman, and K. Kishino. *Epitaxy Feasibility of n-type GaN/AlGaN Nanocolumns on Silica Glass*. Contributed talk at The 44th International Symposium on Compound Semiconductors (Compound Semiconductor Week [CSW] 2017), Berlin, Germany, May 14-18 2017.

[5] **A. Liudi Mulyo**†, B.-O. Fimland, H. Weman, and K. Kishino. *Epitaxial Growth of Vertical n-type GaN/AlGaN Nanocolumns on Graphene/Silica Glass*. Contributed talk at The 12th International Conferences on Nitride Semiconductors, Strasbourg, France July 24-28 2017.

[6] I. M. Høiaas†, **A. Liudi Mulyo**, D.-C. Kim, B.-O. Fimland, K. Kishino, and H. Weman. *Graphene as growth substrate and transparent electrode for flip-chip GaN/AlGaN nanocolumn UV-LEDs*. Poster presentation at The 8th symposium on two-dimensional materials (Carbonhagen 2017), Copenhagen, Denmark, August 16 2017.

[7] **A. Liudi Mulyo**†, I. M. Høiaas, D.-C. Kim, B.-O. Fimland, H. Weman, and K. Kishino. *AlGaN/GaN Nanocolumn Flip-Chip UV LEDs Grown on

Graphene/Silica Glass. Contributed talk at The 11th International Symposium on Semiconductor Light Emitting Devices (ISSLED 2017), Banff, Canada, October 08-12 2017.

[8] I. M. Høiaas†, **A. Liudi Mulyo**, D.-C. Kim, B.-O. Fimland, K. Kishino, and H. Weman. *AlGaN/GaN nanowire flip-chip UV LED using graphene as substrate and transparent electrode*. Contributed talk at Nano@NTNU Symposium, Trondheim, Norway, December 06-07 2017.

[9] **A. Liudi Mulyo**†, I. M. Høiaas, M. K. Rajpalke, B.-O. Fimland, H. Weman, and K. Kishino. *Graphene as a substrate and bottom electrode for high density and vertically aligned GaN nanocolumns*. Poster presentation at Nano@NTNU Symposium, Trondheim, Norway, December 06-07 2017. *No website or pdf file of the conference program is associated with this item.*

[10] I. M. Høiaas†, **A. Liudi Mulyo**, P. E. Vullum, L. Ahtapodov, D.-C. Kim, B.-O. Fimland, K. Kishino, and H. Weman. *Using graphene as substrate and transparent electrode in an GaN/AlGaN nanocolumn flip-chip UV LED*. Contributed talk at Nanowire Week, Hamilton, Canada, June 11-15 2018.

[11] I. M. Høiaas, **A. Liudi Mulyo**, P. E. Vullum, L. Ahtapodov, D.-C. Kim, B.-O. Fimland, K. Kishino, and H. Weman†. *GaN/AlGaN nanocolumn UV LED using graphene as substrate and transparent electrode*. Poster presentation at The International Workshop on Nitride Semiconductors, Kanazawa, Japan, November 11-16 2018.

[12] **A. Liudi Mulyo**, M. K. Rajpalke, H. Kuroe, P. E. Vullum, H. Weman, B.-O. Fimland†, and K. Kishino. *Growth and characterization of GaN nanocolumns grown on graphene using a thin AlN buffer layer*. Poster presentation at The International Workshop on Nitride Semiconductors, Kanazawa, Japan, November 11-16 2018.

[13] **A. Liudi Mulyo**†, D.-C. Kim, I. M. Høiaas, L. Ahtapodov, H. Weman, K. Kishino, and B.-O. Fimland. *Utilization of graphene as substrate and bottom electrode for high-density and vertically-aligned GaN/AlGaN nanocolumns in light-emitting diodes in the UV-A*. Contributed talk at The 10th annual workshop of Norwegian PhD Network on Nanotechnology for Microsystems, Tromsø, Norway, June 17-19 2019.

[14] **A. Liudi Mulyo**, M. K. Rajpalke, P. E. Vullum, H. Weman, K. Kishino, and B.-O. Fimland†. *The influence of AlN buffer layer on the growth of self-assembled GaN nanocolumns on graphene*. Poster presentation at The 13th International Conferences on Nitride Semiconductors, Bellevue, Washington (Seattle), USA, July 07-12 2019.

Copyright permissions

Below is the complete list of the copyright figures shown in this Doctoral thesis, mainly from chapter 1 to chapter 4.

§ Figure 1.1[1] and Figure 2.12[2] are adapted with permission from:
S. Nakamura. Background Story of the Invention of Efficient InGaN Blue-Light-Emitting Diodes (Nobel Lecture). *Angewandte Chemie* **54** (27), 7770-7788 (2015).
Copyright © 2015 John Wiley and Sons.

§ Figure 1.3[3] is adapted with permission from:
K. Hiramatsu, S. Itoh, H. Amano, I. Akasaki, N. Kuwano, T. Shiraishi, and K. Oki. Growth mechanism of GaN grown on sapphire with AlN buffer layer by MOVPE. *Journal of Crystal Growth* **115** (1), 628-633 (1991).
Copyright © 1991 Elsevier.

§ Figure 2.1a[4] is adapted with permission from:
M. Yoshizawa, A. Kikuchi, M. Mori, N. Fujita, and K. Kishino. Growth of Self-Organized GaN Nanostructures on Al_2O_3(0001) by RF-Radical Source Molecular Beam Epitaxy. *Japanese Journal of Applied Physics* **36** (Part 2, No. 4B), L459–L462 (1997).
Copyright © 1997 The Physical Society of Japan and The Japan Society of Applied Physics.

§ Figure 2.1b[5] is adapted with permission from:
M. A. Sanchez-Garcia, E. Calleja, E. Monroy, F. J. Sanchez, F. Calle, E. Munoz, and R. Beres-ford. The effect of the III/V ratio and substrate temperature on the morphology and properties of GaN- and AlN-layers grown by molecular beam epitaxy on Si(1 1 1). *Journal of Crystal Growth* **183** (1), 23 – 30 (1998).
Copyright © 1998 Elsevier.

§ Figure 2.2a[6], Figure 2.3a[7], and Figure 2.4[8] are adapted with permission from:
V. Consonni, M. Knelangen, L. Geelhaar, A. Trampert, and H. Riecher. Nucleation mechanisms of epitaxial GaN nanowires: Origin of their self-induced formation and initial radius. *Physical Review B* **81** (8), 085310 (2010).
Copyright © 2010 American Physical Society.

---

[1] page 3

[2] page 37

[3] page 6

[4] page 15

[5] page 15

[6] page 19

[7] page 20

[8] page 21

[9] page 19
[10] page 20

§ Figure 2.2b[9] [left] and Figure 2.3b[10] [left] are adapted with permission from:
V. Consonni, M. Hanke, M. Knelangen, L. Geelhaar, A. Trampert, and H. Riechert. Nucleation mechanisms of self-induced GaN nanowires grown on an amorphous interlayer. *Physical Review B* **83** (3), 035310 (2011).
Copyright © 2011 American Physical Society.

[11] page 19
[12] page 20

§ Figure 2.2b[11] [right] and Figure 2.3b[12] [right] are adapted with permission from:
T. Stoica, E. Sutter, R. J. Meijers, R. K. Debnath, R. Calarco, H. Luth, and D. Grutzmacher. Interface and Wetting Layer Effect on the Catalyst-Free Nucleation and Growth of GaN Nanowires. *Small* **4** (6), 751-754 (2008).
Copyright © 2008 John Wiley and Sons.

[13] page 23
[14] page 25

§ Figure 2.5[13] and Figure 2.6a[14] are adapted with permission from:
H.-Y. Chen, H.-W. Lin, C.-H. Shen, and S. Gwo. Structure and photoluminescence properties of epitaxially oriented GaN nanorods grown on Si(111) by plasma-assisted molecular-beam epitaxy. *Applied Physics Letters* **89** (24), 243105 (2006).
Copyright © 2006 AIP Publishing.

[15] page 25

§ Figure 2.6b[15] is adapted with permission from:
F. Furtmayr, M. Vielemeyer, M. Stutzmann, J. Arbiol, S. Estrade, F. Peiro, J. R. Morante,and M. Eickhoff. Nucleation and growth of GaN nanorods on Si (111) surfaces by plasma-assisted molecular beam epitaxy - The influence of Si- and Mg-doping. *Journal of Applied Physics* **104** (3), 034309 (2008).
Copyright © 2008 AIP Publishing.

[16] page 28

§ Figure 2.7[16] is adapted with permission from:
L. Geelhaar, *et al*. Properties of GaN Nanowires Grown by Molecular Beam Epitaxy. *IEEE Journal of Selected Topics in Quantum Electronics* **17** (4), 878-888 (2011).
Copyright © 2011 IEEE.

[17] page 30

§ Figure 2.8a[17] is adapted with permission from:
H. Sekiguchi, T. Nakazato, A. Kikuchi, and K. Kishino. Structural and optical properties of GaN nanocolumns grown on (0001) sapphire substrates by rf-plasma-assisted molecular-beam epitaxy. *Journal of Crystal Growth* **300** (1), 259-262 (2007).
Copyright © 2007 Elsevier.

[18] page 30

§ Figure 2.8b[18] is reproduced with permission from:
J. B. Schlager, K. A. Bertness, P. T. Blanchard, L. H. Robins, A. Roshko, and N. A. Sanford. Steady-state and time-resolved photoluminescence from relaxed

and strained GaN nanowires grown by catalyst-free molecular-beam epitaxy. *Journal of Applied Physics* **103** (12), 124309 (2008).
Copyright © 2008 AIP Publishing.

§ Figure 2.9[19] is adapted with permission from:
R. Calarco, M. Marso, T. Richter, A. I. Aykanat, R. Meijers, A. v.d. Hart, T. Stoica, and H. Luth. Size-dependent Photoconductivity in MBE-Grown GaN-Nanowires. *Nano Letters* **5** (5), 981-984 (2005).
Copyright © 2005 American Chemical Society.

[19] page 33

§ Figure 2.14a[20] is adapted with permission from:
H.-M. Kim, Y.-H. Cho, H. Lee, S. I. Kim, S. R. Ryu, D. Y. Kim, T. W. Kang, and K. S. Chung. High-Brightness Light Emitting Diodes Using Dislocation-Free Indium Gallium Nitride/Gallium Nitride Multiquantum-Well Nanorod Arrays. *Nano Letters* **4** (6), 1059-1062 (2004).
Copyright © 2004 American Chemical Society.

[20] page 40

§ Figure 2.14b[21] is adapted with permission from:
A. Kikuchi, M. Kawai, M. Tada, and K. Kishino. InGaN/GaN Multiple Quantum Disk Nanocolumn Light-Emitting Diodes Grown on (111) Si Substrate. *Japanese Journal of Applied Physics* **43** (No. 12A), L1524-L1526 (2004).
Copyright © 2004 The Japan Society of Applied Physics.

[21] page 40

§ Figure 2.15[22] is adapted with permission from:
H. Sekiguchi, K. Kato, J. Tanaka, A. Kikuchi, and K. Kishino. Ultraviolet GaN-based nanocolumn light-emitting diodes grown on n-(111) Si substrates by rf-plasma-assisted molecular beam epitaxy. *Physica Status Solidi A - Applications and Materials Science* **205** (5), 1067-1069 (2008).
Copyright © 2008 John Wiley and Sons.

[22] page 41

§ Figure 3.1a[23] is adapted with permission from:
E. Stolyarova, K. T. Rim, S. Ryu, J. Maultzsch, P. Kim, L. E. Brus, T. F. Heinz, M. S.Hybertsen, and G. W. Flynn. High-resolution scanning tunneling microscopy imaging of mesoscopic graphene sheets on an insulating surface. *Proceedings of the National Academy of Sciences of the United States of America* **104** (22), 9209-9212 (2007).
Copyright © 2007 National Academy of Sciences, U.S.A.

[23] page 56

§ Figure 3.1b[24] is adapted with permission from:
S. Bae, *et al.* Roll-to-roll production of 30-inch graphene films for transparent electrodes. *Nature Nanotechnology* **5**, 574-578 (2010).
Copyright © 2010 Nature Publishing Group.

[24] page 56

[25]page 59 § Figure 3.2[25] is adapted with permission from:
B.-J. Kim, C. Lee, Y. Jung, K. Hyeon Baik, M. A. Mastro, J. K. Hite, C. R. Eddy, and J. Kim. Large-area transparent conductive few-layer graphene electrode in GaN-based ultraviolet light-emitting diodes. *Applied Physics Letters* **99** (14), 143101 (2011).
Copyright © 2011 AIP Publishing.

[26]page 61 § Figure 3.4a[26] is adapted with permission from:
D. Wei, Y. Liu, Y. Wang, H. Zhang, L. Huang, and G. Yu. Synthesis of N-Doped Graphene by Chemical Vapor Deposition and Its Electrical Properties. *Nano Letters* **9** (5), 1752-1758 (2009).
Copyright © 2009 American Chemical Society.

[27]page 61 § Figure 3.4b[27] is adapted with permission from:
N. Peimyoo, J. Li, J. Shang, X. Shen, C. Qiu, L. Xie, W. Huang, and T. Yu. Photocontrolled Molecular Structural Transition and Doping in Graphene. *ACS Nano* **6** (10), 8878-8886 (2012).
Copyright © 2012 American Chemical Society.

[28]page 67 § Figure 3.6a[28] is adapted with permission from:
H. Li, G. Zhao, H. Wei, L. Wang, Z. Chen, and S. Yang. Growth of Well-Aligned InN Nanorods on Amorphous Glass Substrates. *Nanoscale Research Letters* **11**, 270 (2016).
Copyright © 2016 Springer Nature.

[29]page 67 § Figure 3.6b[29] is adapted with permission from:
V. Kumaresan, L. Largeau, F. Oehler, H. Zhang, O. Mauguin, F. Glas, N. Gogneau, M. Tch-ernycheva, and J.-C. Harmand. Self-induced growth of vertical GaN nanowires on silica. *Nanotechnology* **27** (13), 135602 (2016).
Copyright © 2016 IOP Publishing Ltd.

[30]page 68 § Figure 3.7a[30] is adapted with permission from:
S. Kang, A. Mandal, J. H. Chu, J.-H. Park, S.-Y. Kwon, and C.-R. Lee. Ultraviolet photoconductive devices with an n-GaN nanorod-graphene hybrid structure synthesized by metal-organic chemical vapor deposition. *Scientific Reports* **5**, 10808 (2015).
Copyright © 2015 Springer Nature.

[31]page 68 § Figure 3.7b[31] is adapted with permission from:
F. Yuan, B. Liu, Z. Wang, B. Yang, Y. Yin, B. Dierre, T. Sekiguchi, G. Zhang, and X. Jiang. Synthesis, Microstructure, and Cathodoluminescence of [0001]-Oriented GaN Nanorods Grown on Conductive Graphite Substrate. *ACS Applied Materials & Interfaces* **5** (22), 12066-12072 (2013).
Copyright © 2013 American Chemical Society.

§ Figure 3.8a[32] is adapted with permission from:
M. Heilmann, G. Sarau, M. Gobelt, M. Latzel, S. Sadhujan, C. Tessarek, and S. Christiansen. Growth of GaN Micro- and Nanorods on Graphene-Covered Sapphire: Enabling Conductivity to Semiconductor Nanostructures on Insulating Substrates. *Crystal Growth & Design* **15** (5), 2079-2086 (2015).
Copyright © 2015 American Chemical Society.

[32] page 69

§ Figure 3.8b[33] is adapted with permission from:
M. Heilmann, *et al.* Vertically Oriented Growth of GaN Nanorods on Si Using Graphene as an Atomically Thin Buffer Layer. *Nano letters* **16** (6), 3524-3532 (2016).
Copyright © 2016 American Chemical Society.

[33] page 69

§ Figure 3.8c[34] is adapted with permission from:
V. Kumaresan, *et al.* Epitaxy of GaN Nanowires on Graphene. *Nano letters* **16** (8), 4895-4902 (2016).
Copyright © 2016 American Chemical Society.

[34] page 69

§ Figure 3.9a[35] is reproduced with permission from:
J.-J. Zheng and Y.-J. Li. Tuning the work function of graphene by nitrogen plasma treatment with different radio-frequency powers. *Applied Physics Letters* **104** (23), 233103 (2014).
Copyright © 2014 AIP Publishing.

[35] page 70

§ Figure 3.9b[36] is adapted with permission from:
S. Fernandez-Garrido, *et al.* Molecular Beam Epitaxy of GaN Nanowires on Epitaxial Graphene. *Nano Letters* **17** (9), 5213-5221 (2017).
Copyright © 2017 American Chemical Society.

[36] page 70

§ Figure 3.9c[37] is adapted with permission from:
H. Hayashi, Y. Konno, and K. Kishino. Self-organization of dislocation-free, high-density, vertically aligned GaN nanocolumns involving InGaN quantum wells on graphene/SiO_2 covered with a thin AlN buffer layer. *Nanotechnology* **27** (5), 055302 (2015).
Copyright © 2015 IOP Publishing Ltd.

[37] page 70

§ Figure 3.10a[38] is adapted with permission from:
A. M. Munshi, D.-C. Kim, C. P. Heimdal, M. Heilmann, S. H. Christiansen, P. E. Vullum, A. T. J. van Helvoort, and H. Weman. Selective area growth of AlGaN nanopyramid arrays on graphene by metal-organic vapor phase epitaxy. *Applied Physics Letters* **113** (26), 263102 (2018).
Copyright © 2018 AIP Publishing.

[38] page 71

[39] page 71

§ Figure 3.10b[39] is adapted with permission from:
M. Morassi, *et al*. Selective Area Growth of GaN Nanowires on Graphene Nanodots. *Crystal Growth & Design* **20** (2), 552-559 (2020).
Copyright © 2020 American Chemical Society.

[40] page 86

§ Figure 4.1[40] is adapted with permission from:
M. A. Herman. Physical problems concerning effusion processes of semiconductors in molecular beam epitaxy. *Vacuum* **32** (9), 555-565 (1982).
Copyright © 1982 Elsevier.

[41] page 90

§ Figure 4.2[41] is adapted with permission from:
Epiquest Inc. MBE system. online brochure (2012).
Copyright © 2012 Epiquest, Inc.

[42] page 92

§ Figure 4.3a[42] is adapted with permission from:
S. Khromov. Doping effects on the structural and optical properties of GaN. *Doctoral thesis*. Linkoping University (2013).
Copyright © 2013 Sergey Khromov.

[43] page 95

§ Figure 4.4a[43] is adapted with permission from:
J. S. Nilsen. Advanced transmission electron microscopy of III-V nanowires. *Doctoral thesis*. Norwegian University of Science and Technology (2020).
Copyright © 2020 Julie Stene Nilsen.

[44] page 95

§ Figure 4.4b[44] is adapted with permission from:
T. Saito. The Effect of Trace Elements on Precipitation in Al-Mg-Si alloys - A Transmission Electron Microscopy Study. *Doctoral thesis*. Norwegian University of Science and Technology (2014).
Copyright © 2014 Takeshi Saito.

[45] page 100

§ Figure 4.6b[45] is adapted with permission from:
D. L. Dheeraj. Growth and structural characterization of III-V nanowires grown by molecular beam epitaxy. *Doctoral thesis*. Norwegian University of Science and Technology (2010).
Copyright © 2010 Dheeraj Dasa Lakshmi Narayana.

[46] page 103

§ Figure 4.7b[46] is adapted with permission from:
T. Schmid and P. Dariz. Raman Microspectroscopic Imaging of Binder Remnants in Historical Mortars Reveals Processing Conditions. *Heritage* **2** (2), 1662-1683 (2019).
Copyright © 2019 MDPI.

Index

COLOPHON

This thesis was typeset using LaTeX and the `book` documentclass. Main text is contained within the dimension of 115 mm (width)/197.2 mm (length), where the horizontal (top:bottom) and vertical (left:right) margin ratios are 1:1. The width of the margin notes is 12 mm. Style of this thesis is inspired by Friedrich Wiemer's thesis *Security Arguments and Tool-based Design of Block Ciphers* [https://hss-opus.ub.rub.de/opus4/frontdoor/deliver/index/docId/7044/file/diss.pdf].

Sebastian Kosch's *Crimson* [https://github.com/skosch/Crimson] is set as the running text (11 pt) typeface. Matthew Carter's *Charter* acts as the title (14.4 pt), section (10 pt), subsection (10 pt), and header (8 pt) typefaces. Hermann Zapf's *Palatino* serves as the page (9 pt) typeface. Christian Robertson's *Roboto* [https://tug.org/FontCatalogue/roboto/] is utilized for the figure caption (8 pt) typeface. Libertine Open Fonts Project's *Linux Libertine* [https://tug.org/FontCatalogue/linuxlibertine/] and Linus Romer's *Miama Nueva* [https://tug.org/FontCatalogue/miamanueva/] are used for math/equation (11 pt) and calligraphical (14.4 pt) typefaces. The `textgreek` package [https://www.ctan.org/pkg/textgreek] provides Greek letters in normal font (being not *italicized* as in `$math$` mode).

Six different color palettes exploited throughout this thesis are listed as follows: `RGB: 0, 80, 158` , `RGB: 125, 0, 45` , `RGB: 255, 248, 220` , `RGB: 231, 231, 231` , `RGB: 0, 65, 120` , and `RGB: 128, 128, 128` .

The references were processed by `BibTeX/natbib` -backref option enabled-with modified `unsrtnat` bibliography style. Further details on the packages utilized to make this thesis, along with the LaTeX source (template) of this thesis can be found on https://andreasliudimulyo.github.io.

Most of the graphics in this thesis were generated using `Inkscape` [https://inkscape.org] and `Ngraph` [https://forest.watch.impress.co.jp/library/software/ngraph/].

Final Version as of 22nd of March 2021 (Monday) at 22:03:21.
Printed Version as of 31st of May 2021 (Monday) at 13:31:05.

ISBN 978-82-326-6610-2 (printed ver.)
ISBN 978-82-326-5572-4 (electronic ver.)
ISSN 1503-8181 (printed ver.)
ISSN 2703-8084 (online ver.)

NTNU
Norwegian University of
Science and Technology